



UNIVERSIDAD DISTRITAL
FRANCISCO JOSÉ DE CALDAS

REVISTA Ingeniería

Four-monthly scientific journal

2024

Volume 29 - Issue 1 ISSN 0121-750X E-ISSN 23448393

REVISTA Ingeniería

Volume 29 · Issue 1 · Year 2024 · ISSN 0121-750X · E-ISSN 2344-8393

Four-monthly Scientific Journal



UNIVERSIDAD DISTRITAL
FRANCISCO JOSÉ DE CALDAS

Carrera 7 No. 40-53
Edificio Administrativo
Piso 7 - Facultad de Ingeniería
Bogotá, Colombia
Teléfono: + 57 (1) 323 93 00 ext. 2413
Correo revista:
revista_ing@udistrital.edu.co

<http://revistas.udistrital.edu.co/ojs/index.php/reving>

Focus and Scope

The *Ingeniería* journal is an open-access academic-scientific online publication specialized in knowledge related to the fields of Engineering and Technology, according to the classification of scientific areas established by the Organization for Economic Cooperation and Development (OECD). Its main goal is to disseminate and promote debates about advances in research and development in the diverse areas of Engineering and Technology. We focus on disseminating original and unpublished articles in English that are relevant at both the national and international level. We seek to provide a platform to share knowledge and foster collaboration between researchers and professionals in the field. The journal does not request any Article Processing Charges (APC), as it is directly funded by Universidad Distrital Francisco José de Caldas. Moreover, the journal operates following a double-blind review process, thus ensuring the impartiality and quality of the published works. The journal is published in a continuous fashion and follows a quarterly numbering.

Editors

Editor-in-chief

Oscar Danilo Montoya Giraldo, PhD.
Universidad Distrital Francisco José de Caldas, Colombia

Associate Editor

Nelson Leonardo Díaz, PhD.
Universidad Distrital Francisco José de Caldas, Colombia

Scientific and editorial committee

PhD. Alonso Salvador Sanchez
Universidad de Alcalá
Spain

PhD. Arul Rajagopalan
Vellore Institute of Technology
Chennai, India.

PhD. Carlos Andrés Peña
Institute for Information and
Communication Technologies -
HEIG-VD, Switzerland.

PhD. Federico Martin Serra
Universidad Nacional de San Luis
Argentina

PhD. Iván Santelices Malfanti
Universidad del Bío-Bío
Chile

PhD. Jesús de la Casa Hdez
Universidad de Jaén
Spain

PhD. José Marcio Luna
Perelman School of Medicine
University of Pennsylvania
United States

PhD. Josep M. Guerrero
Aalborg University
Dinamarca

PhD. Nelson L. Díaz
Universidad Distrital Francisco
José de Caldas
Colombia

PhD. Sarah Greenfield
Centre for Computational
Intelligence De Montfort Interdisciplinary
England

Directives

Giovanny Tarazona Bermúdez, PhD.
Rector

Nelson Enrique Vera Parra, PhD.
Director Office of Research

José Ignacio Rodríguez Molano, PhD.
Dean Faculty of Engineering

Technical Committee

Ingri Gisela Camacho, BSc.
Editorial Manager

Julian Arcila-Forero, MSc.
Layout Artist (LATEX)

José Daniel Gutiérrez Mendoza
Spanish/English Proofreader

Open Access Policy

The *Ingeniería* journal provides free access to its content. This free access is granted under the principle of making research freely available to the public, which encourages a greater exchange of global knowledge.

Attribution-NonCommercial-ShareAlike 4.0 International (CC BY-NC-SA 4.0)

You are free to:

- **Share** — copy and redistribute the material in any medium or format
- **Adapt** — remix, transform, and build upon the material
- The licensor cannot revoke these freedoms as long as you follow the license terms

Article Processing Charge

No publication fees are charged to the authors or their institutions, nor are any payments made to expert peer reviewers or associate or adjunct editors. The *Ingeniería* journal is funded by Universidad Distrital Francisco José de Caldas, its Faculty of Engineering, and its Central Research Office.

Indexed



Peer-reviewers in this issue

Ayad M. Takhakh
Al-Nahrain University, Iraq

César Augusto Isaza
Universidad Pontificia Bolivariana, Colombia

Jesus Maria Lopez Lezama
Universidad de Antioquia, Colombia

José Matas
Universitat Politècnica de Catalunya, Spain

Juan Manuel Cueva Lovelle
Universidad de Oviedo, Spain

Luis Fernando Grisales Norena
Universidad de Talca, Chile

Mohammad Saber Fallah Nezhad
Department of Industrial Engineering, Yazd University

Pedro Arcos Gonzalez
Universidad de Oviedo, Spain

Tomas Echaveguren
Universidad de Concepción, Chile

Wilfrido Arteaga Sarmiento
Universidad Militar Nueva Granada, Colombia

Celso A. Sánchez-Ramírez
Universidad de Santiago, Chile

César Leonardo Trujillo Rodríguez
Universidad Distrital Francisco José de Caldas, Colombia

José González-Córdoba
Universidad Autónoma de Querétaro, Mexico

Juan Camilo López
Universidade Estadual de Campinas, Brazil

Laura Patricia Martínez-Padilla
Universidad Nacional Autónoma de México, Mexico

Maximiliano Bueno Lopez
Universidad de Cauca, Colombia

Pablo Gamazo
Universidad de la República, Uruguay

Ruben Vazquez-Medina
Instituto Politécnico Nacional, CICATA Queretaro, Mexico

Walter Julián Gil González
Universidad Tecnológica de Pereira, Colombia

Table of contents

Editorial

Network for the Large-Scale Integration of Renewable Energies in Electrical Systems (RIBIERSE-CYTED, 723RT0150): Results for 2023

María Ángeles Medina-Quesada, Federico Martín Serra, Carlos Rodrigo Baier-Fuentes, Oscar Danilo Montoya-Giraldo, Joao André Pinto Soares, Bruno Wanderley França, Fabio Andrade-Rengifo, Jesús de la Casa Hernández

Biomedical Engineering

Dynamic Model of Lower Limb Motion in the Sagittal Plane during the Gait Cycle

Jose Luis Sarmiento-Ramos, Andrés Felipe Meneses-Castro, Pedro José Jaimes-Mantilla

Statistical Analysis by Linear Regression of the Prevalence of Flatfoot in Preschool Children of a Mexican Community

Carlos I. Cabrera-Perez, Juan A. López-Valdez, Horacio Rostro-González, Jatziry S. Cano-Lara, Miroslava Cano-Lara

Civil and Environmental Engineering

Safety Performance Functions for Mountain Two-lane Rural Roads in Ecuador

Yasmany García-Ramírez

How Accurately Are Climatological Characteristics and Surface Water and Energy Balances Represented for the Colombian Amazon Basin?

Carolina Valencia-Monroy, Astrid Baquero-Bernal

Computational Intelligence

Methodology for Inventory Management in Neighborhood Stores Using Machine Learning and Integer Linear Programming

Carlos Alberto Henao-Baena, Bibiana Zuluaga-Zuluaga, Julian Galeano-Castro, Edward Jhohan Marín-García, Andrés Felipe Calvo-Salcedo

Estimating Acceleration from a Single Uniform Linear Motion-Blurred Image using Homomorphic Mapping and Machine Learning

Jimmy Alexander Cortés-Osorio, Juan Bernardo Gómez-Mendoza, Juan Carlos Riaño-Rojas

Transgenic Algorithm Applied to the Job Shop Rescheduling Problem

Néstor Andrés Beltrán-Bernal, José Ignacio Rodríguez-Molano, Diego Ernesto Mendoza-Patiño

Electrical, Electronic and Telecommunications Engineering

Deduction and Application of the Average Switch Model in Power Electronic Devices for Simulation Time Reduction

Santiago Benavides-Córdoba, Anamaria Romero-Carvajal, Nicolas Muñoz-Galeano, Juan Bernardo Cano-Quintero, Jesús María López-Lezama

Stochastic Mixed-Integer Branch Flow Optimization for the Optimal Integration of Fixed-Step Capacitor Banks in Electrical Distribution Grids

Walter Julián Gil-González, Andrés Herrera-Orozco, Alexander Molina-Cabrera

Energy Management Systems for Microgrids: Evolution and Challenges within the Framework of the Energy Transition

Carlos Santiago Vidal-Martínez, Maximiliano Bueno-López, Juan Fernando Flórez-Marulanda, Álvaro Rene Restrepo

Editorial

Network for the Large-Scale Integration of Renewable Energies in Electrical Systems (RIBIERSE-CYTED, 723RT0150): Results for 2023

María Ángeles Medina¹, Federico Martin Serra², Carlos Rodrigo Baier³, Oscar Danilo Montoya¹, Joao André Soares⁵, Bruno Wanderle França⁶, Fabio Andrade-Rengifo², and Jesús de la Casa Hernández¹

¹Universidad de Jaén, Jaén, Spain 

²Universidad Nacional de San Luis, San Luis, Argentina 

³Universidad de Talca, Curicó, Chile 

⁴Universidad Distrital Francisco José de Caldas, Colombia 

⁵GECAD - Research Group on Intelligent Engineering and Computing for Advanced Innovation and Development, LASI - Intelligent Systems Associate Laboratory, Polytechnic of Porto, Porto, Portugal 

⁶Universidade Federal Fluminense, Niterói, RJ, Brazil 

⁷University of Puerto Rico, Mayaguez, Mayaguez, USA 

The RIBIERSE-CYTED network, *i.e.*, the network for the large-scale integration of renewable energies in electrical systems (723RT0150) (2023-2026) is a hub for researchers and technologists belonging to Ibero-American universities, companies, and local administrations. This network promotes cross-training, mobility between centers, and the dissemination and implementation of technical and training activities aimed at analyzing and developing opportunities for the maximal integration of renewable resources, seeking a more sustainable energy model while allowing for the increased use of renewable resources and electric mobility (e-mobility).

This framework of cooperation and joint scientific research allows establishing synergies and exchanging experiences in order to construct a shared vision of Ibero-American society, from suppliers to end users, thanks to the fostering and transfer of knowledge to the business sector and the training of users. To this effect, the proposed lines of action, which are derived from the specific objectives of this network, are grouped into three areas. The first line includes the assessment of energy planning models and tools, as well as the prediction, evaluation, control, and management of

* **Correspondence:** jcasa@ujaen.es, odmontoyag@udistrital.edu.co

Editorial

© The authors;
reproduction
right holder
Universidad
Distrital
Francisco José de
Caldas.

Open access



renewable sources currently in use in Ibero-American countries, with the aim of extending, developing, and systematizing their application. The second line deals with analyzing the effective application of methodologies in real cases. Finally, the third line is dedicated to the technical training of researchers and suppliers of sustainable systems, as well as to the electrical eco-literacy of end users.

The kick-off meeting of the RIBIERSE-CYTED network was held in the second half of 2023, and it was a great challenge to arrange its schedule, as the network is made up of 22 Latin American countries and 214 researchers. As a consequence, all actions, distributed among 13 specific objectives, have led to the following achievements:

- 23 research projects on the development of technical and economic tools for optimal electricity management, which are aimed at hybridizing different renewable energy, storage, and e-mobility technologies as well as improving the transfer of results from research groups to the industrial sector and society in general.
- Three infrastructure works, *i.e.*, the construction of a solar thermal collector testing laboratory (Panama), the expansion of the ETL laboratory at Universidad de Talca (Chile), and the construction of the Pelton hydraulic microturbine's remote laboratory (Bolivia).
- Four technological contracts: one involving energy efficiency consulting for Isla de la Juventud (Cuba) and three related to electric vehicle safety (Cuba).
- 21 final degree projects from network member universities, namely in Spain, Argentina, Cuba, Ecuador, Colombia, Panama, Portugal, and Venezuela.
- Three doctoral theses from partner universities in Spain and Argentina.
- Two utility patents (currently in the process of application or undergoing processing): a power quality analyzer and a system and method for smoothing photovoltaic generation intermittency (Brazil).
- Three internships linked to the selection of electric motors for artisanal fishing boats equipped with photovoltaic panels (Colombia), the Engineering Coop Program at LUMA (Puerto Rico) and, finally, the Faculty Mini Sabbatical Program of Summer 2023 hosted by Lawrence Livermore National Security LLC (LLNS) (Puerto Rico).
- Five short mobilities: from Spain to Brazil, from Spain to Argentina, within Colombia, from Portugal to Spain, and from Portugal to Spain, with funding external to CYTED.
- One cycle of postgraduate conferences with speakers from members from Spain and Colombia, which was published on the CYTED website.
- Five technical courses in Cuba, Ecuador, El Salvador, Panama, and Peru.
- Two postgraduate courses in Argentina and Colombia, two Diploma courses in Panama and, finally, two research conferences in Cuba and Ecuador.
- Two semiannual/annual meetings of the RIBIERSE-CYTED network: the first one (the kick-off meeting) was held online at the University of Jaén (Spain) during June 2023, and the second one, the first annual meeting, was held in the city of Manabí (Ecuador), within in the framework of the VII Scientific Convention of Universidad Técnica de Manabí (UTM), with broad participation by the partners and co-financing members of the University of Jaén and UTM, respectively.

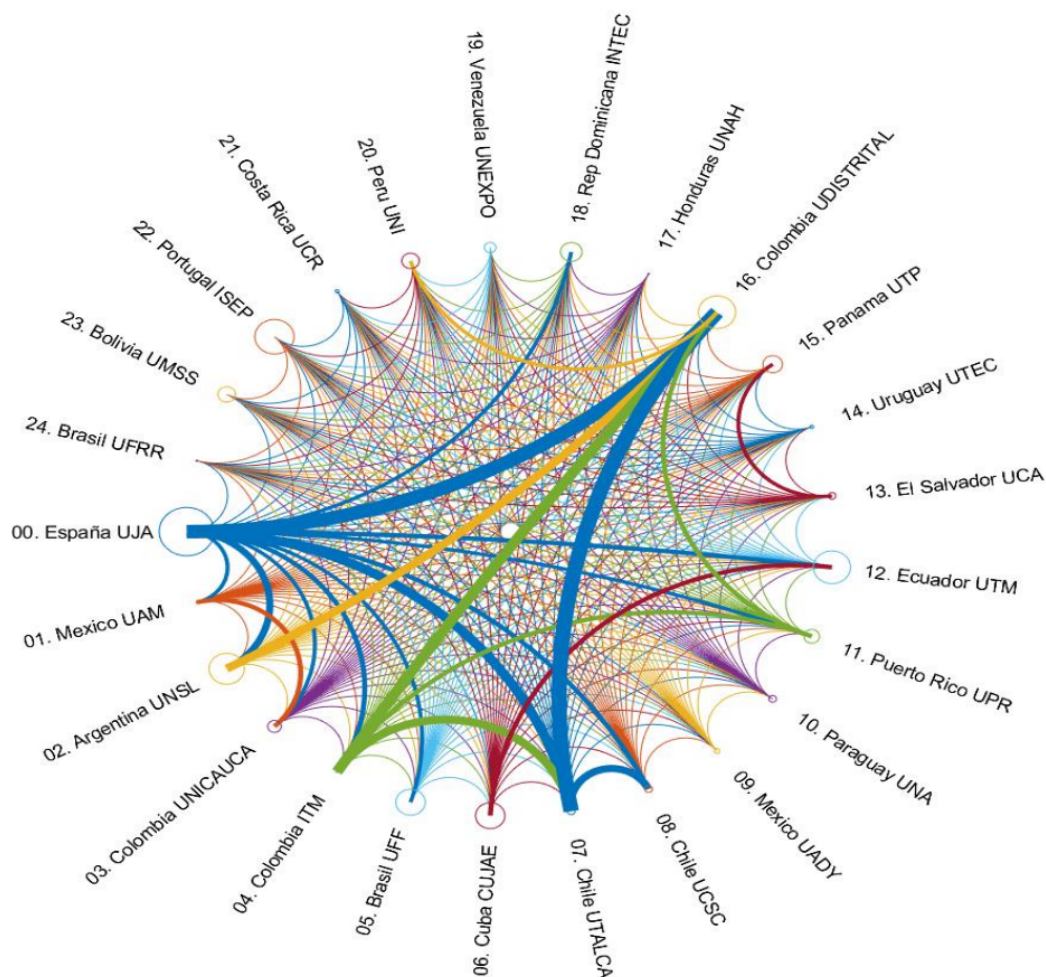


Figure 1. Interrelation between partners in collaborative activities

- Participation in Universidad Nacional de San Luis's Engineering Week (Argentina), two seminars in Argentina and Colombia (one was collaborative, with the participation of more than one member of the network), the II Symposium on Electrical Engineering in Colombia, the Workshop on the Rural Energization Plan for the Cauca Region (Colombia), the 52nd Technical Exhibition at the Ricaldone Institute: Electric Vehicles (El Salvador), and, finally, the V INERGE Workshop (Brazil).
- 113 articles published in scientific journals, 31 of which were collaborative works.
- 34 articles related to participation in scientific events (conferences).
- One event memoir.
- 10 deliverables with the participation of all RIBIERSE members.
- 34 news pieces, eight of which are available on the [CYTED website](#) and are related to the achievements made by the network in Spain, Ecuador, El Salvador, Panama, Chile, and Argentina.

In addition, 28 CYTED pieces have been disseminated through other channels and are related to congresses, courses, conferences, engineering weeks, workshop seminars, doctoral theses, short mobilities, and attendance to scientific events.

Figure 1 describes the interrelation between the participants involved in collaborative activities. This figure faithfully reflects what happened in the first year of the network's journey, as collaboration between member partners is still difficult, sometimes due to lack of knowledge regarding the lines of work of each research group or regarding personal relationships that can benefit professionals in the medium and long term.

Finally, it is worth noting that all the achievements during the network's first year of collaborative work demonstrate the great commitment of its members, who are grateful for the support offered by the Ibero-American Program of Science and Technology for Development (CYTED)**. It is also worth highlighting the funding and patronage provided to the RIBIERSE-CYTED network by the University of Jaén, UTM, and all the participating universities and companies external to the network for its activities.

María Ángeles Medina Quesada

Departamento de Ingeniería Eléctrica, Universidad de Jaén, Jaén, Spain.

Email: aquesada@ujaen.es

Federico Martin Serra

Laboratorio de Control Automático, Facultad de Ingeniería y Ciencias Agropecuarias, Universidad Nacional de San Luis, San Luis, Argentina.

Email: fmserra@unsl.edu.ar

Carlos Rodrigo Baier Fuentes

Departamento de Ingeniería Eléctrica, Universidad de Talca, Curicó, Chile.

Email: cbaier@ieee.org

Oscar Danilo Montoya Giraldo

Grupo de Compatibilidad e Interferencia Electromagnética (GCEM), Facultad de Ingeniería, Universidad Distrital Francisco José de Caldas, Colombia.

Email: odmontoyag@udistrital.edu.co

Joao André Pinto Soares

GECAD - Research Group on Intelligent Engineering and Computing for Advanced Innovation and Development, LASI - Intelligent Systems Associate Laboratory, Polytechnic of Porto, Porto, Portugal.

Email: jan@isep.ipp.pt

**The CYTED program was created by the governments of Ibero-American countries to foster cooperation in science, technology, and innovation while aiming for harmonious development.

Bruno Wanderley França

Departamento de Engenharia Elétrica, Núcleo de Inovação Tecnológica em Engenharia Elétrica - NITEE, Universidade Federal Fluminense, Niterói, RJ, Brazil.

Email: bwfranca@id.uff.br

Fabio Andrade Rengifo

Department of Electrical and Computer Engineering, University of Puerto Rico, Mayaguez, Mayaguez campus, PR 00681, USA.

Email: fabio.andrade@upr.edu

Jesús de la Casa Hernández

Departamento de Ingeniería Eléctrica, Universidad de Jaén, Jaén, Spain.

Email: jcasa@ujaen.es



Research

Dynamic Model of Lower Limb Motion in the Sagittal Plane during the Gait Cycle

Modelo dinámico del movimiento del miembro inferior en el plano sagital durante el ciclo de marcha

José Luis Sarmiento-Ramos¹  *, Andrés Felipe Meneses-Castro², and Pedro José Jaimes-Mantilla²

¹Rambal S.A.S BIC (Bucaramanga, Colombia). Universidad Santo Tomás 

²Universidad Manuela Beltrán (Bucaramanga, Colombia) 

Abstract

Context: This work presents the development of a dynamic model for human lower limb motion in the sagittal plane during the gait cycle. The primary objective of this model is to serve as a powerful tool for the design of rehabilitation and assistive devices, such as exoskeletons, prostheses, and orthoses. It achieves this by facilitating the estimation of joint torques, the detailed analysis of kinematic variables, optimal actuator selection, and the exploration of advanced control techniques.

Method: The dynamic model consists of two primary components: (1) the plant model and (2) a closed-loop controller. The plant model represents the forward dynamics of human gait and is based on a multi-mass pendulum composed of three segments of the lower limb (thigh, lower leg, and foot) and three joints (hip, knee, and ankle). It is analyzed using the Euler-Lagrange formulation and the nonlinear second-order differential equations are implemented in MATLAB's Simulink. To reproduce reference human gait trajectories and simulate the functioning of the neuromusculoskeletal system and the central nervous system, a closed-loop PID controller is incorporated into the plant model. It is noteworthy that the scope of this dynamic model is specifically confined to the sagittal plane.

Results: The dynamic model is evaluated in terms of angular displacement tracking using the relative maximum error (RME) and the root mean square error (RMSE) for reference trajectories of healthy adult male human gait as reported in the literature. The model demonstrates tracking with errors below 2.2 [°] in magnitude and 3,5 % for all three considered segments (thigh, lower leg, and foot).

Conclusions: The quantitative results show that the dynamic model developed in this work is reliable and allows for a precise reproduction of human gait trajectories.

Keywords: biomechanics, Euler-Lagrange, human gait, PID control, Simulink

Article history

Received:
11th/Jan/2023

Modified:
19th/sep/2023

Accepted:
10th/Oct/2023

Ing, vol. 29, no. 1,
2024. e20333

©The authors;
reproduction right
holder Universidad
Distrital Francisco
José de Caldas.

Open access



*  **Correspondence:** joseluis_251094@hotmail.com

Resumen

Contexto: Este trabajo presenta el desarrollo de un modelo dinámico del movimiento del miembro inferior humano en el plano sagital durante el ciclo de marcha. El objetivo principal de este modelo es servir como una herramienta poderosa para el diseño de dispositivos de rehabilitación y asistencia, como exoesqueletos, prótesis y órtesis. Esto lo logra facilitando la estimación de torques en las articulaciones, el análisis detallado de variables cinemáticas, la selección óptima de actuadores y la exploración de técnicas avanzadas de control.

Método: El modelo dinámico se consiste en dos componentes principales: (1) el modelo de la planta y (2) un controlador de lazo cerrado. El modelo de la planta representa la dinámica directa de la marcha humana y se basa en un péndulo de múltiples masas compuesto por tres segmentos del miembro inferior (muslo, pantorrilla y pie) y tres articulaciones (cadera, rodilla y tobillo). Este es analizado utilizando la formulación de Euler-Lagrange y las ecuaciones diferenciales de segundo orden no lineales se implementan en Simulink de MATLAB. Para reproducir las trayectorias de referencia de la marcha humana y simular el funcionamiento del sistema musculoesquelético y del sistema nervioso central, se implementa un controlador PID de lazo cerrado en el modelo de la planta. Es importante destacar que el alcance de este modelo dinámico se limita específicamente al plano sagital.

Resultados: El modelo dinámico es evaluado en términos del seguimiento del desplazamiento angular usando el error relativo máximo (RME) y el error medio cuadrático (RMSE) para trayectorias de referencia de la marcha humana de adultos masculinos sanos reportadas en la literatura. El modelo demuestra un seguimiento con errores por debajo de 2.2 [°] en magnitud y 3,5 % para los tres segmentos considerados (muslo, pantorrilla y pie).

Conclusiones: Los resultados cuantitativos muestran que el modelo dinámico desarrollado en este trabajo es confiable y permite reproducir precisamente las trayectorias de la marcha humana.

Palabras clave: biomecánica, Euler-Lagrange, marcha humana, control PID, Simulink

Table of contents

		2.2. Closed-loop controller	9
	Page	3. Simulations and results	12
1. Introduction	2	4. Conclusions	14
2. Dynamic model	5	5. Author contributions	16
2.1. Plant model	5	References	16

1. Introduction

Gait, also referred to as bipedal locomotion, is a cyclic and fundamental movement that involves a sequence of repetitive events, initiating and concluding with the contact of the initial foot with the ground. This dynamic process encompasses a steady-state gait cycle, comprising the stance phase (when the reference foot is on the ground) and the swing phase (when the reference foot is off the

ground). Gait constitutes a complex functional task that necessitates intricate coordination between numerous major joints within the human body, with particular emphasis on the lower limb (1).

The modeling of human gait has garnered substantial attention from researchers in recent decades due to its profound implications in biomedical engineering. This interest arises from its applications in designing rehabilitation and assistive devices, as well as analyzing abnormal gait patterns and their consequences. Currently, the design of such devices, including exoskeletons, prostheses, and orthoses, often relies on empirical and trial-and-error approaches. Many of these devices are constructed and subsequently tested on individuals before obtaining valuable feedback, resulting in an inefficient and costly design process. Dynamic models provide a robust tool for designers by enabling the estimation of crucial kinematic and kinetic variables, such as angular displacements, velocities, accelerations, joint torques, and muscle forces. This facilitates optimal actuator selection and in-depth investigation into control techniques in order to achieve satisfactory performance before implementation (2–4). A rigorous and precise modeling approach enables the extrapolation of simulation results into practical applications, allowing designers to thoroughly evaluate their devices in a virtual environment before prototyping and human testing, thus reducing risks and costs (5). Additionally, dynamic modeling serves as a valuable resource for clinicians, rehabilitation experts, and researchers, enhancing their comprehension of both normal and pathological gait patterns and assisting in the identification of causes and effects related to abnormal movement patterns. A comprehensive understanding of the gait cycle, its parameters, and the principles underlying the musculoskeletal system and the central nervous system (CNS) provides essential insights for evaluating and treating locomotion dysfunctions in clinical environments (1).

Research regarding the dynamic modelling of human gait can be categorized into two main fields: (1) musculoskeletal models and (2) biped robotics models. Musculoskeletal models (6) focus on the interaction and contributions of individual muscles, tendons, and ligaments during gait, emphasizing in the physiological aspects of bipedal locomotion. These models are highly intricate and computationally intensive, given their numerous degrees of freedom (DOF), diverting attention from the fundamental dynamics of the human gait. In contrast, biped robotics models aim at real-time gait control and the evaluation of kinematic and kinetic variables of joints and body segments. According to (7), biped robotics models can be divided into five groups: (1) pendulum models, (2) passive dynamic walkers, (3) zero-moment-point (ZMP) methods, (4) optimization-based methods, and (5) control-based methods.

Pendulum models are based on the principle of energy conservation, capturing the exchange between the kinetic and potential energy inherent in walking. Research in this area ranges from simple planar (8,9) to 3D (10,11) and multi-mass pendulum models (12,13). Pendulum models offer advantages in terms of simplicity, closed-form analytical solutions, and their ability to represent energy exchange principles during gait. However, they can oversimplify dynamics when certain joints and segments, such as the knee, ankle, lower leg, or foot, are not explicitly considered.

Passive dynamic walkers (14–16) are biped models that emulate a compass-like mechanism driven purely by gravity as they descend gentle slopes. These models do not involve any actuation or control of

joint angles or torques at any point. During their descent, the leg follows a pendulum-like trajectory, and the swing foot's contact with the ground is dictated by the conservation of angular momentum. Passive dynamic walkers are simple and efficient models suitable for investigating the fundamental principles of human gait, including the relationship between step length and velocity, energy expenditure, and the transition from walking to running. However, like pendulum-based models, they may oversimplify dynamics by neglecting certain joints and segments.

ZMP methods (17–19) focus on achieving bipedal walking by enforcing the body's balance to follow predefined locations. Each ZMP represents a point on the ground where the net moment of active forces, including inertia, gravity, and external forces from actuators, is zero. The dynamic equations in this approach primarily serve to ensure balance constraints rather than coordinate the entire gait trajectory. ZMP methods are computationally efficient for the real-time control of biped robots. However, it is essential to note that preplanned ZMP locations do not precisely mimic human walking principles or the CNS's control of gait.

Optimization-based methods (7, 20, 21) are computational approaches that seek to uncover the criteria governing human gait generation by the CNS. In these methods, the objective function – intended for optimization – typically represents a gait-related performance measure, such as dynamic effort, mechanical energy, metabolic energy, jerk, or stability. Constraints encompass the joint range of motion (ROM) and maximum joint torques. These methods offer insights into the relationship between gait and performance measures, shedding light on the working principles of human walking. However, they demand significant computational resources, are not well-suited for real-time applications, and rely on experimental data.

Control-based methods are deployed in humanoid robots to facilitate bipedal walking, allowing for interaction with the environment, responses to external disturbances, and real-time task execution. This approach closely approximates the natural control mechanisms of the human CNS, ensuring accurate analysis, estimation, and tracking of normal and pathological gait motions. Control-based methods can be classified into three categories: (1) tracking control, (2) optimal control, and (3) predictive control. Tracking control (22,23) involves calculating input forces or torques required to achieve desired walking trajectories for body segments using kinematic feedback. In optimal control approaches (24,25), input forces or torques are treated as unknown variables in motion equations and are continuously optimized for the subsequent time step, also employing kinematic feedback. Predictive control methods (5,22) are rooted in iterative finite horizon optimization, where online calculations are used to determine input forces or torques. This process minimizes a cost function incorporating kinematic feedback.

This paper introduces a dynamic model of human lower limb motion in the sagittal plane during the gait cycle. This model falls under the category of biped robotics and represents a hybrid approach incorporating elements of both pendulum and control-based methods. The model comprises two primary components: (1) the plant model, founded on a multi-mass pendulum, and (2) a closed-loop PID controller. The plant model captures the forward dynamics of human gait, employing the Euler-Lagrange formulation while considering the lower limb as consisting of three segments (thigh,

lower leg, and foot) and three joints (hip, knee, and ankle). The PID controller is integrated to estimate the joint torques necessary for replicating human gait reference trajectories. It constitutes a potent tool for the design of rehabilitation and assistive devices, facilitating joint torque estimation, kinematic variable analysis, optimal actuator selection, and the exploration of control techniques.

2. Dynamic model

As mentioned in the introduction, the dynamic model proposed for human lower limb motion encompasses two essential components: (1) the plant model and (2) a closed-loop PID controller. The plant model (the core of the dynamic model) represents the forward dynamics of human gait, and the closed loop controller simulates the working principle of the neuromusculoskeletal system and the CNS.

It is worth noting that the scope of this dynamic model is specifically confined to the sagittal plane. This deliberate limitation stems from the recognition that the motion and dynamic effects of the lower limb within the frontal and transverse planes exhibit diminished relevance compared to those within the sagittal plane (1).

2.1. Plant model

The plant model, responsible for capturing the dynamics of human lower limb motion, is meticulously formulated using the Euler-Lagrange formulation. This mathematical framework is applied to the system depicted in Fig. 1, which comprises three lower limb segments (thigh, lower leg, and foot) interconnected by three joints (hip, knee, and ankle). Each of the lower limb segments is modeled as a rigid bar by specific attributes. These attributes include length L_n , mass m_n , and the proximal gravity center l_n . These segments are positioned at angular positions θ_n relative to the vertical axis. To distinguish between the individual segments within the model, subscripts are employed as follows: '1' for the thigh, '2' for the lower leg, and '3' for the foot. The foundation of this modeling framework is established in a fixed coordinate system with its origin situated at the hip joint.

The Lagrangian L is established as the difference between the system's kinetic energy T and its potential energy V :

$$L = T - V \quad (1)$$

The kinetic energy is defined by Eq. (2), which incorporates the kinetic energy of each individual segment. In this equation, v_n represents the linear velocity, J_n denotes the moment of inertia, and $\dot{\theta}_n$ represents the angular velocity.

$$T = \frac{m_1 v_1^2}{2} + \frac{J_1 \dot{\theta}_1^2}{2} + \frac{m_2 v_2^2}{2} + \frac{J_2 \dot{\theta}_2^2}{2} + \frac{m_3 v_3^2}{2} + \frac{J_3 \dot{\theta}_3^2}{2} \quad (2)$$

The linear velocity can be expressed as the magnitude of the first derivative of the position vector r_n of the gravity center for each segment: $v_n = |\dot{r}_n|$. The centers of gravity for the thigh, lower leg, and foot are situated at positions r_1 , r_2 and r_3 , respectively:

$$r_1 = \begin{bmatrix} l_1 \sin \theta_1 \\ -l_1 \cos \theta_1 \end{bmatrix} \quad (3)$$

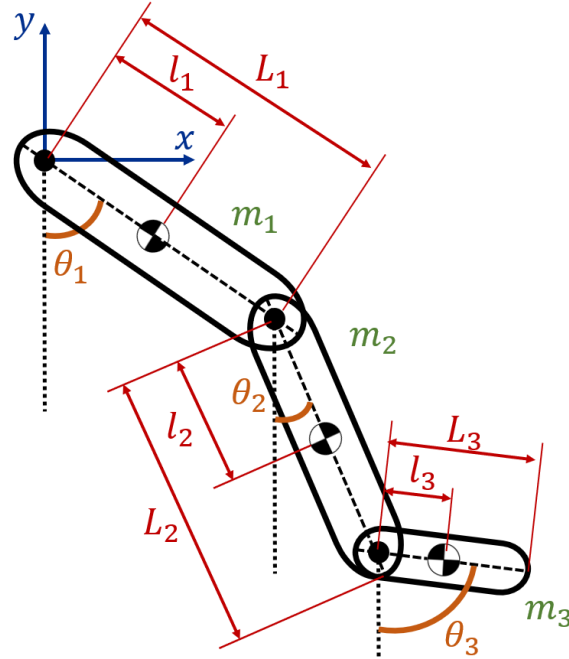


Figure 1. Representation of human lower limb for dynamic modeling

$$r_2 = \begin{bmatrix} L_1 \sin \theta_1 + l_2 \sin \theta_2 \\ -L_1 \cos \theta_1 - l_2 \cos \theta_2 \end{bmatrix} \quad (4)$$

$$r_3 = \begin{bmatrix} L_1 \sin \theta_1 + L_2 \sin \theta_2 + l_3 \sin \theta_3 \\ -L_1 \cos \theta_1 - L_2 \cos \theta_2 - l_3 \cos \theta_3 \end{bmatrix} \quad (5)$$

Therefore, the linear velocities of the thigh, lower leg, and foot are established as:

$$v_1 = \dot{\theta}_1 l_1 \quad (6)$$

$$v_2 = \sqrt{\dot{\theta}_1^2 L_1^2 + \dot{\theta}_2^2 l_2^2 + 2\dot{\theta}_1 \dot{\theta}_2 L_1 l_2 \cos(\theta_1 - \theta_2)} \quad (7)$$

$$v_3 = \sqrt{\dot{\theta}_1^2 L_1^2 + \dot{\theta}_2^2 L_2^2 + \dot{\theta}_3^2 l_3^2 + 2\dot{\theta}_1 \dot{\theta}_2 L_1 L_2 \cos(\theta_1 - \theta_2) + 2\dot{\theta}_2 \dot{\theta}_3 L_2 l_3 \cos(\theta_2 - \theta_3) + 2\dot{\theta}_1 \dot{\theta}_3 L_1 l_3 \cos(\theta_1 - \theta_3)} \quad (8)$$

Substituting Eqs. (6), (7), and (8) into (2) results in the following expression for the kinetic energy of the system:

$$\begin{aligned} T = & \frac{m_1 \dot{\theta}_1^2 l_1^2}{2} + \frac{J_1 \dot{\theta}_1^2}{2} + \frac{m_2 \dot{\theta}_1^2 L_1^2}{2} + \frac{m_2 \dot{\theta}_2^2 l_2^2}{2} + m_2 \dot{\theta}_1 \dot{\theta}_2 l_1 l_2 \cos(\theta_1 - \theta_2) + \frac{J_2 \dot{\theta}_2^2}{2} \\ & + \frac{m_3 \dot{\theta}_1^2 L_1^2}{2} + \frac{m_3 \dot{\theta}_2^2 L_2^2}{2} + \frac{m_3 \dot{\theta}_3^2 l_3^2}{2} + m_3 \dot{\theta}_1 \dot{\theta}_2 L_1 L_2 \cos(\theta_1 - \theta_2) \\ & + m_3 \dot{\theta}_2 \dot{\theta}_3 L_2 l_3 \cos(\theta_2 - \theta_3) + m_3 \dot{\theta}_1 \dot{\theta}_3 L_1 l_3 \cos(\theta_1 - \theta_3) + \frac{J_3 \dot{\theta}_3^2}{2} \end{aligned} \quad (9)$$

The potential energy is defined by Eq. (10), which incorporates the potential energy of each individual segment. In this equation, g denotes the gravity, and h_n represents the height of the center of gravity relative to the coordinate system.

$$V = m_1gh_1 + m_2gh_2 + m_3gh_3 \quad (10)$$

The height of the center of gravity for the thigh, lower leg, and foot can be expressed in terms of the angular displacement as:

$$h_1 = -l_1 \cos \theta_1 \quad (11)$$

$$h_2 = -L_1 \cos \theta_1 - l_2 \cos \theta_2 \quad (12)$$

$$h_3 = -L_1 \cos \theta_1 - L_2 \cos \theta_2 - l_3 \cos \theta_3 \quad (13)$$

Substituting Eqs. (11), (12), and (13) into (10) results in the following expression for the potential energy of the system:

$$V = -m_1gl_1 \cos \theta_1 - m_2gL_1 \cos \theta_1 - m_2gl_2 \cos \theta_2 - m_3gL_1 \cos \theta_1 - m_3gL_2 \cos \theta_2 - m_3gl_3 \cos \theta_3 \quad (14)$$

Eqs. (9) and (14) are substituted into (1) to obtain the Lagrangian of the system:

$$\begin{aligned} T = & \frac{m_1\dot{\theta}_1^2 l_1^2}{2} + \frac{J_1\dot{\theta}_1^2}{2} + \frac{m_2\dot{\theta}_1^2 L_1^2}{2} + \frac{m_2\dot{\theta}_2^2 l_2^2}{2} + m_2\dot{\theta}_1\dot{\theta}_2 l_1 l_2 \cos(\theta_1 - \theta_2) + \frac{J_2\dot{\theta}_2^2}{2} \\ & + \frac{m_3\dot{\theta}_1^2 L_1^2}{2} + \frac{m_3\dot{\theta}_2^2 L_2^2}{2} + \frac{m_3\dot{\theta}_3^2 l_3^2}{2} + m_3\dot{\theta}_1\dot{\theta}_2 L_1 L_2 \cos(\theta_1 - \theta_2) \\ & + m_3\dot{\theta}_2\dot{\theta}_3 L_2 l_3 \cos(\theta_2 - \theta_3) + m_3\dot{\theta}_1\dot{\theta}_3 L_1 l_3 \cos(\theta_1 - \theta_3) + \frac{J_3\dot{\theta}_3^2}{2} \\ & + m_1gl_1 \cos \theta_1 + m_2gL_1 \cos \theta_1 + m_2gl_2 \cos \theta_2 + m_3gL_1 \cos \theta_1 \\ & + m_3gL_2 \cos \theta_2 + m_3gl_3 \cos \theta_3 \end{aligned} \quad (15)$$

The Euler-Lagrange formulation is established by Eq. (16), where k represents the DOF, q_k the set of generalized coordinates, and Q_k the set of external (non-conservative) forces applied to the system. In the context of the system under consideration, there are three DOF associated with the three joints of the lower limb. The external forces encompass the torque T_n acting at each joint and the viscous damping, with b_n representing the viscous damping coefficient. The Euler-Lagrange formulation is applied as seen in Eqs. (17), (18), and (19) for the hip, knee, and ankle, respectively.

$$\frac{d}{dt} \left(\frac{\partial L}{\partial \dot{q}_k} \right) - \frac{\partial L}{\partial q_k} = Q_k \quad (16)$$

$$\frac{d}{dt} \left(\frac{\partial L}{\partial \dot{\theta}_1} \right) - \frac{\partial L}{\partial \theta_1} = T_1 - b_1\dot{\theta}_1 - b_2(\dot{\theta}_1 - \dot{\theta}_2) \quad (17)$$

$$\frac{d}{dt} \left(\frac{\partial L}{\partial \dot{\theta}_2} \right) - \frac{\partial L}{\partial \theta_2} = T_2 - b_2(\dot{\theta}_2 - \dot{\theta}_1) - b_3(\dot{\theta}_2 - \dot{\theta}_3) \quad (18)$$

$$\frac{d}{dt} \left(\frac{\partial L}{\partial \dot{\theta}_3} \right) - \frac{\partial L}{\partial \theta_3} = T_3 - b_3(\dot{\theta}_3 - \dot{\theta}_2) \quad (19)$$

The equations above are solved resulting in the nonlinear second-order differential Eqs. (20), (21), and (22), which describe the motion of the thigh, lower leg, and foot, respectively.

$$\begin{aligned}
& \ddot{\theta}_1(m_1l_1^2 + m_2L_1^2 + m_3L_1^2 + J_1) + \ddot{\theta}_2[m_2L_1l_2 \cos(\theta_1 - \theta_2) + m_3L_1l_2 \cos(\theta_1 - \theta_2)] \\
& + \ddot{\theta}_3[m_3L_1l_3 \cos(\theta_1 - \theta_3)] \\
& + \dot{\theta}_2^2[m_2L_1l_2 \sin(\theta_1 - \theta_2) + m_3L_1L_2 \sin(\theta_1 - \theta_2)] \\
& + \dot{\theta}_3^2[m_3L_1l_3 \sin(\theta_1 - \theta_3)] + m_1gl_1 \sin \theta_1 + m_2gL_1 \sin \theta_1 \\
& + m_3gL_1 \sin \theta_1 = T_1 - b_1\dot{\theta}_1 - b_2(\dot{\theta}_1 - \dot{\theta}_2)
\end{aligned} \tag{20}$$

$$\begin{aligned}
& \ddot{\theta}_2(m_2l_2^2 + m_3L_2^2 + J_2) + \ddot{\theta}_1[m_2L_1l_2 \cos(\theta_1 - \theta_2) + m_3L_1l_2 \cos(\theta_2 - \theta_3)] \\
& + \ddot{\theta}_3[m_3L_2l_3 \cos(\theta_2 - \theta_3)] \\
& + \dot{\theta}_1^2[-m_2L_1l_2 \sin(\theta_1 - \theta_2) - m_3L_1L_2 \sin(\theta_1 - \theta_2)] \\
& + \dot{\theta}_3^2[m_3L_2l_3 \sin(\theta_2 - \theta_3)] + m_2gl_2 \sin \theta_2 + m_3gL_2 \sin \theta_2 \\
& = T_2 - b_2(\dot{\theta}_2 - \dot{\theta}_1) - b_3(\dot{\theta}_2 - \dot{\theta}_3)
\end{aligned} \tag{21}$$

$$\begin{aligned}
& \ddot{\theta}_3(m_3l_3^2 + J_3) + \ddot{\theta}_2[m_3L_2l_3 \cos(\theta_2 - \theta_3)] + \ddot{\theta}_1[m_3L_1l_3 \cos(\theta_1 - \theta_3)] \\
& + \dot{\theta}_2^2[-m_3L_2l_3 \sin(\theta_2 - \theta_3)] + \dot{\theta}_1^2[-m_3L_1l_3 \sin(\theta_1 - \theta_3)] \\
& + m_2gl_3 \sin \theta_3 = T_3 - b_3(\dot{\theta}_3 - \dot{\theta}_2)
\end{aligned} \tag{22}$$

To simplify the aforementioned differential equations, certain parameters are combined into the following constants: $c_1 = m_1l_2 + m_2L_1^2 + m_3L_1^2 + J_1$, $c_2 = m_2L_1l_2$, $c_3 = m_3L_1L_2$, $c_4 = m_3L_1l_3$, $c_5 = m_1gl_1$, $c_6 = m_2gL_1$, $c_7 = m_3gL_1$, $c_8 = m_2l_2^2 + m_3L_2^2 + J_2$, $c_9 = m_3L_2l_3$, $c_{10} = m_2gl_2$, $c_{11} = m_3gL_2$, $c_{12} = m_3l_3^2 + J_3$, and $c_{13} = m_3gl_3$. As a result of these simplifications, Eqs. (23), (24), and (25) are obtained.

$$\begin{aligned}
& c_1\ddot{\theta}_1 + (c_2 + c_3)\ddot{\theta}_2 \cos(\theta_1 - \theta_2) + c_4\ddot{\theta}_3 \cos(\theta_1 - \theta_3) + (c_2 + c_3)\dot{\theta}_2^2 \sin(\theta_1 - \theta_2) \\
& + c_4\dot{\theta}_3^2 \sin(\theta_1 - \theta_3) + c_5 \sin \theta_1 + c_6 \sin \theta_1 + c_7 \sin \theta_1 \\
& = T_1 - b_1\dot{\theta}_1 - b_2(\dot{\theta}_1 - \dot{\theta}_2)
\end{aligned} \tag{23}$$

$$\begin{aligned}
& c_8\ddot{\theta}_2 + (c_2 + c_3)\dot{\theta}_1 \cos(\theta_1 - \theta_2) + c_9\ddot{\theta}_3 \cos(\theta_2 - \theta_3) - (c_2 + c_3)\dot{\theta}_1^2 \sin(\theta_1 - \theta_2) \\
& + c_9\dot{\theta}_3^2 \sin(\theta_2 - \theta_3) + c_{10} \sin \theta_2 + c_{11} \sin \theta_2 \\
& = T_2 - b_2(\dot{\theta}_2 - \dot{\theta}_1) - b_3(\dot{\theta}_2 - \dot{\theta}_3)
\end{aligned} \tag{24}$$

$$\begin{aligned}
& c_{12}\ddot{\theta}_3 + c_9\dot{\theta}_2 \cos(\theta_2 - \theta_3) + c_4\dot{\theta}_1 \cos(\theta_1 - \theta_3) - c_9\dot{\theta}_2^2 \sin(\theta_2 - \theta_3) - c_4\dot{\theta}_1^2 \sin(\theta_1 - \theta_3) \\
& + c_{13} \sin \theta_3 = T_3 - b_3(\dot{\theta}_3 - \dot{\theta}_1)
\end{aligned} \tag{25}$$

Eqs. (23), (24), and (25) are solved for the highest order derivatives $\ddot{\theta}_1$, $\dot{\theta}_1$, and $\ddot{\theta}_3$ respectively, in order to obtain the following set of motion equations:

$$\ddot{\theta}_1 = \frac{1}{c_1} \left[- \left((c_2 + c_3) \ddot{\theta}_2 \cos(\theta_1 - \theta_2) - c_4 \ddot{\theta}_3 \cos(\theta_1 - \theta_3) \right) - (c_2 + c_3) \dot{\theta}_2^2 \sin(\theta_1 - \theta_2) - c_4 \dot{\theta}_3^2 \sin(\theta_1 - \theta_3) - (c_5 + c_6 + c_7) \sin \theta_1 + T_1 - b_1 \dot{\theta}_1 - b_2 (\dot{\theta}_1 - \dot{\theta}_2) \right] \quad (26)$$

$$\ddot{\theta}_2 = -\frac{1}{c_8} \left[-(c_2 + c_3) \ddot{\theta}_1 \cos(\theta_1 - \theta_2) - c_9 \ddot{\theta}_3 \cos(\theta_2 - \theta_3) + (c_2 + c_3) \dot{\theta}_1^2 \sin(\theta_1 - \theta_2) - c_9 \dot{\theta}_3^2 \sin(\theta_2 - \theta_3) - (c_{10} + c_{11}) \sin \theta_2 + T_2 - b_2 (\dot{\theta}_2 - \dot{\theta}_1) - b_3 (\dot{\theta}_2 - \dot{\theta}_3) \right] \quad (27)$$

$$\ddot{\theta}_3 = \frac{1}{c_{12}} \left[-c_9 \ddot{\theta}_2 \cos(\theta_2 - \theta_3) - c_4 \ddot{\theta}_1 \cos(\theta_1 - \theta_3) + c_9 \dot{\theta}_2^2 \sin(\theta_2 - \theta_3) + c_4 \dot{\theta}_1^2 \sin(\theta_1 - \theta_3) - c_{13} \sin \theta_3 + T_3 - b_3 (\dot{\theta}_3 - \dot{\theta}_1) \right] \quad (28)$$

This plant model of human lower limb motion in the sagittal plane was implemented in MATLAB's Simulink, and it utilizes the non-linear second-order differential Eqs. (26), (27), and (28), as illustrated in the block diagram presented in Fig. 2. The inputs to this model consist of the joint torques (T_1 , T_2 and T_3) measured in units of [$N \cdot m$], while the outputs are the angular displacements of the thigh, lower leg, and foot (θ_1 , θ_2 and θ_3), reported in units of [rad].

The parameters that make up the plant model are detailed in Table I. These parameters are derived through an anthropometric analysis that relies on two primary factors: the body mass M and the height H of the individual. The mass of each segment and its corresponding length are linked to the individual's body mass and height, and the gravity center and radius of gyration are associated with the segment length (26,27).

2.2. Closed-loop controller

The neuromusculoskeletal system was conceptualized within a closed-loop feedback control scheme. In this structured framework, the body's segments and joints comprise the plant, muscles serve as the actuators, and an array of sensors, including proprioceptive and tactile sensors alongside visual and vestibular systems, act as sensory inputs. Overseeing this complex system is the CNS, functioning as the controller (28). The CNS receives input signals representing desired positions or reference trajectories, generated by the brain. These inputs are compared against real-time segment locations to compute tracking errors, which, in turn, guide the CNS in sending neural signals to muscles. These signals prompt the exertion of forces on the skeletal system, thereby producing joint torques to achieve the desired motion.

To simulate the neuromusculoskeletal system and the CNS, the model employs three angular displacement feedback PID controllers for the hip, knee, and ankle. Fig. 3 illustrates these controllers. Their inputs are tracking errors, computed as the difference between reference trajectories and actual

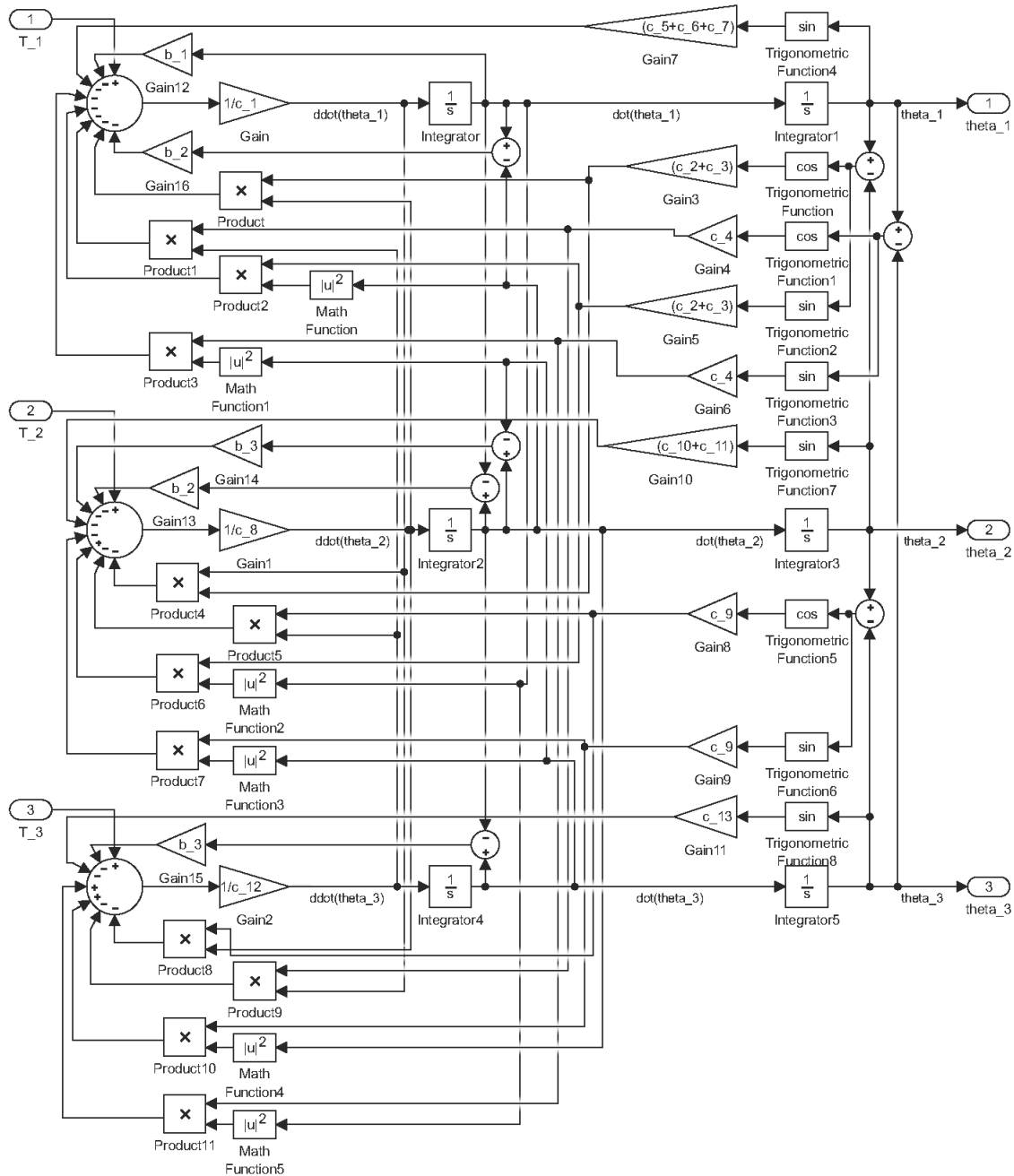


Figure 2. Plant model of human lower limb motion in Simulink

segment angular displacements. The controllers' outputs represent the joint torques required for carrying out the intended motion. These PID controller outputs feed directly into the plant model, depicted in Fig. 2. For the sake of clarity and comprehensibility, this plant model is encapsulated within a Simulink subsystem block, as illustrated in Fig. 3.

Table I. Parameters of the plant model for human lower limb motion

Segment	Parameter	Symbol	Value	Unit
Thigh	Mass	m_1	$0,1 \cdot M$	[kg]
	Length	L_1	$0,284 \cdot H$	[m]
	Proximal center of gravity	l_1	$0,433 \cdot L_1$	[m]
	Radius of gyration	k_1	$0,540 \cdot L_1$	[m]
	Moment of inertia	J_1	$m_1 \cdot k_1^2$	[kg · m ²]
	Viscous damping coefficient	b_1	0.1	[N · m · s]
Lower leg	Mass	m_2	$0,0465 \cdot M$	[kg]
	Length	L_2	$0,246 \cdot H$	[m]
	Proximal center of gravity	l_2	$0,433 \cdot L_2$	[m]
	Radius of gyration	k_2	$0,528 \cdot L_2$	[m]
	Moment of inertia	J_2	$m_2 \cdot k_2^2$	[kg · m ²]
	Viscous damping coefficient	b_2	0.1	[N · m · s]
Foot	Mass	m_3	$0,0145 \cdot M$	[kg]
	Length	L_3	$0,152 \cdot H$	[m]
	Proximal center of gravity	l_3	$0,5 \cdot L_3$	[m]
	Radius of gyration	k_3	$0,690 \cdot L_3$	[m]
	Moment of inertia	J_3	$m_3 \cdot k_3^2$	[kg · m ²]
	Viscous damping coefficient	b_3	0.1	[N · m · s]

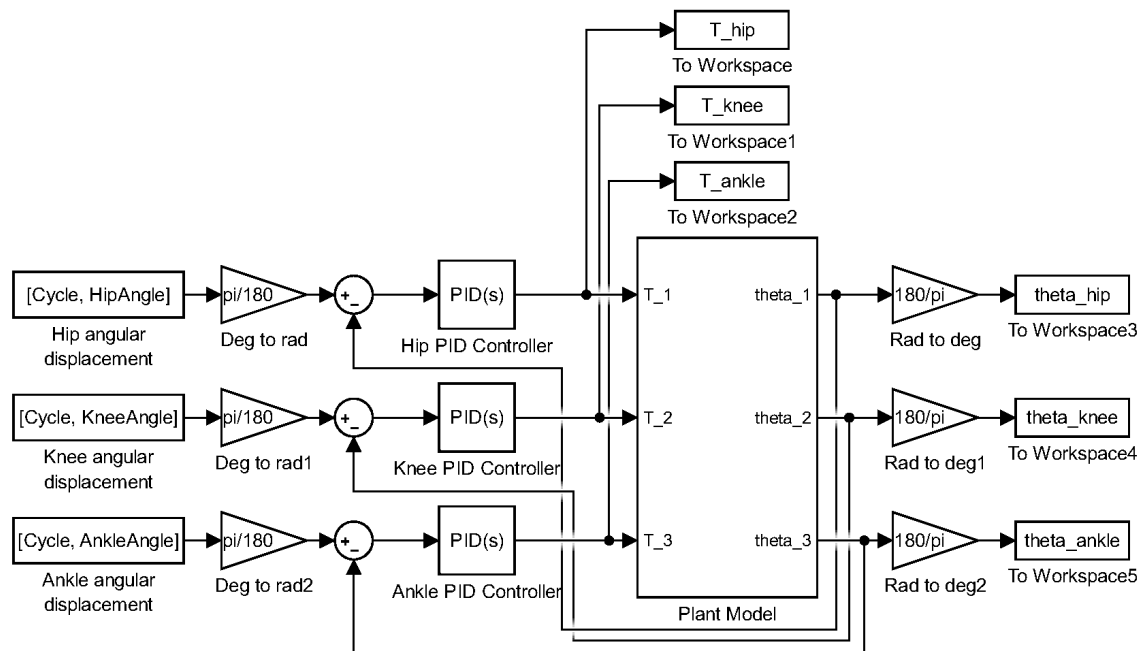


Figure 3. Closed-loop PID controllers implemented in the plant model in Simulink

A notable aspect of this modeling process pertains to unit conversions. While the plant model operates with angular displacements measured in radians, reference trajectories are presented in degrees. To ensure consistency, unit conversion is performed using specialized gain blocks designated as *Deg to rad* and *Rad to deg*. These blocks facilitate the transformation of reference trajectories from degrees to radians before tracking error computation. Furthermore, the angular displacements of the dynamic model are converted from radians to degrees for visualization purposes.

PID control is a classical closed-loop control technique defined by the Laplace domain transfer function shown in Eq. (29). It comprises three essential constants: proportional K_p , integral K_i , and derivative K_d . These constants play distinct roles in shaping system behavior: the proportional constant enhances the system's responsiveness; the integral constant reduces steady-state error; improving precise tracking of reference trajectories; and the derivative constant manages the tracking error's evolution over time (2).

$$PID(s) = K_p + \frac{K_i}{s} + K_d s \quad (29)$$

To optimize controller performance, an experimental tuning process was conducted on the plant model. The objective was to achieve optimal tracking performance while ensuring that joint torques remained within the reported maximum values for normal gait (29). The tuning process resulted in PD controllers for the three joints, configured as follows: the hip controller was configured with $K_p = 10,000$ and $K_d = 1$, the knee controller with $K_p = 1,000$ and $K_d = 10$, and the ankle controller with $K_p = 1,000$ and $K_d = 10$.

3. Simulations and results

Simulations of the dynamic model were conducted using human gait reference trajectories obtained from (29), with due consideration to the anthropometric data (body mass and height) reported in their research. These reference trajectories comprise the angular displacement of the hip, knee, and ankle joints during the gait cycle of healthy male adults.

Graphical simulation results are presented in Figs. 4, 5, and 6, each consisting of three plots corresponding to the three lower limb joints: (a) hip, (b) knee, and (c) ankle. Fig. 4 shows the tracking of angular displacement, with the reference trajectory represented as the dotted line and the angular displacement of the segment in the dynamic model shown as the solid line. Fig. 5 illustrates the tracking error regarding angular displacement, calculated as the difference between the reference trajectory and the angular displacement of the segment. Fig. 6 presents the normalized joint torque during the execution of the desired gait reference trajectory. This normalization is established relative to the individual's body mass.

The assessment of angular displacement tracking in the dynamic model involved the application of two key metrics: the relative maximum error (RME) and the root mean square error (RMSE), both in magnitude and as a percentage. These metrics were calculated using Eqs. (30) to (33), where θ_d represents the reference trajectory, θ_n signifies the angular displacement of the segment in the dynamic

model, and N denotes the signal length (2). Quantitative results from this evaluation are presented in Table II, encompassing data for the three segments under consideration.

Table II. Angular displacement tracking errors of the dynamic model

Segment	RME [°]	% RME	RMSE [°]	% RMSE
Thigh	0,649	1,924	0,240	1,100
Lower leg	2,161	3,410	0,795	2,567
Foot	0,310	0,322	0,125	0,139

$$RME = \max|\theta_d - \theta_n| \quad (30)$$

$$\%RME = \frac{\max|\theta_d - \theta_n|}{\max|\theta_d|} \cdot 100 \quad (31)$$

$$RMSE = \sqrt{\frac{1}{N} \sum (\theta_d - \theta_n)^2} \quad (32)$$

$$\%RMSE = \frac{\sqrt{\frac{1}{N} \sum (\theta_d - \theta_n)^2}}{\sqrt{\frac{1}{N} \sum (\theta_d)^2}} \cdot 100 \quad (33)$$

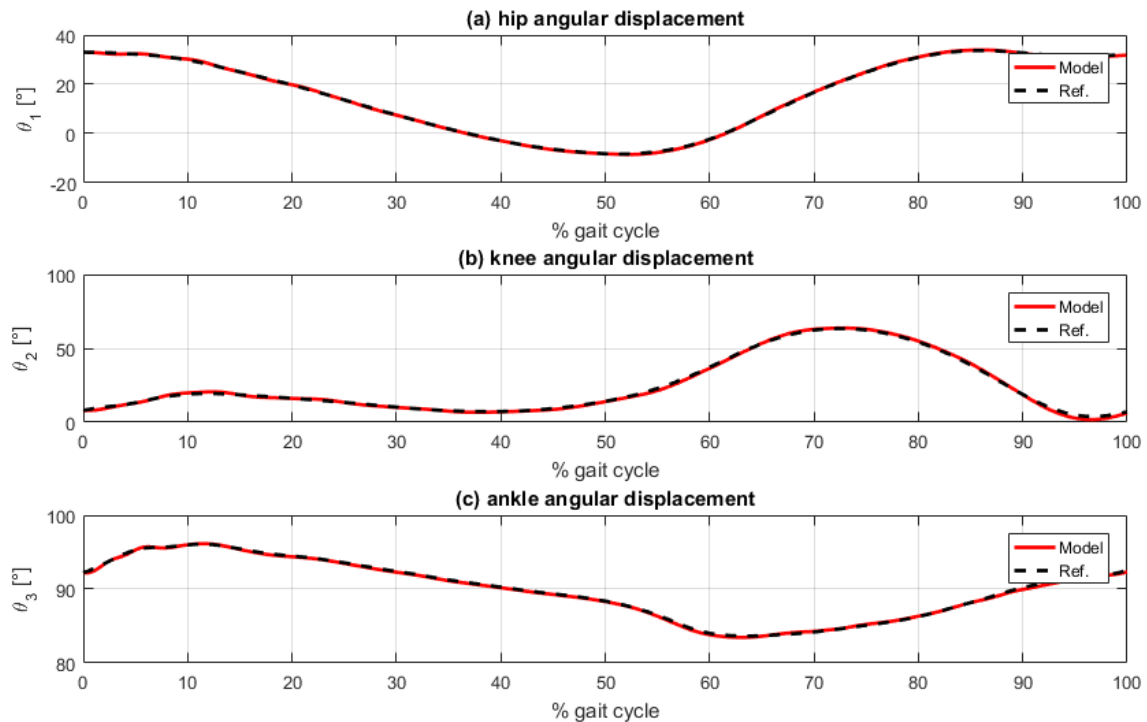


Figure 4. Angular displacement tracking: (a) hip, (b) knee, and (c) ankle

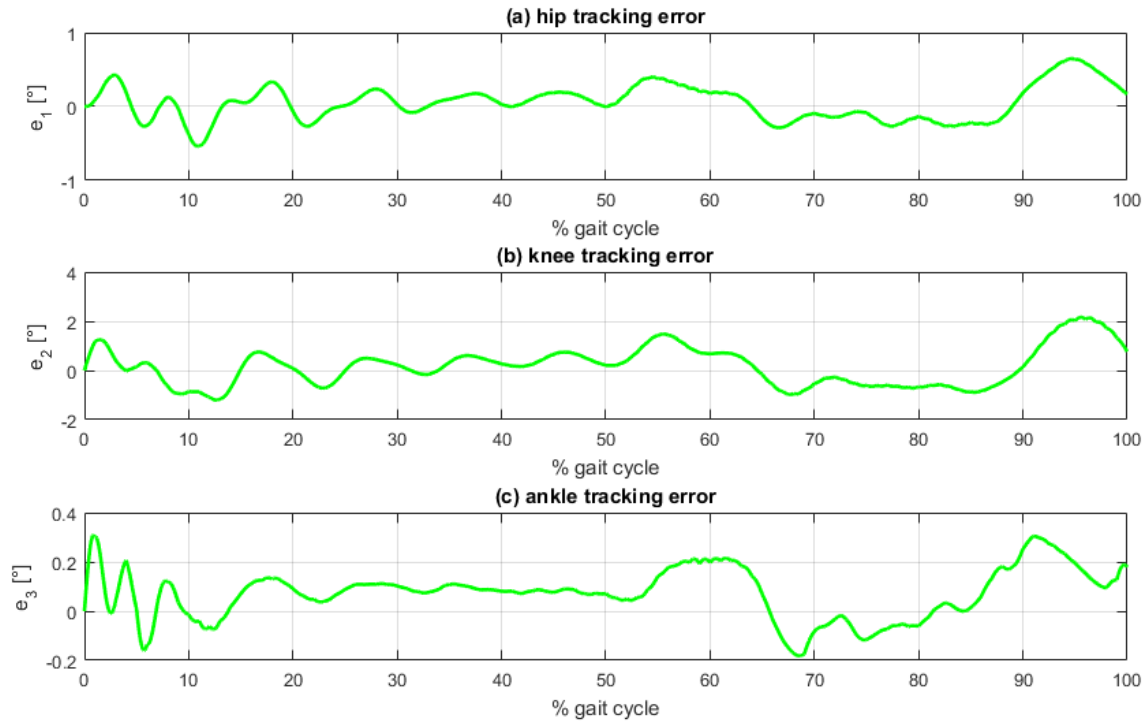


Figure 5. Angular displacement tracking error: (a) hip, (b) knee, and (c) ankle

The analysis of the graphical results, as depicted in Figs. 4 and 5, reveals that the most significant tracking errors tend to appear during the peaks of the reference trajectories. While PID controllers can be finetuned to minimize tracking errors, it is essential to recognize that pushing these controllers to achieve such minimal errors could result in joint torques surpassing the reported values for normal human gait (29).

Angular displacement tracking was effectively accomplished with errors remaining under 2.2 [°] in magnitude and within a margin of 3,5% for all three segments considered. Notably, the lower leg segment exhibited the most substantial tracking errors. This can be attributed to the dynamic interactions between the thigh and foot segments, which, in turn, impact the lower leg's overall performance. Despite these challenges, the tracking errors for the thigh and foot segments were effectively constrained below 0,65 [°] and 2%.

4. Conclusions

This paper presented the development of a dynamic model for human lower limb motion in the sagittal plane during the gait cycle. The dynamic model was composed of two primary components: (1) the plant model and (2) a closed-loop PID controller. The plant model served as the foundation for understanding the forward dynamics of human gait. It was constructed based on a multi-mass pendulum, encompassing three lower limb segments (thigh, lower leg, and foot) and three joints (hip,

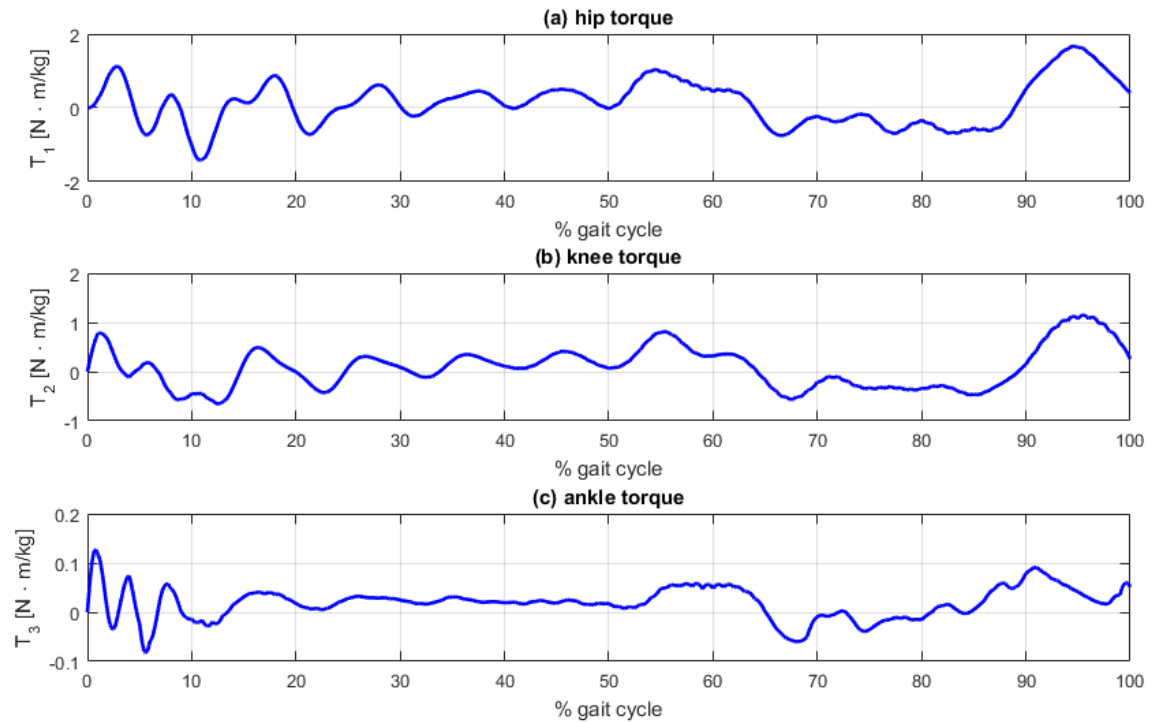


Figure 6. Joint torque: (a) hip, (b) knee, and (c) ankle

knee, and ankle). The governing nonlinear second-order differential equations of the plant model were derived through Euler-Lagrange formulation and subsequently implemented in MATLAB's Simulink. To replicate human gait reference trajectories and simulate the functioning of the neuromusculoskeletal system and the CNS, a closed-loop PID controller was integrated to the plant model for tracking angular displacement.

Simulations were conducted using human gait reference trajectories sourced from healthy adult males. The accuracy of angular displacement tracking was rigorously assessed, quantified by two key metrics: the relative maximum error (RME) and the root mean square error (RMSE). The simulation results affirm the reliability of the dynamic model, demonstrating its ability to faithfully reproduce human gait trajectories with a high degree of precision. The errors observed were consistently below 2,2 [°] in magnitude and 3,5% for all three considered segments (thigh, lower leg, and foot).

Within the domain of dynamic human gait modeling, this model resides within the realm of biped robotics, offering a unique hybrid approach that amalgamates pendulum and control-based methodologies. This model stands as a potent tool, empowering the design of rehabilitation and assistive devices, such as exoskeletons, prostheses, and orthoses. It enables crucial functionalities, including joint torque estimation, analysis of kinematic variables, optimal actuator selection, and exploration of advanced control techniques.

5. Author contributions

José Luis Sarmiento-Ramos: Conceptualization, investigation, software, supervision, writing – original draft, writing – review and editing.

Andrés Felipe Meneses-Castro: Investigation, software, writing – original draft.

Pedro José Jaimes-Mantilla: Investigation, software, writing – original draft.

References

- [1] C. A. Oatis, *Kinesiology: the mechanics and pathomechanics of human movement*, 2nd ed., USA: Lippincott Williams and Wilkins, 2009. ↑3, 5
- [2] J. L. Sarmiento-Ramos, A. P. Rojas-Ariza and Y. Z. Rueda-Parra, “Dynamic model of flexion/extension and abduction/adduction of the shoulder joint complex,” in *2021 IEEE 2nd Int. Cong. Biomed. Eng. Bioeng.*, 2021, pp. 1-4. <https://doi.org/10.1109/CI-IBBI54220.2021.9626105> ↑3, 12, 13
- [3] J. L. Sarmiento-Ramos and M. F. Anaya-Rojas, “Modelling, design and construction of a wrist rehabilitation exoskeleton,” *Scientia et Technica*, vol. 27, no. 3, pp. 177-185, Sept. 2022. <https://doi.org/10.22517/23447214.24748> ↑3
- [4] J. L. Sarmiento-Ramos, J. C. Suárez-Galvis and V. Grisales-Muñoz, “Exoskeleton for ankle joint flexion/extension rehabilitation,” *ITECKNE*, vol. 19, no. 2, art. 2773, Jun. 2022. <https://doi.org/10.15332/iteckne.v19i2.2773> ↑3
- [5] J. Sun, “Dynamic modeling of human gait using a model predictive control approach,” Ph.D. dissertation, Fac. of the Grad. Sch., Marquette Univ., Milwaukee, USA, 2015. [Online]. Available: https://epublications.marquette.edu/cgi/viewcontent.cgi?referer=&httpsredir=1&article=1481&context=dissertations_mu ↑3, 4
- [6] F. De Groote and A. Falisse, “Perspective on musculoskeletal modelling and predictive simulations of human movement to assess the neuromechanics of gait,” *Proc. R. Soc. B.*, vol. 288, art. 2432, Mar. 2021. <https://doi.org/10.1098/rpsb.2020.2432> ↑3
- [7] Y. Xiang, J. S. Arora and K. Abdel-Malek, “Physics-based modeling and simulation of human walking: A review of optimization-based and other approaches,” *Struc. Multidisc. Optim.*, vol. 42, pp. 1-23. 2010. <https://doi.org/10.1007/s00158-010-0496-8> ↑3, 4
- [8] F. L. Buczek, K. M. Cooney, M. R. Walker, M. J. Rainbow, M. C. Concha and J. O. Sanders, “Performance of an inverted pendulum model directly applied to normal human gait,” *Clin. Biomech.*, vol. 21, no. 3, pp. 288-296, 2006. <https://doi.org/10.1016/j.clinbiomech.2005.10.007> ↑3
- [9] P. Sun, Y. Gu, H. Mao, Z. Chen and Y. Li, “Research on walking gait planning and simulation of a novel hybrid biped robot,” *Biomimetics*, vol. 8, no. 2, art. 258, 2023. <https://doi.org/10.3390/biomimetics8020258> ↑3

- [10] G. Yu, J. Zhang and W. Bo, "Biped robot gait planning based on 3D linear inverted pendulum model," *IOP Conf. Ser.: Mater. Sci. Eng.*, vol. 301, art. 012098, 2018. <https://doi.org/10.1088/1757-899X/301/1/012098> ↑3
- [11] T. Dong, D. Wang and D. Zhao, "Gait research and simulation analysis of biped robot," in *Proc. SPIE 12305 Int. Symp. Artif. Intell. App. Tech.*, art. 123050A, 2022. <https://doi.org/10.1117/12.2645550> ↑3
- [12] Y. Liu, S. Peng, Y. Du, and W. H. Liao, "Kinematics modeling and gait trajectory tracking for lower limb exoskeleton robot based on PD control with gravity compensation," in *Proc. 38th Chin. Ctrl. Conf.*, 2019, pp. 4504-4511. <https://doi.org/10.23919/ChiCC.2019.8865916> ↑3
- [13] G. Marconi, A. A. Gopalai and S. Chauhan, "A triple compound pendulum model to analyze the effect of an ankle-foot orthosis on swing phase kinematics," *Med. Eng. Phys.*, vol. 112, art. 103951, 2023. <https://doi.org/10.1016/j.medengphy.2023.103951> ↑3
- [14] M. Irine. R. Hirouji, D. Ura, K. Osuka and T. Kinugasa, "Experimental verification of the characteristic behaviors in passive dynamic walking," *Art. Life Robot.*, vol. 26, pp. 187 – 194, 2021. <https://doi.org/10.1007/s10015-020-00670-y> ↑3
- [15] S. Montazeri, M. Sadeghi, A. Niaty, F. Towhidkhah and S. Jafari, "The simple chaotic model of passive dynamic walking," *Nonlinear Dyn.*, vol. 93, no. 3, pp-1183-1199, 2018. <https://doi.org/10.11007/s11071-018-4252-8> ↑3
- [16] E. Added, H. Gritli and S. Belghith, "Further analysis of the passive dynamics of the compass biped walker and control of chaos via two trajectory tracking approaches," *Complexity*, vol. 2021, art. 5533451, 2021. <https://doi.org/10.1155/2021/5533451> ↑3
- [17] C. Dinesh, M. Deivakani, P. Sunagar, R. Baskar, A. Kumar and G. Kalra, "Biped robot-based walking on uneven terrain: Stability and zero moment point (ZMP) analysis," *AIP Conf. Proc.*, vol. 2831, no. 1, art. 020013, 2023. <https://doi.org/10.1063/5.0162762> ↑4
- [18] A. Fawzi Abdul Kareem and A. Abdul Hussein Ali, "Experimental and theoretical optimal regulator control of balance zero moment point for bipedal robot," *J. Eng. Sustain. Dev.*, vol. 24, no. 6, pp. 68- 82, 2020. <https://doi.org/10.31272/jesd.24.6.6> ↑4
- [19] Y. D. Hong, "Capture point-based controller using real-time zero moment point manipulation for stable bipedal walking in human environment," *Sensors*, vol. 19, no. 15, art. 3407, 2019. <https://doi.org/10.3390/s19153407> ↑4
- [20] B. Ren, J. Liu and J. Chen, "Simulating human-machine coupled model for gait trajectory optimization of the lower limb exoskeleton system based on genetic algorithm," *Int. J. of Adv. Robot. Sys.*, vol. 17, no. 1, 2020. <https://doi.org/10.1177/1729881419893493> ↑4
- [21] M. A. Khan, H. Arshad, R. Damasevicius A. Alqahtani, S. Alsubai, A. Binbusayyis, Y. Nam and B. Kang, "Human gait analysis: a sequential framework of lightweight deep learning and improved moth-flam optimization algorithm," *Comput. Intell. Neurosci.*, vol. 2022, art. 8238375, 2022. <https://doi.org/10.1155/2022/8238375> ↑4
- [22] J. Sun, S. Wu and P. A. Voglewede, "Dynamic simulation of human gait model with predictive capability," *ASME J. Biomech. Eng.*, vol. 140, no. 3, art. 031008, 2018. <https://doi.org/10.1115/1.4038739> ↑4

- [23] J. G. Juang, "Fuzzy neural network approaches for robotic gait synthesis," *IEEE Trans. Syst. Man. Cybern.*, vol. 30, no. 4, pp. 594-601, 2004. <https://doi.org/10.1109/3477-.865178> ↑4
- [24] M. L. Felis, K. Mombaur and A. Berthoz, "An optimal control approach to reconstruct human gait dynamics from kinematic data," in *2015 IEEE-RAS 15th Int. Conf. Humanoid Rob.*, pp. 1044-1051, 2015. <https://doi.org/10.1109/HUMANOIDS.2015.736490> ↑4
- [25] T. Saidouni and G. Bessonnet, "Generating globally optimized sagittal gait cycles of a biped robot," *Robotica*, vol. 41, no. 3, pp. 465-479, Jul. 2010. <https://doi.org/10.1007/s00158-009-0423-z> ↑4
- [26] D. A. Winter, *Biomechanics and motor control of human movements*, USA: John Wiley and Sons, Inc., 2009. ↑9
- [27] Y. Li, C. Xu and X. Guan, "Modeling and simulation study of electromechanically system of the human extremity exoskeleton," *J. Vibroengineering*, vol. 18, no. 1, pp. 551-561, Feb. 2016. [Online]. Available: <https://www.extrica.com/article/16394> ↑9
- [28] M. Oluwatsin, "Modelling and control of actuated lower limb exoskeletons: a mathematical application using central patterns generators and nonlinear feedback control techniques," Ph.D. dissertation, Univ. Paris-Est Et Mstic, 2016. Available: <https://tel.archives-ouvertes.fr/tel-01531927/document> ↑9
- [29] G. Bovi, M. Rabuffetti, P. Mazzoleni and M. Ferrarin, "A multiple-task gait analysis approach: kinematic, kinetic and EMG reference data for healthy young and adult subjects," *Gait Post.*, vol. 33, no. 1, pp. 6-13, Jan. 2011. <https://10.1016/j.gaitpost.2010.08.009> ↑12, 14

José Luis Sarmiento-Ramos

Mechanical Engineer and Master of Science in Mechanical Engineering from Universidad Industrial de Santander, Bucaramanga, Colombia. From 2015 to 2016, he served as a Teaching Assistant in the School of Mechanical Engineering at Universidad Industrial de Santander, Bucaramanga, Colombia. From 2019 to 2022, he worked as Professor and Researcher in the Department of Biomedical Engineering at Universidad Manuela Beltrán, Bucaramanga, Colombia. From 2022 to 2023, he worked as Professor in the Faculty of Mechatronic Engineering at Universidad Santo Tomás, Bucaramanga, Colombia. He has also worked as a Guest Lecturer for the Master's degree in Hydraulics at Universidad Técnica de Manabí, Portoviejo, Ecuador. Currently, he works as CNC Manufacturing Manager at Rambal S.A.S BIC, Bucaramanga, Colombia. His current research interests include biomechanics, dynamic systems, fluid power servo systems, and control engineering.

Email: jefe.fabricacioncnc@rambal.com.co

Andrés Felipe Meneses-Castro

Biomedical Engineering student from Universidad Manuela Beltrán, Bucaramanga, Colombia. His current research interests include biomechanics, dynamic systems, and control engineering.

Email: andres.meneses@academia.umb.edu.co

Pedro José Jaimes-Mantilla

Biomedical Engineering student from Universidad Manuela Beltrán, Bucaramanga, Colombia. His current research interests include biomechanics, dynamic systems, and control engineering.

Email: pedro.jaimes@academia.umb.edu.co





Research

Statistical Analysis by Linear Regression of the Prevalence of Flatfoot in Preschool Children of a Mexican Community

Análisis estadístico por regresión lineal de la prevalencia de pie plano en preescolar de una comunidad de México

Carlos I. Cabrera-Perez¹, Juan A. Lopez-Valdez¹, Horacio Rostro-Gonzalez² , Jatziry S. Cano-Lara³, and Miroslava Cano-Lara¹  

¹Department of Mechatronics of Tecnológico Nacional de México/ITESI Irapuato, Gto. México) 

²Universidad de Guanajuato 

³Instituto Mexicano del Seguro Social (León, Gto. México) 

Abstract

Context: In Mexico's rural towns, it is essential to generate a culture of studying the prevalence of flat feet in children aged 3 to 5, whose arch is still in development and can be corrected. By means of a computer application, statistical bar graph and correlation studies via linear regression can validate the results obtained regarding the categorization of infants' footprint type, which are acquired through the Hernández Corvo index (HCI), Clarke's angle protocol (CA), the Staheli index (SI), the Chippaux index (CI), and the body mass index (BMI).

Methods: A statistical analysis of the plantar footprint of 95 infants in a rural region of Mexico was carried out, employing a computational technique together with a photo-podoscope. Footprint images were acquired, processed, and classified. The footprint type was categorized with respect to the HCI, CA, and the Staheli-Chippaux index (SCI). The footprint distribution was validated via the linear regression method.

Results: We evidenced a prevalence of flat foot of 54,7% in relation to HCI, 58,9% in relation to CA, and 61,05% in relation to SCI, where the male gender was shown to be more susceptible (up to 28, 32, and 33 cases, respectively). The best prediction was obtained using the SI and the CI: 90,7 and 87,0% for the right and left feet, with a positive increase. No dependence on body composition was observed.

Conclusions: The diagnosis of the type of footstep, in its normal, cavus, and flat categories, shows the prevalence of flat feet among infants aged 3 to 5, with at least 28 cases, mostly male and without dependence on weight. Although it is difficult to perform plantar footprint diagnoses in the rural communities of Mexico, this statistical study highlights the importance of monitoring foot development in preschool infants with the advantages and practicality of computational techniques.

Keywords: flatfoot, statistical method, linear regression

Article history

Received:
13th/Jul/2023

Modified:
1st/Nov/2023

Accepted:
05th/Dec/2023

Ing., vol. 29, no. 1,
2024. e21003

©The authors;
reproduction right
holder Universidad
Distrital Francisco
José de Caldas.

Open access



*  **Correspondence:** miroslava.cl@irapuato.tecnm.mx

Resumen

Contexto: En las comunidades de México, es fundamental generar una cultura de estudiar la prevalencia del pie plano en niños de 3 a 5 años, cuyo arco aún está en desarrollo y se puede corregir. Mediante el uso de una aplicación computacional, los estudios estadísticos de gráficos de barras y correlación por medio de regresión lineal validan los resultados sobre la categorización del tipo de pisada del infante, los cuales se adquieren mediante el índice Hernández Corvo (HCI), el protocolo del ángulo de Clarke (CA), el índice Staheli (SI), el índice Chippaux (CI) y el índice de masa corporal (BMI).

Método: Se realizó un análisis estadístico de la huella plantar de 95 infantes de una comunidad de México, empleando una técnica computacional junto con un fotopodoscopio. Se adquirió, procesó y clasificó la imagen de la pisada. Se categorizó el tipo de pisada con respecto al HCI, el CA y el índice Staheli-Chippaux (SCI). La distribución de las huellas se validó mediante el método de regresión lineal.

Resultados: Se evidenció una prevalencia de pie plano de 54,7 % respecto al HCI, 58,9 % respecto al CA y 61,05 % respecto al SCI, donde el sexo masculino fue el más susceptible (hasta 28, 32 y 33 casos). La mejor predicción se obtuvo mediante el SI y el CI: 90,7 y 87,0 % para los pies derecho e izquierdo, con incremento positivo. No se observó dependencia con la composición corporal.

Conclusiones: El diagnóstico del tipo de pisada, en sus categorías normal, cavo y plano, evidencia la prevalencia del pie plano entre los infantes de 3 a 5 años, con al menos 28 casos, en su mayoría masculinos y sin dependencia del peso. Si bien es difícil realizar diagnósticos de huella plantar en las comunidades rurales de México, este estudio estadístico muestra la importancia de monitorear el desarrollo del pie en infantes de preescolar, con las ventajas y la practicidad de las técnicas computacionales.

Palabras clave: pie plano, método estadístico, regresión lineal

Table of contents		3. Results	8
		3.1. Correlation between the protocols and foot type classification	8
1. Introduction	2	4. Discussion	9
2. Methodology	4	5. Conclusion	10
2.1. Statistical analysis	4	References	10
2.1.1. Flat, normal, and cavus foot	5		

1. Introduction

In Mexico, it has become necessary to know the anthropometric characteristics of infants in preschool, especially in regions where it would be difficult to use computational techniques aimed at identifying footprint types. Determining the prevalence of flatfoot and its arch type is an intriguing issue, as this condition can affect children’s posture and walking over the years. To identify the percentage of infants with flatfoot in a Mexican community and to study their statistics, it is necessary

to identify the different anthropometric aspects and nutritional information of said community's infant population. Flat feet are considered to be normal during the first months of life. Starting at two years old, the structure of the foot is adjusted, causing the longitudinal arch to become more pronounced (1). However, most Mexicans do not know that, between four and six years old, it is important to diagnose the child's footprint type, as any anomaly left untreated will persist, making it difficult to correct the morphology of the foot (1,2).

The relationship between nutritional status, age, sex, and other aspects and the type of foot in infants has been studied over the years (3-5), obtaining different results depending on the conditions of the selected population, the method used for evaluating the plantar footprint, and the variables considered. It is therefore complicated to determine the conditions that favor the prevalence of flatfoot in a group of people. For example, (5) related the body mass index (BMI) to alterations in the plantar vault associated with flat and cavus feet in children aged 6 to 13. Cavus feet (11 %) were more frequent than flat ones (8%), and statistical studies did not report a relationship between the nutritional status and the foot type.

There are a variety of anthropometric protocols for foot classification. Some of them are the Hernández Corvo Index (HCI), Clarke's angle (CA), the Chippaux index (CI), and the Staheli Index (SI) (6-11). The Latin American HCI is regarded as the most widely used for the general study of the plantar footprint since it allows for a better observation of the variability in the longitudinal arch according to each zone of the foot, in addition to being precise. Moreover, CA is widely used to complete the classification of the foot with the assessment of the angle of the plantar arch (3,6,16).

Statistical methods involving bar graphs or linear regression are frequently employed to compare the prevalence of foot types against variables such as age, BMI, gender, posture, and load distribution, among others (11,14), although scatter plots, multiple linear regression (15), maximum and minimum diagrams (16), and other methods have also been considered. Linear regression predicts the behavior of the variables by means of the coefficient of determination (R^2). The confidence interval (CI) provides a range of probable values with respect to the mean, while the prediction interval (PI) provides a range of values for an individual response, with which, depending on the percentage, one can be certain that the trend described by the mean will be followed within a specific range (17).

(12) studied the footprints of 300 20-year-olds with the CA, SI, and Chippaux-Smirak index (CSI). They established a correlation between BMI and the indices via linear regression, in addition to evaluating the frequency of flat, normal, and cavus feet with bar graphs and according to each protocol (12). On the other hand, (13) studied the longitudinal arch, establishing a correlation between overpronation, the arch angle, the SI, and the CSI by means of linear regression. The studied group included 71 people around 25 years of age. Using footprints, (14) studied the SI and CSI of 37 people aged 18 to 35, correlating the analysis of the calcaneal resting position, the navicular drop test, the arch angle, and the arch index through linear regression.

This work presents a plantar statistical study in a group of 95 infants from the community of Valtierra in Salamanca, Guanajuato, Mexico. Computational studies validate the baropodometric and

statistical protocols for classifying the prevalence of flatfoot in infants (6). The baropodometric protocols used by the computational system are CA and the Staheli-Chippaux index (SCI), common methods that can be found in similar works (6, 12, 18). Similarly, the Hernández Corvo protocol was used, which is one of the most complete methods to examine the plantar arch and foot type with good accuracy (18, 20). Finally, via linear regression, the indices were related to the body composition of each infant.

2. Methodology

A total of 95 infants (46 males and 49 females) aged 3-5 from the Jaime Torres Bodet preschool in the community of Valtierilla, Salamanca, Guanajuato, Mexico, were evaluated between September 2021 and May 2022. For this study, authorization was requested from the parents and the teaching staff of the institution, clearly explaining the objective and methodology of our work and according to the Helsinki declaration and the Internal Ethics Committee (CIEPCI) of TecNM/ITS Irapuato.

The study required a database of the infant's body composition, including aspects such as sex, age, height, weight, BMI, Helbing line, in addition to the morphological parameters of their footprint, which were acquired using a photo-podoscope. The processing of the images of the plantar footprint was based on the protocols of Hernández Corvo, CA, and the SCI (Fig. 1) (18-20).

Once the data of each infant had been registered, the image of their footprints was captured with the help of a photo-podoscope and white LED strips on the sides. The infant was barefoot, adopting a correct posture without moving their body. The acquired image had a greenish color due to the presence of iron impurities in the glass. In the computing system, the pseudo-color technique was applied, noise was eliminated, and the contour of the plantar prints was acquired on a grayscale. Finally, the values for each footprint (left and right) were recorded according to the aforementioned protocols for later classification (18-20). In addition, a photograph of the back of the legs was taken in order to study the Helbing line and determine the infant's type of footprint. Once the relevant information and diagnostics were available, they were stored in a database. A categorical distribution was considered in order to determine the volume of cases of infants with flat, normal, and cavus feet, as well as the number of underweight, regular-weight, overweight, and obese children with regard to their BMI weight category. All this, while aiming to have a complete perspective of the infants in this community (Fig. 1). Linear regression was employed to find a relationship between the parameters, with the purpose of explaining why the correction of the plantar arch can be affected or not by gender and nutritional habits.

2.1. Statistical analysis

The bar graph statistical method considers the absolute frequency by weight category and the application of the protocols in each foot (*r* for right, *l* for left), followed by the percentage of presence. The distribution by weight category according to the BMI (Fig. 2a) shows the highest number of infants with normal weight (62), followed by those at risk of malnutrition (21), with overweight and obese children being a minority. Fig. 2b shows the distribution according to the HCI protocol. The classification is broadened to *r*: 54,74 % and *l*: 44,21 % for flat and flat-normal and *r*: 26,32 % and *l*: 30,52 % for normal

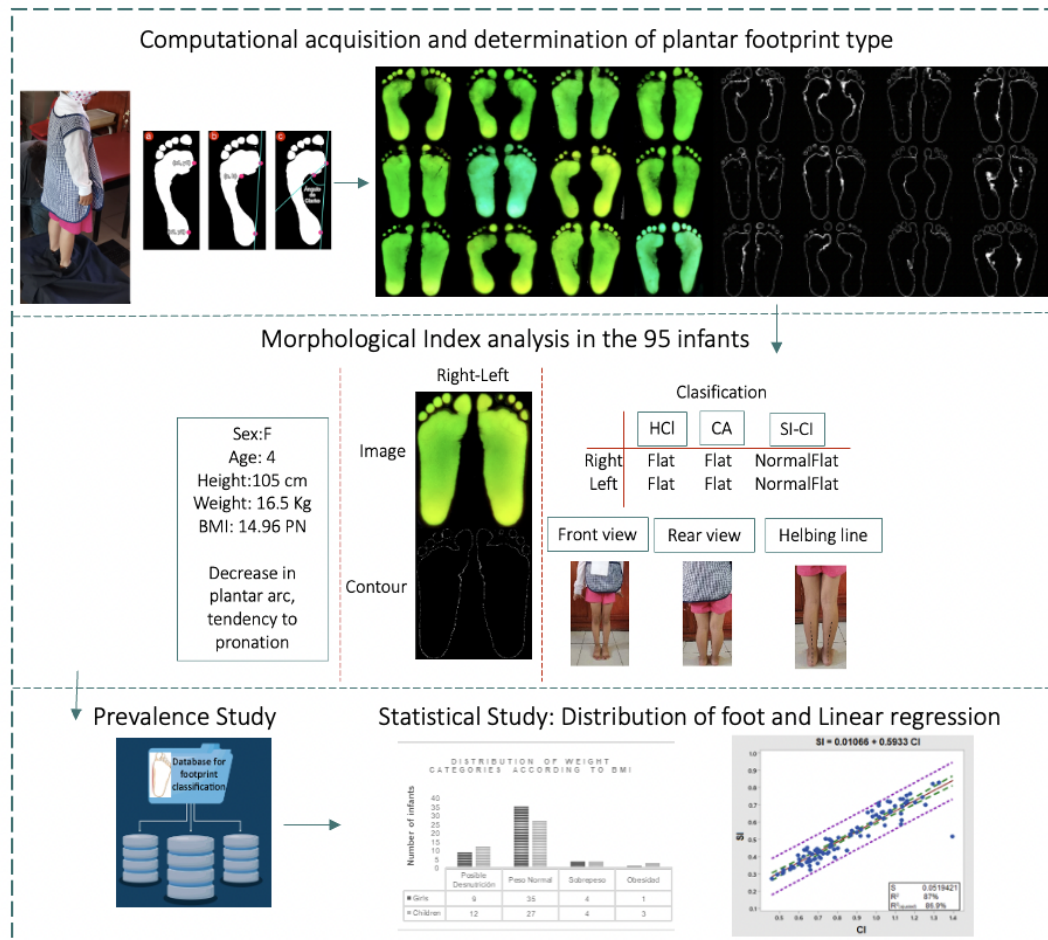


Figure 1. Computational and statistical study on the prevalence of flatfoot in children

feet, with a prevalence of flatfoot. According to the distribution by CA (Fig. 2c), flatfoot prevails with r : 58,95 % and l : 56,84 %. CA contributes with particularities in the shape of the arch. Assessing the arch angle of the plantar vault is important among for aged 3-5, as they are in the early stages of development, so the incidence of this pathology is higher (1). As for the SCI (Fig. 2d), there is a predominance of normal flatfoot, with r : 61,05 % and l : 63,16 %, broadening the classification to flat-flat, flat-normal, and flat-cavus.

2.1.1. Flat, normal, and cavus foot

Linear regression analysis allows comparing HCI and CA values against BMI and sex data. Fig. 3 shows the distribution of cases and line plots fitted according to their respective characteristic equation, R^2 values, and standard deviation (S). The green dotted lines represent 95 % confidence intervals, and the purple dotted lines denote 95 % prediction intervals. Red triangles represent male cases, and blue circles represent female cases. Figs. 3a, 3c, 3e, and 3g show the bar distribution, representing possible

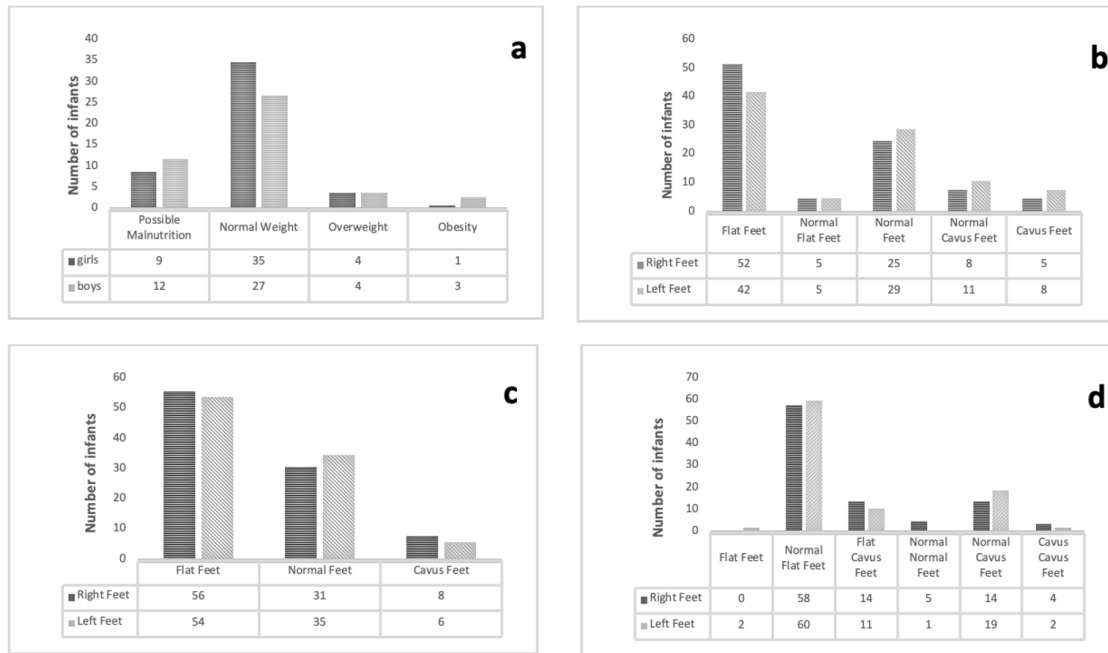


Figure 2. a) Distribution of weight categories according to the BMI and foot types according to b) HCI, c) CA, and d) SCI

malnutrition, normal weight, overweight, and child obesity (right to left). A moderate and statistically significant correlation is observed for flat and normal foot types with a prevalence in normal weight. Figs. 3b, 3d, 3f, and 3h show the tendency of each fit equation of the type $y = mx + b$, representing the point cloud analysis of the male and female cases, which was done via a residual analysis, generating linear prediction regression. The efficacy of the predictions generates the linearity, and the point cloud of cases is parallel to the linearity axis, which maintains a homogeneous axis throughout the distribution. The residuals are normally distributed above and below the line, with the presence of some scattered values. The tendency towards flatfoot in its flat and normal-flat variants is predicted with respect to the HCI and the BMI. These correlations are statistically significant, with a prevalence in males. Based on the R^2 ratio and (17), it can be stated that there is a certain relationship between the BMI and the type of footprint; the higher the BMI value, the greater the tendency towards flatfoot in these children.

Table I shows the relationship between nutritional status and AC and HCI for children in early childhood. The prevalence of flatfoot in the four weight categories is higher than that of normal and cavus foot. The assessments of (5) in children from 6 to 13 years of age in a Mexican community found a prevalence of cavus foot in the four weight categories. Similarly, the overweight and child obesity categories did not influence the results.

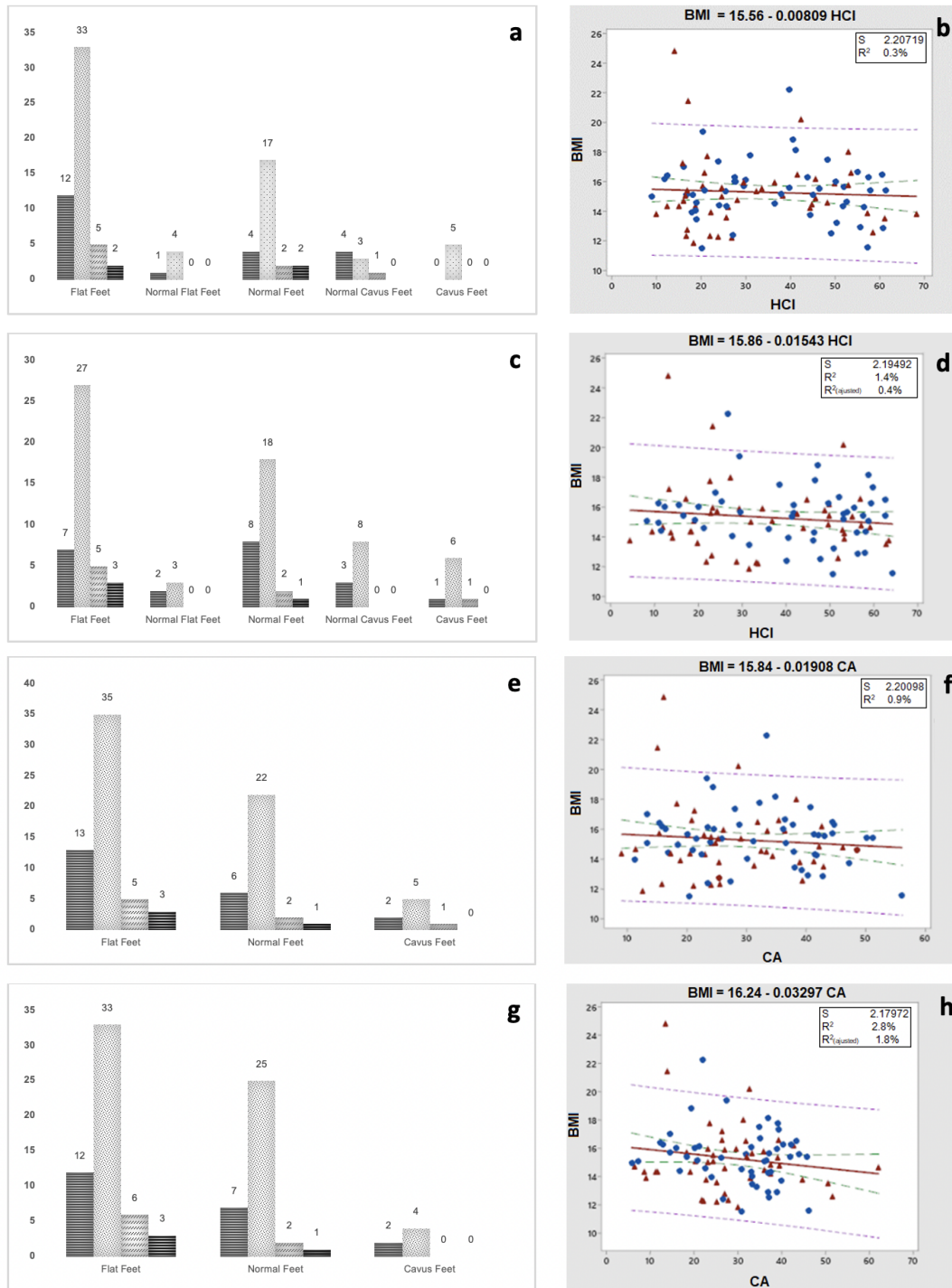


Figure 3. Distribution of foot types evaluated via: HCI in relation to the BMI, right foot (a, b) and left foot (c, d); and AC in relation to the BMI right foot (e, f) and left foot (g, h)

Table I. Relationship of nutritional status and type of footprint

Footprint type [right foot-left foot]		Weight category by BMI				total
		malnutrition	normal weight	overweight	with obesity	
Clarke's angle	Flat	13	35	5	3	56
	Normal	6	22	2	1	31
	Cavus	2	5	1	0	8
Footprint type [right foot-left foot]		Weight category by BMI				total
		malnutrition	normal weight	overweight	with obesity	
Hernández Corvo index	Flat	12	33	5	2	52
	Normal-flat	1	4	0	0	5
	Normal	4	17	2	2	25
	Normal-cavus	4	3	1	0	8
	Cavus	0	5	0	0	5

BMI: body mass index

3. Results

3.1. Correlation between the protocols and foot type classification

Figs. 4a and 4b show positive correlation lines derived from the equations that relate the values of the CA and HCI protocols for both feet, *i.e.*, r and l : $CA(r) = 9,763 + 0,5785HCI(r)$ and $CA(l) = 8,303 + 0,5565HCI(l)$. For the right foot, an R^2 of 70,1% is reported, which indicates that the model can provide predictions with a low error rate and a better distribution. In addition, the R^2 of the left foot is 72,8%. Figs. 4c and 4d compare the SI and CI values to determine the accuracy of the classification when evaluating both r and l : $SI(r) = 0,02306 + 0,5559CI(r)$ and $SI(l) = 0,01066 + 0,5933CI(l)$. This is done while using the specific flat-flat, flat-normal, flat-cavus, normal-normal, normal-cavus, and cavus-cavus foot categories. There is a prevalence of the flat-normal category, and the relationship between the indices reports an R^2 of 90,7% for the right foot and 87,0% for the left one. The prediction of the model maintains the tendency towards a linear relation with positive incremental dispersion and few atypical values.

For the general group, there is a major tendency towards having a flat right foot (above 54,74%) and having a flat left foot (above 44,21%). Statistical analysis via linear regression constitutes a complementary approach to support the values acquired through computational techniques. The prediction of the relationship between the values of the CA and HCI protocols indicates a high R^2 (70,1%). Moreover, as for the ratio between the SI and CI protocols, the R^2 is higher than 87,0%. This, in turn, with a positive upward trend and a few atypical values. Finally, the expected results highlight the need to continue studying infant footprint types in the communities of Mexico. It is necessary to raise awareness in order for families to conduct clinical diagnosis of the footprint at an early age and seek corrections of the longitudinal arc and flat feet with the elaboration of custom insoles. In this way, the footstep is corrected, and the posture is improved. It is alarming to consider that, due to the economy of the families in Mexico, very few will continue with a specialist diagnosis.

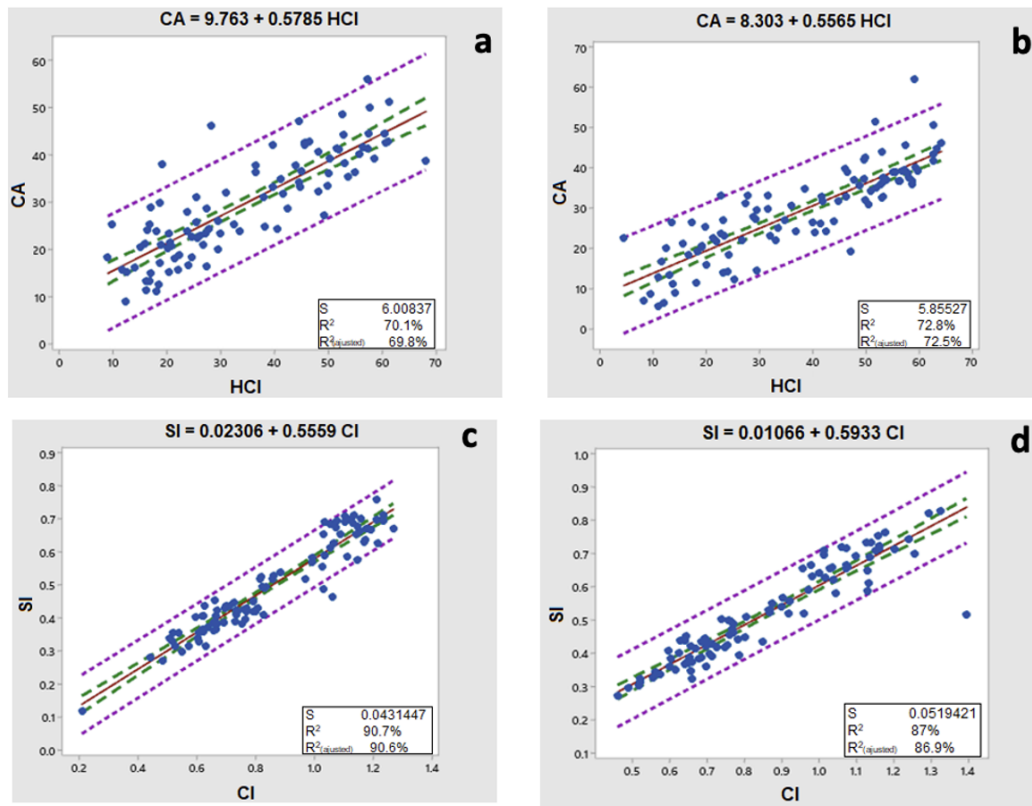


Figure 4. Correlation between values of HCI and CA for a) the right foot and b) the left foot; and between the SI and CI values for c) the right foot and d) the left foot

4. Discussion

This research studied the prevalence of flatfoot in children in a rural region of Mexico, finding some conditions that likely interfere with plantar arch correction. Several research works have attempted the same, but there are no standards to evaluate the characteristics that hinder plantar arch correction, although, in many cases, a correlation between morphological, nutritional, and footprint parameters is reported, albeit without conclusive results. Via a linear analysis of the distribution and the correlation between the BMI and the foot type, it was found that the weight of children does not necessarily have a direct influence on the prevalence of flatfoot. However, regarding sex, flatfoot is apparently more common in males.

As for the protocols for evaluating footprints, there are works that employ comparisons to find the most comprehensive and easy method to make a correct diagnosis of the foot. There are works that use the SI and the CI with different complementary protocols. CA has been widely used to calculate the plantar arch because it is faster and provides a good degree of confidence. The HCI is one of the most complete and assertive procedures to diagnose footprints, but it can be slow and complicated.

Combining these techniques with computational systems allows for complete evaluations and finding faster correlations that can be used by specialists in medical consultations.

In recent years, computational systems and dynamic studies have become more common and complete, as they allow quickly determining aspects such as foot type, posture, and footprint pressure, as well as diagnosing special conditions like diabetic foot, among others. Because of this, many people can get a better and cheaper medical evaluation of their feet, but there are locations where this kind of technology is not available or where information on the issue is limited.

5. Conclusion

Statistical analysis via linear regression does not show the prevalence of flatfoot to be clearly supported by the nutritional habits of the infant or by sex. As for the higher number of cases of flatfoot, the age of the infants must be considered. It may be that 3- to 5-year-olds have not completely developed their plantar arch, but they should exhibit a tendency towards normal foot in individual evaluations. To know if children with flatfoot have a real chance at correcting their longitudinal arch, it is necessary to perform a thorough evaluation of the tendency of the arch, which must be performed by a specialist. Unfortunately, the infants of Mexican communities have limited access to appropriate treatment or comfort shoe insoles.

Consequently, with complete information about plantar issues in infants, the rural regions of Mexico could treat discomforts just in time and prevent posture issues, as well as feet, back, or knee pain or the impossibility to exercise. Moreover, habits could be imparted to ensure the correct development of the longitudinal arch, which could be supported by computational studies aimed at eradicating these problems at every socioeconomic level. This implies a wide field of study focusing on the development of new and more efficient computational systems at low costs, with which the evolution of the plantar arch could be predicted.

References

- [1] M. Larrosa Pardo and S. Mas Moliné, "Alteraciones de la bóveda plantar," *Rev. Esp. Reumatol.*, vol. 30, no. 9, pp. 489-498, Nov. 2003. <https://www.elsevier.es/es-revista-revista-espanola-reumatologia-29-articulo-alteraciones-boveda-plantar-13055069> ↑3,5
- [2] M. Riera Campillo, "El pie normal y su patología," *Pediatría Integral*, vol. 23, no. 4, pp. 203-211, 2019. https://www.pediatriaintegral.es/wp-content/uploads/2019/xxiii04/04/n4-203-211_ManoliRiera.pdf ↑3
- [3] C. González Martín et al., "Variability between Clarke's angle and Chippaux-Smirak index for the diagnosis of flat feet," *Colombia Médica*, vol. 48, no. 1, pp. 25-31, Jan. 2017. <https://doi.org/10.25100/cm.v48i1.1947> ↑3
- [4] M. R. Espichan, F. C. Gonzales, and E. C. Zavala, "Características epidemiológicas del pie plano y pie cavo en niños de 6 a 9 años de dos colegios nacionales de educación primaria," undergraduate

- thesis, Universidad Peruana Cayetano Heredia, Peru, 2015. <https://hdl.handle.net/20.500.12866/446> ↑3
- [5] J. A. Aco Luna *et al.*, "Frecuencia de alteraciones de la huella plantar en escolares de una comunidad mexicana," *Acta Ortopédica Mexicana*, vol. 33, no. 5, pp. 289-291, Sep. 2019. <https://doi.org/10.35366/or195e> ↑3,6
- [6] S. Lara Diéguez *et al.*, "Análisis de los diferentes métodos de evaluación de la huella plantar," *RETOS. Nuevas Tendencias en Educación Física, Deporte y Recreación*, no. 19, pp. 49-53, Jan. 2011. <https://doi.org/10.47197/retos.v0i19.34637> ↑3,4
- [7] J. J. Rodríguez Salvador, "Técnica del radiofotopodograma," *Imagen Diagnóstica*, vol. 2, no. 1, pp. 38-42, Mar. 2011. [https://doi.org/10.1016/S2171-3669\(11\)70027-0](https://doi.org/10.1016/S2171-3669(11)70027-0) ↑3
- [8] C. Murat Ozer and C. Barut, "Evaluation of the sole morphology of Professional football players," *Int. SportMed J.*, vol. 13, no. 1, pp. 8-17, Mar. 2012. ↑3
- [9] R. M. Queen *et al.*, "Describing the medical longitudinal arch using footprint indices and a clinical grading system," *Foot & Ankle Int.*, vol. 28, no. 4, pp. 456-462, April 2007. <https://doi.org/10.3113/fai.2007.0456> ↑3
- [10] C. Ferrin *et al.*, "Sistema de extracción automática de parámetros morfológicos de la huella plantar mediante técnicas de visión por computador en un sistema embebido," *Revista Colombiana de Tecnologías Avanzadas*, vol. 1, no. 23, pp. 80-86, 2014. <https://doi.org/10.24054/rcta.v1i23.1893> ↑3
- [11] A. Rosas Flores, "Diseño de una plantilla ergonómica que regule la presión plantar en jóvenes practicantes de baloncesto femenino: análisis biomecánico y de elemento finito," Master's thesis, CIATEC, Mexico, 2021. <http://ciatec.repositorioinstitucional.mx/jspui/handle/1019/167> ↑3
- [12] S. Koirala *et al.*, "Calculation of Staheli's plantar arch index, Chippaux-Smirak index, Clarke's angle prevalence and predictors of flat foot: A cross sectional study," *Austin J. Anatomy*, vol. 8, no. 1, pp. 1-6, Jan. 2021. <https://doi.org/10.26420/austinjanat.2021.1095> ↑3,4
- [13] J. C. Zuñil Escobar *et al.*, "Evaluating the medial longitudinal arch of the foot: Correlations, reliability, and accuracy in people with a low arch," *Physical Therapy*, vol. 99, no. 3, pp. 364-372, 2019. <https://doi.org/10.1093/ptj/pzy149> ↑3
- [14] J. Marouvo *et al.*, "Correlation between different methods to diagnose foot posture condition," *Multidisciplinary Sci. J.*, no. 4, pp. 233-243, 2021. <https://doi.org/10.3390/j4030019> ↑3
- [15] R. Mahaffey *et al.*, "Age-related changes in three-dimensional foot motion during barefoot walking in children aged between 7 and 11 years old," *Gait & Posture*, no. 95, pp. 38-43, 2022. <https://doi.org/10.1016/j.gaitpost.2022.04.001> ↑3
- [16] C. E. Fuentes Venado *et al.*, "Evaluación comparativa de pie plano en preescolares," *Med. B. Children's Hospital of Mexico*, vol. 77, no. 6, pp. 312-319, 2020. <https://doi.org/10.24875/bmhim.20000135> ↑3
- [17] V. Bewick *et al.*, "Statistics review 7: Correlation and regression," *Critical care*, vol. 7, pp. 1-9, 2003. <https://doi.org/10.1186/cc2401> ↑3,6

- [18] H. A. Miranda Camacho *et al.*, "Interface for contour extraction and determination of morphologic parameters in digital images of footprints based on Hernandez-Corvo protocol," CLAIB, México, 2019. https://dx.doi.org/10.1007/978-3-030-30648-9_48 ↑4
- [19] A. Flores Cu and H. A. Miranda Camacho, "Desarrollo de interfaz para estudio estático de huella plantar en infante utilizando procesamiento digital, con diseño y manufactura de plantilla correctora," undergraduate thesis, TecNM/Irapuato, México, 2020. <http://dx.doi.org/10.13140/RG.2.2.32331.77604> ↑4
- [20] M. Cano *et al.*, "Foot computational diagnosis though Hernández Corvo, Clarke and Staheli Chippaux index", *Int. Conf. Mechat., Elec. Autom. Eng. (ICMEAE)*, pp.35-41,2022. <http://dx.doi.org/10.1109/ICMEAE58636.2022.00014> ↑4

Carlos Ismael Cabrera Pérez

Mechatronics Engineering at National Technological Institute of Mexico, Irapuato. Guanajuato, Mexico.

Email: LIS18110621@irapuato.tecnm.mx

Juan Antonio López Valdez

Mechatronics Engineering at National Technological Institute of Mexico, Irapuato. Guanajuato, Mexico.

Email: LIS18110985@irapuato.tecnm.mx

Horacio Rostro González

He received his Eng. in Electronics from the ITC in 2003 and a ME in Electrical from Guanajuato University in 2006, both in Mexico. He also received a PhD in Computational Neuroscience from the University of Nice-Sophia Antipolis, France, in 2011. Since 2012, he works as a full professor in the Department of Electronics of Universidad de Guanajuato. He currently works at Ramon Llull University in Barcelona, Spain. His research interests include reconfigurable electronics (FPGAs), neuromorphic engineering, computational neuroscience, bio-inspired algorithms, robotics, parallel computing, and signal processing.

Email: horacio.rostro@iqs.url.edu

Jatziry S. Cano Lara

She received a degree in Nutrition from Guadalajara University in 2011, a Master's degree in Nutrition from Universidad Iberoamericana in 2014, and a Specialty in Nutrition and Dietetics from UNAM in 2019. Since 2014, she is a nutrition specialist at IMSS Gto. Mexico.

Email: sirisuri@hotmail.com

Miroslava Cano Lara

She received an Eng. in Communications and Electronics and a Master's degree in Electrical Engineering, both from Universidad de Guanajuato, Mexico, in 2003 and 2006, respectively. She received a PhD in Optics Science from CICESE (Mexico), and a postdoctoral degree in Nonlinear Optics from Universidad de Guanajuato in 2016. She works at the Department of Mechatronics of TecNM/ITS Irapuato. Her research interests include laser material processing, optomechatronics, composite materials, UAVs, biomechatronics, artificial intelligence, and brain-computer interfaces.

Email: miroslava.cl@irapuato.tecnm.mx



Research

Safety Performance Functions for Mountain Two-lane Rural Roads in Ecuador

Funciones de Desempeño de Seguridad para Carreteras Rurales de Dos Carriles en entornos de montaña en Ecuador

Yasmany Damián García-Ramírez¹  

¹Universidad Técnica Particular de Loja (Loja, Ecuador) 

Abstract

Context: The design and operation of two-lane rural roads in mountainous terrain pose unique challenges, potentially leading to specific geometric configurations with an increased risk of road accidents. While predictive models like the Highway Safety Manual (HSM) and Safety Performance Functions (SPF) are widely used around the world, their application in Ecuador's mountainous regions remains unexplored.

Method: This study collected design and operational variables from 25 roads in the Ecuadorian Andes to propose SPFs specific to two-lane rural roads in mountainous environments. Crash data from 2017-2019 were utilized to develop 12 SPFs, which were further validated with information from 2020-2021. The SPFs were categorized based on three types of crashes (total, fatal + injury, property damage only) and various ranges of annual average daily traffic (AADT).

Results: The outcomes of this study include the development of 12 SPFs tailored to Ecuador's mountainous regions. These SPFs estimate the average expected frequency of accidents for existing conditions, alternative scenarios, or proposed new road projects.

Conclusions: The proposed SPFs fill a significant gap in road safety research in Ecuador, offering a valuable tool for assessing accident probabilities in two-lane rural roads in mountainous terrain. This research contributes to enhancing road safety for both existing roads and future projects, providing valuable insights for transportation planning and design. Further research opportunities lie in applying these SPFs to additional regions and refining the models based on evolving traffic and road conditions.

Keywords: safety performance functions, two-lane rural roads, Ecuador

Article history

Received:
15th / Aug / 2023

Modified:
13th / Sep / 2023

Accepted:
20th / Sep / 2023

Ing., vol. 29, no. 1,
2024. e19828

©The authors;
reproduction right
holder Universidad
Distrital Francisco
José de Caldas.

Open access



*  Correspondence: ydgarcia1@utpl.edu.ec

Resumen

Contexto: El diseño y la operación de carreteras rurales de dos carriles en terrenos montañosos plantean desafíos únicos, que podrían conducir a configuraciones geométricas específicas con un mayor riesgo de accidentes de tránsito. Si bien los modelos predictivos como el Manual de Seguridad Vial (HSM) y las Funciones de Rendimiento de Seguridad (SPF) se utilizan ampliamente a nivel mundial, su aplicación en las regiones montañosas de Ecuador aún no ha sido explorada.

Método: Este estudio recopiló variables de diseño y operativas de 25 carreteras en los Andes ecuatorianos para proponer SPFs específicas para carreteras rurales de dos carriles en entornos montañosos. Se utilizaron datos de accidentes de 2017 a 2019 para desarrollar 12 SPFs, que fueron validadas con información de 2020 a 2021. Las SPFs se clasificaron según tres tipos de accidentes (total, fatal + lesión, solo daños materiales) y varios rangos de tráfico diario promedio anual (TPDA).

Resultados: El resultado de este estudio incluye el desarrollo de 12 SPFs adaptadas a las regiones montañosas de Ecuador. Estas SPFs estiman la frecuencia esperada promedio de accidentes para condiciones existentes, escenarios alternativos o nuevos proyectos de carreteras propuestos.

Conclusiones: Las SPFs propuestas llenan una brecha significativa en la investigación de seguridad vial en Ecuador, ofreciendo una herramienta valiosa para evaluar las probabilidades de accidentes en carreteras rurales de dos carriles en terrenos montañosos. Esta investigación contribuye a mejorar la seguridad vial tanto para las carreteras existentes como para los proyectos futuros, proporcionando información valiosa para la planificación y el diseño del transporte. Oportunidades adicionales de investigación radican en aplicar estas SPFs a regiones adicionales y perfeccionar los modelos según la evolución del tránsito y las condiciones de las carreteras.

Palabras clave: funciones de desempeño de seguridad, carreteras rurales de dos carriles, Ecuador

Table of contents

		3.4. Model validation	10
		4. Results and discussion	10
		4.1. Model calibration	10
		4.2. Validation of the models	11
1. Introduction	2	5. Conclusions	14
2. Safety performance functions	4	6. Acknowledgements	15
3. Materials and methods	6	7. Author contribution	15
3.1. Segment selection	6	References	15
3.2. Crash data	7		
3.3. Calibration of the models	9		

1. Introduction

The Highway Safety Manual (HSM) provides a predictive method and analytical procedures to support road projects in various phases, including planning, preliminary design, final design, and construction (1). The HSM procedure aids in identifying locations with a potential for reducing

crashes or their severity, diagnosing issues, selecting countermeasures, conducting economic appraisals, prioritizing projects, and evaluating safety effectiveness (2). The HSM primarily describes the predictive method and crash modification factors (CMF). The predictive model includes the safety performance functions (SPFs) used to forecast crash counts at different roadway elements (3). These SPFs should be adjusted to local conditions for optimal results (4). Calibration is essential because the overall crash frequencies can vary significantly from one location to another due to various factors, such as crash reporting thresholds and crash reporting system procedures (1). To adapt the predictive model or SPF to local conditions, there are two options: calibrating the SPF or developing a new one.

The choice between calibration and development depends on the resources available to the institution and its objectives. The FHWA (Federal Highway Administration) issued report FHWA-SA-14-004, which evaluates these two options (5). Calibration maintains the structure of the original equations, allowing to compare the results across different areas. On the other hand, during development, the equations are more likely to change, leading to differences in the comparisons. SPF calibration can be achieved by either calculating the calibration factor or estimating the calibration function.

The calibration factor procedure involves adjusting the original model proposed by the HSM to fit the local conditions. The calibration factor is calculated as the ratio of the total number of observed crashes to the total number of predicted crashes. At times, the model may either overpredict or underpredict the number of accidents. For instance, in Ecuador, the calibration factor for two-lane rural roads was reported to range between 0,12 and 0,25 (6). In this case, the model overpredicted the crash frequency. Here, it is important to note that rural roads are typically susceptible to more severe accidents due to topographical limitations. Similar studies have been conducted in numerous countries and for various types of roads.

Other works have concentrated on the calibration of SPFs, which are models used to predict the number of crashes. In the HSM, SPFs are negative binomial regression models that establish a log-linear relationship between crash frequency and various site characteristics (7). These models invariably include traffic volume (AADT) and can also incorporate site-specific factors such as section length and lane width, among others. It is important to note that the calibration of SPFs should be conducted separately for different crash types (8) rather than combining all crash types into one model. Models specific to crash types tend to provide a better fit in comparison with using a single model that estimates the total crashes together with the overall proportion of each crash type (9).

There is a substantial amount of research worldwide that involves calibrating SPFs for two-lane rural roads. For instance, the original HSM model consistently underpredicts crashes on two-lane rural roads in Utah (10) and Illinois (4). In Pennsylvania, the findings suggest significant variations in safety performance across engineering districts, a factor that should be considered by other state transportation agencies (11). Similar results have been identified in research conducted in Virginia (12), Oregon, and Georgia (13). The performance of SPFs may also differ depending on the type of pavement, as indicated by results obtained in Michigan (14). Additionally, in flat terrain in Spain, the HSM model

exhibits both underprediction and overprediction tendencies in response to variations in AADT (15). Note that it is necessary to adjust SPF models to local conditions in order to achieve more accurate results. These equations are widely used worldwide because they are fundamental for road safety analysis. However, in Ecuador, there has been limited progress on this issue. Hence, the primary objective of this study is to calibrate SPFs for two-lane rural highways in the mountainous regions of Ecuador, considering various types of accidents and different traffic volume ranges. 25 roads in the Andes mountains were selected for evaluation, totaling approximately 630 km in length. Geometric and operational data were collected for each of these roads and compared to recorded road crashes.

To present this calibration, this document is structured as follows. Firstly, it describes the predictive model of the HSM. Secondly, it provides detailed information on the materials and methods employed, including an analysis of the data collection process, calibration procedure, and validation phase. Subsequently, it presents the results obtained from the models and an analysis of prediction errors. Finally, the document highlights the main findings and conclusions.

2. Safety performance functions

El HSM (1) states that, for rural two-lane and two-way roadway segments, the predictive model takes the form of Eq. (1).

$$N_{\text{predicted}} = N_{\text{spf-rs}} \times C_r \times CMF_{1r} \times CMF_{2r} \times \dots \times CMF_{12r} \quad (1)$$

Where:

$N_{\text{predicted}}$: predicted average crash frequency for an individual roadway segment and a specific year (crashes/year)

$N_{\text{spf-rs}}$: predicted average crash frequency under base conditions for an individual roadway segment (crashes/year)

C_r : calibration factor for roadway segments of a specific type developed for a particular jurisdiction or geographical area (dimensionless)

$CMF_{1r} \dots CMF_{12r}$: crash modification factors for rural two-lane, two-way roadway segments

Eq. (1) in the model predicts either the total average crash frequency or that of specific crash severity or collision types. This model addresses the regression-to-the-mean bias by focusing on the long-term expected average crash frequency, rather than relying solely on the short-term observed crash frequency (1). To account for variations in segment characteristics when compared to base conditions, Crash Modification Factors (CMFs) are employed with the aim of adjusting the number of crashes. While the HSM provides these CMFs, there is also a website known as the *Crash Modification Factors Clearinghouse* (16), which compiles CMFs from various studies, categorized by country or region. In Eq. (1), the model incorporates the safety performance function, the expression of which can be found in Eq. (2).

$$N_{\text{spf-rs}} = AADT \times L \times 365 \times 10^{-6} \times e^{(-0,312)} \quad (2)$$

Where:

$N_{\text{spf-rs}}$: predicted average crash frequency for base conditions using a statistical regression model (crashes/year)

$AADT$: average annual daily traffic (vehicles per day)

L : length of the road segment (miles)

Eq. (2) is based on a negative binomial distribution, which is better suited for modeling the high natural variability of crash data compared to traditional modeling techniques (1). Moreover, this equation involves only two variables, *i.e.*, the average annual daily traffic and the segment length, making it easier to calibrate the model in comparison to other SPFs with more variables. The SPF results can be calculated with a high level of accuracy even when there are only 1-3 years of recorded crashes for the studied site (17). SPFs are developed using statistical multiple regression techniques, employing historical crash data collected over several years at sites with similar characteristics and encompassing a wide range of AADT values (1). These SPFs provide estimates for the average number of crashes when the segments meet the base conditions outlined in Table I. When a segment does not meet the base conditions, it should be adjusted using the CMFs proposed by the HSM model.

Table I. Base conditions for roadway segments on rural two-lane, two-way roads

N°	Road feature	Base condition
1	Lane width (LW)	12 ft
2	Shoulder width (SW)	6 ft
3	Shoulder type	Paved
4	Roadside hazard rating (RHR)	3
5	Driveway density (DD)	5 driveways per mile
6	Horizontal curvature	None
7	Vertical curvature	None
8	Centerline rumble strips	None
9	Passing lanes	None
10	Two-way left-turn lanes	None
11	Lighting	None
12	Automated speed enforcement	None
13	Grade level	0%

Source: Highway Safety Manual (1).

The base conditions shown in Table I may not necessarily be directly applicable or valid in the context of Ecuador. The suitability of these factors for calibration in the country would depend on several factors, namely.

- a) *Local conditions:* Ecuador has different road infrastructures, traffic patterns, and environmental factors in comparison with the United States. Therefore, the relevance and impact of these factors on road safety could vary.

- b) *Regulatory and design standards*: Ecuador has its own set of design standards, regulations, and guidelines for road construction and safety. However, its standards are similar to those of the United States.
- c) *Data availability*: The availability and quality of data related to these factors may vary between countries. Ecuador lacks some comprehensive data on certain factors, which affects the calibration process.
- d) *Geographical and environmental differences*: Ecuador's diverse geography, including mountainous regions, coastal areas, and urban centers, may pose unique challenges and considerations not found in the United States. In this context, it is essential to conduct a thorough assessment and potentially adapt the factors used for SPF calibration to align with the specific conditions and requirements of Ecuador.

3. Materials and methods

To calibrate SPFs, it is essential to gather data on the AADT, the length of the segment, and the number of crashes recorded in it. This section provides an overview of the materials and methods employed for data collection and processing. Additionally, it outlines the procedures for calibrating and validating the models.

3.1. Segment selection

Initially, 25 two-lane roads were selected, with lengths ranging from 7,4 to 40 miles, as indicated in Table II. The AADT values, calculated or measured in 2017, have been included in this table. It is worth noting that the AADT estimation process was primarily carried out by students participating in the Road Projects course at Universidad Técnica Particular de Loja, along with the OSEVI-UTPL traffic counter (18).

The features of every road listed in Table II were analyzed. These roads have a width between 11 and 12 ft, which is similar to the base condition. Additionally, these roads have a shoulder width between 2 and 4 ft, which is less than the base condition. However, it is important to note that these roads were constructed using older standards, where the shoulder width was narrower. The entire shoulder is paved, in accordance with national guidelines and base conditions. The roadside hazard rating (RHR) ranged between 3 and 7, as these are mountain roads. It is common for Ecuadorian mountain roads to have this level of risk, and it can be challenging to find RHR values equal to 3, which is the base condition. The driveway density was less than 5 driveways per mile, which is also common in mountain roads. Despite these differences, the remaining road features were consistent with the base conditions. Even though it may not be possible to meet all base conditions, efforts were made to align with the majority of them.

Table II. Selected two-lane rural roads in this study

N°	Origen-destination of the road	Length (mi)	AADT ₂₀₁₇ (veh per day)
1	Catamayo - San Pedro	7,6	6.153
2	Chambo - Cubijíes	12,4	1.001
3	Cuchaentza - Macuma	12,4	298
4	Cuenca - Girón	12,5	14.777
5	Cuenca - Loja	12,5	5.000
6	Cuenca - Molleturo	12,4	4.006
7	Molleturo - El Empalme	12,5	4.916
8	El Descanso - Malima	17,9	398
9	Gualaceo - Limón Indanza	12,6	2.032
10	La Era - Indiucho	12,9	201
11	Las Chinchas - Zambí	12,4	48
12	Loja - Catamayo	19,6	6.153
13	Loja - Jimbilla	12,5	184
14	Loja - Saraguro	40,0	2.803
15	Loja - Yangana	34,7	4315
16	Loja - Zamora	35,9	2.427
17	Malacatos - La Era	12,4	201
18	Puyo - Nuevos Horizontes	14,4	849
19	Riobamba - Penipe	12,4	4.955
20	San Pedro - Las Chinchas	7,4	6.153
21	Sunamanga - Sacapalca	11,7	111
22	Tabacay - Cochahuayco	14,7	990
23	Villonaco - Chuquiribamba	12,4	355
24	Yangana - Sabanilla	12,5	251
25	Ye de Olmedo - Chaguarpamba	12,4	1.407

Source: Master's students of the Road Projects course at Universidad Técnica Particular de Loja and the OSEVI-UTPL traffic counter (18)

3.2. Crash data

Crash data were sourced from the National Transport Agency of Ecuador's website (19). For each segment listed in Table II, three types of data were collected: total crashes (T), fatal and injury crashes (FI), and property damage only (PDO). It is important to note that these data were not directly available on the website and had to be estimated based on the causes of the accidents. The HSM recommends certain guidelines for data collection. It suggests a minimum sample size of 30-50 sites, with the entire group of calibration sites representing at least 100 crashes per year. It may take one to three years to accumulate a sufficient number of crash events to meet these crash frequency criteria (1).

The road segments were associated with the closest crash record. Subsequently, the database was organized into two time periods: 2017-2019 and 2020-2021. This non-probability sampling division allowed calibrating predictive models via the crash data from the earlier period (2017-2019) and validating them using the more recent data (2020-2021). Initially, an analysis was conducted on individual segments, where 50 sites were randomly selected from those available. Between 2017 and 2019, 1,042 sites had no accidents, while 197 did. In total, 246 crashes were recorded during this period. Due to the low number of records and the high number of sites with no accidents, the random selection did not yield 100 crashes, despite a three-year analysis period. Consequently, we decided to use all 25 road sections as if they were individual segments, as shown in Table III.

Table III. Number of crashes in every road for the period of time analyzed (based on ANT data)

N°	2017-2019			2020-2021		
	T	FI	PDO	T	FI	PDO
1	2	1	1	3	2	1
2	8	5	3	2	1	1
3	1	1	0	1	1	0
4	45	18	27	12	7	5
5	21	14	7	3	1	2
6	28	10	18	9	3	6
7	6	3	3	7	5	2
8	0	0	0	0	0	0
9	0	0	0	0	0	0
10	0	0	0	1	1	0
11	0	0	0	0	0	0
12	24	15	9	10	7	3
13	2	2	0	1	0	1
14	22	14	8	20	12	8
15	32	10	22	19	10	9
16	15	4	11	5	3	2
17	0	0	0	1	0	1
18	19	16	3	16	14	2
19	16	9	7	23	8	15
20	3	2	1	4	1	3
21	0	0	0	0	0	0
22	0	0	0	0	0	0
23	1	0	1	2	1	1
24	1	1	0	0	0	0
25	0	0	0	1	1	0
Total	246	125	121	140	78	62

The data from 2019-2021 were then used for model calibration. It is worth noting that, if more than three years of data were available, they could be useful for assessing potential time trends in annual calibration factor estimates (17).

Table III shows that the highest number of observed accidents took place on road No. 4, which also has the highest AADT. Surprisingly, the longest road (14) does not have the highest number of accidents, possibly due to its low AADT value. This pattern is consistent with previously estimated SPFs. Interestingly, several roads had no recorded accidents in the analyzed period, while others had no records in the first period but did in the second. It is worth noting that the total crashes (T) value is approximately double that of fatal and injury crashes (FI) or property damage only (PDO). However, this is coincidental, as this pattern does not hold when analyzing each site separately. These variations and trends suggest that the selected sites may be representative since they encompass various situations encountered in engineering practice.

3.3. Calibration of the models

The calibration methodology employed in this study aims to refine the SPFs for two-lane rural highways in mountainous environments in Ecuador. Calibration is a crucial step in developing accurate predictive models for road safety, ensuring that the models align with local conditions and offer enhanced predictive accuracy. The specific methods and approaches for calibrating SPFs can vary, but they generally follow a systematic process. Here are the methods and considerations used in this calibration:

- *Data collection.* The calibration process relied on crash data from the National Transport Agency of Ecuador, covering the period from 2017 to 2019. This dataset included information from 25 distinct road sections, allowing for a comprehensive analysis.
- *Data preprocessing.* Before calibration, the crash data underwent preprocessing, which involved categorizing crashes by severity (fatal, injury, property damage only), cleaning the data to remove duplicates or errors, and geocoding crash locations.
- *Selection of predictive variables.* SPFs are typically developed as regression models that relate crash frequency to various roadway and traffic characteristics. The key variables used in the calibration process include AADT and segment length. In instances where no crashes were recorded, an exponent value of zero was assumed.
- *Cluster analysis.* Subsequently, a cluster analysis was performed to categorize data points based on AADT ranges. This analysis helped to identify groups of data points with similar characteristics, aiding in the calibration process. The clustering approach allowed for a more tailored calibration process based on traffic volume.
- *Model formulation.* A negative binomial or Poisson regression model was selected for formulating the model, whose form determines the relationship between crash frequency and the selected predictive variables.
- *Exponent estimation.* The model was then fitted to the data, including the estimation of model parameters and the exponent for each predictive variable. The exponent values indicate how each variable affects crash frequency. An average of all exponents was calculated for each type of accident and for all accidents combined.
- *Calibration.* This process involved modifying the exponent values to account for factors specific to the study area. It aimed to ensure that the model accurately predicts crash frequency in the local

context. To establish a baseline for calibration, an initial analysis was conducted using data from all the road sections.

3.4. Model validation

The calibrated models were put to the test using crash data from 2020-2021. However, due to mobility restrictions resulting from the COVID-19 pandemic, the AADT figures for the sites in Table II needed adjustment. To address this issue, adjustment factors were estimated based on data from the UTPL Road Safety Observatory (18). Specifically, OSEVI-UTPL recorded the number of vehicles circulating on four two-lane roads in mountainous regions in southern Ecuador. The proportion between the traffic volume in 2017 and that in 2020-2021 was calculated for each road, and the adjustment factors were determined as their average. Consequently, the AADT for 2020 was 0,60 when compared to 2017, and for 2021, it was 0,79 compared to 2017. These factors were applied to adjust the AADT values in Table II.

Subsequently, the calibrated models were employed to predict the number of accidents for 2020-2021. These predicted values were compared with the actual recorded values for the same period, as displayed in Table III. Finally, the errors of the calibrated models were analyzed for further refinement. The prediction errors considered for analysis included the Mean Squared Prediction Error (MSPE), Mean Absolute Deviation (MAD), Mean Prediction Bias (MPB), and Mean Absolute Percentage Error (MAPE).

4. Results and discussion

Continuing with the procedure outlined in the previous section, the results of the calibration and validation of the SPFs are presented.

4.1. Model calibration

Table IV presents the calibration results, beginning with the general model for all traffic, and then the AADT ranges resulting from the cluster analysis, which achieved a 95 % similarity. The histogram in Fig. 1 confirms the ranges obtained in the cluster analysis. However, special attention must be paid to the last range, as there is a lack of AADT values until reaching nearly 15.000 vehicles/day. This stratification of AADT for the calibration of the SPF equations is in line with previous findings (15,20).

Table IV shows that the exponents for total crashes are lower than those for fatal and injury crashes, while the exponents for the latter are very similar to those for property damage only. Additionally, as the number of vehicles increases, the absolute value of these exponents increases, and this trend applies to all three categories of accidents. Only in the range of up to 1.000 vehicles per day do positive exponents appear, whereas, in the other models, the exponents are negative, as seen in the original equation.

Given these observed trends, using a single model, such as Eqs. (3), (4), and (5), would likely result in higher prediction errors when compared to using Eqs. (6) through (18). In light of this, the general model will not undergo validation in the following section.

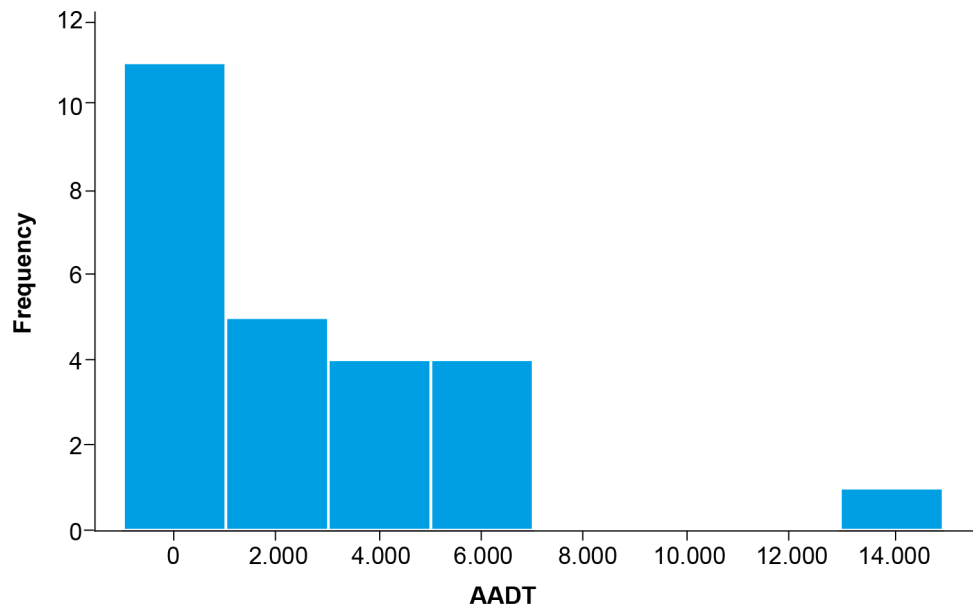


Figure 1. Histogram of AADT

4.2. Validation of the models

For validation purposes, we utilized the adjusted AADT, segment length, and crash data from 2020-2021. Eqs. (6)-(18) in Table IV were employed to predict the number of crashes for 2020-2021, as summarized in Table V. The selection of specific equations was based on the corresponding AADT values for each road segment. Table V shows that the total number of observed crashes in the period was 140, while the predicted count was 166,00. For fatal and injury crashes (F+I), there were 78 observed crashes, compared to a predicted count of 106,50. Property damage only (PDO) crashes had 62 observed crashes, with a predicted count of 102,15.

The scatterplot of values from Table V is presented in Fig. 2. In an ideal scenario, all the points would closely align around a 45° reference line. However, it is essential to remember that SPFs provide 'long-term average results, not 'short-term average' ones (17). Although there are points where the equations overestimate or underestimate the observed crashes, it is necessary to conduct an error analysis to determine the validity of the equations.

Table VI presents the prediction errors for the crashes predicted using Eqs. (6)-(18). Regarding the MSPE, lower values are preferable, as they indicate a better fit of the model to the data. In this case, the values could be deemed acceptable, with the highest value being 27,8.

Table IV. Safety performance function proposed by this study

AADT	Crash type	SPF equation	Inference		
			interval of crashes	Sample size	Eq. No.
All	T	$N_{spf-rs} = AADT \times L \times 365 \times 10^{-6} \times e^{(-0,244)}$	0-45	17	(3)
	FI	$N_{spf-rs} = AADT \times L \times 365 \times 10^{-6} \times e^{(-0,576)}$	0-18	16	(4)
	PDO	$N_{spf-rs} = AADT \times L \times 365 \times 10^{-6} \times e^{(-0,696)}$	0-27	14	(5)
<1.000	T	$N_{spf-rs} = AADT \times L \times 365 \times 10^{-6} \times e^{(0,128)}$	0-19	5	(6)
	FI	$N_{spf-rs} = AADT \times L \times 365 \times 10^{-6} \times e^{(0,155)}$	0-16	4	(7)
	PDO	$N_{spf-rs} = AADT \times L \times 365 \times 10^{-6} \times e^{(-0,080)}$	0-3	2	(8)
1.000-3.000	T	$N_{spf-rs} = AADT \times L \times 365 \times 10^{-6} \times e^{(-0,161)}$	0-22	3	(10)
	FI	$N_{spf-rs} = AADT \times L \times 365 \times 10^{-6} \times e^{(-0,610)}$	0-14	3	(11)
	PDO	$N_{spf-rs} = AADT \times L \times 365 \times 10^{-6} \times e^{(-0,621)}$	0-11	3	(12)
3.000-6.000	T	$N_{spf-rs} = AADT \times L \times 365 \times 10^{-6} \times e^{(-0,369)}$	6-32	5	(13)
	FI	$N_{spf-rs} = AADT \times L \times 365 \times 10^{-6} \times e^{(-1,142)}$	3-14	5	(14)
	PDO	$N_{spf-rs} = AADT \times L \times 365 \times 10^{-6} \times e^{(-1,056)}$	3-22	5	(15)
6.000-15.000	T	$N_{spf-rs} = AADT \times L \times 365 \times 10^{-6} \times e^{(-1,216)}$	2-45	4	(16)
	FI	$N_{spf-rs} = AADT \times L \times 365 \times 10^{-6} \times e^{(-1,838)}$	1-18	4	(17)
	PDO	$N_{spf-rs} = AADT \times L \times 365 \times 10^{-6} \times e^{(-2,037)}$	1-27	4	(18)

T: total crashes; FI: fatal and injury crashes; PDO: property damage only; N_{spf-rs} : predicted average crash frequency for base conditions using a statistical regression model (crashes/year); AADT: average annual daily traffic (vehicles per day); L: length of the road segment (miles).

The MAD provides a measure of the average magnitude of prediction variability, and smaller values are preferred over larger ones. In this case, the maximum value was 3,6, which was deemed acceptable.

The MPB offers insights into whether the equations overpredict or underpredict. A positive value suggests underprediction, while a negative one implies overprediction. As observed in Fig. 2, the equations are slightly underpredicting, consistent with the calculated positive values of MPB.

Lastly, the MAPE calculates the average error percentage between the observed and predicted values, relative to the former. Lower MAPE values indicate better predictions.

However, in this case, the values are relatively high due to their close relationship with the total recorded crash values.

Despite the higher MAPE values, the rest of the error metrics constitute noteworthy results, suggesting that the models can be regarded as validated.

Table V. Observed and expected crashes calculated using the equations 6-18 from Table IV

N°	AADT	Length (mi)	Total crashes		Fatal + injured		PDO crashes	
			Observed	Expected	Observed	Expected	Observed	Expected
1	3.286	7,58	3	6,29	2	2,90	1	3,16
2	535	12,43	2	2,76	1	2,83	1	2,24
3	159	12,43	1	0,82	1	0,84	0	0,67
4	7.891	12,49	12	10,66	7	5,73	5	4,69
5	2.670	12,49	3	10,37	1	6,62	2	6,54
6	2139	12,43	9	8,26	3	5,28	6	5,21
7	2.625	12,49	7	10,19	5	6,51	2	6,43
8	1.497	17,90	0	8,33	0	5,32	0	5,25
9	1.085	12,62	0	4,25	0	2,72	0	2,68
10	107	12,93	1	0,58	1	0,59	0	0,47
11	26	12,43	0	0,13	0	0,14	0	0,11
12	3.286	19,64	10	16,29	7	7,52	3	8,20
13	98	12,49	1	0,51	0	0,52	1	0,41
14	1.497	39,96	20	18,59	12	11,87	8	11,73
15	2.304	34,68	19	24,84	10	15,86	9	15,67
16	1.296	35,86	5	14,45	3	9,22	2	9,11
17	107	12,43	1	0,55	0	0,57	1	0,45
18	453	14,42	16	2,71	14	2,79	2	2,20
19	2.646	12,43	23	10,22	8	6,53	15	6,45
20	3.286	7,40	4	6,14	1	2,83	3	3,09
21	59	11,75	0	0,29	0	0,30	0	0,23
22	529	14,73	0	3,23	0	3,32	0	2,63
23	190	12,43	2	0,98	1	1,00	1	0,79
24	134	12,49	0	0,69	0	0,71	0	0,56
25	751	12,43	1	3,87	1	3,98	0	3,15
TOTAL			140	166,0	78	106,5	62	102,15

Table VI. Prediction errors of the proposed safety performance function

Error	Total crashes	Fatal plus injured crashes	Property damage only crashes
MSPE	27,8	12,3	12,4
MAD	3,6	2,3	2,5
MPB	1,0	1,1	1,6
MAPE	75,4	107,4	103,9

The presented and validated models represent significant progress in the field of road safety for two-lane roads. Using separate equations for different types of accidents, as demonstrated here, addresses the limitation of a single equation, such as the one proposed by the HSM, which can lead to errors when applied without distinction among accident types. This finding is consistent with previous

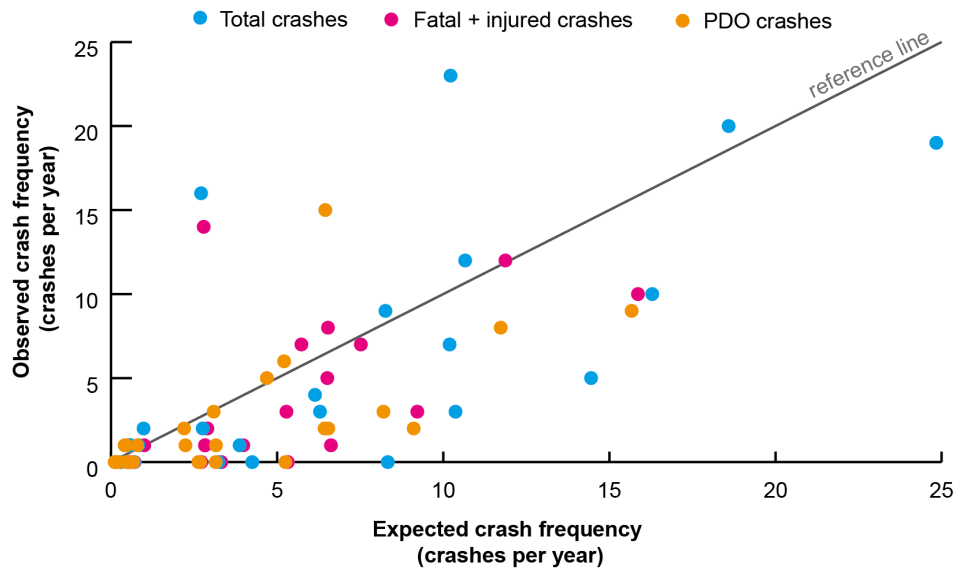


Figure 2. Expected versus observed crash frequency 2020-2021

research (9). Furthermore, the utilization of models based on traffic ranges, as shown in this study, has also been recognized in previous studies, and it is confirmed to provide improved results (17). These advancements contribute to a more nuanced and accurate understanding of road safety, ultimately aiding in the development of more effective safety measures and policies for two-lane roads.

5. Conclusions

The objective of this study was to propose Safety Performance Functions (SPFs) for two-lane rural highways in mountainous environments in Ecuador. After analyzing 25 road sections and accident data from 2017 to 2021, the following conclusions can be drawn: It was possible to successfully calibrate and validate 12 SPFs for two-lane roads. Unlike the Highway Safety Manual (HSM), which provides a single model for all accident types and Average Annual Daily Traffic (AADT) ranges, this study offers four models for total crashes, four for fatal and injury accidents, and four for property damage only. These models cover various AADT ranges, thus enhancing their applicability.

The base conditions, as defined in the HSM, are primarily derived from road characteristics commonly found in the United States. Our study area in Ecuador includes roads that may have different characteristics, such as narrower shoulder widths, variations in roadside hazard ratings, and mountainous terrain, which are not fully aligned with the HSM's base conditions. To address this limitation, we conducted our calibration and validation efforts using the available data, which reflect the local conditions of Ecuadorian mountain roads. While our approach provided valuable insights into road safety in our specific context, we recognize that it may have introduced variations compared to a strict adherence to HSM base conditions.

This study underscores the importance of calibrating models developed elsewhere before applying them to local conditions. The calibrated equations can be used for existing roads, alternative designs for existing ones, or new road projects, ultimately contributing to improved road safety for two-lane rural roads in Ecuador.

However, it is important to acknowledge the study's limitations. Firstly, it focused exclusively on two-lane roads in mountainous environments, which may not fully represent all road types in the country. Additionally, there was limited representation of high-traffic sites, which could lead to inconsistencies in the models for the highest AADT range. Furthermore, the study could not verify whether all road accidents were accurately collected and categorized, relying solely on data provided by the National Transport Agency (ANT).

Despite these limitations, the study significantly contributes by introducing various SPF equations for three types of road accidents and several traffic volume ranges that were previously lacking in the country. These models serve as a valuable starting point for analyzing accident rates in Ecuador and other regions with similar road characteristics.

6. Acknowledgements

Special thanks to the students of the 'Road Projects' course in the Master's Degree program in Civil Engineering with a focus on mountain roads at Universidad Técnica Particular de Loja for their invaluable support in collecting and calculating design and operational variables for the 25 roads included in this study regarding the period from April to August 2022. Additionally, special appreciation goes to ChatGPT 3.5, an advanced language model developed by OpenAI, for its linguistic capabilities in crafting a clear and accurate English version.

7. Author contribution

The author contributed in the following aspects: conceptualizing the study, designing the research methodology, data collection and analysis, writing and drafting the manuscript, and reviewing and editing the manuscript.

References

- [1] AASHTO, *Highway Safety Manual*, First. Washington, EE. UU.: AASHTO, 2010. ↑[2](#), [3](#), [4](#), [5](#), [7](#)
- [2] AASHTO, "Highway Safety Manual," 2016. <https://www.highwaysafetymanual.org/Pages/default.aspx> (accessed Jul. 26, 2022). ↑[3](#)
- [3] M. M. A. Al-Omari, M. Abdel-Aty, and Q. Cai, "Crash analysis and development of safety performance functions for Florida roads in the framework of the context classification system," *J. Safety Res.*, vol. 79, pp. 1-13, Dec. 2021. <https://doi.org/10.1016/J.JSR.2021.08.004> ↑[3](#)

- [4] M. Williamson and H. Zhou, "Develop calibration factors for crash prediction models for rural two-lane roadways in Illinois," *Procedia Soc. Behav. Sci.*, vol. 43, pp. 330-338, Jan. 2012. <https://doi.org/10.1016/J.SBSPRO.2012.04.106> ↑3
- [5] R. Srinivasan, D. Carter, and K. Bauer, "Safety performance function decision guide: SPF calibration vs SPF development (FHWA-SA-14-004)," 2013. <https://rosap.nhtl.bts.gov/view/dot/49504> (accessed Nov. 11, 2022). ↑3
- [6] Y. García, P. Rojas, E. Duque, and H. Rojas-Asuero, "Calibración del modelo predictivo de accidentes de tránsito del HSM en carreteras del Cantón Loja (Ecuador)," *INNOVA Res. J.*, vol. 3, no. 7, pp. 114-123, Jul. 2018. <https://doi.org/10.33890/innova.v3.n7.2018.605> ↑3, 12
- [7] R. Srinivasan and K. Bauer, "Safety performance function development guide: Developing jurisdiction-specific SPFs (FHWA-SA-14-005)," 2013. <https://highways.dot.gov/safety/data-analysis-tools/rsdp/rsdp-tools/safety-performance-function-development-guide-0> (accessed Nov. 11, 2022). ↑3
- [8] K. Bauer and D. Harwood, "Safety Effects of Horizontal Curve and Grade Combinations on Rural Two-Lane Highways (FHWA-HRT-13-077)," 2014. <https://www.fhwa.dot.gov/publications/research/safety/13078/index.cfm> (accessed Nov. 11, 2022). ↑3
- [9] T. Jonsson, C. Lyon, J. N. Ivan, S. P. Washington, I. Van Schalkwyk, and D. Lord, "Differences in the performance of safety performance functions estimated for total crash count and for crash count by crash type," *Transportation Res. Rec.*, vol. 2102, pp. 115-123, 2009. <https://doi.org/10.3141/2102-15> ↑3, 14
- [10] B. K. Brimley, "Calibration of the highway safety manual safety performance function and development of jurisdiction-specific models for rural two-lane two-way roads in Utah," Master's thesis, Fulton College of Engineering and Technology, 2011. [Online]. Available: <http://hdl.lib.byu.edu/1877/etd4337> ↑3
- [11] L. Li, V. V. Gayah, and E. T. Donnell, "Development of regionalized SPFs for two-lane rural roads in Pennsylvania," *Accid. Anal. Prev.*, vol. 108, pp. 343-353, Nov. 2017. <https://doi.org/10.1016/J.AAP.2017.08.035> ↑3
- [12] N. J. Garber, P. R. Haas, and C. Gosse, "Safety performance functions for two-lane roads in Virginia," presented at the Transportation Res. B. 89th Annual Meeting, Washington DC, USA, 2010. [Online]. Available: <https://trid.trb.org/view/910153> ↑3
- [13] P. Alluri, J. Ogle, F. Hie, K. Gladhill, K. K. Dixon, and C. M. Monsere, "Comparison of calibration factors obtained using Oregon and Georgia data to implement HSM procedures on two-way two-lane rural roads," presented at Moving Toward Zero. 2011 ITE Tech. Conf. Exhibit, 2011. [Online]. Available: <https://trid.trb.org/view/1103800> ↑3
- [14] S. Y. Stapleton, A. J. Ingle, M. Chakraborty, T. J. Gates, and P. T. Savolainen, "Safety performance functions for rural two-lane county road segments," *Transportation Res. Rec.*, vol. 2672, no. 52, pp. 226-237, Oct. 2018. <https://doi.org/10.1177/0361198118799035> ↑3, 9
- [15] L. Garach, J. de Oña, G. López, and L. Baena, "Development of safety performance functions for Spanish two-lane rural highways on flat terrain," *Accid. Anal. Prev.*, vol. 95, pp. 250-265, Oct. 2016. <https://doi.org/10.1016/J.AAP.2016.07.021> ↑4, 10

- [16] FHWA, "Crash modification factors clearinghouse," 2022. <http://www.cmfclearinghouse.org/index.cfm> (accessed Jul. 27, 2022). ↑4
- [17] G. Bahar, NAVIGATS Inc., and E. Hauer, "User's guide to develop highway safety manual safety performance function calibration (Project 20-07/332)," 2014. [https://onlinepubs.trb.org/onlinepubs/nchrp/docs/NCHRP20-07\(332\)_FinalGuide.pdf](https://onlinepubs.trb.org/onlinepubs/nchrp/docs/NCHRP20-07(332)_FinalGuide.pdf) (accessed Nov. 11, 2022). ↑5, 8, 11, 14
- [18] OSEVI-UTPL, "Observatorio de Seguridad Vial," 2022. <https://vinculacion.utpl.edu.ec/es/observatorios/osevi> (accessed Aug. 03, 2022). ↑6, 7, 10, 11
- [19] Agencia Nacional de Tránsito del Ecuador, "Estadísticas siniestros de tránsito," 2022. <https://www.ant.gob.ec/estadisticas-siniestros-de-transito-prueba/> (accessed Jul. 27, 2022). ↑7
- [20] J. M. Pardo Mayora, R. B. Manzo, and A. C. Orive, "Refinement of accident prediction models for Spanish national network," *Transportation Res. Rec.*, vol. 1950, pp. 65-72, Jan. 2006. <https://doi.org/10.1177/0361198106195000108> ↑10

Yasmany García-Ramírez

Civil Engineer graduated from Universidad Técnica Particular de Loja (UTPL) in Ecuador in 2006. He obtained a Specialist's degree in Mountain Road Engineering from Universidad Nacional de San Juan (UNSJ) in Argentina in 2009, as well as a PhD in Civil Engineering in 2014. Currently, García-Ramírez works as an associate professor at UTPL, where he imparts knowledge in subjects related to road design at both undergraduate and postgraduate levels. He also holds several leadership roles within UTPL, including the directorship of the Master's degree program in Civil Engineering with an emphasis on mountain roads. García-Ramírez has more than 40 publications in the field of road and civil engineering education.

Email: ydgarcia1@utpl.edu.ec





Research

How Accurately Are Climatological Characteristics and Surface Water and Energy Balances Represented for the Colombian Amazon Basin?

¿Con qué exactitud se representan las características climatológicas y los balances superficiales de agua y energía en la Cuenca Amazónica Colombiana?

Carolina Valencia-Monroy¹, Astrid Baquero-Bernal²  

¹Universidad Nacional de Colombia - Sede Bogotá  - Departamento de Geociencias and Instituto de Hidrología, Meteorología y Estudios Ambientales (IDEAM)

²Universidad Nacional de Colombia - Sede Bogotá  - Departamento de Física

Abstract

Context: The Colombian Amazon basin (CAB) is characterized by having many areas with few or no *in situ* observations. To help fix this shortcoming, there are different gridded datasets that represent meteorological variable estimates from *in situ*, satellite-based, merged, and model-based products. However, before using them, it is necessary to evaluate their performance.

Method: We analyzed the capacity of five grid datasets to represent the annual cycle, the annual means, and the interquartile range of temperature and the variables that intervene in the surface water and energy balances of the CAB. The five datasets were a regional climate model (REMO) and four reanalyses (ERA40, ERA-Interim, NCEP/NCAR, and NCEP-v2). For the temperature and precipitation analyses, the Delaware, GPCP, CPC, CMAP, and CMAP-v2 datasets were also taken into account.

Results: The average annual temperature cycle in the CAB has an unimodal behavior, with higher values between October and March. Only Delaware and ERA-Interim describe this behavior and exhibit values close to those of the observations. The average annual cycle of precipitation is also unimodal, with higher values between March and July. Delaware, GPCP, CPC, and ERA-Interim describe this behavior, although ERA-Interim overestimates precipitation. Additionally, the four reanalyses, especially ERA-Interim, show an unexpected trend of increase in mean annual precipitation. As for the water balance, the precipitation and runoff maps of ERA-Interim and REMO show higher values in the foothills and east of 73° W, a pattern that shows better agreement with the observations than those of the other datasets. ERA-Interim, REMO, and ERA-40 meet the closure condition of both the long-term water and the energy budgets. However, REMO and ERA-Interim overestimated precipitation, ERA-40 underestimated it, and ERA-Interim overestimated solar radiation. This implies that some of the other variables for the water and energy balances are also poorly estimated.

Conclusions: The five gridded datasets that allow studying surface water and energy balances are not adequate, so better models and reanalyses are required.

Keywords: Amazon basin, climate, energy balance, water balance

Article history

Received:
7th / Aug / 2022

Modified:
5th / Jul / 2023

Accepted:
7th / Oct / 2023

Ing., vol. 29, no. 1,
2024. e19774

©The authors;
reproduction right
holder Universidad
Distrital Francisco
José de Caldas.

Open access



*  **Correspondence:** abaquero@unal.edu.co

6. Author contributions	28	References	29
7. Acknowledgment	29		

1. Introduction

Amazonia is the region of northern South America around the Amazon River that includes the greater part of Brazil and the bordering parts of Colombia, Ecuador, Peru, and Bolivia (1). It encompasses the world's largest rainforest and is highly biodiverse, housing approximately a quarter of all terrestrial species in the world. The diverse vegetation in this region plays a crucial role in supplying oxygen on a continental scale. However, due to deforestation and human activities that cause desertification, Amazonia is increasingly becoming a source of carbon dioxide and overall greenhouse gas emissions, which causes increases in air temperature. It is considered to be the second most vulnerable area on Earth after the Arctic. Jungles and forests cover about 45% of the Colombian territory, and include the jungles of the Pacific and Amazonic regions and the remnants of the Andean, the Caribbean, and Orinoquía jungles (2).

At both the national and continental levels, the Colombian Amazon basin plays a vital role in providing ecosystem services related to water and carbon. *Ecosystem services* are defined as the benefits that human beings obtain from ecosystems (*i.e.*, biological systems constituted by a community of living organisms and the physical environment in which they are situated). According to (3), the main ecosystem services in the Colombian Amazonia, as identified by the local people, are of two types: provision and support. The first type corresponds to the supply of wood, straw, resins, wild fruits, fish, animals for hunting, natural medicines, and materials for handicrafts, traditional tools, and ornaments. The second type corresponds to the soil conditions necessary for the practice of traditional agriculture.

Additionally, some of the main ecosystem services in the Amazonia, as identified by the scientific community, are carbon storage regulation, protection against extreme events such as landslides (4), climate regulation (5), and hydrological services. Water for agriculture, navigation, industry, fisheries, and human consumption are part of the ecosystem services provided by these forests through the regulation of regional water and energy balances. Furthermore, there is great interest in beginning to exploit water resources in the Colombian Amazonia for hydroelectricity production (6).

Among the studies that have analyzed the meteorological and climatological aspects of Amazonia are (7), (8), and (9). The first analyzed the spatial-temporal variability of water balance components in the Amazon region using observations and data from the NCEP/NCAR reanalysis (10) for the 1970-1999 period. The second evaluated the transferability of the Regional climate model REMO (11) with a standard setup over different regions of the world. REMO was integrated over six domains, one of them being South America, finding significant temperature overestimation over Amazonia and near the coasts of major upwelling regions. The third evaluated the capabilities of a set of seven coordinated regional climate model (RCM) simulations to reproduce the mean climate conditions over the South American continent. The analysis focused on evaluating the reliability of simulating mean precipitation

and surface air temperature. The evaluation considered the seasonal means, the area-averaged annual cycles, and the frequency distributions of monthly means over target sub-regions, among them the region defined approximately between 5° and 15° S and 50° and 65° W and named *South Amazonia* (S-Amazonia). (9) found that the multi-model ensemble exhibits high uncertainty (as defined by the standard deviation of the models) and high bias regarding tropical regions across South America (including S-Amazonia), which suggests the low reliability of RCM simulations and limited capabilities in reproducing observed climate conditions for both temperature and precipitation in these regions.

(12) estimated the water balance in the Amazon River basin with data from the ERA-40 reanalysis (13) and the observational products CPC (14) and GPCP (15) for the 1980-2002 period. Their work evidenced the importance and necessity of a deeper analysis in each one of the countries that share the basin.

There are currently few studies that address the evaluation of reanalyses and climate models for Colombian territory, and even less in relation to the hydrological cycle. Some studies carried out by Instituto de Hidrología, Meteorología y Estudios Ambientales (IDEAM) show maps for the entire country regarding some important variables for the evaluation of water and energy balances upon the basis of observed data (16,17). However, these studies fail to address the actual evaluation of water and energy balances or that of reanalyses and climate models. The studies by (18), (19), and (20) address these issues in the Colombian Pacific and Caribbean Basins but do not encompass all Colombian catchment areas. In this work, the Colombian Amazon Basin (CAB) was analyzed.

The Colombian Amazonia has a surface area of approximately 470.000 km² (21). However, the spatial distribution of its meteorological stations is not uniform and is almost non-existent in the departments of Guanía and Guaviare (Fig. 1). Therefore, regional climate models and reanalyses should be useful in providing substantial information, particularly in these remote regions with little observational data. This study focuses on assessing the terrestrial branch of the water and energy balances of REMO and four reanalyses (ERA40, ERA-Interim (22), NCEP/NCAR, and NCEP-v2 (23)) for the CAB. The annual cycle, the interannual variability, the extreme values of air temperature and precipitation, and the relationship between the extremes and the phases of ENSO (El Niño Southern Oscillation) are also analyzed.

Section 2 details the study area, the main characteristics of the datasets used, and the methodology. Sections 3 and 4 provide the results, and Section 5 presents the discussion and draws conclusions.

2. Study area, data, and methodology

2.1. Study area

The CAB comprises territory of the departments of Amazonas, Caquetá, Guainía, Guaviare, Putumayo, and Vaupés (Fig. 1). The hydrological resources of the CAB and other basins are summarized in (17). According to this study, the CAB has an average water yield of 81 L/s·km²,

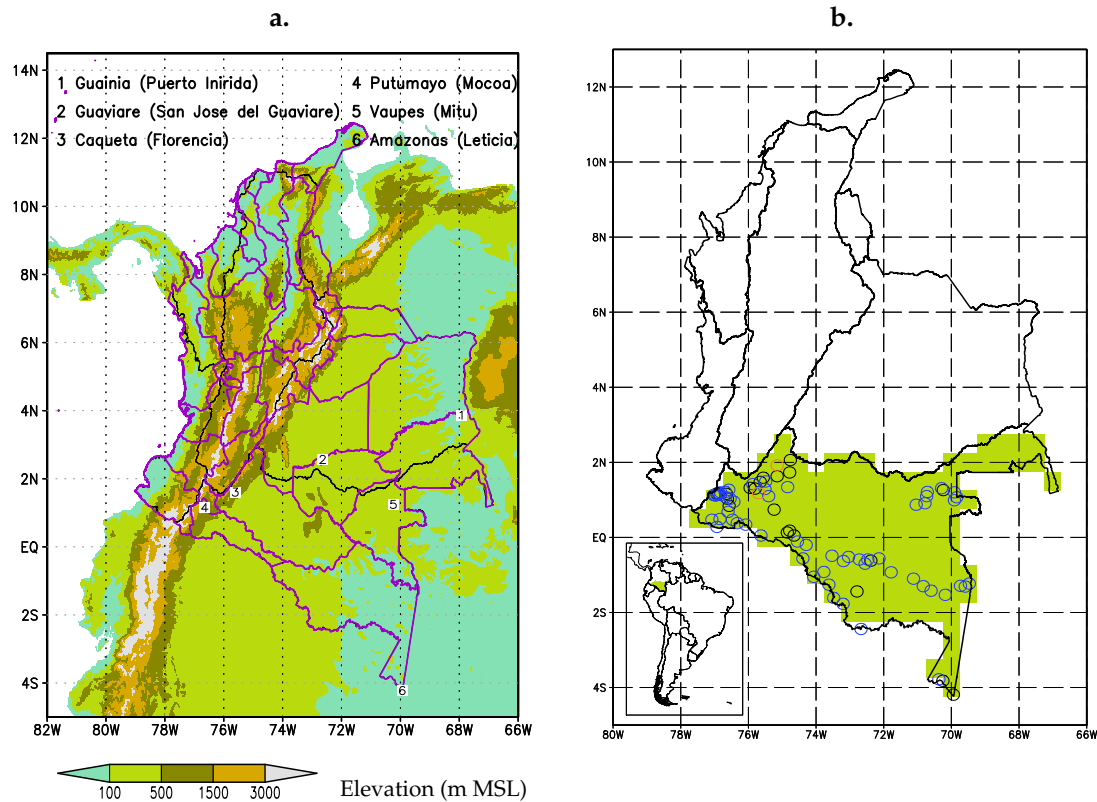


Figure 1. Study area. a) Political map, basins, and topography of Colombia. Purple lines are the departments, and black lines denote the basins. These overlap in several cases. The numbers represent the geographical location of the capital cities of the departments within the CAB. The department names are listed, as well as the capital cities in parentheses (San José de Guaviare and Puerto Inírida are not within the CAB, but part of their departments are). b) Basins of Colombia. The location of the CAB is represented in green in a $0,5^{\circ} \times 0,5^{\circ}$ grid. As in the map of panel a), the black lines indicate basins. Circles indicate the location of the stations selected in this study. Orange circles correspond to stations that measure temperature, blue circles to the stations that measure precipitation, and black circles to the stations that measure both temperature and precipitation.

which is eight times the world average ($10 \text{ L/s}\cdot\text{km}^2$) and about four times the average yield of Latin America ($21 \text{ L/s}\cdot\text{km}^2$). The CAB has the highest percentage regarding the annual water supply and the distribution of the river flow in the country, *i.e.*, approximately 39%. As is typical throughout the basin, there is a wide tropical forest that covers a third of the Colombian territory, containing a great variety of ecosystems and great biodiversity. In the CAB, in the foothills of the Eastern Mountain Range, the Orteguaza and Yari Rivers are born, which are tributaries of the Caquetá River, considered to be the mightiest in Colombia. There are also rivers like the Apaporis, which flows into Colombia's border with Brazil and is born at the center of the Colombian Amazonia. The Caquetá, Putumayo, Caguán, and Yari Rivers amount to 29% of the water discharged into the Amazon River in Colombia, and the

remaining 71 % are born in the Colombian Amazonia plain, as a consequence of the high precipitation in this area, which includes rivers such as the Apaporis and the Vaupés. With respect to water yields, values between 60 and 100 L/s·km² have been found in the Caguán, Caquetá, Yari, Apaporis, Vaupés, Napo, and Guainía Rivers, as well as values above 100 L/s·km² in the Orteguzza, Pescado, Sencella, and Putumayo Rivers.

The climates of Colombia are summarized in (16). Different classifications are presented therein, among them those of Martonne, Holdridge, and Koeppen. According to the climatic classification of Martonne, the climate of the CAB is between humid and humid rainy. According to the classification of Koeppen, the climate of the basin is of the tropical rainforest type. In the Holdridge climate classification, the climates are humid warm almost everywhere and very humid warm in part of the northwestern sector of the department of Putumayo, as well as in the northeastern part of the department of Amazonas.

According to (16), most of the Colombian Amazonia receives rainfall between 2.000 and 4.500 mm per year, and there are between 200 and 250 rainy days in the departments of Caquetá, Amazonas, Vaupés, and Putumayo. Towards the piedmont, there can be up to 300 days of rain per year. The region experiences a single annual peak in precipitation. However, the regime is different on each side of the terrestrial equator. To the north, the maximum precipitation value occurs in the middle of the year, and, in the south, towards the first months of the year.

In the north, there is a minimum of precipitation in January and February, and, in the south, in July and August. In both cases, months with more than 15 days of rain may occur. Due to the homogeneous physiography of the region, there is little spatial variability in the temperature; in most of the CAB, temperatures typically range from 24 to 28 °C. Towards the piedmont, there is greater variability. The average temperatures fluctuate between 12 and 20 °C and depend on the elevation above sea level. In Fig. 1a the five basins of Colombia and the topographic characteristics of the study area are shown. Fig. 1b depicts the geographical locations of the stations in the CAB which were selected for this study.

2.2. Data and methodology

The monthly mean fields of surface temperature, precipitation, and the variables involved in the water and energy budgets of several state-of-the-art datasets were analyzed in order to assess how well they represent the climatological characteristics of the study area. To facilitate the comparison of meteorological variables of interest, all gridded datasets (observational products, reanalyses, and the regional model) were transformed into a 0,5° × 0,5° spatial grid, which was symmetrical with respect to the Earth's equator. All this, through the conservative first- and second-order remapping method proposed by (30).

Reanalysis data

Reanalysis products combine observations with simulations using state-of-the-art numerical models. Computer models are run to simulate many decades, with observed fields incorporated into

the model at the time they were observed to produce a reanalysis climatology, *i.e.* data assimilation is used in generating climatology. Winds and temperatures are assimilated variables and are therefore accurate. Other variables, as is the case of precipitation and evaporation, may not be as reliable, since they are model-dependent outputs (31). Table I presents a summary of the datasets and the variables considered in this study. In the table, the variables are classified according to the influence of the observations. Free-access data from observations and from the NCEP/NCAR, NCEP-v2, ERA-40, and ERA-Interim reanalyses was included in this study.

Reanalyses are regarded as climate databases with a wide range of applications. They are commonly used in studies with restricted observational data. In spite of their virtues and scientific popularity, they have limitations related to climate representation, and their quality varies on a regional basis (32). The National Centers for Environmental Prediction (NCEP)/National Center for Atmospheric Research (NCAR) (10) and the European Centre for Medium-Range Weather Forecasts (ECMWF) (33) have carried out the two main global reanalysis projects. NCEP/NCAR has two reanalysis versions: the NCEP-1 Reanalysis (hereafter NCEP/NCAR) and the NCEP-2 Reanalysis (hereafter NCEP-v2). Although NCEP-v2 is a rerun of NCEP/NCAR, with the same horizontal and vertical resolution and input data, it improves the physical process and corrects known errors in NCEP/NCAR (23). For example, existing issues with orography are improved by correcting Gibbs phenomena such as

Table I. Datasets and variables considered in this study. The variables are temperature (T), precipitation (P), evapotranspiration (E), runoff (R), latent heat flux (LHF), sensible heat flux (SHF), solar radiation (SR), and thermal radiation (TR). The availability of each variable is indicated by the 'X' symbol. The variables strongly influenced by observations are shown in blue, and those strongly influenced by the reanalysis or by the model are shown in red. *The energy balance for the NCEP/NCAR dataset was determined for the 1948-2012 period because the SR and TR variables were only available until 2012.

Dataset	Original horizontal resolution	Original time-period	Intersection time-period	Surface variables								References
				T	P	E	R	LHF	SHF	SR	TR	
ERA-40	1,125° × 1,125°	1958-2001	1994-2001	X	X	X	X	X	X	X	X	(13)
ERA-Interim	0,75° × 0,75°	1979-2013	1994-2010	X	X	X	X	X	X	X	X	(22)
NCEP/NCAR	1,875° × 1,875°	1948-2013*	1994-2010	X	X	X	X	X	X	X	X	(10)
NCEP-v2	1,875° × 1,875°	1979-2013	1994-2010	X	X	X	X	X	X	X	X	(23)
REMO	0,5° × 0,5°	1958-2000	1994-2000	X	X	X	X	X	X	X	X	(24,25)
Delaware	0,5° × 0,5°	1948-2008	1994-2008	X	X							(26,27)
GPCP	2,5° × 2,5°	1979-2013	1994-2010		X							(15)
CMAP	2,5° × 2,5°	1979-2013	1994-2010		X							(28)
CMAP-v2	2,5° × 2,5°	1979-2013	1994-2010		X							(28)
CPC	2,5° × 2,5°	1948-2007	1994-2007		X							(14)
Observations	-	1994-2010	-	X	X							(29)

precipitation, especially in the case of the Amazon basin (23). Despite these improvements, NCEP-v2 is not a next-generation reanalysis and is regarded as an updated and improved version of NCEP/NCAR.

In contrast to NCEP-v2, ERA-Interim is considered to be a second-generation reanalysis since it includes an assimilation system based on a four-dimensional variational data assimilation (4D-VAR) approach, which more efficiently uses available observations but is computationally intensive and more complex than the three-dimensional variational data assimilation (3D-VAR) used by ERA-40, NCEP/NCAR, and NCEP-v2 (22). The list of variables that are assimilated in ERA-40 and ERA-Interim are presented in (34), and the variables assimilated in NCEP/NCAR are presented in (35).

Reanalyses use either an incremental updating technique or a four-dimensional data assimilation system. These techniques allow the analyzed fields to evolve smoothly in time, instead of exhibiting jumps at times of analysis. This largely eliminates the spinup problem of the hydrological cycle. However, these techniques preclude reanalyses from satisfying physical closure constraints in the water or energy cycles (36).

Regional climate model REMO

The REMO model was developed by the Max Planck Institute for Meteorology in the context of the BALTIC Sea Experiment (24, BALTEX;). This regional model has two main components: a physical parameterization scheme from the ECHAM4 global climate model and the dynamical component given by the numerical weather prediction model of the German Weather Service (EUROPA-MODELL). REMO is a suitable model for climate studies, and it has been widely used in Europe and many other regions around the world (25, 37, 38). An important characteristic of REMO is that it is designed to meet the water and energy balance closures. The data used in this work correspond to a climate model simulation for South America in the 1958-2000 period, with boundary conditions provided by ERA-40. The same simulation was analyzed by (25).

Gauge and merged satellite-gauge products

Most temperature and precipitation observational products may be categorized into one of three broad categories: gauge datasets, satellite-only datasets, and merged satellite-gauge products. The Delaware (26, 27) and the Climate Prediction Center (14, CPC;) datasets belong to the first category, and the Global Precipitation Climatology Project (15, GPCP;) and the CPC Merged Analyses of Precipitation (CMAP and CMAP-v2) datasets belong to the third one. CMAP merges gauge and satellite observations, and the NCEP/NCAR reanalysis and CMAP-v2 include the same inputs except for reanalysis precipitation (28).

Observations and methodology

Table II lists the *in situ* stations considered in this study. The *in situ* data were obtained from (29) and were taken as a reference or point of comparison for the gridded datasets. In light of this, the methodology proposed by (39) was used. According to this methodology, the observations of each of the stations were compared with four to nine neighboring boxes of the gridded data. The comparison

Table II. Characteristics of the *in situ* stations included in the analysis of the CAB. For each station, the international code (Station ID), latitude (Lat), longitude (Lon), height (masl), precipitation (P), and temperature (T) are shown. The availability of each variable is indicated by an 'X'. The *in situ* data were obtained from (29).

Station ID	Lat(°)	Lon(°)	Height (m)	P	T	Station ID	Lat(°)	Lon(°)	Height (m)	P	T
48015030	-3.82	-70,25	82	X	X	47060020	-2,44	-72,67	120	X	
44045010	1.32	-75,95	320	X	X	47075010	-1,44	-72,79	150	X	X
4404502	1.18	-75,70	270		X	48010020	-3,78	-70,37	93	X	
44045030	1.30	-75,80	300	X	X	48015010	-4,19	-69,94	84	X	X
46015020	1.73	-74,78	240	X	X	44030060	1,49	-75,49	500	X	
46035010	1.63	-75,15	270	X	X	44030080	1,29	-75,51	260	X	
4603502	1.92	-75,15	285		X	44035020	1,59	-75,56	244	X	X
44035030	1.48	-75,65	280	X	X	44040020	1,42	-75,87	300	X	
44015010	1.03	-76,62	440	X	X	44050010	1,10	-75,40	250	X	
44115020	0.05	-74,65	153	X	X	44100010	-0,11	-74,55	152	X	
4401002	1.07	-76,67	760	X		44120010	-0,49	-73,53	139	X	
4401008	0.95	-76,43	500	X		44130080	-0,59	-72,47	132	X	
4401009	1.27	-76,58	500	X		44135010	-0,62	-72,38	150	X	X
4701002	1.12	-76,97	2,070	X		44140020	-0,52	-73,04	137	X	
4701003	0.47	-76,47	260	X		46015010	2,06	-74,76	300	X	X
4701005	1.13	-76,92	2.100	X		46040010	1,34	-74,84	300	X	
4701009	1.17	-76,88	2.140	X		44055010	0,74	-75,24	219	X	X
4701011	0.68	-76,60	300	X		44120020	-0,20	-74,29	148	X	
4701015	1.13	-77,03	2.300	X		44010030	1,21	-76,68	1.400	X	
4701018	1.13	-76,83	3.000	X		44010040	1,20	-76,82	2.300	X	
4702002	0.47	-77,08	500	X		44010110	1,03	-76,54	430	X	
4703001	0.38	-76,33	200	X		44015040	1,16	-76,65	650	X	X
44130030	-0.92	-73,77	143	X		47010020	1,12	-76,98	2,070	X	
44130040	-0.63	-73,19	137	X		47010220	0,49	-76,84	360	X	
44130060	-0.59	-72,72	134	X		47015040	1,18	-76,88	2.100	X	X
44130070	-0.70	-72,55	133	X		47015070	0,84	-76,57	358	X	X
44150010	-0.56	-72,14	129	X		4701509	1,17	-76,93	2.067	X	X
44150020	-1.30	-70,83	116	X		47020010	0,28	-76,93	406	X	
44150030	-1.42	-70,60	114	X		47030020	0,05	-75,63	195	X	
44150040	-1.53	-70,18	116	X		47030030	0,34	-76,08	240	X	
44160010	-0.93	-71,78	125	X		47035020	0,13	-74,85	190	X	X
4416002	-1.10	-71,12	118	X		47045010	0,18	-74,78	147	X	X
44180010	-1.29	-69,73	104	X		42040010	0,87	-71,04	200	X	
44180020	-1.31	-69,59	102	X		42050020	1,10	-70,73	190	X	
44180030	-1.23	-69,47	101	X		42060010	0,91	-70,78	195	X	
47040020	-0.56	-74,39	140	X		42070010	1,21	-70,71	185	X	
47040030	-1.05	-74,07	135	X		42070020	1,31	-70,29	185	X	
47040040	-1.26	-73,62	130	X		42070030	0,99	-69,91	175	X	
47040050	-1.61	-73,48	125	X		42075010	1,26	-70,24	180	X	X
4706001	-1.77	-73,20	120	X		42080010	1,20	-69,91	175	X	
42080020	1.07	-69,84	172	X							

consisted of contrasting the value observed at the station against the average value of four to nine grid boxes. It was necessary to include a $6\text{ }^{\circ}\text{C}/1000\text{ m}$ height correction for the temperature variable in the gridded data (40), since the compared meteorological stations were located at different heights, while the temperature values of the different datasets corresponded to heights determined by the topography considered in the underlying atmospheric model. For the analysis, only the observations of the *in situ* stations located inside the CAB were taken into account. The number of stations used was 81 (Table II). The neighboring boxes of the gridded data were also located in the basin or within the macro-basin of the Amazon River. This meant that the grid boxes of areas bordering Colombia in countries like Brazil, Ecuador, and Peru were also taken into account. The height difference between the stations and the model could not be greater than 1.000 m. This method of point-to-point comparison allows for 'comparable regions'.

Additionally, a date-to-date comparison was made. This was done because the *in situ* stations had a high percentage of missing data. The date-to-date comparison consisted of taking exactly the same dates with both *in situ* data (daily temporal resolution) and data for the gridded datasets that were available or could be calculated with a daily temporal resolution (ERA-40, ERA-Interim, NCEP/NCAR, and NCEP-v2). From these daily values, the monthly averages corresponding to each dataset were calculated, thus obtaining a fairer comparison. For the REMO, Delaware, CPC, CMAP and CMAPv2 gridded datasets, only a point-to-point comparison was performed using monthly values, since these data only had this temporal resolution.

The climatological characterization of the CAB through the precipitation and temperature variables was performed by means of statistical analysis. For each year, the annual mean and annual anomalies were taken into account. For each month of the year, the mean, bias, and interquartile range (IQR) were calculated. The anomalies of each dataset were calculated as the difference between the annual means and the average of the whole period (1994-2000, *i.e.*, the time period corresponding to the observations), and the bias was obtained as the difference between each dataset and the values obtained with the observations.

3. Results

Figs. 2 and 3 present a comparison between the observations and the different datasets considered for the temperature and precipitation variables in the CAB. The annual means are presented for the periods available in each dataset (column 3 in Table I). Regarding the annual cycle, anomalies, bias, and interquartile range, the results correspond to the 1994-2010 period. For the datasets that did not have information on the entire range of the selected period, its period of intersection (column 4 in Table I) was taken. In addition, Table III shows a numerical summary with the averages of the monthly means of the annual cycle and the averages of the monthly biases of temperature and precipitation for the analyzed datasets.

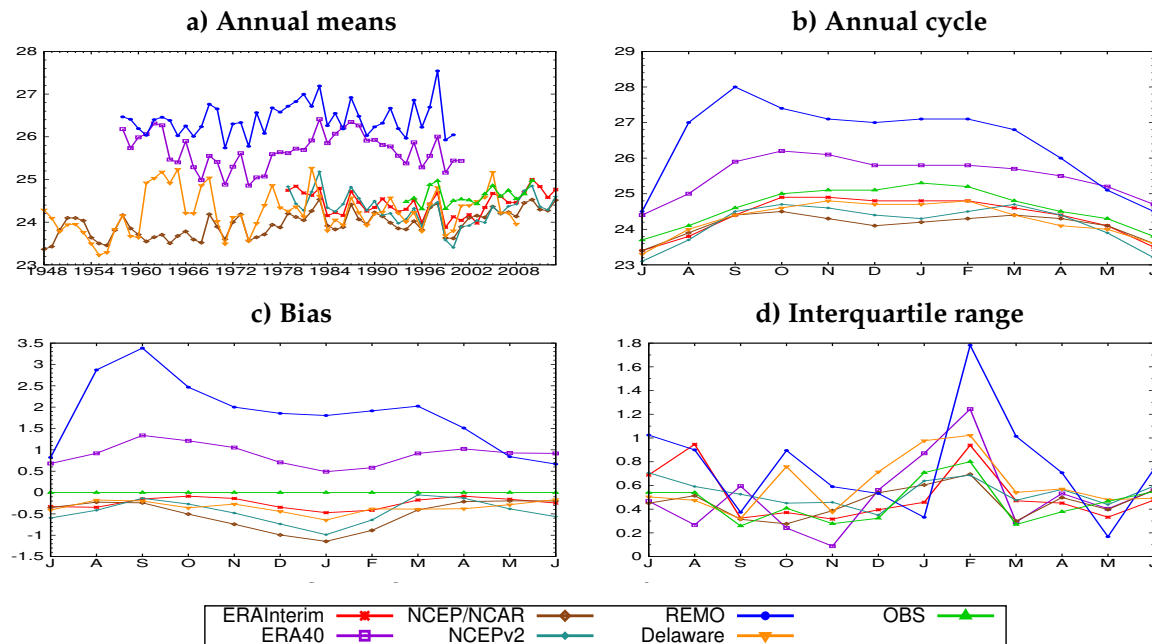


Figure 2. Temperature analysis of the CAB. a) Annual means, b) mean annual cycle, c) bias, and d) interquartile range. The units of measurement are $^{\circ}\text{C}$. Annual means are presented for the periods available in each dataset (column 3 in Table I). The mean annual cycle, bias, and interquartile range are presented for the periods in column 4 in Table I.

3.1. Temperature

Regarding the observations, the REMO and ERA-40 datasets overestimate the temperature in both the annual means and the annual cycle. In contrast, the other datasets underestimate it (Figs. 2a and 2b). As for the annual cycle, observations show a clearly unimodal behavior, with a minimum in June-July and a maximum in December-February). The variation range is between $23,7^{\circ}\text{C}$ and $25,3^{\circ}\text{C}$. This implies a small range of variation of $1,6^{\circ}\text{C}$ in temperature throughout the year. It is important to clarify that, due to the geographical distribution of the *in situ* temperature measurement stations, there is a significant bias in the dataset. Approximately 78% of these stations are situated north of the equator and west of 73°W , resulting in a pronounced bias toward the northwestern region of the CAB (as illustrated in Fig. 1b and detailed in Table II). When evaluating different datasets (Delaware, ERA-40, ERA-Interim, REMO, NCEP/NCAR, and NCEP-v2), it becomes apparent that some (Delaware, ERA-40, ERA-Interim) align closely with the observed unimodal pattern in the annual cycle, while others (REMO, NCEP/NCAR, NCEP-v2) deviate from it.

The datasets closest to the observations are ERA-Interim and Delaware. These datasets also have an intra-annual range of variation of about $1,6^{\circ}\text{C}$. The most variable datasets were REMO and ERA-40, with approximate ranges of variation of 3°C and $1,8^{\circ}\text{C}$ respectively. This is evidenced in Fig. 2c and

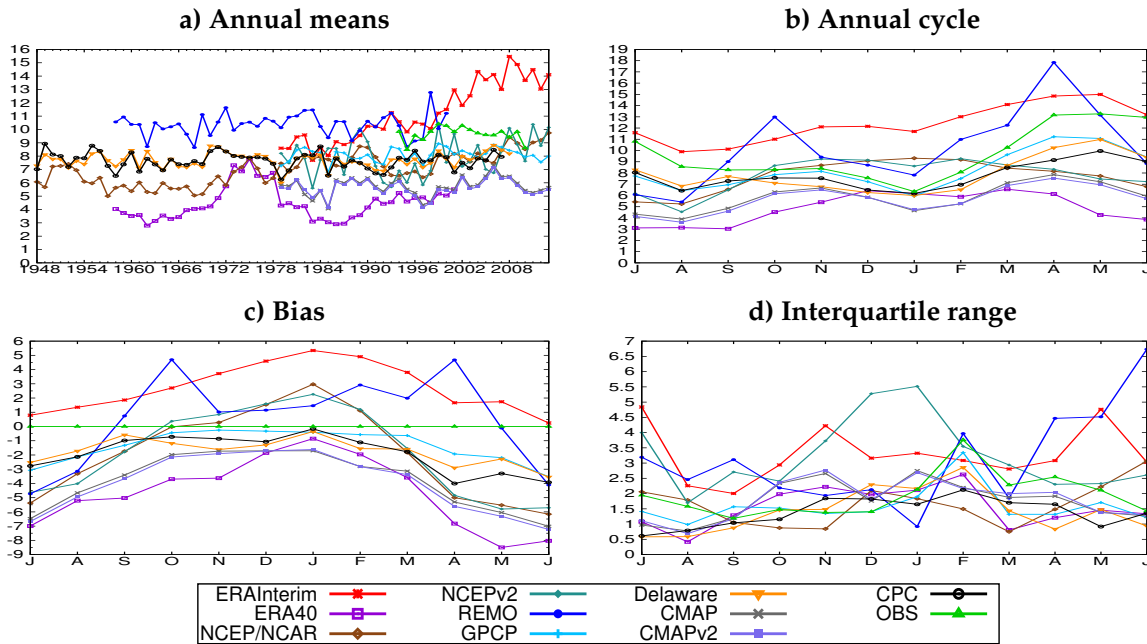


Figure 3. Precipitation analysis of the CAB. a) Annual means, b) mean annual cycle, c) bias, and d) interquartile range. The units of measurement are mm/day. Annual means are presented for the periods available in each dataset (column 3 in Table I).

agrees with the values obtained for the temperature bias in Table III. On the other hand, the various datasets showed a different month-to-month behavior regarding the dispersion of temperature values (Fig. 2d), which was estimated with the interquartile range (IQR), a resistant and robust statistic. REMO had the greatest variability in the CAB.

Fig. 4 shows long-term mean temperature maps for the observations and the different gridded datasets. The observed temperature varied mainly between 23 and 26 °C. The lowest temperature values were observed in the area west of 76,5° W. All gridded datasets showed the lowest temperatures in that area. However, REMO and ERA-40 showed a predominantly positive bias (or overestimation) throughout the basin, while ERA-Interim, NCEP/NCAR, and NCEP-V2 exhibited a predominantly negative bias (or underestimation). This is consistent with the values shown in the graphs of panels a, b, and c of Fig. 2.

3.2. Precipitation

Precipitation observations show a predominantly unimodal annual cycle, with a maximum in April-May-June and a minimum in January. However, since 63% of the *in situ* stations that measured precipitation and were available for this study are located north of the equator, there is a bias in the information towards the northern zone of the CAB (Fig. 1b, Table II). The range of intra-annual

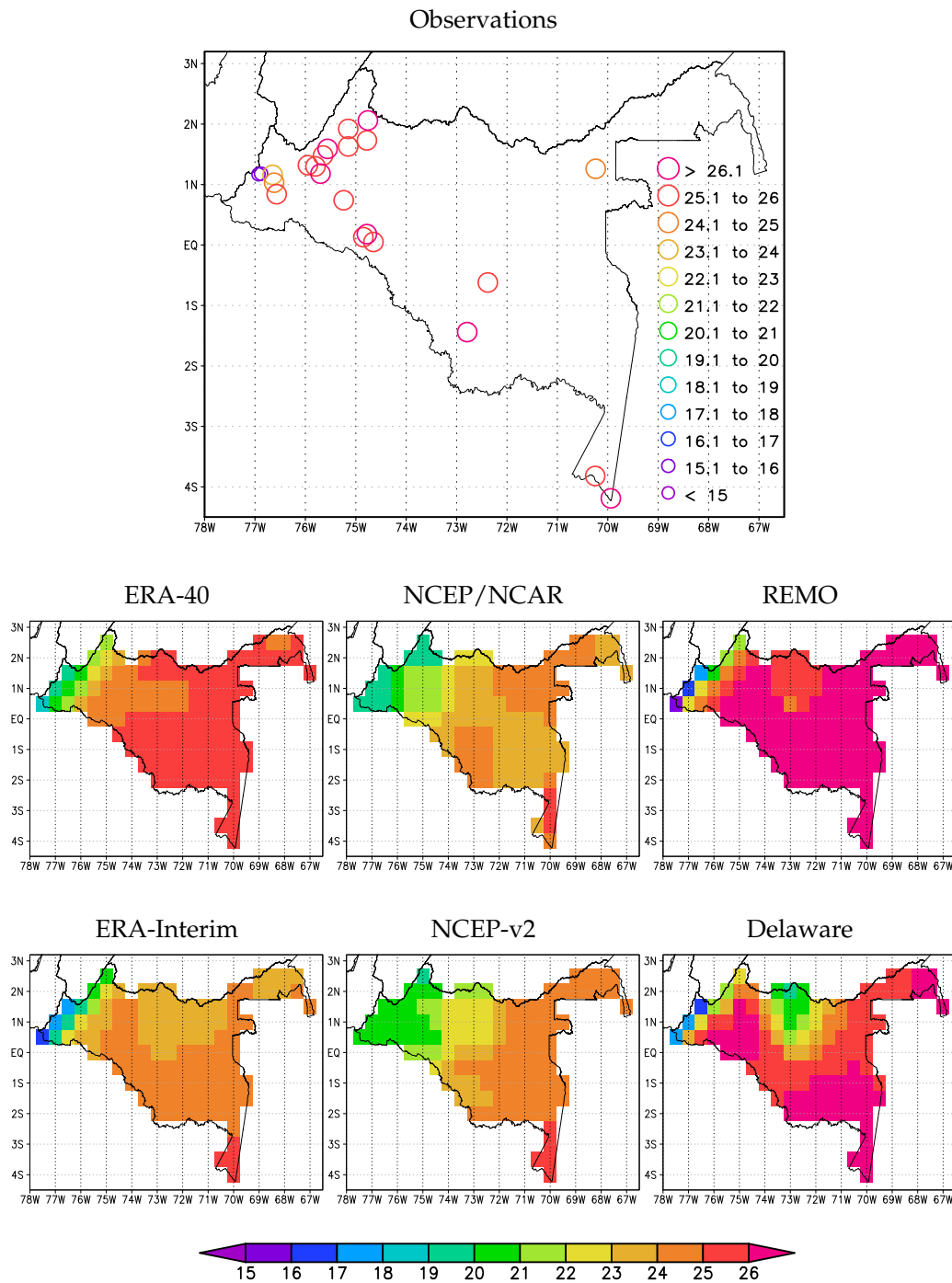


Figure 4. Long-term mean temperature reported by observations, ERA-40, ERA-Interim, NCEP/NCAR, NCEP-v2, REMO, and Delaware in the CAB for the periods shown in column 4 of Table I. This is expressed in °C.

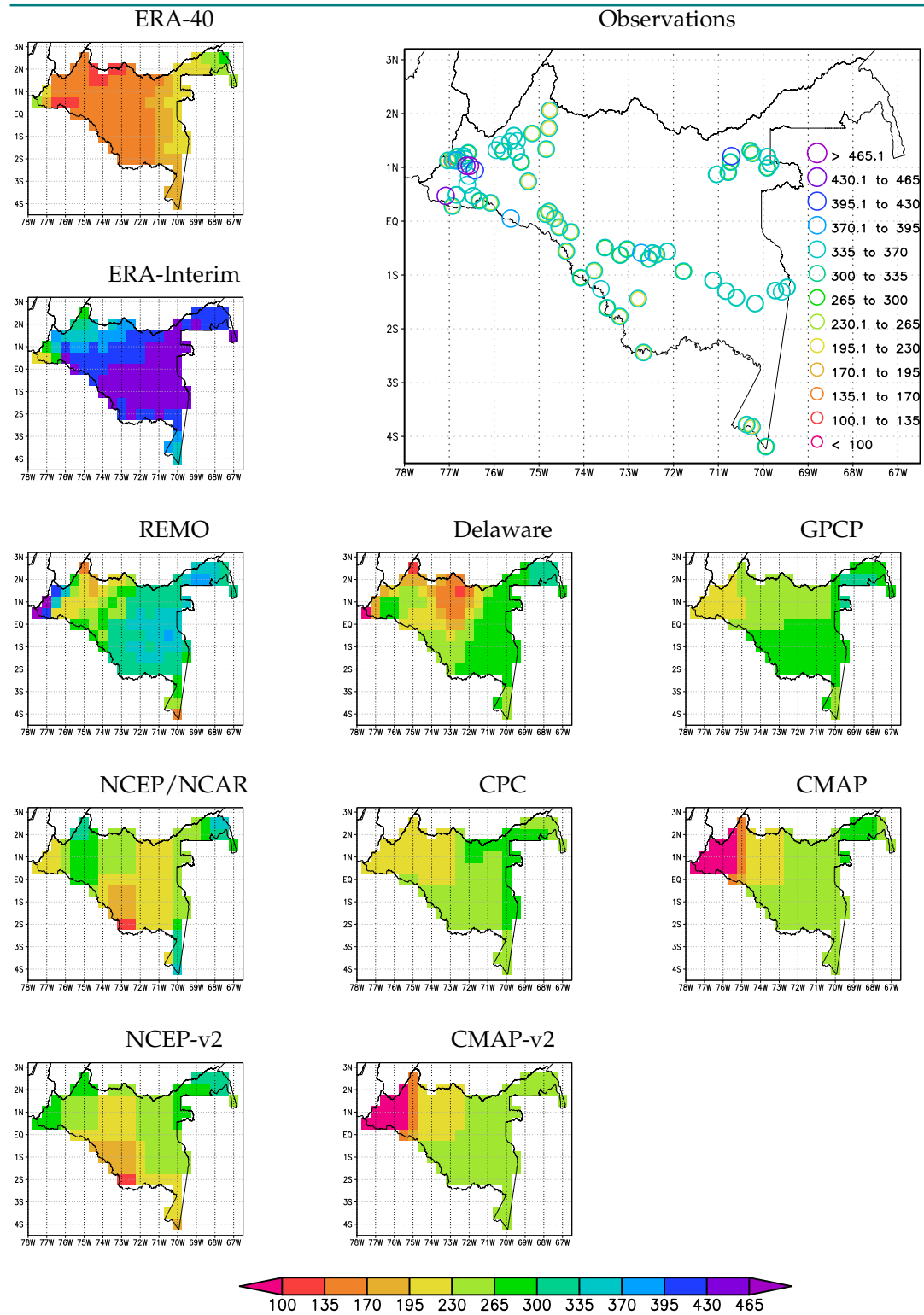


Figure 5. Long-term mean precipitation (mm/month) reported by observations, ERA-40, ERA-Interim, REMO, NCEP/NCAR, NCEP-v2, Delaware, GPCP, CMAP, CMAP-v2, and CPC the in CAB for the periods shown in column 4 of Table I.

Table III. Average of the monthly means of the annual temperature and precipitation cycle in the CAB for the different datasets considered. To calculate each bias, the reference value is that corresponding to the observations. The bias is in °C for the temperature and expressed as a percentage for the precipitation.

Dataset	Temperature		Precipitation	
	Mean (°C)	Bias (°C)	Mean (mm/day)	Bias (%)
ERA-40	25,5	0,9	4,97	49
ERA-Interim	24,4	-0,2	12,38	28
NCEP/NCAR	24,1	-0,5	7,74	20
NCEP-v2	24,2	-0,4	7,81	19
REMO	26,5	1,8	10,21	6
Delaware	24,3	-0,3	7,89	18
GPCP	-	-	8,26	15
CMAP	-	-	5,83	40
CMAP-v2	-	-	5,66	41
CPC	-	-	7,76	20
Observations	24,6	-	9,66	-

variation was between 13.3 mm/day in May and 6,3 mm/day in January and the average annual cumulative value is 3,540 mm.

All observational products, along with ERA-40, consistently underestimated precipitation year-round, as depicted in Figs. 3a, 3b, and 3c. Specifically, ERA-40 reported its maximum underestimation in May, with a peak difference of 8.5 mm/day, and its minimum value in January, with just a 1 mm/day difference. In contrast, ERA-Interim consistently overestimated precipitation, reaching its highest difference in January, at 5.3 mm/day, and its lowest in June, with a minimal difference of 0.02 mm/day. On the other hand, REMO showed a pattern of overestimating precipitation from September to April, underestimating it during the remaining months. NCEP/NCAR and NCEP-v2 consistently overestimated precipitation from November to February while underestimating it in the remaining months. ERA-Interim exhibited a noteworthy trend of increased precipitation, with a rise of 2 to 3 mm/month over the last few decades in its available data period, a phenomenon not observed in the actual measurements.

As for the modal character of the annual cycle, REMO, CMAP, and CMAP-v2 described a similar behavior, which was very different from that of the observations. None of these three datasets clearly showed the unimodal character presented by the observations. On the contrary, they were more inclined towards a bimodal regime (Fig. 3b).

On the other hand, the NCEP/NCAR and NCEP-v2 reanalysis described a monomodal cycle that was out of phase and with a very short dry season. Fig. 3c shows that the dataset that best describes the annual cycle is GPCP, followed by Delaware and CPC, although all three exhibit negative bias. This is not fully evident in Table III, since REMO had the lowest percentage of bias in the calculation of the intra-annual average, despite the fact that it was a dataset with a bimodal annual cycle, which has periods of underestimation and overestimation throughout the year. With respect to the dispersion of values for each month, GPCP showed the highest agreement with the observations. However, in general, there was no agreement between the different datasets considered (Fig. 3d).

Fig. 5 shows the long-term mean precipitation maps for the observations and the different gridded datasets.

The observations showed a relatively homogeneous spatial pattern of precipitation, with values ranging from 195 to 395 mm/month throughout the basin, except for ten stations. Five stations reported values above 395 mm/month, four of them located near the western border in the area west of 76,0° W (WB76). Meanwhile, the other five stations recorded values below 170 mm/month, all of which are also situated near WB76. The observations, ERA-Interim, REMO, and Delaware showed that this is an area of high spatial variability regarding precipitation. CMAP, CMAP-v2, GPCP, and CPC underestimated precipitation in that area. ERA-40 showed a generalized underestimation throughout the basin, and ERA-Interim showed overestimation mainly in the eastern part of the study area. NCEP/NCAR and NCEP-v2 underestimated precipitation in the area south of the equator and west of 72° W. As will be seen later, it was in this area where NCEP/NCAR and NCEP-v2 exhibited the highest errors regarding the water balance. ERA-40, NCEP/NCAR, the observational products Delaware, GPCP, CMAP, CMAP-v2, and CPC showed a predominantly negative bias throughout the basin, while ERA-Interim and REMO showed a positive one. This is consistent with the values shown in the graphs on panels a, b and c of Fig. 3.

4. Surface water and energy balances in the CAB

This section presents a comparison of the water and energy balances in the CAB for the datasets where the different components of the hydrological cycle were available. These were ERA-40, ERA-Interim, NCEP/NCAR, NCEP-v2, and REMO. Furthermore, the condition of closure of the balances was evaluated.

The surface water balance of REMO and the reanalyses is expressed in Eq. (1):

$$\frac{\Delta WS}{\Delta t} = P - E - R - RES, \quad (1)$$

where WS is the surface water storage (mm), t is time (months), P is the total precipitation (mm/month), E is the total surface evapotranspiration (mm/month), and R is the total runoff (mm/month). RES (mm/month) corresponds to the residual that comes from the assimilation process. During this process, a new state of the atmosphere is generated, which is closer to the observations but different from the one simulated by the model. Therefore, the atmospheric states are discontinuous,

which disturbs the water balance. RES can also be regarded as an estimate of the general error in the water balance. Thus, Eq. (1) can be reorganized as Eqs. (2) and (3) (41):

$$AB = P - E - R \quad (2)$$

$$RB = 100 \left(\frac{P - E - R}{P} \right) \quad (3)$$

where AB is the absolute water balance and RB is the relative water balance (% of P), and AB and RB include both RES and the change of WS. According to (42), RES contributes more significantly to the annual time scale than the temporal change in WS. In the first part of this section (*Components of the water and energy balances*), the spatial averages of P, E, R, and B were computed for the entire CAB. The annual cycles of P, E, and R were produced (one value per month per variable) following Eq. (4):

$$Y = \frac{1}{pk} \sum_{j=1}^k \sum_{i=1}^p x_{ij} \quad (4)$$

where x_{ij} is the value of P, E, or R (mm/month) in month i and on tile j ; p is the number of dataset tiles within Amazonia; and k is the total number of months throughout each dataset's entire time period (e.g., $k = 66$ for January, NCEP/NCAR, as described in column 3 of Table I).

Finally, one value (Y ; mm/month) is computed for each month. The AB of datasets is averaged annually (one value per year) for the entire CAB. To this effect, the annual average values of P, E, and R are first computed using Eq. (4), except that k is now 12, the number of months within the period from 1 January to 31 December of the same year. AB is then calculated using Eq. (2) for each year.

In the second part of this section (*Long-term mean of the water balance components*), precipitation, evaporation, runoff, and the relative water balance from the four reanalyses and REMO were averaged on a monthly time scale for the 1994-2010 period (or the period of intersection with 1994-2010, as shown in column 4 of Table I) for each dataset tile. For REMO, this was not necessary since it is available with a monthly temporal resolution. The values of P, E, and R were then averaged for the entire period of each tile, following Eq. (5):

$$X = \sum_{i=1}^n \frac{x_i}{n} \quad (5)$$

where X (mm/month) is the averaged variable P, E, or R; x_i is the value of P, E, or R in year i ; and n is the total number of years in the 1994-2010 period (17, 8, or 7 values, as explained above).

RB is computed from the averaged values of P, E, and R using Eq. (3). To consider only data for the Amazonia, the mask shown in Figure 1b is applied.

According to Equation 4.1 in (43), the storage of energy G on the surface of the earth can be written in the following terms:

$$G = SR - TR - LHF - SHF \quad (6)$$

where SR is the solar radiation, TR is the terrestrial radiation, LHF is the latent heat flux, and SHF is the sensible heat flux. $G \approx 0$ for long periods of time (in the order of years).

Table IV. Individual components of the surface water balance in the CAB for the period available in each of the datasets, as indicated in column 3 of Table I. *P* Precipitation, *R* runoff, *E* evaporation, and *AB* absolute water balance, expressed in mm/month. The runoff is also reported as a percentage with respect to precipitation (numbers in parentheses). *AB* is calculated according to Eq. (2).

Dataset	P	R (%P)	E	AB
ERA-40	166,58	65,63 (39)	111,015	10,06
ERA-Interim	370,16	185,33 (50)	181,17	3,65
NCEP/NCAR	211,88	79,53 (38)	185,029	52,68
NCEP-v2	203,24	25,59 (13)	202,01	24,36
REMO	283,22	130,31 (46)	149,89	3,01

In section 4.1, an analysis of the components of the surface water and energy balances is carried out. This analysis is based on the ERA40, ERA-Interim, NCEP/NCAR, NCEP-v2, and REMO reanalyses. In contrast, no analysis of the balances was performed using direct observations, since, for Colombia, components such as runoff, sensible heat flux, latent heat flux, and thermal radiation, are not directly measured on a regular basis. For example, in 2010, IDEAM published a national water study (17) for the first time and has since conducted updates every four years ((44); (45); (46)). In these three updates, IDEAM estimates runoff based on evapotranspiration and precipitation, and it estimates evapotranspiration based on precipitation and temperature.

4.1. Components of the water and energy balances

Table V. Individual components of the surface energy balance in the CAB for the period available in each of the datasets, as indicated in Table I. *SR* solar radiation, *TR* thermal radiation, *LHF* latent heat flux, *SHF* sensible heat flux, and *G* storage of surface energy. *LHF* is also reported as a percentage relative to *SR* (numbers in parentheses). These parameters are expressed in W/m^2 . *G* is calculated according to Eq. (6). For NCEP-v2, there are missing *LHF* values from 2003, so the climatological *LHF* value was calculated for the 1994-2002 period.

Dataset	SR	TR	LHF (%SR)	SHF	G
ERA-40	171,52	38,98	105,58 (62)	27,42	0,46
ERA-Interim	241,65	36,61	172,31 (71)	33,55	0,83
NCEP/NCAR	176,61	36,91	131,88 (75)	12,28	4,47
NCEP-v2	152,69	32	112,08 (73)	6,38	4,03
REMO	190,69	33,72	146,69 (77)	9,64	0,64

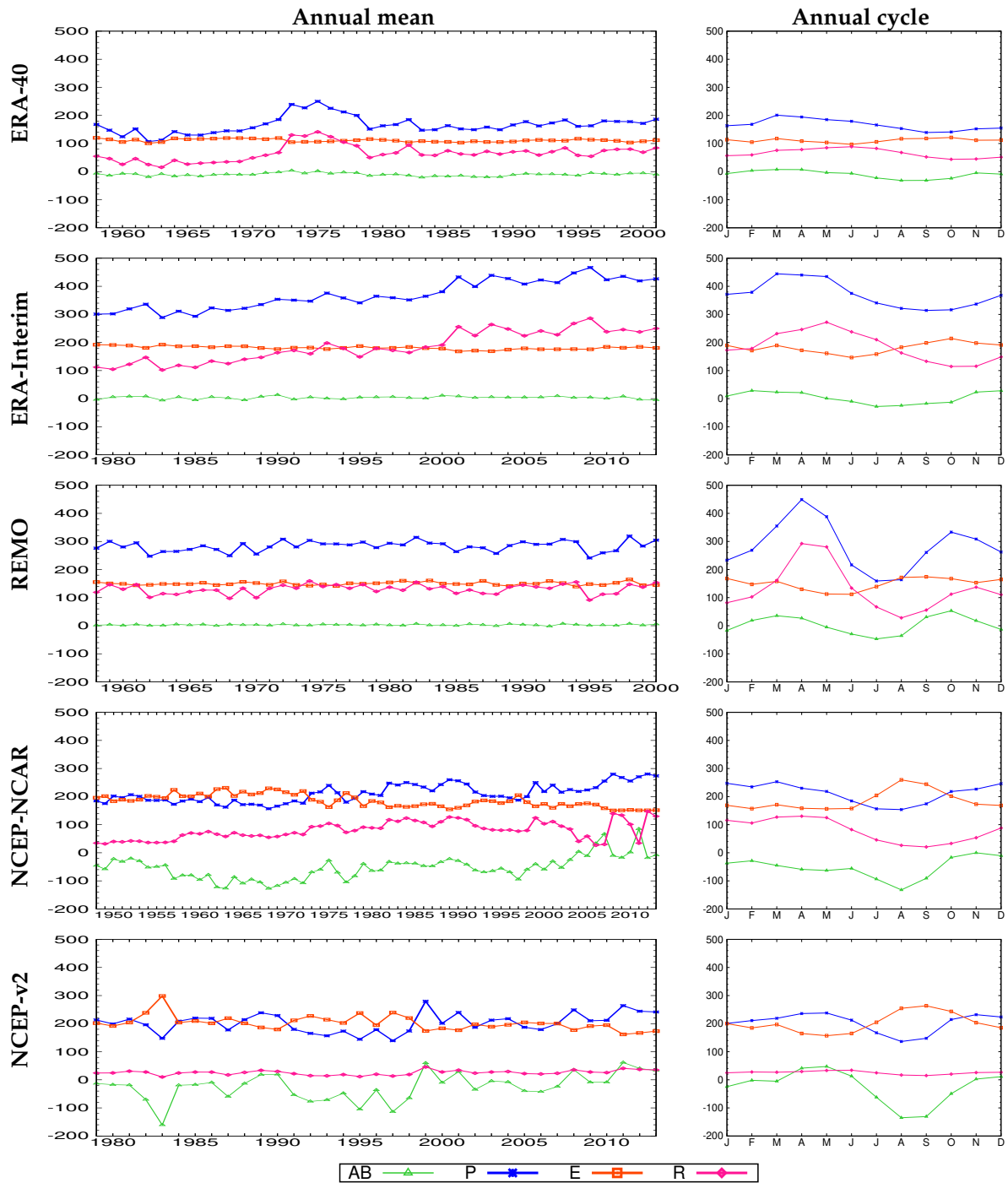


Figure 6. P Precipitation, R runoff, E evaporation, and AB absolute water balance for the available periods indicated in column 3 of Table I, expressed in mm/month. Annual averages (left) and annual cycle (right).

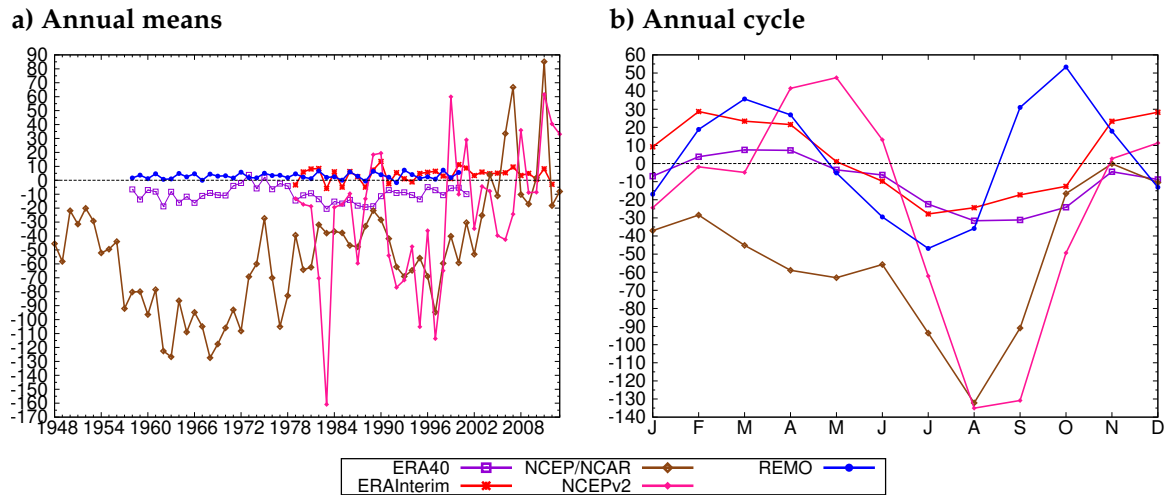


Figure 7. Comparison of absolute water balances (AB). a) Annual means, b) annual cycle, expressed in mm/month.

The annual means and the annual cycle of the individual AB components for the ERA-40, ERA-Interim, NCEP/NCAR, NCEP-v2 reanalysis, and REMO are shown in Fig. 6. The values were calculated for the periods available in each of the datasets and are shown in Table I.

The annual means and the annual cycle of AB for each of these five datasets are shown in Fig. 7. Table IV summarizes the averages of the water balance components in the periods available in each of the datasets. The different components of the energy balance are shown in Fig. 8 in terms of the annual means and the annual cycle for the CAB. In Fig. 9, a comparison regarding energy storage G in the CAB is presented which includes each of the five datasets. In addition, Table V shows a summary of the energy balance component averages for the periods available in each dataset.

ERA-40 exhibited increased precipitation and runoff from 1962 to 1975 (Fig. 6). ERA-Interim also recorded an increase in these two variables, albeit over the entire period, and had the highest precipitation values of all datasets. In addition, from 2000 on, ERA-Interim had the highest runoff values. NCEP/NCAR also exhibited increased precipitation from 1997 to 2013. In general, REMO and NCEP-v2 reported no tendency in the precipitation. However, REMO showed the second-highest precipitation value (Table IV).

Regarding ERA40, ERA-Interim, and REMO, it is evident that the runoff followed precipitation variations in both the annual means and the annual cycle. In contrast, for NCEP/NCAR, in the 2002-2006 period and again in 2011, there were declines in runoff that were not accompanied by decreases in precipitation. On the other hand, NCEP-v2 did not show correspondence between precipitation and runoff in the annual cycle. In addition, NCEP/NCAR and NCEP-v2 sometimes showed evaporation values that were higher than the precipitation values in both annual means and the annual cycle.

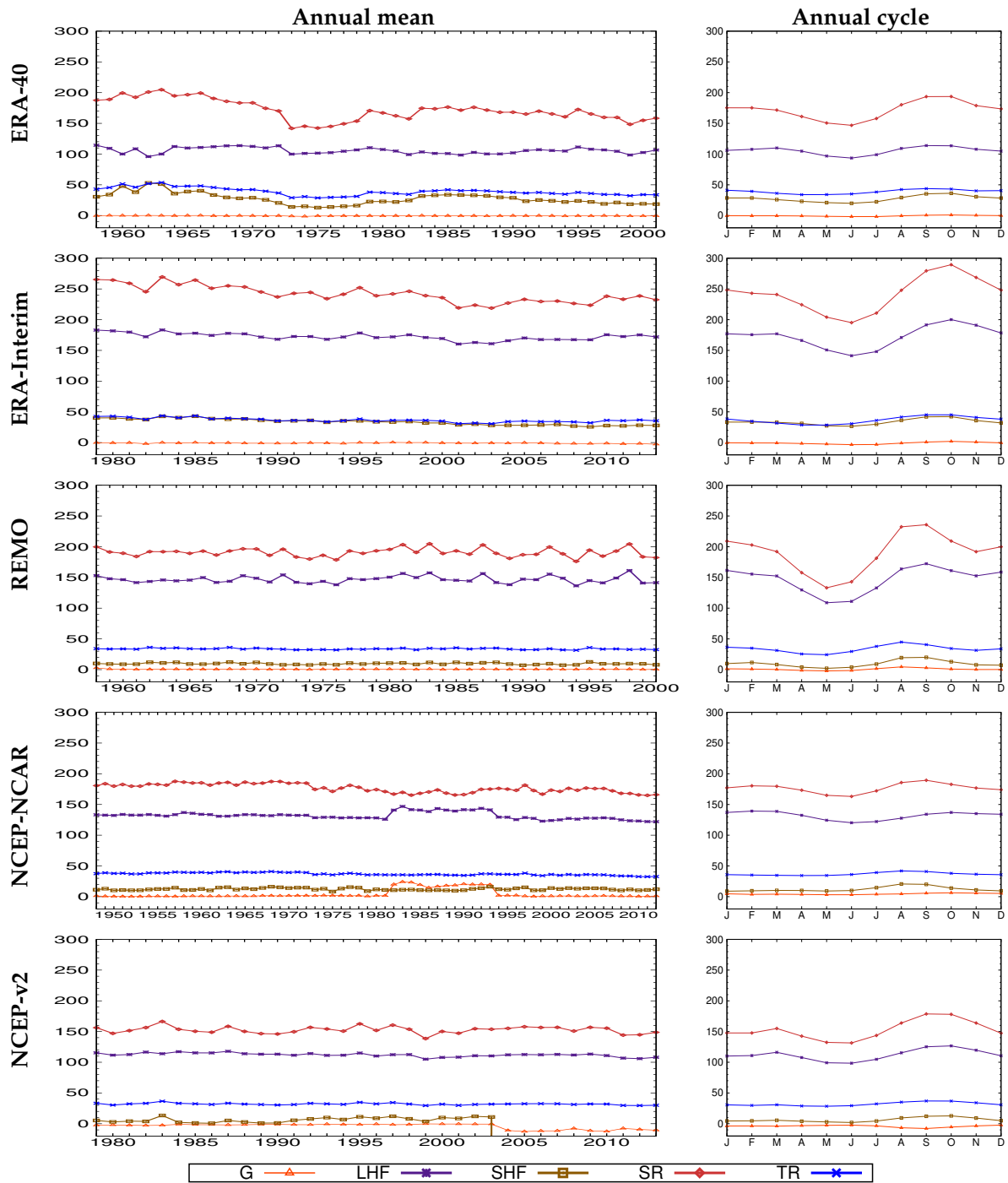


Figure 8. Energy balance components in the CAB for the available periods indicated in Table I. *SR* solar radiation, *TR* thermal radiation, *LHF* latent heat flux, *SHF* heat flow, and *G* stable energy storage, expressed in W/m^2 . Annual mean (left) and annual cycle (right).

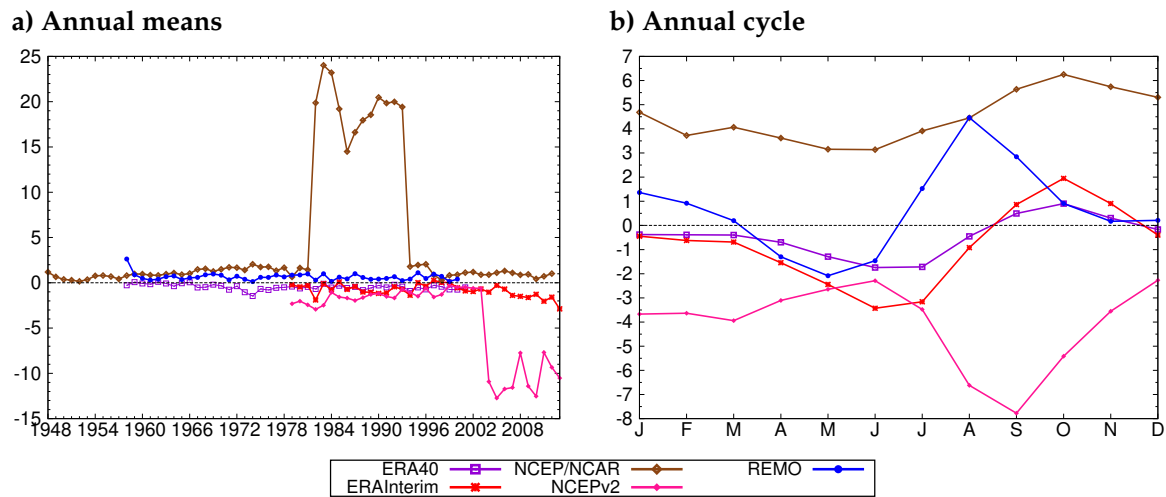


Figure 9. Comparison of the energy storage (G) in the CAB. a) Annual means, b) annual cycle, expressed in W/m^2 . For the NCEP-v2, there are missing LHF values from 2003, so the climatological LHF value was calculated for the 1994-2002 period.

When comparing the evaporation values in the CAB to the evaporation map provided by IDEAM (Fig. 10), it is evident that NCEP/NCAR, NCEP-v2, ERA-Interim, and REMO show similar values to those observed in the northern regions of the country, such as the departments of La Guajira and Atlántico. These northern regions are classified as having an arid or subhumid climate according to the Martonne climate classification, unlike CAB, which experiences a humid and rainy climate.

The long-term closure conditions of the water balance ($AB \approx 0$) for the datasets evaluated was mainly fulfilled for REMO, followed by ERA-Interim and ERA-40 (green lines in the graphs on the left side of Fig. 6). On the other hand, NCEP/NCAR exhibited an average deficit of 53 mm/month throughout the data series. Its updated version, NCEP-v2, also showed a deficit, with an average value of 24 mm/month (Fig. 7, Table IV).

In most of the five datasets evaluated regarding the water and energy balances, the physical relation between latent heat flux and evaporation was clearly evident (Figs. 6 and 8), both in the annual means and the annual cycle (with the exception of NCEP/NCAR), despite the different behaviors of these two variables in each dataset. Likewise, the relation between solar radiation and latent heat flux in the five datasets was evident. This relation was reflected in the high percentage of latent heat flux with respect to solar radiation, which, for all datasets, was above 60% (Table V). However, for NCEP/NCAR, there was a discrepancy in the period from 1981 to 1994 with regard to these components. This could be the main cause of the alteration in the energy storage observed in the same period for this dataset. For the NCEP-v2 dataset, from 2003 on, a deficit in the energy balance was noted, which was due to missing values in the latent heat flux from that year. According to the average energy storage (Table V) and the comparison presented in Fig. 9, the closure in long-term energy storage was generally well described in the five datasets, to a greater extent by ERA-40, followed by REMO and ERA-Interim.

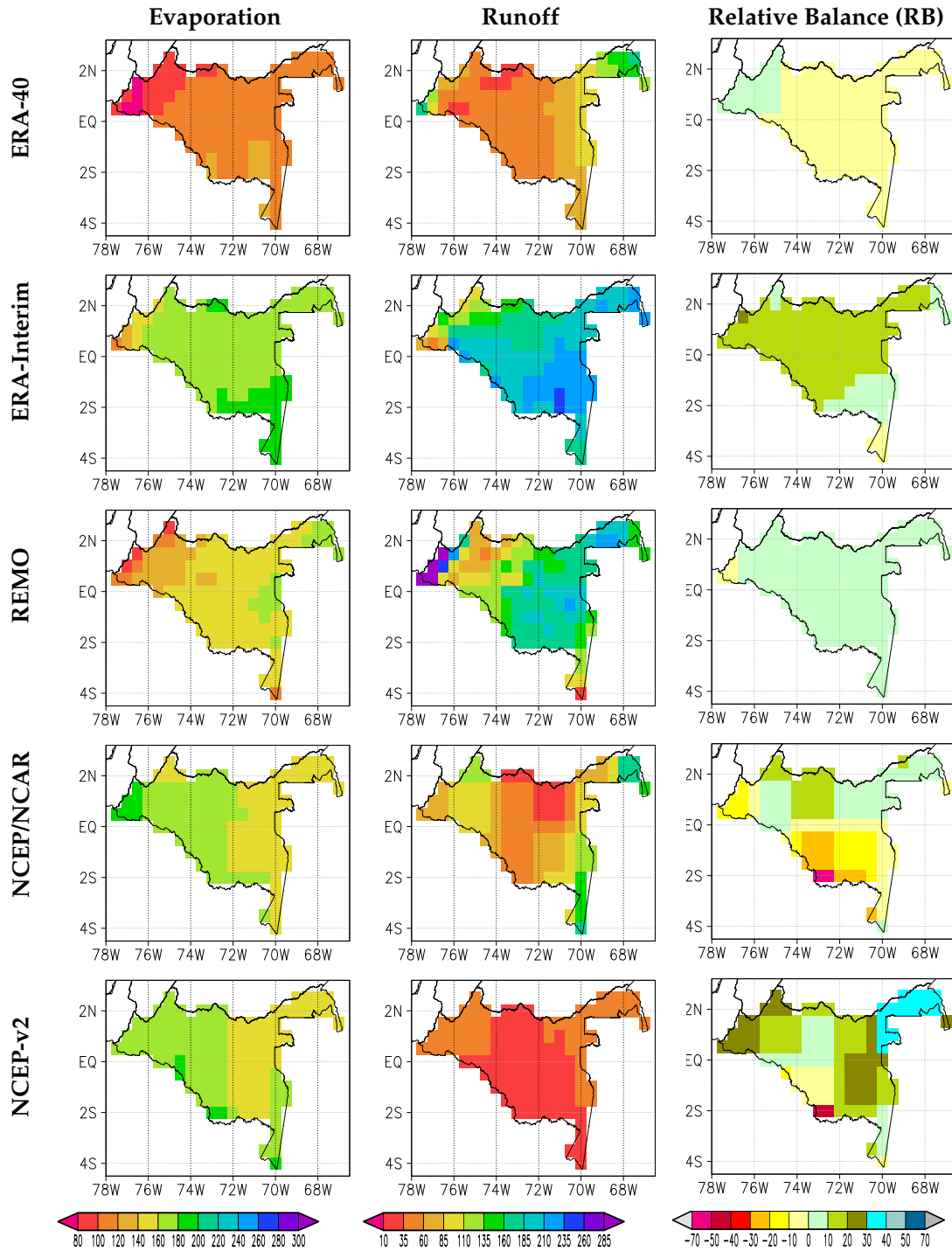


Figure 11. Long-term mean evaporation, runoff, and relative balance (RB) values (mm/month) for ERA-40, ERA-Interim, REMO, NCEP/NCAR, and NCEP-v2 in the CAB for the periods shown in column 4 of Table I.

values mainly between 1.500 and 2.500 mm/year (125 and 208 mm/month) for the CAB. The runoff values closest to those of IDEAM corresponded to ERA-Interim and REMO, with a predominance of values between 60 and 285 mm/month. For the other datasets, values of 110 mm/month and less are predominant.

Column 3 of Fig. 11 shows the closure of the water balance using the long-term mean RB values computed for ERA-40, ERA-Interim, REMO, NCEP/NCAR, and NCEP-v2 for the CAB. As expected, the water balance of REMO was closed, with values of RB almost equal to 0% (values mainly between -6 and 6%). The water balance of ERA-40 was also closed, and that of ERA-Interim was almost closed, since 85% of the reanalysis tiles had a RB value between -2,5 and 15%. Conversely, the water balances of NCEP/NCAR and NCEP-v2 were not closed. NCEP/NCAR (NCEP-v2) exhibited negative RB values between -6 and 60% (-6 and -54%) mainly in the southern (southwestern) area of the region. This is due to underestimation of precipitation in that region, as shown in Fig. 5. Furthermore, NCEP-v2 presented positive RB values (between 20 and 40%) in the region north of 2° S and west of 71,5° W, as well as in the region east of 76° W.

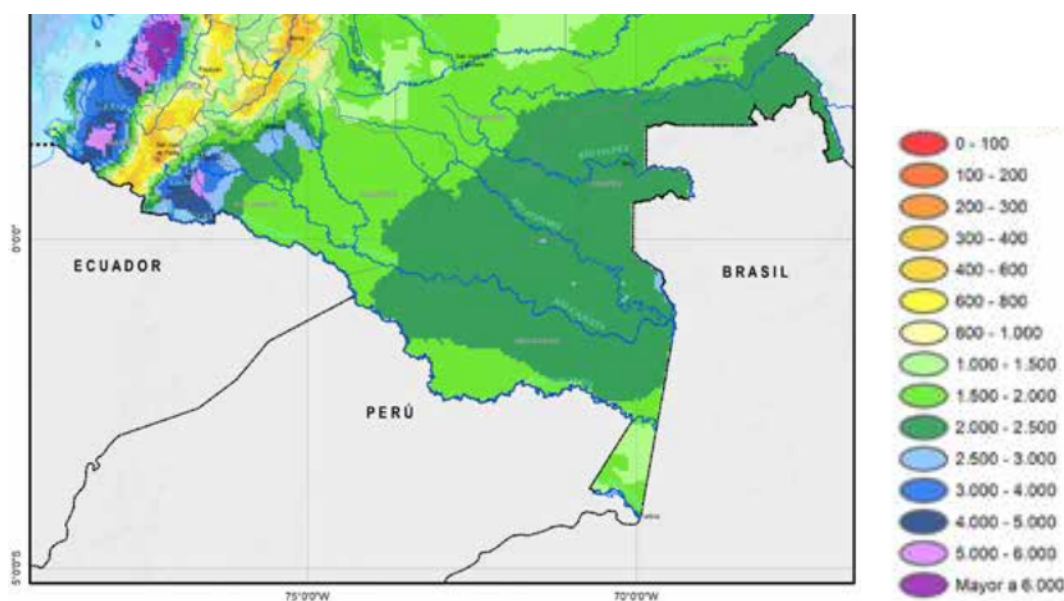


Figure 12. Multi-year average of total annual runoff (mm/year). Adapted from Fig. 17 in Instituto de Hidrología Meteorología y Estudios Ambientales (46) and reproduced with their permission.

5. Discussion and conclusions

For this study, *in situ* stations were identified, where the temperature and precipitation variables inside the CAB were measured. Most of the stations did not have long periods in common, exhibited considerable amounts of missing data, and their geographical distribution was not uniform. There is greater availability of information for precipitation, but the number of stations per department is not

proportional to its area. This is especially true for the department of Vaupés, where there is only one station. The departments of Guainía and Guaviare have no stations available within the CAB. In this study, we implemented a methodology that allowed for both an unbiased spatial comparison and a fair temporal comparison. The inclusion of date-to-date comparisons ensures a fair temporal assessment since *in situ* observations often have a significant volume of missing data (in most cases, up to 55%), which can substantially alter the results.

The scope of this study involved an exploration of the potential of REMO, ERA40, ERA-Interim, NCEP/NCAR and NCEP-v2, and some observational products to provide meteorological variables where few or no observations are available, as well as to determine their reliability for representing both:

- the general climatological characteristics of temperature and precipitation and
- the surface water and energy balances of the CAB.

5.1. Temperature and precipitation

Based on the combination of the observations made at the *in situ* stations selected for the 1994-2010 period, a unimodal behavior in the annual temperature cycle was found as a general characterization of the CAB, with a minimum in June-July and a maximum in January, as well as average variations between 23,7 and 25,3 °C. This indicates little variability in the area, with a range of variation of only 1,6 °C.

When comparing the observed temperature in the CAB with that from the different datasets, it was found that most of the latter underestimated the temperature in both the annual means and the annual cycles, except for the ERA-40 reanalysis and the regional climate model REMO, which overestimated it. Delaware, ERA-40, and ERA-Interim exhibited consistency in the predominant unimodal character of the annual temperature cycle within the CAB. REMO, NCEP/NCAR, and NCEP-v2 did not display this consistency. The dataset closest to the observed temperatures was ERA-Interim, followed by Delaware, while the farthest were REMO and ERA-40. REMO is driven by ERA-40, which could explain why they have similar temperature biases.

Without glossing over the location bias along the western zone of the CAB due to the geographic location and the number of stations used in the assessment, it was found that the annual cycle of the observed precipitation showed a predominantly unimodal character, with a maximum in April-June and a minimum in January. The range of intra-annual variation was between 13,3 mm/day in May and 6,3 mm/day in January, and the average accumulated rainfall for one year was 3.540 mm.

The datasets that best reproduced the annual cycle of the precipitation were the observational products Delaware, CPC, and GPCP. The ERA-Interim reanalysis reproduced the unimodal character of the annual precipitation cycle relatively well.

The work of (7), also obtained from observational data, states that the highest precipitations occur in March-May in the north of the entire Amazon basin. However, there are two slight discrepancies

with this study. First, (7) showed a slightly bimodal annual cycle, with the highest rainy season in the first part of the year. Another important difference was that he found an average value of precipitation of 6 mm/day for the northern region of the Amazon basin, whereas our analysis of the CAB found that the average of the monthly averages was 9,7 mm/day. This difference could be due to the fact that he included not only the south of Colombia, but also sectors of other countries like Peru, Brazil, Venezuela, Guyana, Suriname, and French Guiana.

Most of the datasets underestimated precipitation, with the exception of REMO and ERA-Interim, which showed the highest annual averages for this variable. However, there was a generalized increase in precipitation for ERA-40, ERA-Interim, NCEP/NCAR, and NCEP-v2 throughout their available periods, an aspect that is not evident in the observations conducted during the study period. The datasets with lower bias both in the annual cycle and in the annual means of precipitation correspond to GPCP, followed by Delaware and CPC. This coincides with the results of (19) for the Colombian Caribbean Basin. They show that the observational products Delaware and CPC have the closest proximity to *in situ* observations in relation to the annual cycle and the annual means of precipitation.

5.2. Water and energy balances

We studied the long-term mean of the water balance and the water cycle components for the regional model and the four reanalyses. The water balances of REMO and ERA40 are closed ($|AB| \lesssim 10\%P$) in comparison with the other three reanalyses, whereas ERA-Interim revealed a positive water balance in much of the basin ($10\%P \lesssim |AB| \lesssim 20\%P$), and NCEP/NCAR and NCEP-v2 revealed a mixed water balance, with positive and negative values of greater magnitude. The negative part of the water balances of NCEP/NCAR and NCEP-v2 was strongly influenced by inconsistencies in their components, e.g., large biases of evaporation and runoff throughout the basin and underestimations of precipitation mainly over the southern or southwestern area of the basin. On contrast, the high precipitation from ERA-Interim, when compared with those of the observations, contributed to the positive values of the water balance for a large proportion of the basin.

Precipitation, evaporation, and runoff were also assessed on a multiyear monthly basis for the basin. For REMO and the four reanalyses, the mean annual cycles of the water balance components showed a different temporal evolution. Furthermore, the amounts of water differed, especially the precipitation and runoff of ERA-40, NCEP/NCAR, and NCEPv-2. The NCEP/NCAR and NCEPv-2 reanalyses did not accurately allocate a sufficient quantity of precipitated water between evaporation and runoff. Notably, there are years, especially prior to 1974, in which more water evaporates than precipitates. On the other hand, although the water balance of ERA-Interim was almost closed and its runoff values were the most consistent in comparison with the runoff map of IDEAM 12, ERA-Interim was the dataset with the greatest increase in precipitation for the whole period, an aspect that was not evidenced in the observations. NCEP/NCAR and NCEP-v2 appeared to be the least consistent among the five datasets for the CAB (as shown in Section 4, Figs. 7 and 11, and Table IV). This agrees with the results of (7) obtained for the entire Amazon basin using the NCEP-v2 reanalysis. Each of the four reanalyses and REMO have their own strengths and weaknesses. Therefore, care should be taken in using any of the reanalyses of terrestrial water cycle components, especially for impact studies.

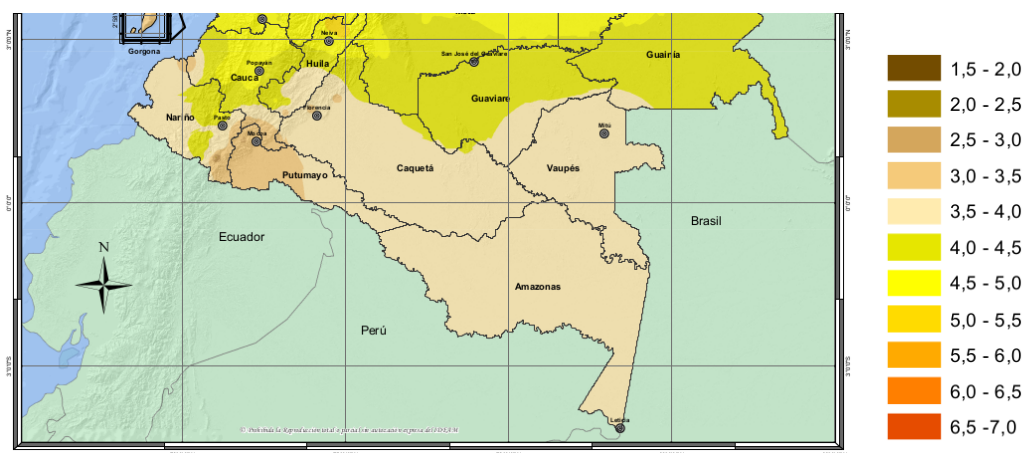


Figure 13. Multi-year average of daily annual horizontal global irradiation (KWh/m²/day). Adapted from Instituto de Hidrología Meteorología y Estudios Ambientales (47) and reproduced with their permission.

According to the comparison between the horizontal global irradiation map elaborated by IDEAM (Fig. 13) and Fig. 8, the observed solar radiation reaching the surface of the CAB was between 3 and 4,5 kWh/m²-day (125,0 and 187,5 W/m²) and was relatively well represented by NCEP-v2, ERA-40, NCEP/NCAR, and REMO – in that order. In contrast, ERA-Interim overestimated it by a high percentage (about 40 %).

In general, the five datasets fulfill the long-term closure condition of the energy balance. This is done to the greatest extent by ERA-40, followed by REMO and ERA-Interim. However, the overestimation of solar radiation in ERA-Interim suggests that the other fields involved in the energy balance would also be overestimated.

In summary, the results presented in this study regarding the water and energy balances in the CAB suggest that the five datasets considered (the four reanalyses and REMO) should be treated with special care in research, as their precipitation values may exhibit overestimation, underestimation, or both. In addition, regarding the temperature, which is directly related to solar radiation, the five datasets also show bias. Thus, these datasets could provide an unrealistic representation of the hydrological and energy fields, although this is fulfilled to some extent by the closure conditions of the water and energy balances.

6. Author contributions

All authors contributed equally to the research.

7. Acknowledgment

We are very grateful to the Instituto de Hidrología, Meteorología y Estudios Ambientales de Colombia (IDEAM), who kindly supplied the *in situ* data, and to Dr. Daniela Jacob for the REMO data. This work was funded by Fundación para la Promoción de la Investigación y la Tecnología del Banco de la República (FPIT; Hermes project 27129) and Universidad Nacional de Colombia through Convocatoria del Programa Nacional de Proyectos para el Fortalecimiento de la Investigación, la Creación y la Innovación en Posgrados de la Universidad Nacional de Colombia, Modalidad 3: Proyectos de Investigación, Creación o Innovación en Desarrollo [Call of the National Program of Projects for Strengthening Research, Creation, and Innovation in Postgraduate Studies of Universidad Nacional de Colombia, Modality 3: Research, Creation, or Innovation projects in Development] (Hermes project 19140).

References

- [1] "Merriam-webster online dictionary," 2006. [Online]. Available: <https://www.merriam-webster.com> ↑ 3
- [2] E. Rodríguez, D. Kleinn, and R. C Davis, "Breve descripción de los recursos forestales de la república de colombia," in *Taller sobre el programa de evaluación de los recursos forestales en once países latinoamericanos: México, Guatemala, Belice, El Salvador, Honduras, Nicaragua, Costa Rica, Panamá, Venezuela, Colombia, Ecuador, Turrialba, Costa Rica*, 1999. ↑ 3
- [3] S. O. Ramirez-Gomez *et al.*, "Analysis of ecosystem services provision in the colombian amazon using participatory research and mapping techniques," *Ecosystem Ser.*, vol. 13, pp. 93–107, 2015. [Online]. Available: <https://doi.org/10.1016/j.ecoser.2014.12.009> ↑ 3
- [4] N. Rodríguez, D. Armenteras, and J. Retana, "National ecosystems services priorities for planning carbon and water resource management in colombia," *Land Use Pol.*, vol. 42, pp. 609–618, 2015. [Online]. Available: <https://doi.org/10.1016/j.landusepol.2014.09.013> ↑ 3
- [5] L. S. Lima *et al.*, "Feedbacks between deforestation, climate, and hydrology in the southwestern amazon: Implications for the provision of ecosystem services," *Landscape Ecol.*, vol. 29, no. 2, pp. 261–274, 2014. [Online]. Available: <https://doi.org/10.1007/s10980-013-9962-1> ↑ 3
- [6] E. P. Anderson *et al.*, "Fragmentation of andes-to-amazon connectivity by hydropower dams," *Sci. Adv.*, vol. 4, no. 1, p. eaao1642, 2018. [Online]. Available: <https://doi.org/10.1126/sciadv.aao1642> ↑ 3
- [7] J. Marengo, "Characteristics and spatio-temporal variability of the amazon river basin water budget," *Climate Dynamics*, vol. 24, no. 1, pp. 11–22, January 2005. [Online]. Available: <https://doi.org/10.1007/s00382-004-0461-6> ↑ 3, 26, 27
- [8] D. Jacob *et al.*, "Assessing the transferability of the regional climate model remo to different coordinated regional climate downscaling experiment (cordex) regions," *Atmosphere*, vol. 3, no. 1, pp. 181–199, 2012. [Online]. Available: <https://doi.org/10.3390/atmos3010181> ↑ 3
- [9] S. A. Solman *et al.*, "Evaluation of an ensemble of regional climate model simulations over south america driven by the era-interim reanalysis: Model performance and uncertainties,"

- Climate Dyn.*, vol. 41, no. 5-6, pp. 1139–1157, 2013. [Online]. Available: <https://doi.org/10.1007/s00382-013-1667-2> ↑ 3, 4
- [10] E. Kalnay *et al.*, “The ncep/ncar 40-year reanalysis project,” *Amer. Meteor. Soc.*, vol. 77, no. 3, pp. 437–470, March 1996. [Online]. Available: [https://doi.org/10.1175/1520-0477\(1996\)077<0437:TNYRP>2.0.CO;2](https://doi.org/10.1175/1520-0477(1996)077<0437:TNYRP>2.0.CO;2) ↑ 3, 7
- [11] D. Jacob *et al.*, “A comprehensive model inter-comparison study investigating the water budget during the baltex-pidcap period,” *Meteor. Atm. Phys.*, vol. 77, no. 1-4, pp. 19–43, 2001. [Online]. Available: <https://doi.org/10.1007/s007030170015> ↑ 3
- [12] K. Fernandes, R. Fu, and A. Betts, “How well does the era40 surface water budget compare to observations in the amazon river basin?” *J. Geophys. Res.*, vol. 113, p. D11117, 2008. [Online]. Available: <https://doi.org/10.1029/2007JD009220> ↑ 4
- [13] S. Uppala *et al.*, “The era-40 re-analysis,” *Quarterly J. Royal Meteor. Soc.*, vol. 131, no. 612, pp. 2961–3012, October 2005. ↑ 4, 7
- [14] M. Chen, P. Xie, J. Janowiak, and P. Arkin, “Global land precipitation: A 50-yr monthly analysis based on gauge observations,” *J. Hydrometeorology*, vol. 3, no. 3, pp. 249–266, June 2002. [Online]. Available: [https://doi.org/10.1175/1525-7541\(2002\)003<0249:GLPAYM>2.0.CO;2](https://doi.org/10.1175/1525-7541(2002)003<0249:GLPAYM>2.0.CO;2) ↑ 4, 7, 8
- [15] R. Adler *et al.*, “The version 2 global precipitation climatology project (gpcp) monthly precipitation analysis (1979-present),” *J. Hydrometeorology*, vol. 4, no. 6, pp. 1147–1167, December 2003. [Online]. Available: [https://doi.org/10.1175/1525-7541\(2003\)004<1147:TVGPCP>2.0.CO;2](https://doi.org/10.1175/1525-7541(2003)004<1147:TVGPCP>2.0.CO;2) ↑ 4, 7, 8
- [16] IDEAM, “Atlas interactivo climatológico,” 2014. [Online]. Available: <http://atlas.ideam.gov.co/visorAtlasClimatologico.html> ↑ 4, 6, 23
- [17] *Estudio nacional del agua 2010*. Bogotá, Colombia: IDEAM, 2010. ↑ 4, 18
- [18] I. Sánchez-Rodríguez and A. Baquero-Bernal, “Estimación de la representatividad del modelo de descarga hidrológica (mdh hydrological model) en la cuenca vertiente del pacifico colombiano,” *Revista Colombiana de Física*, vol. 43, no. 2, pp. 295–300, 2011. ↑ 4
- [19] I. Hoyos, A. Baquero-Bernal, and S. Hagemann, “How accurately are climatological characteristics and surface water and energy balances represented for the colombian caribbean catchment basin?” *Climate Dyn.*, vol. 41, no. 5-6, pp. 1269–1290, February 2013. [Online]. Available: <https://doi.org/10.1007/s00382-013-1685-0> ↑ 4, 27
- [20] I. Hoyos, A. Baquero-Bernal, D. Jacob, and B. A. Rodríguez, “Variability of extreme events in the colombian pacific and caribbean catchment basins,” *Climate Dyn.*, vol. 40, pp. 1985–2003, April 2013. [Online]. Available: <https://doi.org/10.1007/s00382-012-1487-9> ↑ 4
- [21] A. Meisel Roca *et al.*, “Geografía económica de la amazonia colombiana,” Banco de la Republica de Colombia, Tech. Rep., 2013. ↑ 4
- [22] D. Dee *et al.*, “The era-interim reanalysis: Configuration and performance of the data assimilation system,” *Quarterly J. Royal Meteor. Soc.*, vol. 137, no. 656, pp. 553–597, April 2011. [Online]. Available: <https://doi.org/10.1002/qj.828> ↑ 4, 7, 8
- [23] M. Kanamitsu, W. Ebisuzaki, J. Woollen, S. Yang, J. Hnilo, M. Fiorino, and G. Potter, “Ncep–doe amip-ii reanalysis (r-2),” *Amer. Meteor. Soc.*, vol. 83, no. 11, pp. 1631–1643, November 2002. ↑ 4, 7, 8

- [24] D. Jacob, "A note to the simulation of the annual and interannual variability of the water budget over the baltic sea drainage basin," *Meteor. Atm. Phys.*, vol. 77, no. 1-4, pp. 61–73, June 2001. [Online]. Available: <https://doi.org/10.1007/s007030170017> ↑ 7, 8
- [25] G. Silvestri, C. Vera, D. Jacob, S. Pfeifer, and C. Teichmann, "A high-resolution 43-year atmospheric hindcast for south america generated with the mpi regional model," *Climate Dynamics*, vol. 32, no. 5, pp. 693–709, April 2009. [Online]. Available: <https://doi.org/10.1007/s00382-008-0423-5> ↑ 7, 8
- [26] D. Legates and C. Willmott, "Mean seasonal and spatial variability in gauge-corrected, global precipitation," *Int. J. Climatology*, vol. 10, no. 2, pp. 111–127, 1990. [Online]. Available: <https://doi.org/10.1002/joc.3370100202> ↑ 7, 8
- [27] "Mean seasonal and spatial variability in global surface air temperature," *Theor. App. Climatology*, vol. 41, no. 1-2, pp. 11–21, 1990. [Online]. Available: <https://doi.org/10.1007/BF00866198> ↑ 7, 8
- [28] P. Xie and P. Arkin, "Global precipitation: A 17-year monthly analysis based on gauge observations, satellite estimates, and numerical model outputs," *Amer. Meteor. Soc.*, vol. 78, no. 11, pp. 2539–2558, November 1997. [Online]. Available: [https://doi.org/10.1175/1520-0477\(1997\)078<2539:GPAYMA>2.0.CO;2](https://doi.org/10.1175/1520-0477(1997)078<2539:GPAYMA>2.0.CO;2) ↑ 7, 8
- [29] IDEAM, "Consulta y descarga de datos hidrometeorológicos," 2023. [Online]. Available: <http://dhime.ideam.gov.co/atencionciudadano/> ↑ 7, 8, 9
- [30] P. Jacob, "First- and second- order conservative remapping schemes for grids in spherical coordinates," *Mon. Wea. Rev.*, vol. 127, no. 9, pp. 2204–2210, September 1999. [Online]. Available: [https://doi.org/10.1175/1520-0493\(1999\)127<2204:FASOCR>2.0.CO;2](https://doi.org/10.1175/1520-0493(1999)127<2204:FASOCR>2.0.CO;2) ↑ 6
- [31] K. H. Cook, *Climate dynamics*. Princeton University Press, 2013. ↑ 7
- [32] CCSP, *Reanalysis of historical climate data for key atmospheric features: Implications for attribution of causes of observed change*. US Climate Change Science Program, 2008. ↑ 7
- [33] A. J. Simmons and J. Gibson, *The ERA-40 project plan*. Reading, UK: ECMWF, 2000. 7
- [34] P. Poli, *List of observations assimilated in ERA-40 and ERA-interim:(v 1.0)*. Reading, UK: ECMWF, 2010. ↑ 8
- [35] R. Kistler et al., "The ncep–ncar 50-year reanalysis: Monthly means cd-rom and documentation," *B. Amer. Meteor. Soc.*, vol. 82, no. 2, pp. 247–268, 2001. ↑ 8
- [36] K. E. Trenberth, J. T. Fasullo, and J. Mackaro, "Atmospheric moisture transports from ocean to land and global energy flows in reanalyses," *J. Climate*, vol. 24, no. 18, pp. 4907–4924, 2011. [Online]. Available: <https://doi.org/10.1175/2011JCLI4171.1> ↑ 8
- [37] S. Hagemann et al., "Evaluation of water and energy budgets in regional climate models applied over europe," *Climate Dynamics*, vol. 23, no. 5, pp. 547–567, 2004. [Online]. Available: <https://doi.org/10.1007/s00382-004-0444-7> ↑ 8
- [38] M. Beniston et al., "Future extreme events in european climate: An exploration of regional climate model projections," *Climatic Change*, vol. 81, no. 1, pp. 71–95, 2007. [Online]. Available: <https://doi.org/10.1007/s10584-006-9226-z> ↑ 8

- [39] E. Kjellström, B. L. D. Jacob, G. Lenderink, and C. Schär, "Modelling daily temperature extremes: Recent climate and future changes over Europe," *Climatic Change*, vol. 81, no. 1, pp. 249–265, March 2007. [Online]. Available: <https://doi.org/10.1007/s10584-006-9220-5> ↑ 8
- [40] J. Pabón, J. Eslava, and R. Gómez, "Generalidades de la distribución espacial y temporal de la temperatura del aire y de la precipitación en Colombia," *Meteorología Colombiana*, vol. 4, pp. 47–59, 2001. ↑ 10
- [41] F. Sabarly, G. Essou, P. Lucas-Picher, A. Poulin, and F. Brissette, "Use of four reanalysis datasets to assess the terrestrial branch of the water cycle over Quebec, Canada," *J. Hydrometeor.*, vol. 17, no. 5, pp. 1447–1466, 2016. [Online]. Available: <https://doi.org/10.1175/JHM-D-15-0093.1> ↑ 17
- [42] J. Roads, S.-C. Chen, M. Kanamitsu, and H. Juang, "Vertical structure of humidity and temperature budget residuals over the Mississippi River basin," *J. Geophysical Res.: Atm.*, vol. 103, no. D4, pp. 3741–3759, 1998. [Online]. Available: <https://doi.org/10.1029/97JD02759> ↑ 17
- [43] D. L. Hartmann, *Global physical climatology*. London, UK: Academic Press, 1994, vol. 56. ↑ 17
- [44] IDEAM, "Estudio nacional del agua 2014," 2014. ↑ 18
- [45] *Estudio Nacional del Agua 2018*. Bogotá, Colombia: IDEAM, 2018. ↑ 18
- [46] *Estudio Nacional del Agua 2022*. Bogotá, Colombia: IDEAM, 2022. ↑ 18, 25
- [47] "Atlas interactivo. radiación." 2014. [Online]. Available: <http://atlas.ideam.gov.co/visorAtlasRadiacion.html> ↑ 28

Carolina Valencia-Monroy

Bachelor of Education in Physics and Master of Science in Meteorology. Researcher in the field of weather forecasting, Instituto de Hidrología, Meteorología y Estudios Ambientales (IDEAM).

Email: cvalencia@ideam.gov.co

Astrid Baquero-Bernal

Bachelor of Science in Physics, PhD in Natural Sciences, professor and researcher in the fields of climatology, weather forecasting, and atmospheric pollution.

Email: abaquerobe@unal.edu.co



Research

Methodology for Inventory Management in Neighborhood Stores Using Machine Learning and Integer Linear Programming

Metodología para la gestión de inventario en tiendas de barrio utilizando aprendizaje de máquina y programación lineal entera

Carlos Alberto Henao-Baena¹  *, Bibiana Zuluaga-Zuluaga² , Julian Galeano-Castro² ,
Edward Jhohan Marín-García³ , Andrés Felipe Calvo-Salcedo⁴ 

¹Professor at the Electronics Engineering Program of Universidad Tecnológica de Pereira 

²Instructor linked to research processes at SENA Risaralda, Mercator group (Pereira, Colombia) 

³Professor at Universidad del Valle, Cartago Campus (Cartago, Colombia) 

⁴Full professor at Universidad Tecnológica de Pereira (Pereira, Colombia) 

Abstract

Context: Nowadays, inventory management poses a challenge given the constant demands related to temporality, geographic location, price variability, and budget availability, among others. In neighborhood shops, this process is manually done based on experience (the data generated are ignored), which is sometimes not enough to respond to changes. This shows the need to develop new strategies and tools that use data analysis techniques.

Method: Our methodology predicts the weekly demand for 14 common products in neighborhood stores, which is later refined based on investment capital. The method is validated using a database built with synthetic information extracted from statistical sampling. For the prediction model, three supervised learning models are used: support vector machines (SVM), AutoRegressive models (ARx), and Gaussian processes (GP). This work proposes a restricted linear model given an inversion and the predicted quantity of products; the aim is to refine the prediction while maximizing the shopkeeper's profit. Finally, the problem is solved by applying an integer linear programming paradigm.

Results: Tests regarding the prediction and inventory adjustment stages are conducted, showing that the methodology can predict the temporal dynamics of the data by inferring the statistical moments of the distributions used. It is shown that it is possible to obtain a maximum profit with a lower investment.

Conclusions: Our method allows predicting and refining inventory management in a neighborhood store model where quantities are managed to maximize the shopkeeper's profits. This opens the way to explore this approach in a real scenario or to introduce new techniques that can improve its performance.

Keywords: machine learning, inventory, constrained optimization, demand estimation

Acknowledgements: The authors would like to thank Universidad Tecnológica de Pereira and Universidad de Valle for their support during this project.

Article history

Received:
25th / May / 2022

Modified:
27th / Jun / 2023

Accepted:
29th / Aug / 2023

Ing., vol. 29, no. 1,
2024. e19423

©The authors;
reproduction right
holder Universidad
Distrital Francisco
José de Caldas.

Open access



*  Correspondence: caralbhenao@utp.edu.co

Resumen

Contexto: En la actualidad, la administración del inventario representa un reto dadas las constantes exigencias de temporalidad, ubicación geográfica, variabilidad en los precios, disponibilidad presupuestal, entre otros. En las tiendas de barrio, este proceso se realiza de forma manual y con base en la experiencia (se ignoran los datos generados), lo que en ocasiones no es suficiente para responder a los cambios. Esto muestra la necesidad de desarrollar nuevas estrategias y herramientas que utilicen técnicas de análisis de datos.

Método: Nuestra metodología predice la demanda semanal para 14 productos comunes en tiendas de barrio, la cual se refina posteriormente en función del capital de inversión para optimizar la ganancia. El método se valida a través de una base de datos construida con información sintética extraída a partir de muestreo estadístico. Para la predicción, se utilizan tres modelos de aprendizaje supervisado: máquinas de soporte vectorial (SVM), modelos AutoRegresivos (ARx) y procesos Gaussianos (GP). Luego, se plantea un modelo lineal restringido dada una inversión y las cantidades pronosticadas; el propósito es refinar la predicción maximizando la ganancia del tendero. Finalmente, el problema se soluciona aplicando un paradigma de programación lineal entera.

Resultados: Se realizan pruebas para las etapas de predicción y ajustes del inventario, donde se demuestra que la metodología logra predecir la dinámica temporal de los datos infiriendo los momentos estadísticos de las distribuciones utilizadas. Se muestra que es posible obtener una máxima ganancia con un monto menor de inversión.

Conclusiones: Nuestra metodología que permite predecir y refinar la gestión de inventario en un modelo de tienda de barrio en el que las cantidades se administran para maximizar las ganancias del tendero. Lo anterior abre el camino para explorar este enfoque en un escenario real o introducir nuevas técnicas que puedan mejorar su desempeño.

Palabras clave: aprendizaje de máquina, inventario, optimización restringida, estimación de la demanda

Table of contents

	Page		
1. Introduction	3	3.3.2. Validation	10
2. Basic nomenclature	5	3.4. Integer linear programming model (ILP)	11
3. Methodology	6	3.5. Experiments	12
3.1. Database	6	4. Results	13
3.2. Regression model	8	5. Conclusions	19
3.3. Model training	8	6. Acknowledgements	20
3.3.1. Supervised learning model	9	7. Author Contributions	20
		References	20

1. Introduction

Over the years, the world economy has oriented its markets towards globalized supply and demand. In the case of Colombia, this process started in the 90s with the beginning of the economic opening, when new competitors were allowed to enter the market, many of which were foreign producers. Due to this situation, several economic sectors disappeared, as it was not possible to compete with the wide range of products and prices in offer (1,2).

In light of the above, a large number of international companies entered the Colombian market, especially in the retail sector, which represents 56 % of retail sales. Within this business paradigm, large sales chains such as Éxito, Carrefour (today Jumbo), Carulla, Olímpica, Super Inter, and Makro stand out. These companies assess the procurement of supplies based on efficiency indicators, aiming to maximize the return on investment. However, there is a second model that concerns the neighborhood convenience stores of the traditional channel. The most noticeable difference between these two models corresponds to administration, which is carried out by the owner or head of the family unit in the second case (1,2).

Despite stiff competition, neighborhood stores have survived due to their closeness to the final consumer, their trust and empathy with customers, and the payment methods offered (interest-free credit). Neighborhood stores have been hit hard by the advent of large discount store chains, such as ARA, D1, and Justo & Bueno, which aim to get closer to the end customer and compete with low prices (3, 4). Therefore, the traditional channel in Colombia must improve, update, and transform its processes, specifically in making decisions on the projection of supply and demand, as well as in inventory rotation (5).

In general terms, the store administrator manages the investments in the purchase of the products offered according to their expertise and knowledge acquired from the market. It should be stressed that this is a subjective forecasting method based on experience. This strategy generates a high bias in facing the uncertainties presented by changes in the demand for certain items according to the season and the economic variations in prices, state policies, and social events (6).

Likewise, it has been identified that demand forecasting is a common problem in supply chains. Here, the objective is to achieve greater precision and less error. According to (7), given the diversity of demand patterns, it is unlikely that any single demand forecasting model can offer the highest accuracy across all items. On the other hand, managers frequently have more information that should be considered to improve forecast results. For example, they know customer habits and purchase intentions, among others (8). A better forecast should include all this information. However, this requires more advanced methods than those offered by the prediction techniques of machine learning.

Considering the above, artificial intelligence (AI) and machine learning techniques have been proposed in the literature, aiming to reduce bias and provide business units with decision-making tools under a data-based paradigm, largely because AI models allow them to carry out forecasting with

regard to the demand for items (9). In the state of the art, two major stages are identified in which these procedures are focused. The first involves collecting and characterizing the data, with the purpose of describing the behavior of the products and its variability over time. In the second stage, different machine learning techniques are used to estimate computational models that can predict and reproduce the dynamics of the data, so that the sales dynamics can be emulated over time for a set of specific items (10–13).

Usually, the forecast of pure units or goods follows a uniform or normal probability distribution (14). More specialized developments introduce planning aspects that drive the supply chain as customer expectations increase, shortening delivery times, and pressure for resource optimization (15). On the other hand, demand forecasting is generally carried out using machine learning techniques. An example of this is the use of neural networks, which emulate the forecast of items through a non-linear function in time. Historical sales data are included in the network design in combination with the effectiveness of advertising, promotions, and marketing events. However, this model is sensitive to the network architecture (*i.e.*, the number of hidden layers and the value of neurons per layer), which affects the generality of the method (16). Other methods also predict demand, such as the Auto Regressive Moving-Average (ARMA), Support Vector Machine (SVM), Multiple Linear Regression (MLR), and Random Forest models, showing competitive results adjusted to reality. Still, this approach predicts the quantities of products required without considering the investment and profit capabilities of the shopkeeper (17, 18). Other works demonstrate the application of chaotic methods, such as (19–21), achieving demand adjustment.

As of today, the sudden changes in the market have generated new paradigms of competition. These circumstances are experienced by emerging businesses such as neighborhood stores (22). Studies such as (23) show that more than 90 % of the data generated by these businesses are not exploited and are not used to make sense of the changing dynamics of the market. There are success stories where machine learning has been used to better predict and manage expenses (23). This optimizes business profits, thus allowing for small businesses' economic survival. Some sources claim that including these methodologies can add significant value to their demand forecasting processes, while more than half state that they can improve other eight critical supply chain capabilities (24).

The above-mentioned study added that retailers with the technology to predict these changes model contingency plans and options and quickly adapt their supply chain strategy to meet high demand and avoid excess inventory. Those who cannot do it risk falling behind with sales not meeting the goals, in addition to incurring losses through waste (23). This research describes and structures a methodology for forecasting the quantities needed to order certain products in neighborhood stores. The method proposes a linear model to maximize the shopkeeper's profits based on an available investment value that, combined with a machine learning procedure, allows inferring the amounts to be requested. This method constitutes an alternative detached from the traditional paradigm of neighborhood stores, which is built daily and considers the last order requested, ignoring the behavior in sales and the dynamics of customers (25).

This proposal employs three models for sales forecasting, i.e., the performance of an SVM, a Gaussian process (GP), and an ARx model are examined using synthetic data generated via statistical sampling according to the Probability Distribution Function (PDF) that is accentuated to the sales of the products under analysis. The selection criteria for the PDFs of the products studied are in accordance with (14), which suggests using uniform or Gaussian PDFs for products offered in neighborhood stores. Additionally, the methodology proposes error metrics and statistical analysis to evaluate and validate each of the models selected in this research. The results show that our proposal allows maximizing the shopkeeper's profits by considering the dynamics in sales and the available investment. The main contributions of this research are the following:

- A methodology to forecast sales (demand) for a neighborhood store over a specific period which maximizes the shopkeeper's profits while considering the dynamics of demand and the number of products to invest in.
- A comparative study that evaluates the performance of forecast models applied to the prediction of demand in neighborhood stores.
- A validation procedure to measure the performance of each step in the proposed method.

This paper is organized as follows. Section 2 presents the basic nomenclature. Section 3 describes the proposed methodology, as well as the validation procedure, and the results obtained are shown in section 4. In the final section, the concluding remarks of our research are presented.

2. Basic nomenclature

Table I. Paper nomenclature

Symbol	Description
X_{Train}	Selected weeks for the learning model training
X_{Test}	Selected weeks for validating the learning model
Y_{Train}	Demands for the model training at X_{Train} instants
Y_{Test}	Demands for validating the model at X_{Test} instants
m	Analysis week in the [1-108] weeks window
n	n -th product under analysis $n \in Z^*[1 - 14]$
Z_{Test}	Validation matrix of the learning model
Z_{Train}	Training matrix for the learning model
W_n	Prediction model parameters for the n product
Z	Prediction of the trained model given the W_n vector parameters
A_G	Return gain
G_m	Investment to be made in the m week
ARMA	Auto Regressive Moving Average
SVM	Support Vector Machine
MLR	Multiple Linear Regression
GP	Gaussian Processes
PDF	Probability Distribution Function
ILP	Integer Linear Programming

3. Methodology

Fig. 1 shows the implemented method in a block diagram. In short, it consists of three phases: firstly, a database with information on the demands per week for 14 everyday items offered in neighborhood stores; secondly, a regression model that emulates the prediction $Z = \{Z_1 Z_2 \dots Z_n\}$, where Z_n is the prediction of the n -th product; and, finally, an integer linear programming model that refines the weekly orders to maximize the profit return A_G given a weekly investment rate. Traditionally, inventory management models include a systematic methodology to establish inventory control policies for products. This allows determining the security list, the reorder point, or when the order must be placed (26). This research aims to reduce the overall costs by predicting the demand for key products in neighborhood stores. It analyzes projected profits based on the model's predictions. It must be acknowledged that this study does not encompass all aspects of defining inventory control policies.

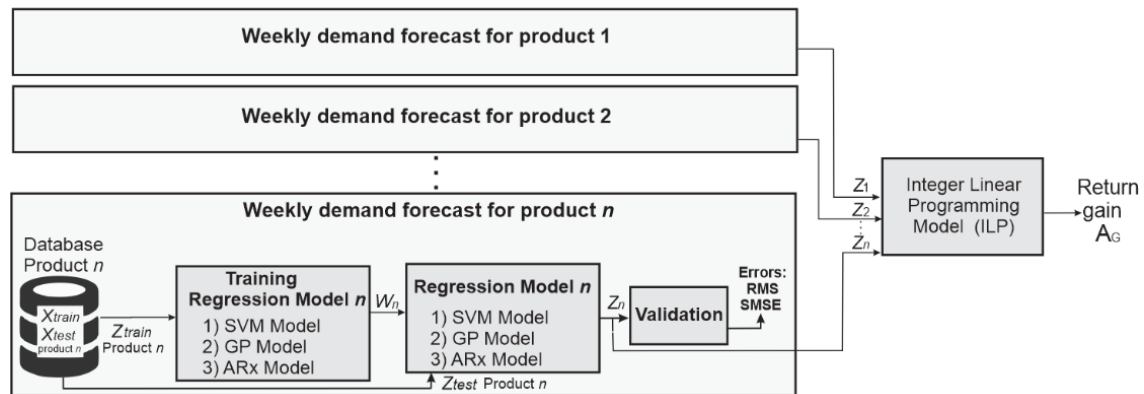


Figure 1. Implemented methodology

3.1. Database

In this study, seven categories that cover 14 product varieties in neighborhood stores were selected, as summarized in Table II. Each product is independent, so all analyses are proposed and done for each one of them.

This selection was done by visiting shopkeepers in neighborhoods of Pereira (these items were selected since they were representative of the sales during the analyzed time horizon) and identifying common items such as those shown in Table II. Additionally, the variability in their demand was validated, finding that some exhibit a temporary behavior, as is the case of category 6 (products of great demand on celebration dates, *i.e.*, holidays, commemorative days, among others).

Conversely, other items show a stable behavior over time, as is the case of the products in categories 5 and 7. The literature states that the demand follows a certain PDF, which, in the case of basic products, can be adjusted to a normal or uniform behavior (27). Due to the above, it is possible to generate

Table II. Selected categories and products

	Product 1	Product 2
Category 1	Shampoo	Body soap
Category 2	Detergent	Bleach
Category 3	Milk	Yogurt
Category 4	Beer	Wine
Category 5	Chicken	Frozen food
Category 6	Rice	Salt
Category 7	Supplements	Vitamins

synthetic data from a statistical sample while assuming a PDF for each category, establishing the distribution parameters for each item (Table III).

Table III. Definition of the model for data generation

	PDF employed	Product 1	Product 2
Category 1	Gaussian	$\mu = 12$ and $\sigma = 5$	$\mu = 25$ and $\sigma = 8$
Category 2	Uniform	$a = 10$ and $b = 24$	$a = 20$ and $b = 80$
Category 3	Gaussian	$\mu = 60$ and $\sigma = 15$	$\mu = 40$ and $\sigma = 15$
Category 4	Gaussian	$\mu = 120$ and $\sigma = 40$	$\mu = 20$ and $\sigma = 10$
Category 5	Gaussian	$\mu = 40$ and $\sigma = 13$	$\mu = 30$ and $\sigma = 15$
Category 6	Uniform	$a = 15$ and $b = 110$	$a = 20$ and $b = 120$
Category 7	Gaussian	$\mu = 12$ and $\sigma = 3$	$\mu = 12$ and $\sigma = 2$

The expected values u_Y (where Y is the weekly demand) and the standard deviation σ_Y of the distribution given in Table III, are summarized in Table IV. The first moments for a normal and uniform distribution are $u_Y = \mu$ and $u_Y = \frac{b+a}{2}$, respectively. Similarly, the variance in the case of a Gaussian and uniform PDF is $\sigma_Y = \sigma$ and $\sigma_Y = \frac{b-a}{\sqrt{12}}$ (14).

Thus, the demand per week (for each product) was sampled over a time window of 78 weeks, *i.e.*, the data generated emulate the dynamics of the demands per product for this sales interval. Once the database was formed, it was segmented as follows: $X = \{X_{Train}, Y_{Train}, X_{Test}, Y_{Test}\}$. Then, a characteristic was added to the vectors X_{Train} and X_{Test} which models the increase or decrease in the number of requested units of a product with respect to the previous week. Eq. (1) shows the transformation for the Y_{Train} case, following a similar procedure for Y_{Test} .

Table IV. Expected values and distributions from Table III

	u_Y		σ_Y	
	Product 1	Product 2	Product 1	Product 2
Category 1	12	25	5	8
Category 2	18	50	4	17.3
Category 3	60	40	15	15
Category 4	120	20	40	10
Category 5	40	30	13	15
Category 6	62.5	70	27.4	28.9
Category 7	12	12	3	2

$$\nabla M_{Train}^{m,n} \begin{cases} 1 & \text{if } Y_{Train}^{m,n} - Y_{Train}^{m-1,n} > 0 \\ -1 & \text{if } Y_{Train}^{m,n} - Y_{Train}^{m-1,n} < 0 \text{ and } m > 1 \text{ and } \nabla M_{Train}^{1,n} = 0 \\ 0 & \text{if } Y_{Train}^{m,n} - Y_{Train}^{m-1,n} = 0 \end{cases} \quad (1)$$

The sub-index m refers to the analyzed week for product n (defined in Table II). Eq. (1) indicates that, if the value of $\nabla M_{Train}^{m,n}$, there was an increase when ordering product n in week m regarding the $m - 1$ period. On the other hand, a value of $\nabla M_{Train}^{m,n}$ implies a stable behavior in week m regarding the moment $m - 1$. This descriptor seeks to guide the learning model at the moments when changes occur in the demands of the n products. For more details, the reader should consult (28). With these changes, the terms are defined as follows: $Z_{train} = \{[X_{train}, \nabla M_{train}], Y_{train}\}$ where $\nabla M_{Train} = \{\nabla M_{Train}^{1,1}, \nabla M_{Train}^{2,1}, \dots, \nabla M_{Train}^{m,1}, \nabla M_{Train}^{m,2}, \dots, \nabla M_{Train}^{m,n}\}$, similarly $Z_{test} = \{[X_{Test}, \nabla M_{Test}], Y_{test}\}$.

3.2. Regression model

This phase is divided into two processes: model training and simulation. The first process consists of computing the set of parameters W_n given the demands per week for an item n of a specific category. On the other hand, the simulation process consists of predicting the behavior regarding the future demands of product n once the parameters W_n are found.

3.3. Model training

Fig. 2 shows each of the stages that make up the training phase. In short, it consists of a database that integrates synthetic data of demands per week for a family of products, as well as a supervised learning model to emulate the dynamics of weekly demands. The purpose is to transfer the data content to the model through a learning rule that allows finding the set of parameters W_n .

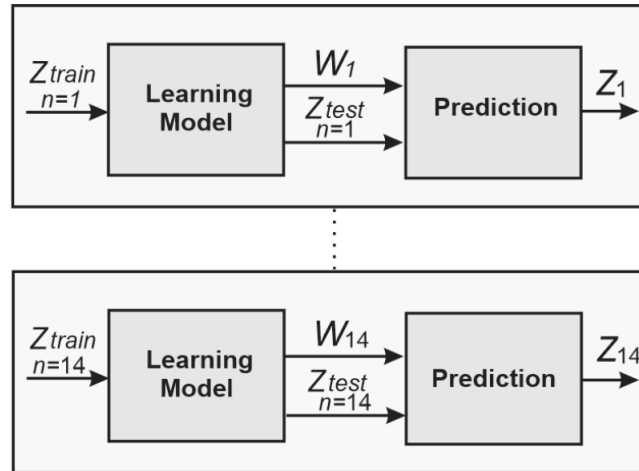


Figure 2. Prediction model diagram

3.3.1. Supervised learning model

In this paper, three supervised options for state-of-the-art training are examined. Each of these is described below.

SVM

The use of an SVM as a prediction model is mainly due to its robustness against data with noise. It is a widely studied method, and it is easy to implement. This method is characterized by being a linear model in the W_n parameters, which are tuned by minimizing a regularized error function subject to a set of linear constraints.

Generally, the problem is usually transformed into an equivalent dual one by applying the KKT (Karush-Kuhn-Tucker) conditions, obtaining a quadratic representation that allows the value W_n to be inferred when it is solved. Once the parameter values W_n are known, the model is trained. However, the equivalent objective function will depend on some variables assumed to be known, such as the Z_{Train} data set, as well as the Kernel structure (covariance function) (29,30).

ARx Model

The acronym ARx refers to an autoregressive model of exogenous terms. It involves an input signal in its structure. Eq. 2 shows this model. The meaning of each term is shown in Table V.

$$A(q)y(t) = B(q)u(t-l) + e(t) \quad (2)$$

The set of parameters to infer W_n corresponds to the set of values of the coefficients a_{n_a} and b_{n_b} . These are tuned via least squares through the Z_{Train} dataset. Then, once the values of W_n are known, the model is determined for any value of t , assuming that W_n is known. For more details, the reader can refer to (31).

Table V. Nomenclature associated with the ARx model

Parameter	Definition
$y(t)$	Output in instant t
q	Delay operator
$u(t)$	Input in instant t
$e(t)$	Gaussian white noise disturbance value
$A(q)$	$A(q) = 1 + a_1q^{-1} + \dots + a_{n_a}q^{-n_a}$
$b(q)$	$B(q) = 1 + b_1q^{-1} + \dots + b_{n_b}q^{-n_b}$
n_a	Number of poles
n_b	Number of zeros
l	The system's dead time

Gaussian process (GP)

Contrary to previous methods, the GP introduces a probabilistic non-linear prediction function, preventing a fixed structure in the model. From its base, the model assumes that the nature of the data follows a Gaussian distribution function established by a mean function $m(x)$ and a covariance $cov(x, x)$. In the literature, $cov(x, x)$ is also known as *Kernel*, so the model training consists of tuning the parameters of $m(x)$ and $cov(x, x)$ (i.e., W_n) given the input X_{Train} and output $Y_{Train}(Z_{Train})$ dataset. The prediction process (once the model has been trained) is performed from the mean predictive function, as shown in Eq. (3).

$$Z = m'(X_{Test}) = cov(X_{Test}, X_{Train}) \cdot [cov(X_{Train}, X_{Train})]^{-1} \cdot Y_{Train} \quad (3)$$

where $m'(x_1)$ is the prediction in space x_1 given the input x and the corresponding output y . An interesting feature of the GP allows computing the evolution of uncertainty (Eq. (4)) in the prediction using the predictive standard value (Eq. (3)), where $\sigma(m'(x_1))$ evaluates the uncertainty (variance) of $m'(x_1)$. The GP implicitly assumes that the function $m'(x_1)$ obeys – as does $m(x)$ – a Gaussian behavior (32).

$$\sigma(m'(X_{Test})) = cov(X_{Test}, X_{Test}) - cov(X_{Test}, X_{Train}) \cdot [cov(X_{Train}, X_{Train})]^{-1} \cdot cov(X_{Train}, X_{Test}) \quad (4)$$

3.3.2. Validation

In this process, the performance of the trained models is evaluated through the dataset $[X_{Test}, \nabla M_{Test}]$ and the corresponding prediction Z (Fig. 2). In the first place, the effective error is used as a performance metric (Eq. (5)) where E is the RMS error between the synthetic data validation vector and the prediction of the model (30). Here, N refers to the size of the vector Y_{Test} .

$$E = \sqrt{\frac{\|Z - Y_{Test}\|^2}{N}} \quad (5)$$

This metric allows evaluating the fidelity of the trained model to emulate the prediction process of product demands. However, the Y_{Test} and Y_{Train} data must be normalized to avoid bias regarding

strong changes. In this work, they are normalized with respect to the mean value of the data as follows: $Y_{Test} \rightarrow \frac{Y_{Test} - \mu_Y}{\sigma_Y}$. A similar transformation applies to Y_{Train} . Thus, Eq. (5) is transformed into the following expression:

$$E = \sigma_Y \sqrt{\frac{\|Z - Y_{Test}\|^2}{N}} \quad (6)$$

On the other hand, Eq. (7) defines the form of the standardized mean squared error (SMSE) (33):

$$SMSE = \frac{1}{\sigma_{Train}^2 + \mu_{Train}^2} \|Z - Y_{Test}\|^2 \quad (7)$$

where σ_{Train}^2 and μ_{Train} are the variance and arithmetic mean of the Y_{Test} data. The metric given in Eq. (6) has the purpose of evaluating the stability of the prediction model Z when considering changes in the training data Z_{Train} .

3.4. Integer linear programming model (ILP)

Z is an expected value of the demand. However, the shopkeeper will not always have sufficient resources to meet the quota established by the prediction model, which is why a strategy that refines the suggested Z values through a linear optimization model is adopted. The objective function to be minimized is presented in Eq. (8).

$$f(Z^*) = p_1 Z_1^* + p_2 Z_2^* + \dots + p_{14} Z_{14}^* = P Z^{*T} \quad (8)$$

where $Z^* = [Z_1^*, Z_2^*, \dots, Z_{14}^*]$ are the quantities demanded weekly to be refined for each of the items defined in Table II, and $P = [p_1, p_2, p_3, \dots, p_{14}]$ denotes the corresponding percentages of profit from the sale of each product. The restrictions associated with the maximum number of items allowed are as follows:

$$\begin{aligned} Z_n^* - Z^{m,n} &= g(Z) \leq 0 \\ Z_n^* &= r(Z) \geq 0 \end{aligned} \quad (9)$$

where $Z^{m,n}$ refers to the predictions of item n ($n : 1 : 14$) for week m . Therefore, Eq. (9) yields 28 linear constraints given a value of m . Finally, the equality associated with the investment in week m is

$$G_m - c_1 Z_1^* - c_2 Z_2^* - \dots - c_{14} Z_{14}^* = G_m - C Z^{*T} = 0 = h(Z^*) \quad (10)$$

where $C = [c_1, c_2, c_3, \dots, c_{14}]$ are the purchase costs per item. Now, the refined quantities Z^* are found by solving the following ILP problem (Eq. (11)) for an investment G associated with week m .

$$\begin{aligned} &\max_{Z^*} f(Z^*) \\ &\text{Subject to:} \\ &g(Z^*) \leq 0 \\ &r(Z^*) \geq 0 \\ &h(Z^*) = 0 \end{aligned}$$

Note that the presumption of solving the problem stated in Eq. (11) is due to the fact that the quantities to be refined have a discrete characteristic. The values of P and C have been extracted from the portal www.megatiendas.co, and they are condensed in Table VI.

Table VI. Definition of the values for the percentage gain vector P and the cost per product C

Category	Cost (\$)		Profit (%)	
	Product 1	Product 2	Product 1	Product 2
1	10.550 $\rightarrow c_1$	8,000	25 $\rightarrow p_1$	25
2	4,700	4,400	25	25
3	3,100	6,250	15	15
4	2,500	14,700	20	20
5	10,650	12,950	15	15
6	3,900	1,250	10	10
7	4,550	11.320 $\rightarrow c_{14}$	25	25 $\rightarrow p_{14}$

3.5. Experiments

The test procedures evaluated the performance of the learning rules and the ILP. For the first case, the performance of the three strategies was evaluated by computing the values of E and $SMSE$ (Eqs. (6) and (7)) for the prediction Z produced by the model and the test dataset Y_{Test} . Out of the 78 weeks, the first 55 were selected with their corresponding demands to build the vectors X_{Train} , Y_{Train} , and ∇M_{Train} . Then, with the other weeks (56 to 78), the validation array X_{Test} , Y_{Test} , and ∇M_{Test} was made. The test in Algorithm 1 shows the process that summarizes the above.

Algorithm 1 Training and validation algorithm

Input: Z_{train} , $Z_{test} \leftarrow$ to interaction i

Output: Prediction Z , RmsError E , Standardized Square Error, SMSE \leftarrow to interaction i , Average $Z(\mu)$, standard deviation of $E(\sigma)$

- 1: **for** $i = 1$ to j **do**
 - 2: $\mu_{train} \leftarrow \text{Mean}(Y_{train}[i, :])$
 - 3: $\sigma_{train}^2 \leftarrow \text{Var}(Y_{train}[i, :])$
 - 4: $Y_{train}[i, :] \leftarrow \frac{Y_{train}[i, :] - \mu_{train}}{\sqrt{\sigma_{train}^2}}$
 - 5: $Z_{train} \leftarrow [Y_{test}, \nabla M_{test}, Y_{train}]$
 - 6: $Y_{test}[i, :] \leftarrow \frac{Y_{test}[i, :] - \mu_{train}}{\sqrt{\sigma_{train}^2}}$
 - 7: $W_n \leftarrow \text{Train}(Z_{train}, \text{Model})$ $\triangleright \text{Model} \leftarrow \{ARx, SVM, GP\}$
 - 8: $Z[i] \leftarrow \text{Predicr}(X_{test}, \nabla M_{test}, W_n, \text{Model})$
 - 9: $E[i] \leftarrow \sqrt{\frac{\sigma_{train}^2 \times \|Z - Y_{test}\|^2}{N}}$
 - 10: $SMSE_{[i]} \leftarrow \frac{1}{\sigma_{train}^2 + \mu_{train}^2} \cdot \|Z - Y_{test}\|^2$
 - 11: **end for**
 - 12: $\mu \leftarrow \text{Mean}(Z)$
 - 13: $\sigma \leftarrow \text{Var}(E)$
-

For the case of GP and SVM, a radial basis covariance function (RBF) with scale factor ρ^2 was assumed (32). This parameter was tuned given the Z_{Train} dataset. The GPML (34) toolbox was used to train (find W_n) and validate the GP (the value of ρ^2 was also tuned with this toolbox). For the SVM, MATLAB's regression toolbox in MATLAB was employed. In this case, a value of $\tau^2 = 0,001$ (length scale) was set for the tests. The results are presented by means of tables and figures depicting the behavior of each model. In the case of the GP, the results are based on Eqs. (3) and (4). Finally, based on the results, the best prediction model was selected in order to evaluate the performance of the ILP.

The experiments carried out in the ILP consist of validating the problem stated in (11). For this purpose, weekly test investments G_m , are defined. Thus, the refined quantities Z^* are calculated given the weekly investment G_m and $Z^{m,n}$. Finally, the expected return earning rate A_G is calculated according to the suggested amount Z^* by the model in week m (Eq. (??)). Algorithm 2 shows a summary of the refinement process of the quantities Z and the profits for each of the weeks m under analysis.

$$A_G^m = c_1 p_1 Z_1^{*m} + c_2 p_2 Z_2^{*m} + \dots + c_{14} p_{14} Z_{14}^{*m} \quad (11)$$

Algorithm 2 Algorithm for calculating A_G^m profits given vector Z^*

Input: $G_m, C, Z^{m,n}, P \leftarrow$ to week m

Output: $Z^*, A_G^m \leftarrow$ to week m

- 1: **for** $i = m$ **to** j **and** $j > m$ **do**
 - 2: $Z^*[i] \leftarrow \text{Linprog}(Z^n, C, P, G_i)$
 - 3: $A_G^{m*} \leftarrow c_1 p_1 Z_1^* + \dots + c_n p_n Z_n^*$
 - 4: **end for**
-

4. Results

This section presents the analysis and discussion of the results obtained by implementing the methodology and performing the validation tests proposed in the methodology section. Fig. 3 shows the demand estimation made via the proposed prediction methods for product 14. In 3c, it can be seen that the ARx is the predictor that manages to capture the trend of the data and the demand variability for the item in the time window.

Fig. 3b shows GP's low performance, as it fails to predict the variability of the demands when estimating an average value. Although the SVM manages to improve the prediction concerning the GP, this variation is not enough to emulate the dynamics of the weekly demands of the products (Fig. 3a). The quantitative results are shown in Fig. 3b. The results regarding the effective errors are condensed (Eq. (5)) once the Monte Carlo experiment has been simulated (Algorithm 1). As per Fig. 4b, the ARX shows a lower error when compared to the SVM (Fig. 4d) and the GP (Fig. 4f), which corroborates the results shown in Fig. 3. It is noteworthy that the minimum error for the training demands is reached by GP (Fig. 4e). This suggests that the model is overtrained, which explains the result in Fig. 3b. On the

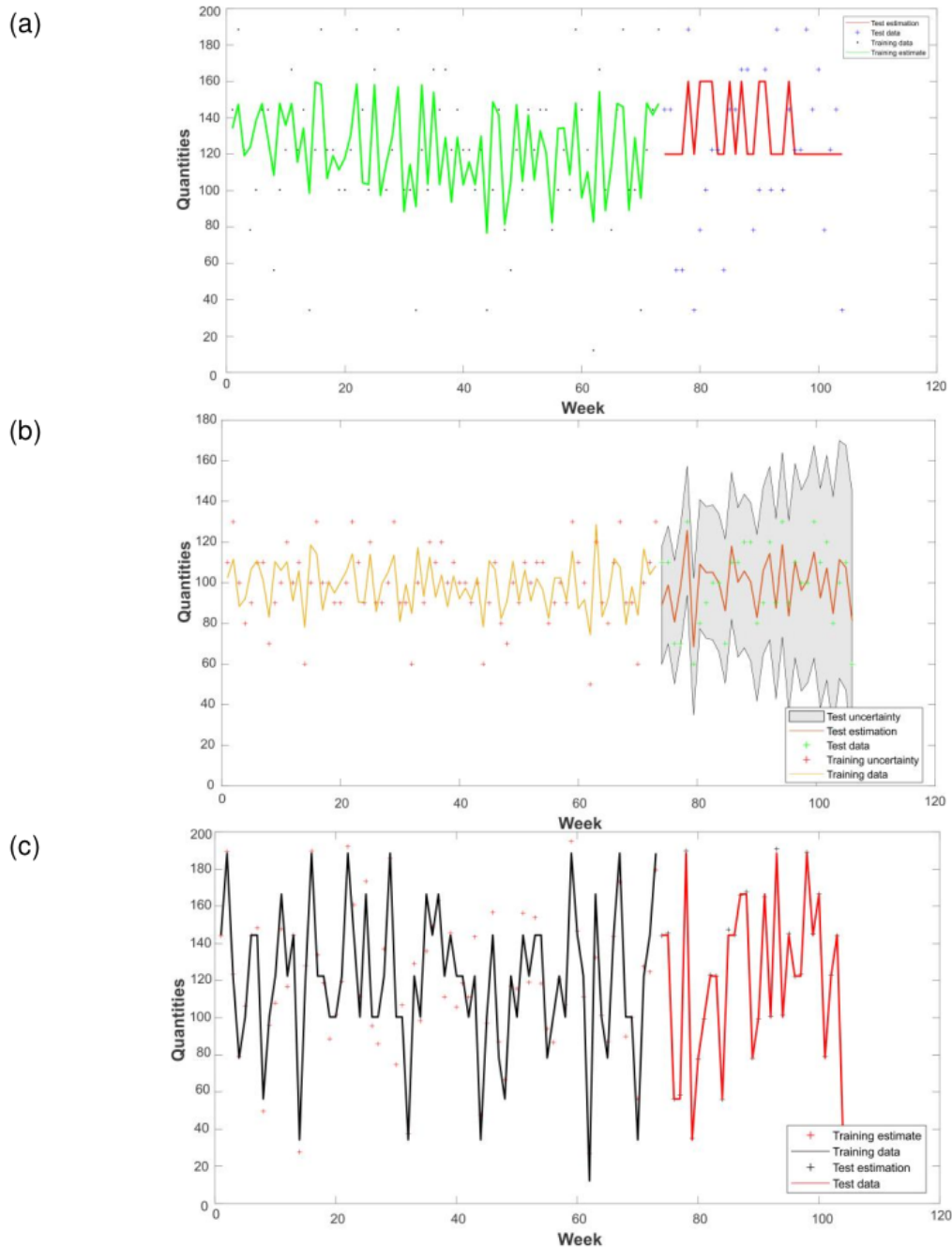


Figure 3. a) Demand estimation using the SVM method. b) Demand estimation using the GP method. c) Demand estimation using the ARX method

other hand, Fig. 4d shows that the SVM responds adequately to products with low variability, as is the case of the items in categories 1 and 7 (Table II).

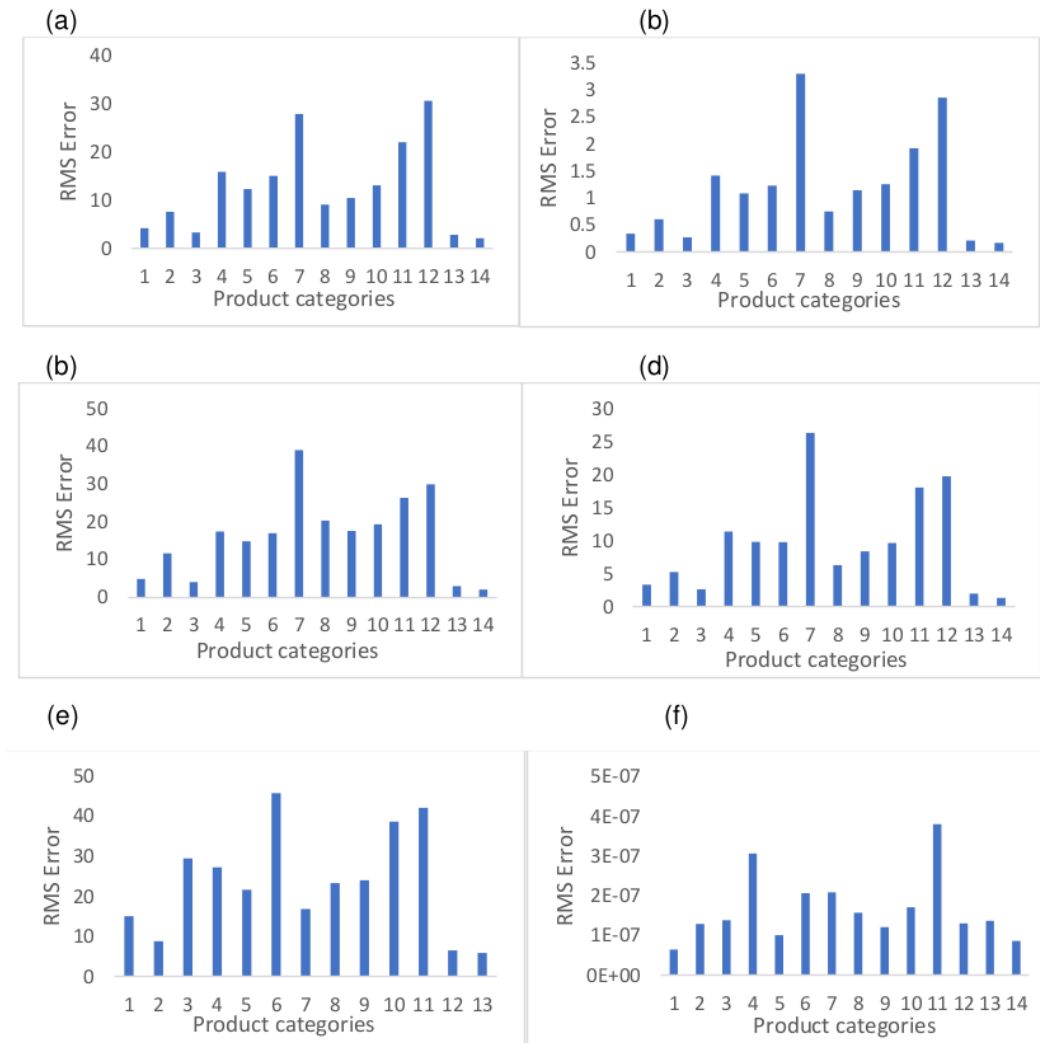


Figure 4. a) Training RMS error for the ARX method. b) Test RMS error for the ARX method. c) Training RMS error for the SVM method. d) Test RMS error for the SVM method. e) Training RMS error for the GP method. f) Test RMS error for the GP method

Fig. 5 synthesizes the results for the $SMSE$ metric. The GP fails to stabilize in the training phase regarding the categories $\{1,2,7, 12, 13\}$. On the other hand, the SVM and the ARx exhibit a similar qualitative behavior in all the product categories under study, both in the training stage and during the validation. The results suggest that the prediction computed by the three methods evaluated is stable. This corroborates what is evidenced in Figs. 5 and 6, where the change in the datasets Z_{Train} and Z_{Test} fails to capture the dynamics of the data, nor does it significantly reduce the effective errors, mainly in the case of the SVM and the GP. The above insinuates that they fail to satisfactorily emulate the behavior of the demands. This may be due to the nature of the application, where the analysis time window (104 weeks) is restricted for these models.

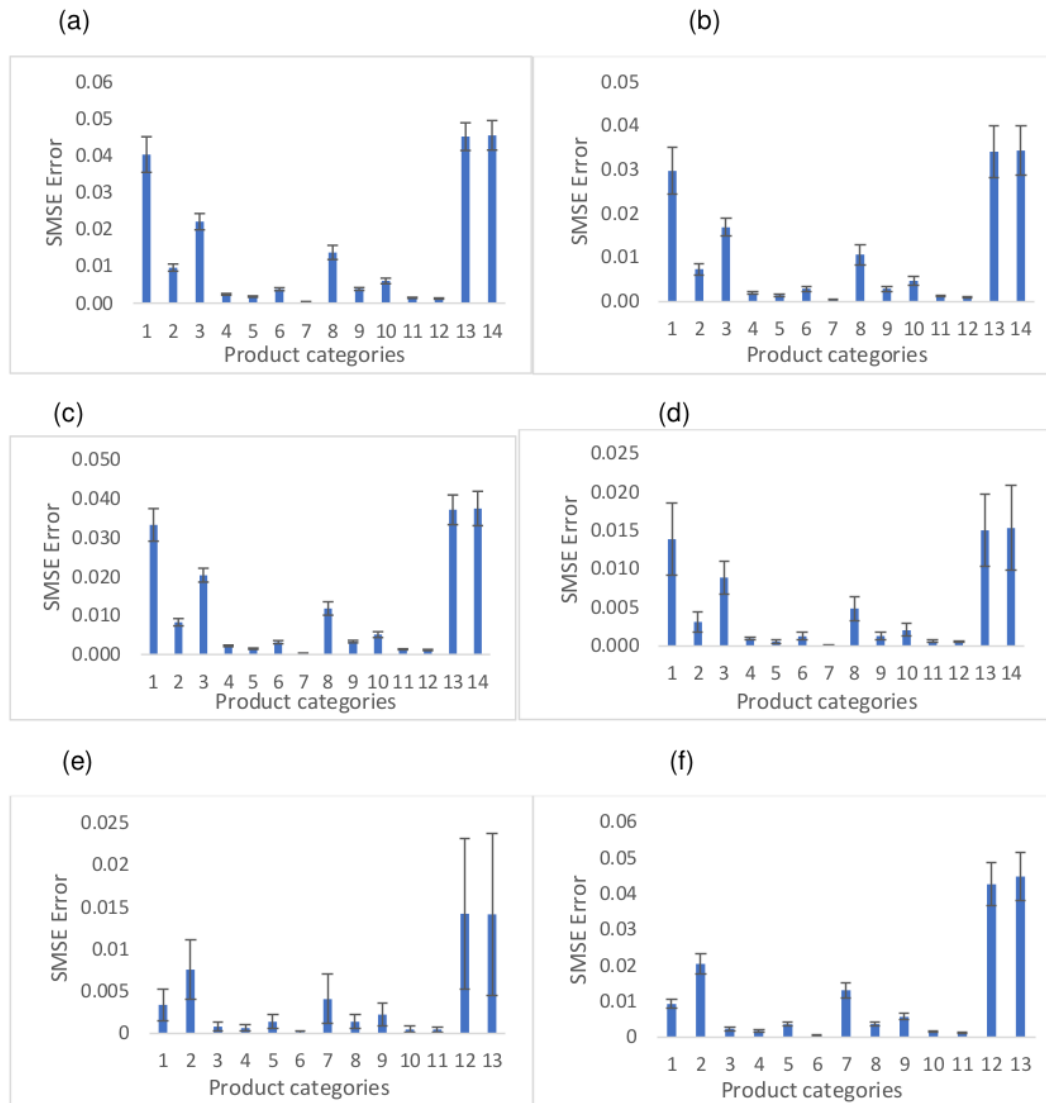


Figure 5. a) Training RMS error for the ARX method. b) Test RMS error for the ARX method. c) Training RMS error for the SVM method. d) Test RMS error for the SVM method. e) Training RMS error for the GP method. f) Test RMS error for the GP method

Table VII summarizes the results obtained by calculating the first expected value and the variance of the predictors for each of the studied products' demands. The ARx manages to approach the theoretical statistics, which is a significant result, suggesting that it manages to capture the variability and the mean value of the distributions associated with each of the demands. However, although the SVM and the GP approach the first theoretical moment of the data, they fail to capture the variability; these predictors have a variance bias in this application.

Table VII. Results regarding the expected value and variance for each of the predictors

	Theoretical		GP		SVM		ARX	
	E[Y]	\sqrt{VAR}	E[Y]	$\sqrt{VAR}[Y]$	E[Y]	\sqrt{VAR}	E[Y]	$\sqrt{VAR}[Y]$
Product 1	12	5	12.18	11.84	14.35	0.86	11.25	4.07
Product 2	25	8	37.44	28.42	32.84	1.24	22.71	7.76
Product 3	18	4	18.70	17.84	20.64	0.64	16.91	3.55
Product 4	50	17.3	54.35	49.35	48.39	2.96	48.03	16.60
Product 5	60	15	52.48	59.00	57.73	2.56	60.28	12.02
Product 6	40	15	34.35	39.45	36.42	2.49	38.42	16.71
Product 7	120	40	115.95	110.35	117.24	7.10	120.80	25.32
Product 8	20	10	18.19	21.03	19.08	1.50	23.85	8.22
Product 9	40	13	43.18	36.90	38.64	2.26	39.03	10.00
Product 10	30	15	38.93	30.65	36.75	2.45	28.64	12.61
Product 11	62.5	27.4	65.22	69.39	64.72	4.10	66.71	23.89
Product 12	70	28.9	52.74	60.87	45.69	4.70	52.72	31.38
Product 13	12	3	14.96	12.65	11.99	0.43	11.95	2.92
Product 14	12	2	11.81	12.06	12.35	0.30	11.56	2.22

Given that the ARx exhibits a good performance in estimating the demands in each of the categories, and considering that the SVM and GP do not reach competitive performances (Table VII, Figs. 3, 4, 5), the outputs Z inferred by the ARx are selected to build the integer programming model described in Eq. (11) in such a way that it is possible to refine the quantities Z by defining a weekly investment index to determine Z^* . Fig. 6 shows the difference between the profits when considering a sufficient investment to acquire the amounts Z versus the profits gained when examining a smaller investment to obtain Z^* in a cumulative period of 22 weeks. Notice how, in the linear programming method, the profits approach the maximum values as the investment grows. This is an expected result since the formulation aims to provide further weight to the products with the highest profit; the method suggests the amounts that maximize profit to the shopkeeper. It should be noted that, from an investment of 1.200.000 COP, it is possible to obtain the same profit as the one obtained with the Z amounts, *i.e.*, the values suggested by the ARx.

Fig. 7a shows the expected profit for 22 weeks according to the amounts Z . It also shows the profit for the amounts Z^* corresponding to an investment of 1.220.000 COP. This shows that the linear programming model does not affect the trend of expected profits. Note that this result is still valid for smaller investments (Fig. 7b), and it is important because the method guarantees proportionality in profits, even if the investment is low.

Fig. 8 shows how the solution to the problem given by Eq. (11) refines the number of products and prioritizes those that generate greater profits. For example, in Fig. 8a, the model gives priority to

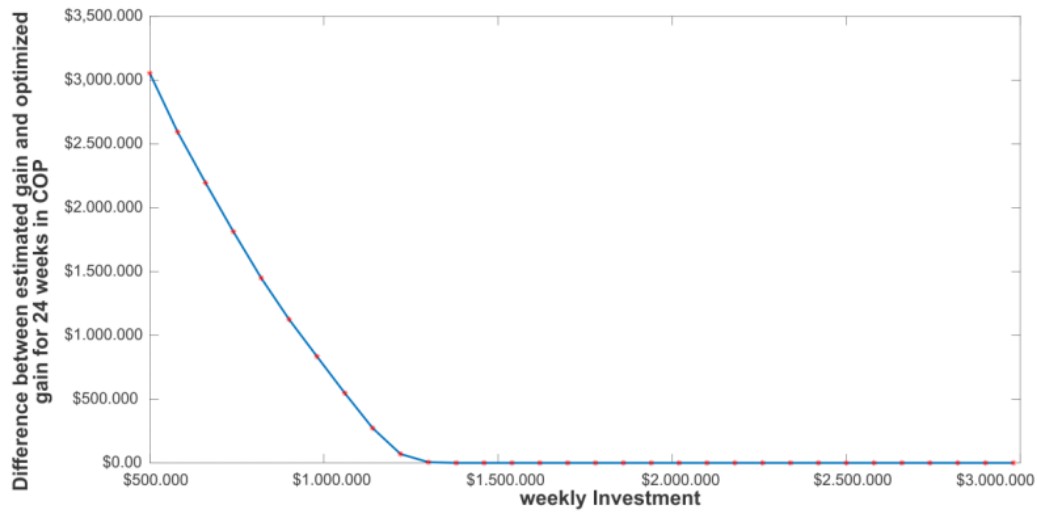


Figure 6. Difference between the profit projected by the estimation of the product and the profit obtained by the integer programming model for 22 weeks of analysis

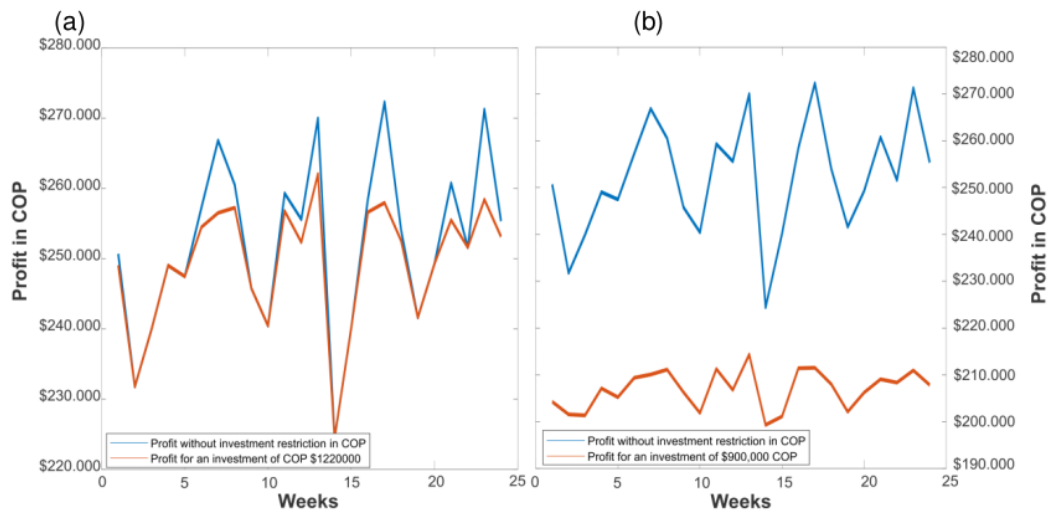


Figure 7. a) Expected profit with Z vs. profit obtained with Z^* for 22 weeks, corresponding to an investment of 1.220.000 COP. b) Expected profit with Z vs. profit obtained with Z^* for 22 weeks given an investment of 920.000 COP

products 1, 2, 3, 4, 13, and 14 when comparing them against the utility portions defined in Table ?? . They coincide with the items that report the highest percentage of utility per sale. Similarly, it should be noted (Fig. 8b) that, as the investment value increases, the amounts Z^* tend to equal the values of Z , which corrects the results reported in Figs. 6 and 7.

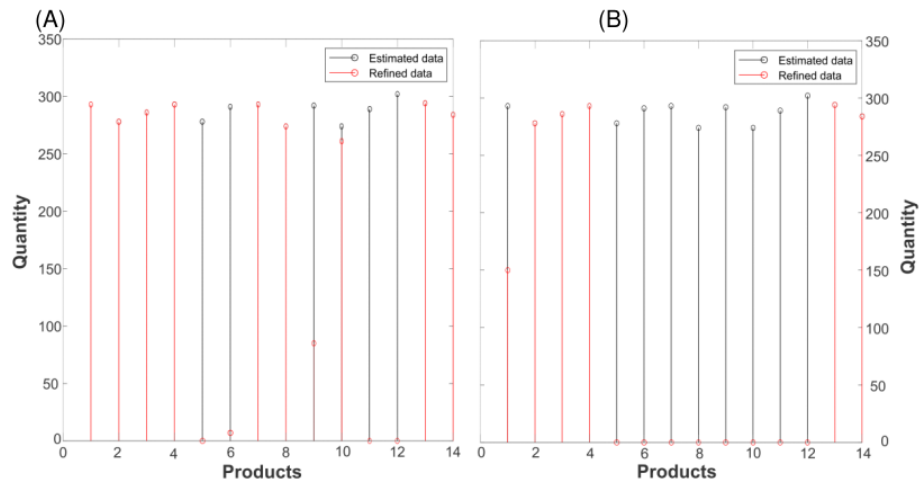


Figure 8. a) Estimated amounts for the 14 products in 22 weeks vs. refined amounts for a weekly investment of 500.000 COP. b) Estimated amounts for the 14 products in 22 weeks vs. refined amounts for a weekly investment of 1.000.000 COP

5. Conclusions

In this research, a methodology is designed and implemented with the aim of estimating the demand for products sold in neighborhood stores. This is achieved based on the history of the weeks of sales for previous months and weeks. This method estimates demand and suggests which products to buy in order to maximize profit based on an available investment cost. Based on the results, it is observed that the model proposed in Eq. (11) is functional to the extent that the investment available per week is not sufficient to acquire the amounts Z . This is inferred by analyzing that reported in Figs. 8a and 8b, where the behavior of the amounts Z and Z^* is described as an investment value. The aforementioned is an expected result because, at a higher level of investment, the amounts Z^* are closer to Z . Therefore, it is concluded that the refinement process of the proportions of Z becomes unnecessary at high levels of investment.

On the other hand, the results show that, for this application, the ARx is the model that is closest to the data dynamics (Table VII), managing to reproduce the first moment and the variance of the probability distributions assumed in Table III. This is verified by analyzing the values of the effective errors reported in Fig. 4b, where the ARx proves to be more competitive than the SVM and the GP.

The differences per product regarding the behavior of the effective error for the studied learning models can be explained by analyzing some categories' variances. For example, from Table IV, items 11 and 12 have a high variability concerning the others, *i.e.*, they exhibit a greater range of fluctuation in demand. Note that, in these particular cases, the effective error is significantly higher when compared to products with low variability, as for those belonging to category 1. The above suggests that the prediction models' yields are sensitive to solid changes in demand.

As further work, the proposed method must incorporate other relevant variables, allowing for qualitative and/or quantitative variables to be weighted in order to refine the Z quantities. This is essential, given that, in a competitive environment such as the neighborhood grocery store market, the supply of different products should not be strictly conditioned as being a problem of maximizing the shopkeeper's profits according to the items that yield the highest profit. However, on the contrary, it should consider the client's needs, so that these are incorporated into the strategy for calculating Z^* . On the other hand, it is also important to validate this methodology with different neighborhood stores, as well as to measure the possible impact of the methodology, for it is imperative to build software that allows the shopkeeper to manage it with ease. This information can be valuable to grow the model and thus correlate other variables currently unknown to the method.

6. Acknowledgements

The authors would like to thank Universidad Tecnológica de Pereira and Universidad de Valle for their support during this project.

7. Author Contributions

The study was designed, implemented, and validated by Carlos Alberto Henao Baena. Andrés Felipe Calvo Salcedo supported the experiments. The collaborative efforts of Bibiana Zuluaga Zuluaga and Julián Galeano Castro involved identifying the problem and constructing the database. Edward Jhohan Marín García reviewed and supported the editing process of the paper. It is important to note that all authors have rigorously reviewed the content and have provided their collective consent and approval for the final manuscript.

References

- [1] F. E. Castro and J. A. Oviedo, "Tiendas de barrio a la vanguardia de la competitividad," in *XIX Congreso Internacional AECA*, 2017, pp. 72. ↑3
- [2] E. J. Albarracín and S. C. Erazo, "Influencia de las tecnologías de la información y comunicación en el rendimiento de las micro, pequeñas y medianas empresas Colombianas," *Estudios Gerenciales*, vol. 30, no. 133, pp. 355-364, 2014. <https://doi.org/10.1016/j.estger.2014.06.006> ↑3
- [3] J. M. Caicedo and J. M. Quiceno, "Situación actual de la tienda de barrio frente a la aparición de la nuevas superficies ARA y D1 en la ciudad de Manizales," Undergraduate thesis, Univ. Manizales. Manizales, Caldas, Colombia. [Online]. Available: <https://ridum.umanizales.edu.co/xmlui/handle/20.500.12746/2080> ↑3
- [4] Semana, "El fenómeno D1: la revolución de las tiendas de descuento," 2016. [Online]. Available: <https://www.semana.com/edicion-impresa/caratula/articulo/como-funcionan-las-tiendas-d1/218767/> ↑3

- [5] Portafolio, "Los tenderos no conocen a un competidor directo: la cadena D1," 2016. [Online]. Available: <https://www.portafolio.co/negocios/tenderos-conocen-competidor-directo-cadena-d1-495847> ↑3
- [6] J.M. Paúcar, E. Vargas, "Propuesta de mejora de la gestión de inventarios en una empresa del sector retail," Undergraduate thesis, Univ. Peruana Ciencias Aplicadas, Fac. Ing., Lima, Perú. [Online]. Available: <http://hdl.handle.net/10757/623832> ↑3
- [7] M. Ulrich and H. Jahnke, "Classification-based model selection in retail demand forecasting," *Int. J. Forecast.*, vol. 30, no. 1, pp. 209-223, 2022. <https://doi.org/10.1016/j.ijforecast.2021.05.010> ↑3
- [8] M. Doszyń, "Expert systems in intermittent demand forecasting," *Procedia Comp. Sci.*, vol. 192, pp. 3598-3606, 2021. <https://doi.org/10.1016/j.procs.2021.09.133> ↑3
- [9] F. Tao and Q. Qi, "Data-driven smart manufacturing," *J. Manuf. Syst.*, vol. 48, part C, pp. 157-169, 2018. <https://doi.org/10.1016/j.jmsy.2018.01.006> ↑4
- [10] J. A. Arango and J. A. Giraldo, "Gestión de compras e inventarios a partir de pronósticos Holt-Winters y diferenciación de nivel de servicio por clasificación ABC," *Scientia et Technica*, vol. 18, no. 4, pp. 743-747, Dec. 2013. <https://doi.org/10.22517/23447214.7171> ↑4
- [11] J. E. Montemayor, *Métodos de pronósticos para negocios*, Monterrey, Nuevo León, México: Tecnológico de Monterrey. [Online]. Available: <http://hdl.handle.net/11285/621230> ↑4
- [12] T. Tanizaki and T. Hoshino, "Demand forecasting in restaurants using machine learning and statistical análisis," *Procedia CIRP*, vol. 79, pp. 679-683, 2019. <https://doi.org/10.1016/j.procir.2019.02.042> ↑4
- [13] J. P. Usuga and S. Lamouri, "Trends in machine learning applied to demand & sales forecasting: A review," presented at *International Conference on Information Systems, Logistics and Supply Chain*, Jul. 2018, Lyon, France. [Online]. Available: <https://hal.science/hal-01881362> ↑4
- [14] D. A. Collier and J. R. Evans, *Administración de operaciones*, Boston, MA, USA: Cengage, 2019. ↑4, 5, 7
- [15] T. Boone and R. Ganeshan, "Forecasting sales in the supply chain: Consumer analytics in the Big Data era," *Int. J. Forecast.*, vol. 35, no. 1, pp. 170-180, 2019. <https://doi.org/10.1016/j.ijforecast.2018.09.003> ↑4
- [16] A. Kumar and R. Shankar, "A Big Data driven framework for demand-driven forecasting with effects of marketing-mix variables," *Ind. Marketing Manag.*, vol. 90, pp. 493-507, 2020. <https://doi.org/10.1016/j.indmarman.2019.05.003> ↑4
- [17] S. Chopra, "The evolution of omni-channel retailing and its impact on supply chains," *Transport. Res. Procedia*, vol. 30, pp. 4-13, 2018. <https://doi.org/10.1016/j.trpro.2018.09.002> ↑4
- [18] S. Mou and D.J. Robb, "Retail store operations: Literature review and research directions," *European J. Oper. Res.*, vol. 265, no. 2, pp. 399-422, 2018. <https://doi.org/10.1016/j.ejor.2017.07.003> ↑4
- [19] E. Casado and M. La Civita, "Estimated time of arrival sensitivity to aircraft intent uncertainty," *IFAC-PapersOnLine*, vol. 51, no. 9, pp. 162-167, 2018. <https://doi.org/10.1016/j.ifacol.2018.07.027> ↑4

- [20] M. A. Sellitto and E. Balugani, "Spare parts replacement policy based on chaotic models", *IFAC-PapersOnLine*, vol. 51, no. 11, pp. 945-950, 2018. <https://doi.org/10.1016/j.ifacol.2018.08.486> ↑4
- [21] F. Hamilton and A. Lloyd, "Hybrid modeling and prediction of dynamical systems", *PLoS Comp. Biology*, vol. 13, no. 7, pp. 1-20, 2017. <https://doi.org/10.1371/journal.pcbi.1005655> ↑4
- [22] J. C. Sanclemente, "La reputación del tendero de barrio ante su mercado y sus consecuencias," PhD thesis, Univ. EAFIT, Medellín, Colombia. ↑4
- [23] Servinformación, "Estudio revela que los tenderos barranquilleros madrugan más que los bogotanos", 2019. [Online]. Available: <https://www.colombia.com/actualidad/nacionales/barranquilleros-madrugan-mas-que-los-bogotanos-241787> ↑4
- [24] eSemanal, "Estudio global de la cadena de suministro de retail", 2020. [Online]. Available: <https://esemanal.mx/2020/07/estudio-global-de-la-cadena-de-suministro-de-retail/> ↑4
- [25] El Espectador, "Un estudio comparó las tiendas de barrio de bogotá con las de barranquilla", 2019. [Online]. Available: <https://www.elespectador.com/bogota/un-estudio-comparo-las-tiendas-de-barrio-de-bogota-con-las-de-barranquilla-article-879317/> ↑4
- [26] R. Gaku, "Demand forecasting procedure for short life-cycle products with an actual food processing enterprise," *Int. J. Comp. Intel. Syst.*, vol. 7, no. 2, pp. 85-92, 2014. <https://doi.org/10.1080/18756891.2014.947121> ↑6
- [27] J. E. Hanke and D. W. Wichern, *Pronósticos en los negocios*, 9th ed., Mexico DF, Mexico: Pearson Educación, 2010. ↑6
- [28] P. L. Meyer and C. P. Campos, *Probabilidad y aplicaciones estadísticas*, Mexico DF, Mexico: Fondo Educativo Interamericano, 1973. ↑8
- [29] M.T. Farrell, A. Correa, "Gaussian process regression models for predicting stock trends," *Relation*, vol. 10, pp. 3414-3423. <https://api.semanticscholar.org/CorpusID:16646484> ↑9
- [30] B. Schölkopf and A. J. Smola, *Learning with kernels: Support vector machines, regularization, optimization, and beyond*, Cambridge, MA, USA: MIT press, 2002. ↑9, 10
- [31] C. M. Bishop, *Pattern recognition and machine learning (information science and statistics)*, 1st ed., New York, NY, USA: Springer, 2006. ↑9
- [32] K. S. Shanmugan and A. M. Breipohl, *Random signals: Detection, estimation and data analysis*, Hoboken, NJ, USA: Wiley, 1988. ↑10, 13
- [33] C. E. Rasmussen, "Gaussian processes in machine learning," in *Advanced Lectures on Machine Learning*, O. Bousquet, U. von Luxburg, and G. Rätsch, Eds., Berlin, Heidelberg, Germany: Springer, 2003, pp. 63-71. ↑11
- [34] C. Krzysztof and C. K. Williams, "Empirical evaluation of Gaussian Process approximation algorithms," Master's thesis, S. Informatics, Univ. Edinburgh, 2011. [Online]. Available: <https://homepages.inf.ed.ac.uk/ckiw/postscript/Chalupka2011diss.pdf> ↑13

Carlos Alberto Henao Baena

An accomplished electrical engineer with degrees from Universidad Tecnológica de Pereira (UTP), including a Master's in Electrical Engineering, is currently a distinguished professor within the Electronic Engineering program of UTP. His academic pursuits encompass a broad spectrum, with a keen focus on electronic design, probabilistic models, and machine learning. Through his expertise and research, he contributes significantly to the field, bridging theory and application while advancing the boundaries of electronic engineering.

Email: caralbhenao@utp.edu.co

Bibiana Zuluaga Zuluaga

Holds a degree in Business Administration from Universidad del Quindío, and she has furthered her education with an Electronic Commerce Specialist certification from SENA, as well as a Specialization in Integral Project Management from Universidad Militar Nueva Granada. Additionally, she is certified in PRINCE2 Foundation project management. With four years as an Administrative Coordinator at GPS Logistics and Events, three years as a Specialized Coordinator at Contact Center Bank GNB Sudameris, and over four years as an Instructor at SENA, Bibiana has demonstrated her proficiency in administrative roles, project management, and education. Currently, she is an instructor linked to research processes at SENA Risaralda within the Mercator group.

Email: bzuluagaz@sena.edu.co

Julián Galeano Castro

Is an industrial engineer from Universidad Tecnológica Pereira, specializing in Operations and Logistics Management, and has a Master's in Engineering from Universidad EAFIT. With three years as a Project Coordinator at Innovative Education: Services and Solutions and two years as a Business Logistics Instructor at Servicio Nacional de Aprendizaje (SENA), Julián brings a wealth of experience. He currently serves as an instructor linked to research processes at SENA Risaralda within the Mercator group, showcasing his commitment to education and research.

Email: jugaleano@sena.edu.co

Edward Jhohan Marín García

Holds a solid academic foundation, having earned degrees in Electronic Engineering and Electronic Technology from Universidad del Quindío, alongside a Master's in Electrical Engineering from Universidad Tecnológica de Pereira. With an impressive fifteen-year tenure as a university professor and as the Director of the Center for Eventualities and Equipment Recovery (CERETEC) at Universidad del Quindío, his expertise is substantial. Currently, he serves as a professor at Universidad del Valle. He holds the esteemed position of Director of the Innovation and Development in Applied Electronics Research Group (GIIDEA) at the same institution, underscoring his dedication to education and advancements in the field.

Email: marin.edward@correounivalle.edu.co

Andrés Felipe Calvo Salcedo

An accomplished electronic engineer, holds a master's degree in electrical engineering from the Universidad Tecnológica de Pereira. He excels as a dedicated professor and serves as the Director of the Department of Electronic Engineering at the same institution. He centers his research around machine learning applications in industrial and agronomic sectors, utilizing digital image processing and instrumentation. His work delves into crucial areas such as the automatic detection of manufacturing faults through vector support machines and applying space-frequency descriptors for supervised learning in identifying texture patterns within textile products. These pursuits underscore his commitment to advancing the realms of both academia and practical industry.

Email: afcalvo@utp.edu.co





Research

Estimating Acceleration from a Single Uniform Linear Motion-Blurred Image using Homomorphic Mapping and Machine Learning

Estimación de la aceleración a partir de una única imagen borrosa de movimiento lineal uniforme utilizando el enfoque de mapeo homomórfico y aprendizaje automático

Jimmy Alexander Cortés-Osorio¹  , Juan Bernardo Gómez-Mendoza² , Juan Carlos Riaño-Rojas² 

¹Universidad Tecnológica de Pereira, Pereira, Risaralda, Colombia 

²Universidad Nacional de Colombia sede Manizales. Manizales, Caldas, Colombia 

Abstract

Context: Vision-based measurement (VBM) systems are becoming popular as an affordable and suitable alternative for scientific and engineering applications. When cameras are used as instruments, motion blur usually emerges as a recurrent and undesirable image degradation, which in fact contains kinematic information that is usually dismissed.

Method: This paper introduces an alternative approach to measure relative acceleration from a real invariant uniformly accelerated linear motion-blurred image. This is done by using homomorphic mapping to extract the characteristic Point Spread Function (PSF) of the blurred image, as well as machine learning regression. A total of 125 uniformly accelerated motion-blurred pictures were taken in a light- and distance-controlled environment, at five different accelerations ranging between 0,64 and 2,4 m/s². This study evaluated 19 variants such as tree ensembles, Gaussian processes (GPR), and linear, support vector machine (SVM), and tree regression.

Results: The best RMSE result corresponds to GPR (Matern 5/2), with 0,2547 m/s² and a prediction speed of 530 observations per second (obs/s). Additionally, some novel deep learning methods were used to obtain the best RMSE value (0,4639 m/s² for Inception ResNet v2, with a prediction speed of 11 obs/s).

Conclusions: The proposed method (homomorphic mapping and machine learning) is a valid alternative for calculating acceleration from invariant motion blur in real-time applications when additive noise is not dominant, even surpassing the deep learning techniques evaluated.

Keywords: acceleration, computer vision, deep learning, machine learning, motion blur, vision-based measurement

Article history

Received:
25th/Oct/2022

Modified:
31st/Aug/2023

Accepted:
16th/Nov/2023

Ing., vol. 29, no. 1,
2024. e20057

©The authors;
reproduction right
holder Universidad
Distrital Francisco
José de Caldas.

Open access



*  **Correspondence:** jacoper@utp.edu.co

Resumen

Contexto: Los sistemas de medición basados en visión (VBM) están ganando popularidad como una alternativa asequible y apta para aplicaciones científicas y de ingeniería. Cuando se utilizan cámaras como instrumentos, el desenfoque de movimiento suele surgir como una degradación de imagen recurrente e indeseable, que de hecho contiene información cinemática que normalmente se descarta.

Método: Este artículo introduce un enfoque alternativo para medir la aceleración relativa a partir de una imagen borrosa real de movimiento lineal uniformemente acelerado invariante. Esto se hace utilizando mapeo homomórfico para extraer la *point spread function* (PSF) característica de la imagen borrosa, así como regresión de aprendizaje automático. Se tomaron un total de 125 imágenes borrosas de movimiento uniformemente acelerado en un entorno de luz y distancia controladas, en cinco aceleraciones diferentes en un rango de 0,64 a 2,4 m/s². Este estudio evaluó 19 variantes tales como ensambles de árboles, procesos Gaussianos (GPR) y regresión lineal, regresión con máquina de vectores de soporte (SVM) y regresión con árboles.

Resultados: El mejor resultado de RMSE corresponde a GPR (Matern 5/2), con 0,2547 m/s² y una velocidad de predicción de 530 observaciones por segundo (obs/s). Además, se utilizaron algunos métodos novedosos de aprendizaje profundo para obtener el mejor valor de RMSE (0,4639 m/s² para Inception ResNet v2, con una velocidad de predicción de 11 obs/s).

Conclusiones: El método propuesto (mapeo homomórfico y aprendizaje automático) es una alternativa válida para calcular la aceleración a partir del desenfoque de movimiento invariante en aplicaciones en tiempo real cuando el ruido aditivo no es dominante, incluso superando las técnicas de aprendizaje profundo evaluadas.

Palabras clave: aceleración, visión artificial, aprendizaje profundo, aprendizaje automático, desenfoque de movimiento, medición basada en la visión

Table of contents

	Page		
1. Introduction	3	3. Methodology	14
1.1. Acceleration model for linear motion blur	4	3.1. Rig setup parts	15
1.2. Kinematic quantities using vision-based approaches	6	4. Experimental results	16
1.2.1. Motion blur approaches . .	7	4.1. Instrument calibration	17
1.2.2. Multi-frame approaches . .	8	4.2. Data acquisition results – Machine learning	18
1.3. Works related to machine learning	10	4.3. Data acquisition results – Deep learning	19
1.4. Works related to deep learning . .	10	5. Discussion	20
2. Proposed measurement method	12	6. Conclusions	22
		7. Author Contributions	22
		References	22

1. Introduction

Vision-based measurement (VBM) systems use cameras as an instrument (1). This emerging trend is becoming increasingly popular as an affordable and suitable alternative for many applications such as on-road vehicle detection, tracking, behavior understanding (2), robotics (3), physics (4), biology (5), and engineering (6).

This work introduces a method to calculate acceleration from a real uniformly accelerated motion-blurred image. It uses homomorphic mapping to extract the characteristic point spread function (PSF) of the degraded image, in order to train a machine learning regression model with 125 known instances and responses that finally predicts acceleration as a regression. This approach considers the motion angle to be equal to zero, even though constant acceleration is obtained from an inclined slider. The ground-truth acceleration of each blurred image was measured independently since the sliding camera platform's friction could slightly change the acceleration from measurement to measurement.

Homomorphic filtering is widely used in several applications, as shown in (7, 8), and (9). Although image restoration based on homomorphic filtering is a usual task in image processing, this approach has not been proposed in the literature for acceleration estimation. Homomorphic filtering objectively enhances the image but does not calculate acceleration in the filtering process.

There are two classes of acceleration measurement techniques. The first one involves direct measurements carried out by accelerometers without the need for individual calculations. These accelerometers can be classified based on their operation principle: the piezoelectric effect, the capacitive effect, microelectromechanical systems (MEMS), and the electromechanical servo principle. Some drawbacks of this class are that they are range-fixed, more expensive, and invasive. Direct measurement accelerometers usually need wires that run from the moving target to the analysis system. In some cases, cables can negatively influence the action measured (4). The second class is indirect measurements, where acceleration is estimated from another kinematic variable, using circuits or a computational algorithm.

Kinematic quantities, such as acceleration, are related to the forces that engineering structures can support (10). For instance, some constructions such as floors, footbridges, buildings, and bridges must be continually monitored to evaluate their structural safety (11). Usually, motion sensors need to be connected to a monitoring system, which is often hard to place due to wiring and power issues. Some vision-based displacement measurement systems have been recently developed for structural monitoring because they overcome the already listed issues (6, 12).

Motion, velocity, and acceleration are related to kinematic quantities through time. This means that it is possible to obtain one from another via integration or differentiation. The differential of displacement is called velocity, and the differential of velocity is *acceleration*. Conversely, the integral of acceleration is velocity and, if velocity is integrated, displacement is obtained. In real-world applications, integration is widely used due to its beneficial noise attenuation. Differentiation, on the contrary, amplifies noise.

This makes acceleration more suitable for calculating other kinematic quantities when initial conditions are known. Lastly, it is noteworthy that knowing the instant acceleration provides information about the physical forces applied to moving systems which other quantities cannot supply (13).

Machine learning methods involve mathematical techniques that automatically provide systems with the ability to learn, improve, and predict from training data without being explicitly programmed to do so (14).

Classification and regression are the main tasks of supervised machine learning. The first predicts the specified class to which some input variables belong, and the second one calculates a numerical value within a range that does not necessarily correspond to an exact, previously trained response, as classification indeed does.

The well-known linear regression model assumes a direct relationship between the input variables and the response. Linear regression is the most manageable regression model, as it is effortless to follow and code. Furthermore, it is faster when compared to other approaches. Sensitivity to outliers is one of the drawbacks, which affects its prediction accuracy (15).

In this regard, the Gaussian process regression (GPR) is a Bayesian learning algorithm that has recently gained significant attention due to its usability and accuracy in multivariate regression. GPR considers the joint probability distribution of model outputs to be Gaussian. It shows the predictors as a linear combination of nonlinear basis functions instead of a linear combination of coefficients, as other approaches do (16, 17). Our study also used support vector machines (SVMs) because of their efficiency in multi-variable spaces. Furthermore, they are suitable for regression when the data's dimensionality is greater than the number of instances, which was the case (18). Even though the method's main characteristics are known, we assessed one by one with the PSF data obtained from the extraction.

1.1. Acceleration model for linear motion blur

The PSF plays an essential role in image formation theory. All-optical systems have a characteristic PSF, which intrinsically describes the degradation process of the image during its formation. Therefore, the PSF can include information about kinematic quantities such as motion, velocity, and acceleration over the exposure time.

Its nature can classify blur as optical, mechanical, and medium-induced blur (19). This document only considers the mechanical blur that happens when the objects and the camera that captures the image move during the exposure time of the light sensors (20).

A formulation for the PSF in the presence of accelerated motion (introduced in (21)). Even though this research focused on image formation on light-sensitive emulsion film during exposure, it has been a reference for many modern types of research, given its visionary usability in digital image processing.

This PSF model of linear uniformly accelerated motion is shown in Eq. (1):

$$h(x, y) = \begin{cases} \frac{1}{T(v_0^2 + 2ax)^{\frac{1}{2}}} & 0 \leq |x| \leq L \\ 0 & \text{otherwise} \end{cases} \quad (1)$$

where a , v_0 , x , and T are the values of the uniform acceleration, the initial velocity, the displacement, and the exposure time interval, respectively. Fig. 1a illustrates the PSF for constant velocity, and Fig. 1b does so for constant acceleration. Notice that Eq. (1) becomes Eq. (2) when $a = 0$, which corresponds to a uniform velocity. The product Tv_0 is equal to L , the blur's length. Additionally, the Fourier Transform of both is depicted in Figs. 1c and 1d, respectively. Moreover, note that a constant acceleration causes a smear in the Fourier Transform of the PSF, which complicates parameter extraction.

$$h(x, y) = \begin{cases} \frac{1}{Tv_0} & 0 \leq |x| \leq L \\ 0 & \text{otherwise} \end{cases} \quad (2)$$

We cannot infer where the camera is moving towards using the PSF shown in Eq. (1). When the capture system is moving at a constant velocity, the PSF is symmetrical with respect to the y -axis. It does not provide any clue as to whether the motion is from right to left or from left to right. A particular situation arises when the system is accelerated. When this happens, the initial velocity is different from the final one, so the PSF curve is not symmetrical. There are two cases: if the initial velocity is lower than the final one (positive acceleration), the PSF curve is higher on the left side. On the contrary, when the final velocity is lower than the initial one (negative acceleration), the function is higher on the right. Thus, the PSF does not allow determining the motion's direction.

When the camera is not operating horizontally, the angle of motion can be measured regardless of the velocity and the acceleration if the motion blur is long enough.

In some cases, such as velocity estimation, the PSF height $\frac{1}{Tv_0}$ is not explicitly required. Velocity can be calculated using the blur length L and the exposure time T , although height is also related to the initial velocity (Fig. 1a). On the other hand, acceleration can be calculated using Eq. (3). The blur length L in pixels can be obtained from the inverse Fourier transform of Fig. 1d. However, to estimate the acceleration a , information about the change in velocity $v_f^2 - v_0^2$ is also needed. Although v_0 and v_f are, at first glance, inferable from the PSF (Fig. 1b), they do not correspond to the values obtained, since the extracted PSF is also altered by the exposure time, the brightness, the contrast, the noise, and the image's frequency content, among other aspects.

$$a = k \frac{(v_f^2 - v_0^2)}{2L} \quad (3)$$

Some authors have concluded that uniform acceleration causes less degradation to the image than uniform velocity (22–24). Partly for this reason, it is more difficult to estimate acceleration than velocity from a single motion-blurred image. As an example, Fig. 2 depicts the difference between constant velocity and accelerated motion. Most frequency methods use the zero crossings of the collapsed Fourier transform of the motion-blurred image to estimate the blur length (25–28). The zero crossing

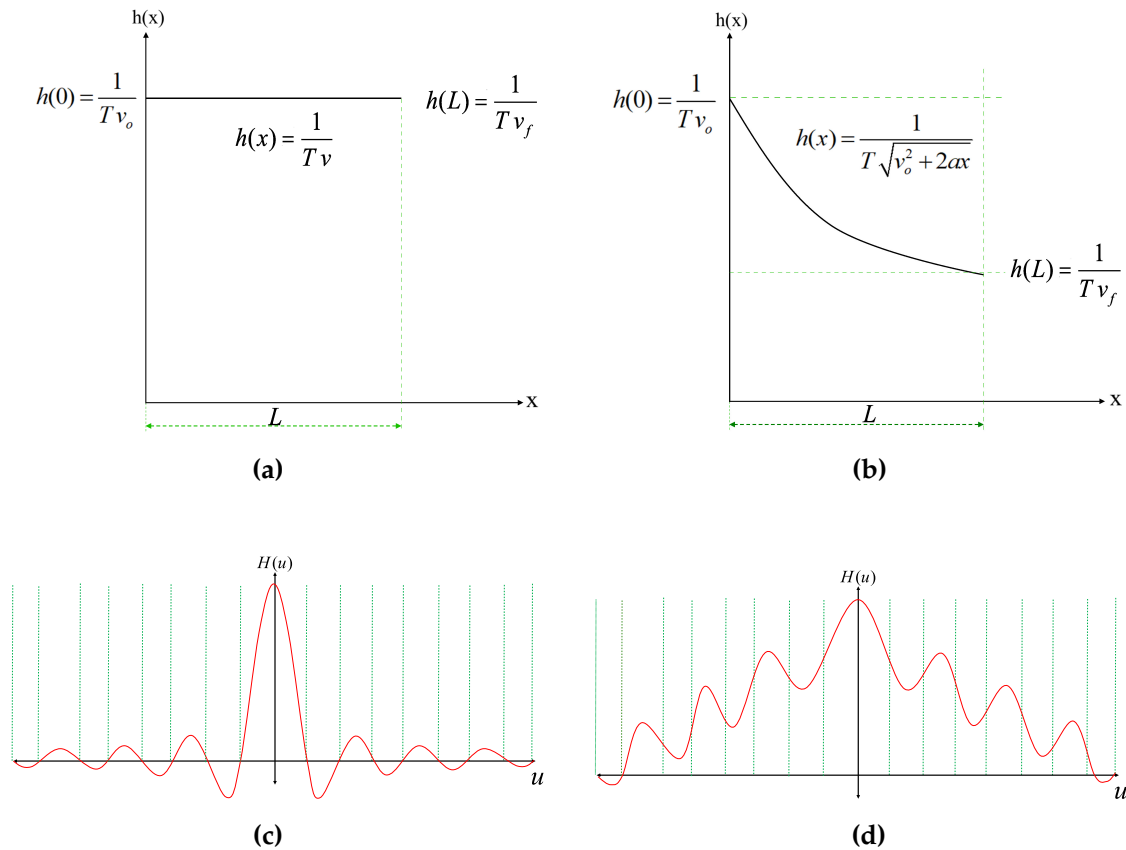


Figure 1. PSF for (a) uniform velocity and (b) uniformly accelerated motion. (c) Fourier transform of the PSF in (a) and (d) Fourier transform of (b). These are only illustrative examples

values are inversely related to the PSF length. When a uniformly accelerated blur degrades the image, its Fourier transform valleys move away from the zero-crossing line axis.

1.2. Kinematic quantities using vision-based approaches

The PSF has an essential role in image formation theory. All-optical systems have a characteristic PSF, which intrinsically describes the degradation process of the image during its formation. Therefore, the PSF can include information about kinematic quantities such as motion, velocity, and acceleration over the exposure time.

Its nature can help to classify blur as optical, mechanical, and medium-induced blur (19). This document only considers the mechanical blur that happens when the objects and the camera capturing the image move during the exposure time of the light sensors (20).

1.2.1. Motion blur approaches

(20) and (29) introduced a way to calculate the speed of vehicles from a single motion-blurred picture, with the aim of supporting transit authorities. Their proposal used the geometry of the scene, the camera parameters, and the blur length. These authors stated that their method's error was less than 10% when applied in real speed detection scenarios.

(30) suggested an approach to measure the speed of a vehicle using motion blur analysis which involves inspecting the speedometer of automotive vehicles. Speed was calculated by analyzing the characteristics and regularities in a single blurred image of a simulated road surface. The authors reported errors of less than 10%. Moreover, there is some research on speed estimation from actual motion-blurred, as is the case of (31, 32), and (33).

(34) used code exposure for the accurate reconstruction of motion-blurred images. They proposed statistical blur calculations to obtain precise motion measurements of constant velocity, constant acceleration, and harmonic rotation in actual pictures. For their experiments, they took pictures of a toy car that slid freely on a tilted track only under the influence of gravity. Alternatively, they generated harmonic rotation by using a pendulum-like system. The authors set the camera at the same angle as the tilted platform in order to make the blur almost horizontal in the captured image. They validated their method by measuring the quality of de-blurred images. These authors only estimated motion because their work was mainly focused on image restoration, which does not require a precise reconstruction of the point spread function to improve the image. Their study was based on (35).

(36, 37), and (38) introduced a method for estimating the velocity of a vehicle using a camera moving in the opposite direction to generate blur. They argued that the inclination of the motion blur pattern line in a single image was inherently linked to the velocity of the vehicle and the modulation speed. They also denoted that the inclination level could be calculated by employing line detection techniques such as the Hough transform or the Gabor filter. They estimated that the absolute velocity error was below 2,13 km/h and concluded that their method was independent of the exposure time. Lastly, they inferred that their proposal could be used for vehicular technology.

(39) introduced a defocus correction procedure to obtain the velocity of particles from a single-frame and single-exposure image (SFSEI). They based their proposal on the changes in focus, size, and shape of particles, both close and distant, captured in a blurred snapshot. This method was confirmed in a free-falling particle experiment.

(40) presented a method to determine the position and calculate the velocity of an object by locating the blur's initial and final position. The researchers noticed that, under constant illumination, the motion's start and end could not be determined. To solve this issue, they used modulated illumination, i.e., red light at the beginning and blue light at the end, in order to tag the blurred image. They reported that their method had not yet been implemented in real conditions.

The work by (42) and (43) introduced a technique to calculate velocity from a single linear motion-blurred picture. The discrete cosine transform was used to extract the PSF of the actual motion-blurred images as a basis to measure the blur extent L and the angle. This was done in combination with the exposure time T .

(44) proposed a novel approach involving adversarial blur attack against visual object tracking algorithms. Rather than adding imperceptible noise, they actively synthesized natural motion blur on video frames in order to mislead state-of-the-art trackers. The attack was performed by tuning two sets of parameters controlling the motion pattern and light accumulation process that generate realistic motion blur. An optimization-based attack iteratively solved an adversarial objective function to find the blurring parameters. A one-step attack predicted the parameters using a trained neural network. Experiments on four tracking benchmarks demonstrated significant performance drops for multiple trackers, showing the threat of adversarial motion blur. The key contributions of this work were introducing adversarial motion blur as a new attack angle and designing optimization and learning-based approaches to craft natural adversarial examples. The limitations included heavy computation loads for the optimization attack and reliance on a specific tracker for training examples. All methods proposed by the authors used video frame sequences instead of a single image, and this attack revealed the brittleness of trackers against common video corruptions, thus motivating the development of robust motion-blur algorithms.

1.2.2. Multi-frame approaches

(45) introduced a cell segmentation and competitive survival model (CSS) together with the traditional methods of particle image velocimetry (PIV). They used their algorithm with actual and artificial pictures and made comparisons with other strategies.

(3) presented a system to estimate the position, velocity, and acceleration of a planar moving robot using a calibrated digital black-and-white camera and light emission diodes as markers. They employed a multi-frame approach that made use of the Kalman filter to calculate velocity and acceleration. These authors stated that the blur motion should be limited, so that the exposure time was short when compared to the change in the position of the light markers. They concluded that their video approach method is accurate, but they suggested that using a faster CCD sensor would yield better results.

(4) suggested an acceleration measurement approach using various synchronized video cameras based on videogrammetric reconstructions. Their method located the centroid of visible marks set by the researchers on a shaft run by a shaker. They built a prototype to carry out the proof of concept. They also attached some calibrated accelerometers directly below the target marks in order to obtain ground-truth data to compare with their results. They calculated the second derivative of the videogrammetric position data using the seven-point numerical algorithm to estimate the acceleration. Finally, they provided some overlapped plots aimed at contrasting their results to the accelerometer's measurements. They concluded that their results were similar to those obtained using accelerometers. No error was explicitly calculated.

(13) proposed a variational method to estimate the acceleration of dynamic systems based on image sequences. They stated that their approach went further than the traditional optical flow methods because they can calculate acceleration. They also pointed out that fluid flow images for calculating acceleration have not been thoroughly studied, even though they are of significant interest. They suggested the use of acceleration fields and an energy function for their calculations, relying on space-time constraints. When they confronted their results to ground-truth data, they estimated a 7% average relative error.

Moreover, (46) described a non-invasive method to estimate the pressure distribution in a flow field while employing PIV.

(47) proposed an approach to measure the speed of a rotating item. They used a pair of cameras to capture a temporal sequence of pictures from coded targets (CTs), which were set on the rotating surface of the object to work as visual marks. This feature matching-based algorithm depends on the motion estimation of contiguous target image pairs. In their experiments, the authors used a rotating fan at 120 rpm and a convolutional neural network (CNN) to identify changes in the position of the CTs during the exposure time. Even though they did not explicitly calculate the speed of the blades, they concluded that their method benefits high-speed object measurement applications. This technique used multiple consecutive images to calculate speed and acceleration.

(48) introduced a computationally efficient computer vision method to estimate the trunk's flexion angle, angular speed, and angular acceleration during lifting by extracting simple bounding box features from video frames. Regression models estimated trunk kinematics from these features. The advantages of this approach are computational efficiency, non-intrusiveness, and the potential for practical lifting assessments in the workplace, and its limitations include reliance on simulated training data and lower precision than motion capture methods. This study demonstrated the feasibility of using simple video features to estimate biomechanical quantities related to injury risk, allowing for automated ergonomic evaluation over extended periods.

In their review, (49) covered deep learning methods for the estimation of fluid velocity fields, including fluid motion estimation from particle images and velocity field super-resolution reconstruction. Supervised and unsupervised convolutional neural network approaches have shown excellent performance in estimating fluid motion from particle image pairs. GAN and physics-informed neural network methods have also shown potential for the high-resolution reconstruction of velocity fields. The key advantage of deep learning is the ability to learn feature representations directly from data, thus surpassing traditional methods. Limitations included the need for extensive training datasets and difficulties in incorporating physical knowledge. All reviewed methods used video sequences or image pairs for estimation. Overall, this review demonstrated that computer vision and deep learning hold great potential for estimating kinematic quantities in fluid flow and human biomechanics applications, with anticipated growth in the future integration of these methods.

Further reading about PIV acceleration measurement can be found in (50) and (51), and other multi-frame video strategies for velocity are shown in (52,53), and (54).

1.3. Works related to machine learning

(55) used support vector machines (SVM) regression to forecast water flow velocity. Even though they asserted that their approach was not fully successful – as expected –, it was promising and useful for future research.

(56) suggested a method for estimating the velocity profile of small streams by using robust machine learning algorithms such as artificial neural networks (ANNs), SVMs, and k-nearest neighbor algorithms (k-NN), with the latter outperforming the others in the results.

(57) introduced a machine learning approach based on a CNN model to estimate velocity fields using PIV with missing regions. These authors also argued that, despite recent advances, no studies have focused on machine learning applications using this approach. They used artificial images generated with a direct numerical simulation, concluding that it is possible to estimate the velocity fields with less than 10 % error.

The work by (58) should be highlighted, as they suggested a method to assess structural damage by estimating acceleration at multiple points via a traditional sensor approach. Alternatively, they interpreted the results using the supervised machine learning algorithm called *random forest*.

As mentioned above, some remarkable studies have been carried out to estimate velocity and acceleration from multi-frame and multi-camera methods. However, we did not find any strategy based on motion-blurred images for measuring acceleration.

1.4. Works related to deep learning

Deep learning is a technique derived from neural networks that has recently supported instrumentation and measurement. In the scientific literature, it can already be found in combination with traditional instrumentation, such as light detection and ranging (LiDAR) (59), radars (60), and PIV (61,62), in order to estimate the velocity of objects and particles. However, we found no evidence of similar works using deep learning and a single motion-blurred image.

Estimating kinematic quantities from a single image is a challenging yet potentially beneficial issue. A moving system, such as a vehicle, a robot, or a drone, can use motion-blurred images to estimate these parameters without the need for bulkier, heavier, and more expensive devices. Moreover, processing one image is often easier than processing a video sequence.

The contributions of this study are as follows:

- The construction and metrological calibration of an electromechanical incline slider to generate different acceleration values.

- The development of a dataset with 125 invariant, uniformly accelerated motion-blurred images in a controlled environment.
- The comparison of some machine learning techniques against deep learning for acceleration estimation.

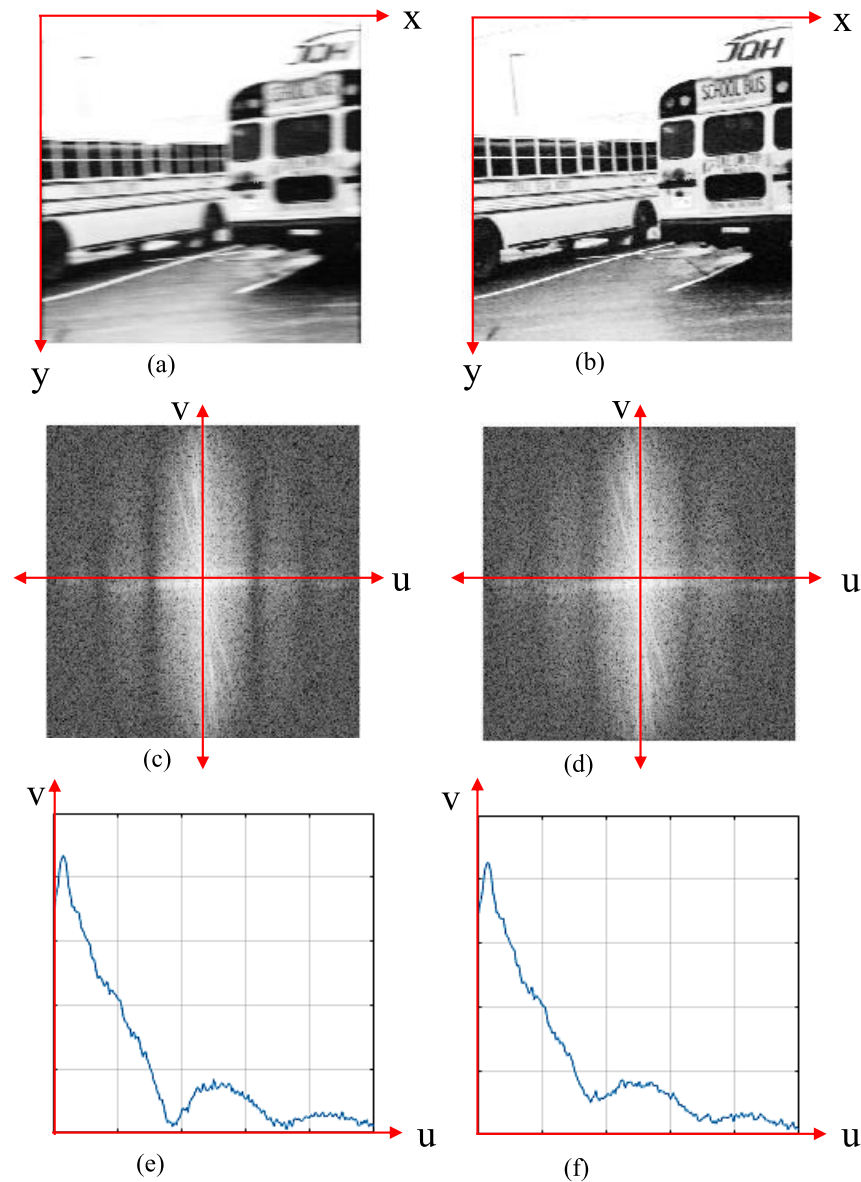


Figure 2. Differences between a degraded image with a uniform and a uniformly accelerated motion blur. (a) Invariant motion-blurred image related to constant velocity. Here, the blur is more visible to the naked eye. (b) Invariant motion-blurred image related to constant acceleration. Here, the blur is lower. (c) Modulation transfer function of (a). (d) Modulation transfer function of (b). (e) Collapsed MTF on the u -axis of (c). (f) Collapsed MTF on the u -axis of (d)

- A proposal for the estimation of acceleration from a real single invariant, uniformly accelerated motion-blurred image.

The remainder of this paper is organized as follows. Section 2 introduces our proposal for acceleration estimation using machine learning and the PSF as a source of characteristic feature patterns. Section 3 presents the experimental setup and the testing carried out. Section 4 outlines the results obtained in the experiments by comparing different regression approaches (including deep learning) and their metrics. Section 4 contrasts the results with those of previous authors and discusses the limitations and benefits of the method. Finally, Section 5 presents the conclusions of this work.

This paper is a product of and reuses, with due authorization, content from the PhD thesis and research project entitled “*A contribution to the estimation of kinematic quantities from linear motion-blurred images*” cited in (43).

2. Proposed measurement method

An image system is modeled as the convolution of the PSF with the blur-free image. This does not allow for the use of linear filtering approaches to extract the PSF. Alternatively, homomorphic filtering uses nonlinearity transformations, such as logarithmic transformations, to map convolution into a separable linear additive domain (63–66). As a theoretical basis, this research used the homomorphic filtering principle to extract the PSF.

Consider that $g(x, y)$ corresponds to the degraded blur image, $i(x, y)$ is the blur-free image, and $h(x, y)$ represents the degradation kernel (PSF). If noise of any kind is not added and the blur system, it is considered to be linear and stationary, and the process can be described as seen in Eq. (4):

$$g(x, y) = i(x, y) * h(x, y) \quad (4)$$

The product $*$ denotes convolution in two dimensions. Additionally, the image convolution from (4) can be also represented as an integral, as shown in Eq. (5):

$$i(x, y) * h(x, y) = \int_{-\infty}^{+\infty} \int_{-\infty}^{+\infty} i(x', y') h(x - x', y - y') dx' dy' \quad (5)$$

Considering that Eq (5) deals with finite blur images in space, it is defined in the intervals $x_2 \leq x' \leq x_1$ and $y_2 \leq y' \leq y_1$. It should be noted that the convolution interval must be larger than the PSF interval of the blur.

Now, the discrete Fourier transform (DFT) is applied to both sides of Eq. (4) to obtain Eq. (6), which represents a point-wise multiplication in frequency domain instead of a convolution in space.

$$G(u, v) = I(u, v)H(u, v) \quad (6)$$

$G(u, v)$, as shown in (6), is a complex value, so it can also be written in polar coordinates using magnitude and angle, as shown in Eq. (7).

$$|G(u, v)|e^{j\phi_G} = |I(u, v)|e^{j\phi_I} |H(u, v)|e^{j\phi_H} \quad (7)$$

This relation can be split into magnitude and phase components, as shown in Eqs. (8) (10), respectively.

$$|G(u, v)| = |I(u, v)||H(u, v)| \quad (8)$$

$$\begin{aligned} \phi_G &= \text{ang}[I(u, v) + H(u, v)] \\ \log |G(u, v)| &= \log |I(u, v)H(u, v)| \end{aligned} \quad (9)$$

Only the log magnitude portion of the complex logarithm of the DFT is used, as shown in Eq. (10).

$$\log |G(u, v)| = \log |I(u, v)| + \log |H(u, v)| \quad (10)$$

Although some images can be very different in space, their average frequency is usually very much alike and almost indistinguishable to the naked eye. This allows using the average of Q hypothetical blur-free images $I(u, v)_k$ to estimate the prototype clear blur-free image $P(u, v)$ in frequency, as shown in Eq. (11) (65).

$$P(u, v) = \frac{1}{Q} \sum_{k=1}^Q I(u, v)_k \quad (11)$$

in such a way that

$$\log |I(u, v)| \cong \log |P(u, v)| \quad (12)$$

$$\log [I(u, v)] \cong \frac{1}{Q} \sum_{k=1}^Q \log |I(u, v)_k| \quad (13)$$

Replacing Eq. (13) into Eq. (10), and then solving for $|H(u, v)|$,

$$|H(u, v)| \cong \exp \left[\log |G(u, v)| - \frac{1}{Q} \sum_{k=1}^Q \log |I(u, v)_k| \right] \quad (14)$$

where $|H(u, v)|$ is the modulation transfer function (MTF) of an arbitrary blur, which can be estimated without knowledge of the actual blur-free image using a set of Q reference images to generate a prototype-average log spectrum.

Even though the classical approach for the PSF estimation of an image suggests using statistically close images to generate the prototype average log spectrum, this study used 5 still background images as the clear image in order to estimate the MTF only once for all the experiments. $Q = 5$ was recommended in (65). Subsequently, the inverse Fourier transform ($iDFT$) of $H(u, v)$ is applied to obtain $h(x, y)$, the PSF, as seen in Eq. (15).

$$h(x, y) = iDFT(H(u, v)) \quad (15)$$

Fig. 3 presents the proposed method for acceleration estimation using homomorphic filtering and machine learning regression. In this method, five blur-free images $i(x, y)_k$ are taken to the unchangeable background with the camera at rest. This helps reduce the additive noise, subtracting the average of a set of hypothetical blur-free images. Consequently, the MTF is obtained for each of the five images and then averaged, added, and divided by five. This yields a prototype blur-free background $\log |P|$,

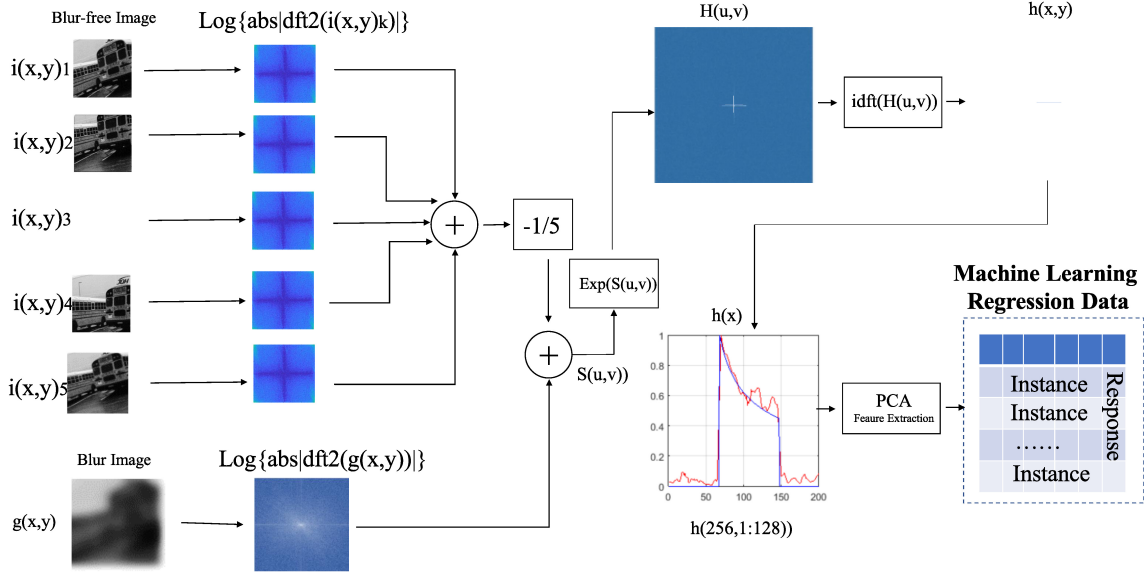


Figure 3. Diagram depicting the process followed to estimate acceleration using homomorphic filtering while applying machine learning. Some blur-free images of the background are needed to separate the PSF for training

which is subtracted from the MTF of the motion-blurred image $\log |G(u, v)|$ to obtain the output $s(u, v)$. Afterwards, the exponential function is used to remove the logarithm. This allows obtaining the optical Fourier transform $H(u, v)$ of the blurred image, which leads to the PSF $h(x, y)$ in two dimensions via the inverse Fourier transform. As the motion occurs only in the horizontal axis, the actual PSF in one dimension $h(x)$ can be extracted from the central horizontal line of the PSF $h(x, y)$.

Therefore, this research took only the central horizontal row of the inverse Fourier transform, yielding a one-dimension vector containing the characteristic PSF.

If the motion is not horizontal, the one-dimension PSF can also be extracted, but the angle of rotation of the line must be estimated and then rotated. This angle can be calculated using the Radon transform, the Hough transform (42), or principal components analysis (PCA).

Before training, the instances are space-reduced to avoid redundancy using PCA. Finally, a set of uniformly accelerated motion-blurred images with a known acceleration is used for training.

3. Methodology

The experiments presented in this section were carried out to measure constant acceleration from a linear motion-blurred image by using homomorphic filtering to extract the PSF and machine learning to predict the actual response. First, all parts of the rig setup are introduced, with the purpose of providing a more detailed description of the procedure. Then, an overview of the aforementioned machine learning

and deep learning methods is presented, and, finally, the evaluation metrics are described regarding the regression methods evaluated.

3.1. Rig setup parts

This section shows the materials and the laboratory equipment needed for the experiments, some of which were specifically constructed within the framework of this study.

Slider

A 185-cm-long aluminum slider constructed for previous speed experiments was used (42), which was slightly modified for our study. Fig. 5 shows the physical layout parts modeled in order to validate the proposed method. Five preset posters were used as a background scene (Fig. 4). Additionally, the camera was placed in parallel to and 171 cm away from the rig. An inclinometer was also installed on the camera. A constant acceleration was achieved by raising an end of the platform to one of the five possible preset angles (A1, A2, A4, A5, and A7) listed in Table I. Sliding occurred evenly and only under the force of gravity. Fig. 6 presents the rig setup used to carry out the experiments. More information about its construction and calibration can be found in (67).

Image analysis system

Motion-blurred image capture and processing were performed on a 64-bit desktop computer with a Core I3 processor and 2GB RAM. Additionally, a 64-bit laptop computer with an AMD A3 processor and 2GB RAM was used for analyzing the acceleration data from the controller system. Both computers used Windows 7 and were running MATLAB 2017b.

Images

Our experiments were carried out in a controlled environment. A scientific digital camera (Basler acA2000-165um USB 3.0) (68) was used to take the pictures. In addition, the artificial white light from the led panel lamps was about 255 Lux, the distance to pattern poster was set at 171 cm, the maximum exposure time of the camera was 100 ms, the slider acceleration was between 0,6 and 2,40 m/s², and the aperture of the lens diaphragm (69) was F/4.

Blurred images of five different pattern posters were taken (Fig. 4). Afterwards, the captured digital images were clipped and converted to grayscale (70). These experiments considered the angle of motion at zero degrees. Although the camera slid on an inclined plane, the motion blur was horizontal with respect to the camera angle. The background scene posters were not rotated, so, at the naked eye, they looked crooked. Fig. 5 shows each of the elements described.

PCA feature extraction

Feature extraction is a relevant topic in signal processing, mostly due to the high dimensionality of data and their redundancy (71). PCA is a classical and widely accepted statistical approach for feature

extraction in pattern recognition and computer vision (72). In this study, PCA feature extraction was used to reduce redundant data from the extracted PSF. The multidimensional space was transformed from 125 to 76 characteristics.

Machine learning regression

Five different approaches were used to predict the acceleration from the PSF data of actual motion-blurred images. Tree ensembles, Gaussian processes (GPR), and linear, SVM, and tree regression and their variations were evaluated, as presented in Table II.

Regression model assessment

The metrics applied to assess the regressions were the root mean square error (RMSE), the prediction speed in observations per second, and the training time in seconds.

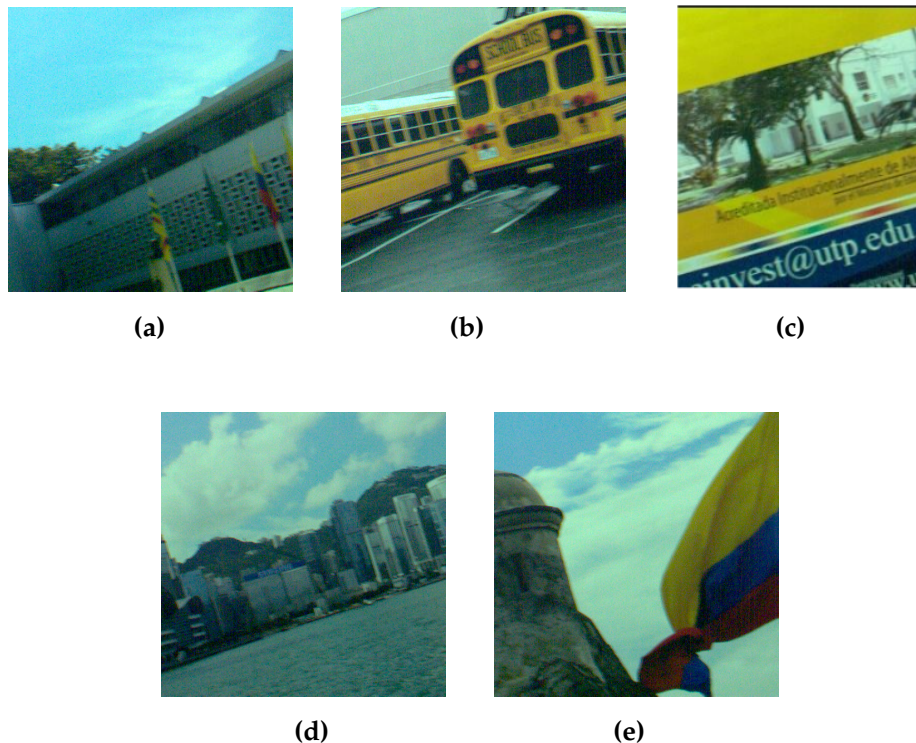


Figure 4. Color version of some accelerated motion-blurred images. The degradation is almost imperceptible by visual inspection

4. Experimental results

Five pictures were taken at each of the five preset accelerations. Additionally, five background scene posters were used, for a total of 125 motion-blurred images.

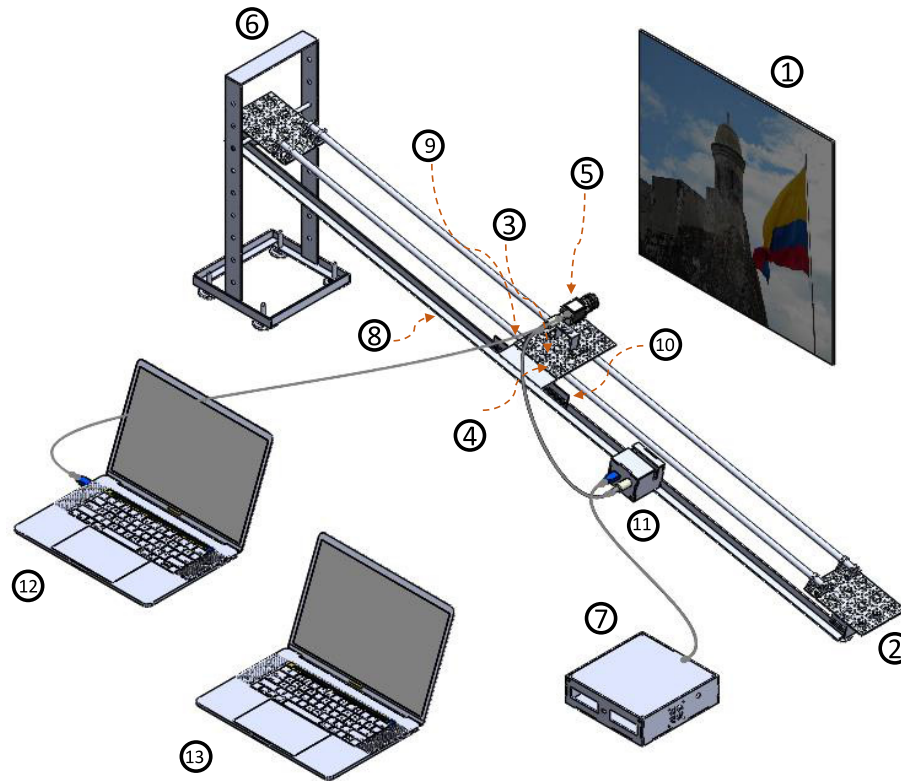


Figure 5. Setup parts and their location. Background pattern poster (1), leveling rubber feet (2), digital pitch gauge-inclinometer (3), camera sliding carriage platform (4), camera (5), lifting base (6), controller (7), oiled stainless steel rods (8), low-friction linear bearings (9), laser-cut toothed steel sheet (10), camera trigger (11), image capture computer (12), and data analysis computer (13)

Although the acceleration values were almost always the same as in Table I, the error was estimated individually using the electromechanical instrument and our vision-based acceleration values.

4.1. Instrument calibration

The uniformly accelerated motion system involved an Arduino Nano microcontroller, which was responsible for measuring the time it took to block each tooth of the steel sheet. Its operation consisted of allowing the camera carriage platform on the steel rods to slide at five different angles, yielding different accelerations depending on the height. The angles and their accelerations are shown in Table I.

Calibration was performed by measuring the acceleration with both the controller system and the Phywe Cobra4 Sensor-Unit 3D-Acceleration standard instrument (± 2 g and a resolution of 0,001 g), using the Cobra4 wireless link to transmit the acceleration data (73). The combined uncertainty and the sensitivity coefficients were evaluated to estimate the total expanded uncertainty according to guidelines regarding the expression of uncertainty in measurement (74,75). See (67) for more detailed information about the calibration process.



Figure 6. Rig setup to generate uniformly accelerated motion-blurred images

Table I. Acceleration values and uncertainties obtained from the calibration procedure

Index	Angle (Degree)	Acceleration (m/s^2)
A0	15°	$2,4630 \pm 0,0285$
A1	13,3°	$2,1782 \pm 0,0233$
A2	10,1°	$1,5416 \pm 0,0161$
A3	7,9°	$1,2292 \pm 0,0130$
A4	4,5°	$0,6448 \pm 0,0074$

4.2. Data acquisition results – Machine learning

Five folds were used to validate all of the proposed regression models. Table II shows the results for the basic regression models and their variants. Note that, even though only five major approaches were assessed, each one had a subset of variants, for a total of 19. The best RMSE results were reported by GPR (Matern 5/2), linear regression, and SVM (quadratic) regression, with 0,2547, 0,2553, and 0,2843 m/s^2 , respectively. GPR (Matern 5/2), linear regression, and SVM (quadratic) regression reported values of 530, 470, and 540 obs/s, respectively. Finally, the fastest training time corresponded to GPR (Matern 5/2), with 1,373 s. See Table II for more details.

Moreover, predicted *vs.* actual and residuals plots were employed for the best three RMSE results. The residuals plots for GPR (Matern 5/2), linear regression, and SVM (quadratic) regression (Figs. 8a, 8b, and 8c, respectively) showed that the acceleration residuals tend to change their sign from negative to positive when the acceleration is higher than 1,4 m/s^2 . Furthermore, the acceleration residuals are smaller in all cases when the acceleration is higher than 1,0 m/s^2 . This makes GPR (Matern 5/2) more

suitable for real-time applications. In summary, the plots for GPR (Fig. 8a) and linear regression (Fig. 7) are almost identical.

As expected, decision trees showed the worst results since they tend to fail when training data is limited.

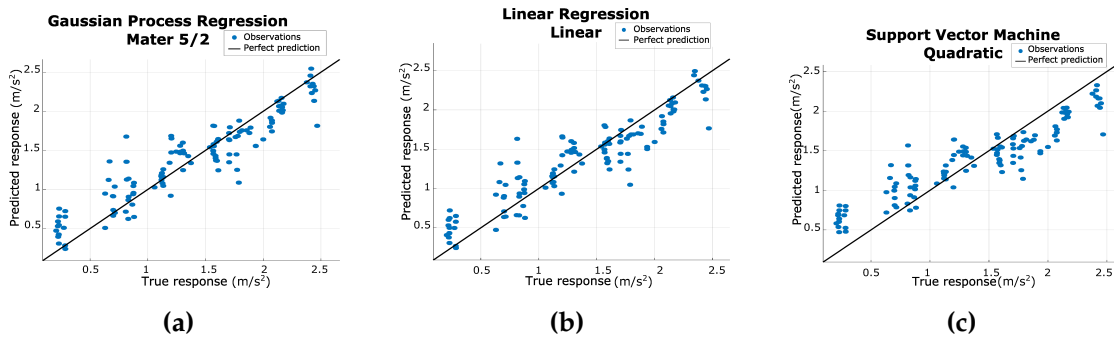


Figure 7. Predicted vs. actual plots for (a) Matern 5/2 regression, (b) Linear regression, and (c) SVM regression

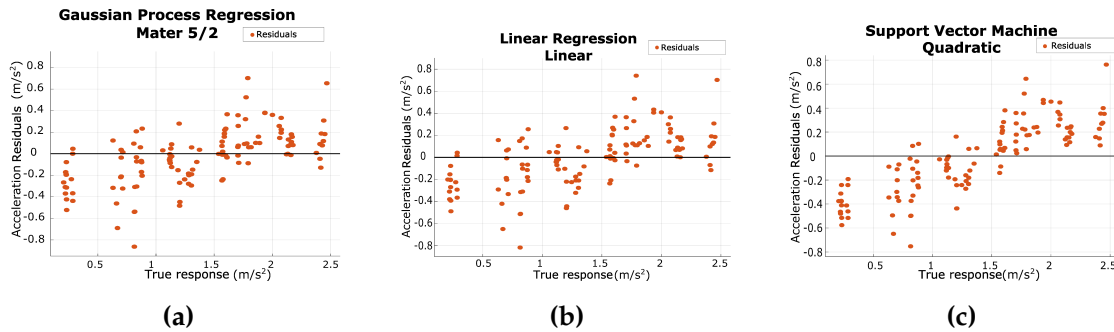


Figure 8. Residual plots for (a) Matern 5/2 regression, (b) linear regression, and (c) SVM regression

4.3. Data acquisition results – Deep learning

Deep learning techniques have some advantages, such as the automatic extraction of features. In addition, input images can be used without any prior processing beyond the geometric transformations of the training images when expanding the dataset becomes necessary. Therefore, in this part of the experimentation process, homomorphic mapping was not used as a source of features for the regression.

The executed algorithms were coded in MATLAB R2020b, using the Deep Network Designer toolbox. It is crucial to emphasize that the learning algorithm corresponds to a regression instead of a classification process, which allows generating response values outside the training data.

As mentioned earlier, 125 training images were used, which were $512 \times 512 \times 3$ pixels in size. However, the pre-trained networks required different dimensions. Therefore, the pixel size of the images was set at $224 \times 224 \times 3$ for GoogleNet and VGG-16, at $227 \times 270 \times 3$ for AlexNet, and at $299 \times 299 \times 3$ for Inception ResNet-v2.

The performance of a CNN depends mainly on hyperparameters such as the learning rate, the mini-batch size, the number of epochs, the number of iterations, and the solver algorithm. For a good performance, a determining factor is the pre-trained model, which typically uses hundreds or thousands of images. Therefore, in our study, it was necessary to extend the image dataset by performing rotations and reflections to obtain 750 images. The image size scale was not changed, as it implicitly includes the blur length attributes.

The dataset was divided as follows: 80 % for training, 10 % for validation, and 10 % for testing. Thus, the 750 images were divided into 600 training images, 75 validation images, and 75 testing images. All of them were randomly selected from the dataset.

As can be seen in Table III, AlexNet offered the shortest training and prediction times while using the GTX1650 and the GTX1050 GPUs. Regarding the RMSE, the lowest value ($0,4639 \text{ m/s}^2$) was obtained using Inception ResNet v2. However, this is far from what was achieved using homomorphic mapping, which showed a smaller RMSE ($0,2547 \text{ m/s}^2$).

It should be noted that only GPUs were used with the deep learning algorithms and CPUs with the machine learning algorithms.

5. Discussion

Even though there are some studies on estimating speed using vision-based measurement (VBM), to the best of our knowledge, only a few deal with acceleration. Likewise, there is no evidence of studies that estimate acceleration from a motion-blurred image.

Some approaches have been introduced to measure acceleration, and all of them require at least two consecutive frames (45, 46, 76), while others also use high-speed or multiple cameras (4, 77), thus making make classical approaches more expensive and bulkier.

This field of research has great potential across various applications, including forensic sciences, particle physics, and autonomous drones. The proposed technique can extract essential motion parameters from a single image, simplifying processes that traditionally rely on multiple video frames or complex sensor configurations. Consequently, it reduces the complexities associated with runtime and computation, resulting in substantial savings regarding storage space and energy consumption. This efficiency makes it an environmentally sustainable and cost-effective approach, underscoring its importance.

The acquisition of blurred images relies on the adjustment of camera settings, particularly the exposure time relative to the scene's motion. While creating motion blur is relatively straightforward in general photography, achieving controlled motion blur in scientific or forensic contexts often requires specific conditions. Moreover, analyzing the variables, conditions, or parameters involved in obtaining motion blur becomes more intricate when the subject or object in motion is not the camera itself. In such scenarios, both the camera and the subject's movements affect the resulting blur, necessitating the application of specialized methodologies. The attributes of a camera employed to capture motion blur data are not rigidly prescribed, but several critical features contribute to its effectiveness. These encompass adjustable exposure settings, sensor sensitivity, image stabilization capabilities, and the camera's lens and sensor quality. These attributes significantly influence the quality and reliability of the analysis. Consequently, the selected camera and its settings emerge as a pivotal consideration, with a substantial influence over the outcomes of motion blur analysis in diverse applications.

Table II. Machine learning results obtained using tree ensembles, GPR, and linear, SVM, and tree regression

Regression models	Variant	RMSE (m/s ²)	Prediction Speed (Obs/s)	Training Time (s)
Ensembles of trees	Bagged trees	0,4124	420	1,7598
	Boosted trees	0,3507	480	1,8514
GPR	Exponential	0,3187	460	1,4044
	Matern 5/2	0,2547	530	1,373
	Rational	0,2553	530	1,6424
	Quadratic squared exponential	0,2553	470	1,5473
SVM	Linear	0,2553	470	1,5175
	Coarse	0,6607	510	1,0678
	Gaussian fine	0,4611	480	1,0486
	Gaussian medium	0,5243	500	1,0921
	Gaussian linear	0,3747	500	1,0779
	Quadratic	0,2843	540	1,804
Trees	Coarse tree	0,6327	570	0,9837
	Fine tree	0,4915	540	1,0379
	Medium tree	0,4604	540	1,0037

This alternative blur-based method has benefits. Motion blur is a usual and undesirable degradation, but it is possible to take advantage of it, as it allows for acceleration estimations. In addition, this approach can be implemented with low-cost cameras, instead of high-speed multi-frame video equipment, which is more expensive.

Likewise, the proposed method has some limitations. One is that it needs a set of blur-free images as reference for training. However, in some cases, this is easy to obtain from the background. For example, a drone can obtain the prototype images from an initial image (a prototype with no motion blur) of a crop and then fly over it while estimating the acceleration. Noise is another limitation of this proposal: when the noise is dominant, the extraction of the PSF can fail along with the estimation. Finally, the

Table III. Deep learning results for AlexNet, GoogleNet, VGG-16, and inception ResNet v2

Regression models	Variant	RMSE (m/s ²)	Prediction speed (Obs/s)	Training time (s)
AlexNet	GTX 1050	0,8088	74	125
	GTX 1650	0,6585	52	95
GooleNet	GTX 1050	0,5918	44	667
	GTX 1650	0,6112	43	432
VGG-16	GTX 1050	0,7334	4	1.655
	GTX 1650	0,6377	21	755
Inception	GTX 1050	3,0234	13	8.229
ResNet v2	GTX 1650	0,4639	11	5.582

space-invariant model introduced in this study assumes that the exposure time is relatively short, and the length from the rig setup to the camera is fixed to ensure invariant blur on all images.

6. Conclusions

With some degree of accuracy, the machine learning models successfully estimate relative acceleration from a single motion-blurred image, using homomorphic filtering to extract the features of the PSF, which depends on the initial velocity, the acceleration, and the exposure time, as shown in Eq. (1).

The proposed method is a valid alternative to estimate acceleration with invariant motion blur. The best machine learning methods were GPR (Matern 5/2) and linear regression, with RMSE values of 0,2547 and 0,2553 m/s², respectively. These methods were able to perform 530 and 470 obs/s, respectively. Finally, the best results were obtained when the acceleration was above 1,0 m/s². This makes machine learning an alternative approach that can be used in real-time applications for estimating acceleration when motion blur is invariant, and noise is not dominant.

7. Author Contributions

All authors contributed equally to the research.

References

- [1] S. Shirmohammadi and A. Ferrero, "Camera as the instrument: the rising trend of vision based measurement," *IEEE Instrumentation Measurement Magazine*, vol. 17, no. 3, pp. 41–47, 2014. <https://doi.org/10.1109/MIM.2014.6825388> ↑3
- [2] S. S. Beauchemin, M. A. Bauer, T. Kowsari, and J. Cho, "Portable and scalable vision-based vehicular instrumentation for the analysis of driver intentionality," *IEEE Transactions on Instrumentation and*

- Measurement*, vol. 61, no. 2, pp. 391–401, 2012. <https://doi.org/10.1109/TIM.2011.2164854> ↑3
- [3] P. Dutkiewicz, M. Kielczewski, K. Kozłowski, and D. Pazderski, “Vision localization system for mobile robot with velocities and acceleration estimator,” *Bulletin of the Polish Academy of Sciences: Technical Sciences*, vol. 58, no. 1, pp. 29–41, 2010. <https://doi.org/10.2478/v10175-010-0003-9> ↑3,8
- [4] J. Leifer, B. Weems, S. C. Kienle, and A. M. Sims, “Three-dimensional acceleration measurement using videogrammetry tracking data,” *Experimental Mechanics*, vol. 51, no. 2, pp. 199–217, 2011. <https://doi.org/10.1007/s11340-010-9352-4> ↑3,8,20
- [5] F. Karimirad, S. Chauhan, and B. Shirinzadeh, “Vision-based force measurement using neural networks for biological cell microinjection,” *Journal of Biomechanics*, vol. 47, no. 5, pp. 1157–1163, 2014. <https://doi.org/10.1016/j.jbiomech.2013.12.007> ↑3
- [6] Y. Fukuda, M. Q. Feng, and M. Shinozuka, “Cost-effective vision-based system for monitoring dynamic response of civil engineering structures,” *Structural Control and Health Monitoring*, vol. 17, no. 8, pp. 918–936, 2010. <https://doi.org/10.1002/stc.360> ↑3
- [7] S. Benameur, M. Mignotte, and F. Lavoie, “An homomorphic filtering and expectation maximization approach for the point spread function estimation in ultrasound imaging,” in *Image Processing: Algorithms and Systems X; and Parallel Processing for Imaging Applications II*, International Society for Optics and Photonics, vol. 8295, 2012, 82950T. <https://doi.org/10.1117/12.903785> ↑3
- [8] O. Mattausch and O. Goksel, “Image-based psf estimation for ultrasound training simulation,” in *International Workshop on Simulation and Synthesis in Medical Imaging*, Springer, 2016, pp. 23–33. https://doi.org/10.1007/978-3-319-46630-9_3 ↑3
- [9] A. P. Janwale and S. S. Lomte, “Enhancement of cotton leaves images using various filtering techniques,” in *Data Management, Analytics and Innovation (ICDMAI), 2017 International Conference on*, IEEE, 2017, pp. 303–305. <https://doi.org/10.1109/ICDMAI.2017.8073530> ↑3
- [10] J. Kim, K. Kim, and H. Sohn, “Autonomous dynamic displacement estimation from data fusion of acceleration and intermittent displacement measurements,” *Mechanical Systems and Signal Processing*, vol. 42, no. 1-2, pp. 194–205, 2014. <https://doi.org/10.1016/j.ymsp.2013.09.014> ↑3
- [11] F. Zheng, L. Shao, V. Racic, and J. Brownjohn, “Measuring human-induced vibrations of civil engineering structures via vision-based motion tracking,” *Measurement*, vol. 83, pp. 44–56, 2016. <https://doi.org/10.1016/j.measurement.2016.01.015> ↑3
- [12] D. Ribeiro, R. Calçada, J. Ferreira, and T. Martins, “Non-contact measurement of the dynamic displacement of railway bridges using an advanced video-based system,” *Engineering Structures*, vol. 75, pp. 164–180, 2014. <https://doi.org/10.1016/j.engstruct.2014.04.051> ↑3
- [13] D. Béréziat and I. Herlin, “Motion and acceleration from image assimilation with evolution models,” *Digital Signal Processing*, vol. 83, pp. 45–58, 2018. <https://doi.org/10.1016/j.dsp.2018.08.008> ↑4,9
- [14] A. Y. Sun, D. Wang, and X. Xu, “Monthly streamflow forecasting using gaussian process regression,” *Journal of Hydrology*, vol. 511, pp. 72–81, 2014. <https://doi.org/10.1016/j.jhydrol.2014.01.023> ↑4

- [15] S. Chatterjee and A. S. Hadi, *Sensitivity analysis in linear regression*. John Wiley Sons, 2009, vol. 327. ↑4
- [16] A. Girard, C. Rasmussen, J. Q. Candela, and R. Murray-Smith, "Gaussian process priors with uncertain inputs application to multiple-step ahead time series forecasting," *Advances in neural information processing systems*, vol. 15, pp. 545–552, 2002. ↑4
- [17] C. E. Rasmussen, "Gaussian processes in machine learning," *Summer School on Machine Learning*, pp. 63–71, 2003. https://doi.org/10.1007/978-3-540-28650-9_4 ↑4
- [18] D. Anguita, A. Ghio, N. Greco, L. Oneto, and S. Ridella, "Model selection for support vector machines: Advantages and disadvantages of the machine learning theory," in *The 2010 international joint conference on neural networks (IJCNN)*, IEEE, 2010, pp. 1–8. <https://doi.org/10.1109/IJCNN.2010.5596450> ↑4
- [19] T. Chan and J. Shen, *Image processing and analysis*. Society for Industrial and Applied Mathematics SIAM, 2005, vol. 94. ↑4, 6
- [20] H. Lin and K. Li, "Motion blur removal and its application to vehicle speed detection," *Electrical Engineering*, no. 2, pp. 3407–3410, 2004. ↑4, 6, 7
- [21] S. Som, "Analysis of the effect of linear smear on photographic images," *JOSA*, vol. 61, no. 7, pp. 859–864, 1971. <https://doi.org/10.1364/JOSA.61.000859> ↑4
- [22] X. Y. Qi, L. Zhang, and C. L. Tan, "Motion deblurring for optical character recognition," in *Document Analysis and Recognition, 2005. Proceedings. Eighth International Conference on*, IEEE, 2005, pp. 389–393. ↑5
- [23] Y. Yitzhaky and A. Stern, "Restoration of interlaced images degraded by variable velocity motion," *Optical Engineering*, vol. 42, no. 12, pp. 3557–3565, 2003. <https://doi.org/10.1117/1.1621406> ↑5
- [24] Y. Yitzhaky, I. Mor, A. Lantzman, and N. Kopeika, "Direct method for restoration of motion-blurred images," *Journal of the Optical Society of America*, vol. 15, no. 6, pp. 1512–1519, 1998. <https://doi.org/10.1364/JOSAA.15.001512> ↑5
- [25] M. Cannon, "Blind deconvolution of spatially invariant image blurs with phase," *Acoustics, Speech and Signal Processing, IEEE Transactions on*, vol. 24, no. 1, pp. 58–63, 1976. <https://doi.org/10.1109/TASSP.1976.1162770> ↑5
- [26] M. Sakano, N. Suetake, and E. Uchino, "Robust identification of motion blur parameters by using angles of gradient vectors," in *Intelligent Signal Processing and Communications, 2006. ISPACS'06. International Symposium on*, IEEE, 2006, pp. 522–525. <https://doi.org/10.1109/ISPACS.2006.364711> ↑5
- [27] M. E. Moghaddam and M. Jamzad, "Linear motion blur parameter estimation in noisy images using fuzzy sets and power spectrum," *EUR-ASIP Journal on Advances in Signal Processing*, vol. 2007, no. 1, pp. 1–8, 2007. <https://doi.org/10.1155/2007/68985> ↑5
- [28] M. A. Lata, S. Ghosh, F. Bobi, and M. A. Yousuf, "Novel method to assess motion blur kernel parameters and comparative study of restoration techniques using different image layouts," in *2016 5th International Conference on Informatics, Electronics and Vision (ICIEV)*, IEEE, 2016, pp. 367–372. <https://doi.org/10.1109/ICIEV.2016.7760027> ↑5

- [29] H.-Y. Lin, "Vehicle speed detection and identification from a single motion blurred image," in *Application of Computer Vision, 2005. WACV/MOTIONS'05 Volume 1. Seventh IEEE Workshops on*, IEEE, vol. 1, 2005, pp. 461–467. ↑7
- [30] M. Celestino and O. Horikawa, "Velocity measurement based on image blur," *Computer graphics and image processing*, vol. 3, pp. 633–642, 2008. ↑7
- [31] H. Pazhoumand-Dar, A. M. T. Abolhassani, and E. Saeedi, "Object speed estimation by using fuzzy set," *World Academy of Science, Engineering and Technology, International Journal of Computer, Electrical, Automation, Control and Information Engineering*, vol. 4, no. 4, pp. 688–691, 2010. ↑7
- [32] S. Rezvankhah, A. A. Bagherzadeh, H. Moradi, and B. N. A. Member, "A Real-time Velocity Estimation using Motion Blur in Air Hockey," in *2012 IEEE International Conference on Robotics and Biomimetics (ROBIO)*, 2012, pp. 1767–1772, <https://doi.org/10.1109/RO-BIO.2012.6491223> ↑7
- [33] J. Mohammadi and A. Taherkhani, "Object Speed Estimation in Frequency Domain of Single Taken Image," *Journal of Basic and Applied Scientific Research*, vol. 3, pp. 120–124, 2013. ↑7
- [34] S. McCloskey, Y. Ding, and J. Yu, "Design and estimation of coded exposure point spread functions," *IEEE transactions on pattern analysis and machine intelligence*, vol. 34, no. 10, p. 2071, 2012. <https://doi.org/10.1109/TPAMI.2012.108> ↑7
- [35] A. Agrawal, Y. Xu, and R. Raskar, "Invertible motion blur in video," in *ACM Transactions on Graphics (TOG)*, vol. 28, 2009, p. 95. <https://doi.org/10.1145/1531326.1531401> ↑7
- [36] M. Lee, K.-S. Kim, and S. Kim, "Measuring vehicle velocity in real time using modulated motion blur of camera image data," *IEEE Transactions on Vehicular Technology*, vol. 66, no. 5, pp. 3659–3673, 2016. <https://doi.org/10.1109/TVT.2016.2600281> ↑7
- [37] M. Lee, "A study on measuring vehicle velocity in real time using modulated motion blur of camera image data," Ph.D. dissertation, Korea Advanced Institute of Science and Technology, 2017. <https://doi.org/10.1109/TVT.2016.2600281> ↑7
- [38] M. Lee, K.-S. Kim, J. Cho, and S. Kim, "Development of a vehicle body velocity sensor using modulated motion blur," in *2017 IEEE International Conference on Advanced Intelligent Mechatronics (AIM)*, IEEE, 2017, pp. 406–411. <https://doi.org/10.1109/AIM.2017.8014051> ↑7
- [39] J. Jing, F. Xiao, L. Yang, S. Wang, and B. Yu, "Measurements of velocity field and diameter distribution of particles in multiphase flow based on trajectory imaging," *Flow Measurement and Instrumentation*, vol. 59, pp. 103–113, 2018. <https://doi.org/10.1016/j.flow-measinst.2017.12.005> ↑7
- [40] K. Matsuo and T. Yakoh, "Position and velocity measurement method from a single image using modulated illumination," in *2018 IEEE 15th International Workshop on Advanced Motion Control (AMC)*, IEEE, 2018, pp. 353–359. <https://doi.org/10.1109/AMC.2019.8371117> ↑7
- [41] J. A. Dwicahya, N. Ramadijanti, and A. Basuki, "Moving object velocity detection based on motion blur on photos using gray level," in *2018 International Electronics Symposium on Knowledge Creation and Intelligent Computing (IES-KCIC)*, IEEE, 2018, pp. 192–198. <https://doi.org/10.1109/KCIC.2018.8628598> ↑

- [42] J. A. Cortes-Osorio, J. B. Gomez-Mendoza, and J. C. Riano-Rojas, "Velocity estimation from a single linear motion blurred image using discrete cosine transform," *IEEE Transactions on Instrumentation and Measurement*, vol. 68, no. 10, pp. 4038–4050, 2019. <https://doi.org/10.1109/TIM.2018.2882261> ↑8, 14, 15
- [43] J. A. Cortes-Osorio, "A contribution to the estimation of kinematic quantities from linear motion blurred images," Ph.D. dissertation, Universidad Nacional de Colombia Sede Manizales, 2020. ↑8, 12
- [44] Q. Guo et al., "Learning to Adversarially Blur Visual Object Tracking," in *Proceedings of the IEEE/CVF International Conference on Computer Vision*, 2021. <https://doi.org/10.1109/ICCV48922.2021.01066> ↑8
- [45] M. Li, H. Du, Q. Zhang, and J. Wang, "Improved particle image velocimetry through cell segmentation and competitive survival," *IEEE Transactions on Instrumentation and Measurement*, vol. 57, no. 6, pp. 1221–1229, 2008. <https://doi.org/10.1109/TIM.2007.915443> ↑8, 20
- [46] X. Liu and J. Katz, "Instantaneous pressure and material acceleration measurements using a four-exposure piv system," *Experiments in Fluids*, vol. 41, no. 2, p. 227, 2006. <https://doi.org/10.1007/s00348-006-0152-7> ↑9, 20
- [47] H. Zhou, M. Chen, L. Zhang, N. Ye, and C. Tao, "Measuring shape and motion of a high-speed object with designed features from motion blurred images," *Measurement*, vol. 145, pp. 559–567, 2019. <https://doi.org/10.1016/j.measurement.2019.05.023> ↑9
- [48] L. Li, T. Martin, and X. Xu, "A novel vision-based real-time method for evaluating postural risk factors associated with musculoskeletal disorders," *Appl. Ergon.*, vol. 87, p. 103 138, 2020. <https://doi.org/10.1016/j.apergo.2020.103138> ↑9
- [49] C. Yu, X. Bi, and Y. Fan, "Deep learning for fluid velocity field estimation: A review," *Ocean Engineering*, vol. 271, p. 113 693, 2023. <https://doi.org/10.1016/j.oceaneng.2023.113693> ↑9
- [50] P. Chu, B. T. Wolfe, and Z. Wang, "Measurement of incandescent microparticle acceleration using stereoscopic imaging," *Review of Scientific Instruments*, vol. 89, no. 10, 2018. <https://doi.org/10.1063/1.5034311> ↑10
- [51] G. Chen, L. Li, C. Zhao, R. Huang, and F. Guo, "Acceleration characteristics of a rockslide using the particle image velocimetry technique," *Journal of Sensors*, vol. 2016, 2016. <https://doi.org/10.1155/2016/2650871> ↑10
- [52] D. C. Luvizon, B. T. Nassu, and R. Minetto, "A video-based system for vehicle speed measurement in urban roadways," *IEEE Transactions on Intelligent Transportation Systems*, vol. 18, no. 6, pp. 1393–1404, 2017. <https://doi.org/10.1109/TITS.2016.2600281> ↑10
- [53] J. X. Wang, "Research of vehicle speed detection algorithm in video surveillance," in *Audio, Language and Image Processing (ICALIP), 2016 International Conference on*, IEEE, 2016, pp. 349–352. <https://doi.org/10.1109/ICALIP.2016.7846482> ↑10
- [54] K. V. K. Kumar, P. Chandrakant, S. Kumar, and K. J. Kushal, "Vehicle speed detection using corner detection," in *2014 Fifth International Conference on Signal and Image Processing*, 2014, pp. 253–258. <https://doi.org/10.1109/ICSIP.2014.46> ↑10

- [55] J. Dong, Y. Song, H. Wang, J. Zeng, and Z. Wu, "Predicting flow velocity affected by seaweed resistance using svm regression," in *Computer Application and System Modeling (ICCASM), 2010 International Conference on*, vol. 2, 2010, pp. V2-273. <https://doi.org/10.1109/IC-CASM.2010.5620588> ↑10
- [56] O. Genç and A. Dağ, "A machine learning-based approach to predict the velocity profiles in small streams," *Water Resources Management*, vol. 30, no. 1, pp. 43–61, 2016. <https://doi.org/10.1007/s11269-015-1123-7> ↑10
- [57] M. Morimoto, K. Fukami, and K. Fukagata, "Experimental velocity data estimation for imperfect particle images using machine learning," *arXiv preprint arXiv:2005.00756*, 2020. <https://doi.org/10.1063/5.0060760> ↑10
- [58] P. J. Chun, T. Yamane, S. Izumi, and N. Kuramoto, "Development of a machine learning-based damage identification method using multipoint simultaneous acceleration measurement results," *Sensors*, vol. 20, no. 10, p. 2780, 2020. <https://doi.org/10.3390/s20102780> ↑10
- [59] W. Kim, M. Tanaka, M. Okutomi, and Y. Sasaki, "Learning-based human segmentation and velocity estimation using automatic labeled lidar sequence for training," *IEEE Access*, vol. 8, pp. 88 443–88 452, 2020. <https://doi.org/10.1109/ACCESS.2020.2993299> ↑10
- [60] B. Major, D. Fontijne, A. Ansari, et al., "Vehicle detection with automotive radar using deep learning on range-azimuth-doppler tensors," in *2019 IEEE/CVF International Conference on Computer Vision Workshop (ICCVW)*, 2019, pp. 924–932. <https://doi.org/10.1109/ICCVW.2019.00121> ↑10
- [61] C. Guo, Y. Fan, C. Yu, Y. Han, and X. Bi, "Time-resolved particle image velocimetry algorithm based on deep learning," *IEEE Transactions on Instrumentation and Measurement*, vol. 71, pp. 1–13, 2022. <https://doi.org/10.1109/TIM.2022.3141750> ↑10
- [62] S. Cai, J. Liang, Q. Gao, C. Xu, and R. Wei, "Particle image velocimetry based on a deep learning motion estimator," *IEEE Transactions on Instrumentation and Measurement*, vol. 69, no. 6, pp. 3538–3554, 2020. <https://doi.org/10.1109/TIM.2019.2932649> ↑10
- [63] A. Oppenheim, R. Schafer, and T. Stockham, "Nonlinear filtering of multiplied and convolved signals," *IEEE Transactions on Audio and Electroacoustics*, vol. 16, no. 3, pp. 437–466, 1968. <https://doi.org/10.1109/TAU.1968.1161990> ↑12
- [64] I. Pitas and A. N. Venetsanopoulos, "Homomorphic Filters," in *Nonlinear Digital Filters: Principles and Applications*, Springer US, 1990, pp. 217–243. https://doi.org/10.1007/978-1-4757-6017-0_7 ↑12
- [65] T. M. Cannon, "Digital image deblurring by nonlinear homomorphic filtering," Utah University, Salt Lake City School of Computing, Tech. Rep., 1974. <https://doi.org/10.21236/ADA002735> ↑12, 13
- [66] Y. Yitzhaky, R. Milberg, S. Yohaev, and N. S. Kopeika, "Comparison of direct blind deconvolution methods for motion-blurred images," *Applied Optics*, vol. 38, no. 20, pp. 4325–4332, 1999. <https://doi.org/10.1364/AO.38.004325> ↑12
- [67] J. A. Cortes-Osorio, D. A. Muñoz-Acosta, and C. D. López-Robayo, "Design and construction of an electromechanical slider for the kinematic study of linear motion blurred images," *INGE CUC*, vol. 16, no. 1, pp. 80–90, 2020. <https://doi.org/10.17981/ingecuc.16.1.2020.06> ↑15, 17

- [68] Basler, *aca2000-165um-baslerace*, <https://www.baslerweb.com/en/products/cameras/area-scan-cameras/ace/aca2000-165um/>, (Accessed on 06/11/2017), Nov. 2017. ↑15
- [69] Ricoh *lens fl-cc0814a-2m*, <https://www.baslerweb.com/en/products/vision-components/lenses/ricoh-lens-fl-cc0814a-2m-fl-4-f8mm-2-3/>, (Accessed on 06/11/2017), Nov. 2017. ↑15
- [70] *BT.601: Studio encoding parameters of digital television for standard 4:3 and wide screen 16:9 aspect ratios*, <http://www.itu.int/rec/rrec-bt.601>, 2017. ↑15
- [71] E. Izquierdo-Verdiguier, L. Gomez-Chova, L. Bruzzone, and G. Camps-Valls, "Semisupervised kernel feature extraction for remote sensing image analysis," *IEEE Transactions on Geoscience and Remote Sensing*, vol. 52, no. 9, pp. 5567–5578, 2014. <https://doi.org/10.1109/TGRS.2013.2290372> ↑15
- [72] T. Bouwmans, S. Javed, H. Zhang, Z. Lin, and R. Otazo, "On the applications of robust PCA in image and video processing," *Proceedings of the IEEE*, vol. 106, no. 8, pp. 1427–1457, 2018. <https://doi.org/10.1109/JPROC.2018.2853589> ↑16
- [73] P. S. GmbH, *Cobra4 sensor unit 3D acceleration*, <https://repository.curriculab.net/files/bedanl.pdf/12650.00/1265000e.pdf>, 2018. ↑17
- [74] L. Kirkup and R. B. Frenkel, *An introduction to uncertainty in measurement: using the GUM (guide to the expression of uncertainty in measurement)*. Cambridge University Press, 2006. <https://doi.org/10.1017/CBO9780511755538> ↑17
- [75] R. H. Dieck, *Measurement uncertainty: methods and applications*. ISA, 2007. ↑17
- [76] A. J. Sederman, M. D. Mantle, C. Buckley, and L. F. Gladden, "MRI technique for measurement of velocity vectors, acceleration, and auto-correlation functions in turbulent flow," *Journal of Magnetic Resonance*, vol. 166, no. 2, pp. 182–189, 2004. <https://doi.org/10.1016/j.jmr.2003.10.016> ↑20
- [77] K. Komiya, T. Kurihara, and S. Ando, "3D particle image velocimetry using correlation image sensor," in *Proc. SICE Annual Conf.* 2011, Sep. 2011, pp. 2774–2778. ↑20

Jimmy Alexander Cortés-Osorio

JA Cortés-Osorio is an accomplished academic who has significantly contributed to engineering and physics. Born in Pereira, Colombia. He obtained a BE in Electrical Engineering and an MS in Physics Instrumentation from Universidad Tecnológica de Pereira (UTP) in 1999 and 2009, respectively. In 2020, he received a PhD in Automatic Engineering from Universidad Nacional de Colombia, Manizales campus. Since 2013, Cortés-Osorio has served as a full professor of the Departments of Physics and Engineering at UTP. He has conducted research in various fields of engineering, including image processing, image motion analysis, machine vision, machine learning, data mining, and instrumentation and measurement. His current research interests are focused on these areas, and he has made significant contributions to the field through his research and publications. Cortés-Osorio is an affiliate member of the Society for Industrial and Applied Mathematics (SIAM) and the Institute of Electrical and Electronic Engineers (IEEE). Additionally, he has served in various academic committees, including

UTP's research committee and the academic council, where he has contributed to developing academic programs and research initiatives.

Email: jacoper@utp.edu.co

Juan Bernardo Gómez-Mendoza

J.B. Gómez-Mendoza obtained his bachelor's degree in electronic engineering, a master's degree in industrial Automation, and a Doctoral degree in Engineering – Automation from Universidad Nacional de Colombia in 2002, 2004, and 2012, respectively. He has been attached to the Department of Electrical, Electronic, and Computer Engineering of Universidad Nacional de Colombia at Manizales since February 2005, currently holding the position of associate professor. His areas of interest include image processing, machine vision, artificial intelligence and data analysis, and robotics.

Email: jbgomezm@unal.edu.co

Juan Carlos Riaño-Rojas

JC Riano-Rojas is an academic who has contributed significantly to mathematics in Manizales. He was born in Bogotá, Colombia. He obtained a bachelor's and a master's degree in mathematical sciences from Universidad Nacional de Colombia in 1992 and 1998, respectively. In 2013, he received a PhD in Automatic Engineering, and, in 2020, he received a Specialist's degree in Statistics from Universidad Nacional de Colombia, Manizales campus. Since 1999, Riano-Rojas has served as an associate professor of the Department of Mathematics and Statistics of Universidad Nacional de Colombia. He has conducted research in various fields of mathematics and engineering, including image processing, image motion analysis, computer vision, machine learning, topology, mathematical logic, and data sciences. His current research interests focus on these areas, and he has made significant contributions to the field through his research and publications.

Email: jcrianoro@unal.edu.co





Research

Transgenic Algorithm Applied to the Job Shop Rescheduling Problem

Algoritmo transgénico aplicado al Job Shop Rescheduling Problem

Néstor Andrés Beltrán-Bernal¹✉, José Ignacio Rodríguez-Molano²ORCID, Diego Ernesto Mendoza-Patiño³

¹Universidad de la Salle (Bogotá, Colombia)ORCID

²Universidad Distrital Francisco José de Caldas, (Bogotá, Colombia)ORCID

³Universidad Antonio Nariño (Bogotá, Colombia)ORCID

Abstract

Context: Job sequencing has been approached from a static perspective, without considering the occurrence of unexpected events that might require modifying the schedule, thereby affecting its performance measures.

Method: This paper presents the development and application of a genetic algorithm to the Job Shop Rescheduling Problem (JSRP), a reprogramming of the traditional Job Shop Scheduling Problem. This novel approach seeks to repair the schedule in such a way that theoretical models accurately represent real manufacturing environments.

Results: The experiments designed to validate the algorithm aim to apply five classes of disruptions that could impact the schedule, evaluating two performance measures. This experiment was concurrently conducted with a genetic algorithm from the literature in order to facilitate the comparison of results. It was observed that the proposed approach outperforms the genetic algorithm 65 % of the time, and it provides better stability measures 98 % of the time.

Conclusions: The proposed algorithm showed favorable outcomes when tested with well-known benchmark instances of the Job Shop Scheduling Problem, and the possibility of enhancing the tool's performance through simulation studies remains open.

Keywords: disruptions, efficiency, stability, job shop, rescheduling, transgenic algorithm

Article history

Received:
14th / Aug / 2023

Modified:
27st / Oct / 2023

Accepted:
4th / Nov / 2023

Ing, vol. 29, no. 1,
2024. e21162

©The authors;
reproduction right
holder Universidad
Distrital Francisco
José de Caldas.

Open access



*✉ Correspondence: nbeltran@unisalle.edu.co

Resumen

Contexto: La secuenciación de trabajos ha sido abordada desde un enfoque estático, sin considerar la aparición de eventos inesperados que requieran modificar el cronograma, lo que incide en sus medidas de desempeño.

Método: Este artículo expone el desarrollo y aplicación de un algoritmo transgénico al *Job Shop Rescheduling Problem* (JSRP), una reprogramación del tradicional *Job Shop Scheduling Problem*. Este enfoque novedoso busca reparar el cronograma de modo que los modelos teóricos representen los entornos de manufactura reales.

Resultados: Los experimentos diseñados para validar el algoritmo pretenden aplicar cinco clases de interrupciones que pueden afectar el cronograma, evaluando dos medidas de desempeño. Este experimento se realizó simultáneamente en un algoritmo genético de la literatura para facilitar la comparación de los resultados. Se observó que el enfoque propuesto tiene un desempeño superior al del algoritmo genético el 65 % de las veces y lo supera en la medida de estabilidad el 98 % de las veces.

Conclusiones: El algoritmo propuesto mostró buenos resultados al ser probado con instancias de comparación reconocidas del *Job Shop Scheduling Problem* (JSSP), y queda abierta la posibilidad de mejorar el desempeño de la herramienta por medio de estudios de simulación.

Palabras clave: interrupciones, eficiencia, estabilidad, *job shop*, *rescheduling*, algoritmo transgénico

Table of contents

		2.4.1. Manufacturing environment	11
		2.4.2. Transgenic algorithm	12
		3. Results	19
		3.1. Predictive phase	19
		3.2. Reactive phase	23
		4. Conclusions	32
		5. Future work	33
		6. Author Contributions	33
		References	33
1. Introduction	2		
2. Proposal	3		
2.1. Job Shop Scheduling Problem . . .	3		
2.2. Job Shop Rescheduling Problem . .	5		
2.2.1. Rescheduling framework .	6		
2.3. Transgenic algorithm	7		
2.4. Proposed algorithm	11		

1. Introduction

Job sequencing is one of the main challenges faced by the people in charge of planning and scheduling production. This is due mostly to the combinatorial nature of the task and the fact that these types of problems can be classified as NP-Hard ones (1), which requires the development of advanced algorithms that may offer nearly optimal solutions, thus allowing for an efficient use of computational resources.

On another note, static models (such as bifurcation and dimensioning) have approached job scheduling without contemplating the appearance of unexpected events in the execution of production processes. This has created a gap between theoretical models and real manufacturing environments (2).

Hence, this work studies the Job Shop Scheduling Problem (JSSP) from a rescheduling-oriented perspective, seeking a better representation of the actual conditions of manufacturing environments. Rescheduling is a process that can react to unexpected events as a part of the dynamics of said environments (3). In this sense, the Job Shop Rescheduling Problem (JSRP) (4–7) is conceived as a problem of higher complexity.

Studies focused on the rescheduling of manufacturing systems are wide and diverse. Therefore, this work is framed within the search for methods to fix production timetables that have been affected by an unexpected event (3). The method developed in the subsequent sections is based on the architecture of a transgenic algorithm (8), which is characterized by metaheuristics applied to diverse problems of high complexity, leading to competitive results compared to more renowned techniques (9–14).

The main objective was to develop a computational algorithm based on the metaphor of transgenic computation (53) which allows production schedulers to generate high-quality timetables in terms of efficiency and stability while also being able to react to unexpected events or interruptions arising during the execution of said timetables, thus mitigating the impact on the performance of the manufacturing system.

2. Proposal

2.1. Job Shop Scheduling Problem

Sequencing problems can be as diverse as manufacturing environments. The JSSP is one of the most studied topics in the research field of operations and computer science. This is mostly due to its relationship with production planning activities within the industry. The JSSP is recognized as an NP-Hard problem (1) and is considered to be among the highly complex and unmanageable optimization problems (15,55).

JSSP is defined as a manufacturing environment containing a set $J = \{1, \dots, j, \dots, n\}$ of n jobs that must be scheduled in a set $M = \{1, \dots, i, \dots, m\}$ of m machines. Each job has a technological sequence of machines (stages) for it to be processed. The use of machine i for the processing of job j is denoted as *operation* O_{ij} with a duration equal to t_{ij} , which is known as the *processing time*. Furthermore, the problem revolves around constraints and suppositions such as the following:

- Each machine can only process one job at a time.
- Each job can only be processed by one machine at a time.
- Jobs must only be processed once in each machine.
- The technological sequence of each job has been completely defined.

- The processing times of all operations are known.
- The machines are always available and never interrupted.

The problem consists of determining the sequence of operations to be defined for the machines in order to minimize the makespan (C_{max}), whose value is the time necessary to complete all the operations. The JSSP with makespan as the target can be mathematically described via Eqs. (1), (2), (3), (4), and (5):

$$\text{Min } C_{max} \tag{1}$$

$$r_{kj} - r_{ij} \geq t_{ij} \quad \forall O_{ij} \rightarrow O_{kj} \in A \tag{2}$$

$$C_{max} - r_{ij} \geq t_{ij} \quad \forall O_{ij} \in N \tag{3}$$

$$r_{ij} - r_{il} \geq t_{il} \quad \forall r_{il} - r_{ij} \geq t_{ij} \quad \forall O_{il} \wedge O_{ij}, i = 1, \dots, m \tag{4}$$

$$r_{ij} \geq 0 \quad \forall O_{ij} \in N \tag{5}$$

where r_{ij} is the time at which operation O_{ij} starts, N is the set of all operations O_{ij} , and A is the set of all constraints given by the technological sequence of each job, such as $O_{ij} \rightarrow O_{kj}$, which requires job j to be processed by machine i before being processed by machine k . This formulation of the JSSP is called *disjoint scheduling* given the third set of constraints (16). Furthermore, the JSSP can be defined as an integer scheduling problem (17).

An instance of three jobs for three machines (3×3) of JSSP is represented as: As evidenced in this

Table I. Example of a 3×3 instance

O_{ij}	j			t_{ij}	j		
i	1	2	3	i	1	2	3
1	(2)	(1)	(1)	1	3	6	4
2	(3)	(2)	(3)	2	2	8	6
3	(1)	(3)	(2)	3	7	3	3

table, matrix O_{ij} describes the order in which the jobs for each machine are processed. For instance, job 1 ($j = 1$) has the following technological sequence: (1) $O_{31} \rightarrow$ (2) $O_{11} \rightarrow$ (3) O_{21} . Matrix t_{ij} contains the processing times of each operation O_{ij} .

There are different representations of the solution for this problem. The Gantt diagram is one of the most commonly used forms in this regard. Fig. 1 shows an example of the representation obtained for a solution of the instance in Table I.



Figure 1. Gantt diagram

The Gantt diagram depicts what is known as the *production timetable*. It shows a feasible solution to the JSSP when all constraints are satisfied. It is worth noting that this definition of the JSSP corresponds to a theoretical problem that constitutes one approximation to a more complex scenario.

On another note, researchers studying the JSSP have opted to define a set of assumptions and constraints, leading to a gap between theoretical models and real manufacturing environments (2).

2.2. Job Shop Rescheduling Problem

The definition of the JSSP described in the previous section is a deterministic and static sequencing model, as its parameters and variables are known beforehand and do not change over time. Thus, this model only represents an approximation of a real manufacturing environment, since the industry experiences some scenarios encompassing variables that are dynamic or have a high degree of uncertainty.

In this sense, when a production timetable is built, both the supervisors and the operators attempt to execute it as closely as possible. The issue lies in unexpected events that alter the execution of the current production timetable, causing it to become inappropriate and unmanageable. Said events are called *interruptions* and need to be treated swiftly in order to minimize any effects that can deteriorate the system performance (55). This is where rescheduling becomes the proper tool to handle interruptions and complete all scheduled jobs.

Rescheduling is defined as the process of updating the existing production timetable in response to the interruptions or changes (3), whose integration with the Job Shop manufacturing environment results in what is referenced in the literature as the *Job Shop Rescheduling Problem* (JSRP) (4–7).

Studies on rescheduling from different perspectives are numerous. The most common approaches are the following: (i) methods to fix a timetable that has been interrupted, (ii) methods to create robust timetables to face interruptions, and (iii) studies on how rescheduling policies affect the performance of dynamic manufacturing systems.

Some of the articles include, for instance, the study of the Job Shop environment under the dynamic arrival of new jobs, variations in processing times, and machine failure (18). Other authors, such as (19), propose an algorithm capable of predicting and absorbing the effects of interruptions while

maintaining system performance. In (20), a genetic algorithm is applied to scheduling and rescheduling in a non-deterministic Job Shop environment.

Given that the studies on rescheduling are as numerous as they are diverse, this work adopts the rescheduling framework defined in (3). This framework allows for the understanding of rescheduling studies, in addition to classifying the technique discussed herein.

In order to properly narrow down the study of rescheduling in manufacturing environments, it is necessary to include an appropriate framework, given that its study can become widely diverse and complex depending on the scope defined by the researcher. According to (3), the rescheduling framework is composed of these elements: rescheduling environments, strategies, policies, and methods.

2.2.1. Rescheduling framework

• Rescheduling environments

Rescheduling environment refers to the set of jobs that must be scheduled. The environment can be static (finite set of jobs) or dynamic (infinite set of jobs). The environment can be deterministic (all the information is given) or stochastic (some information is uncertain). Dynamic environments may also be classified according to the variability in which the arrival takes place: without variability (cyclical production), with variability (flow shop), and with variability in the process flow (job shop).

• Rescheduling strategies

Rescheduling strategies refer to how production is controlled in the aforementioned environments, whether timetables are generated or not. Two common strategies have been identified in this regard: dynamic sequencing and predictive-active sequencing. The former does not generate production timetables, since the jobs are dispatched when necessary, using the information available at the moment of dispatch and with the help of dispatch rules or theoretical control models for manufacturing systems. The second strategy is characterized by two phases: a predictive phase, during which the initial production timetable is generated; and a reactive phase, in which the production timetable is updated as a response to interruptions in order to minimize their impact on system performance. The predictive-reactive strategy includes three policies: periodic, given event, and hybrid. These refer to the moment of rescheduling.

• Rescheduling methods

Rescheduling methods describe how to generate and update production timetables (54). Two approaches have been proposed: the generation and repair of timetables. The generation of production timetables can be coordinated through different techniques, in the form of analytical, heuristic, or more complex algorithms. The timetable repair approach (*i.e.*, update process) includes three main variants: right-shift rescheduling, partial rescheduling, and complete rescheduling.

- **Performance metrics**

In addition to the previously discussed elements, performance metrics are an important guideline in rescheduling studies. They can be classified into three groups: efficiency metrics, stability metrics, and timetable costs. The first group is made up of the most common time-based metrics, such as makespan, average delay, and average flow time. The second group refers to the variables that measure changes within a timetable in terms of launch times or the differences between sequences. Lastly, the cost variables include benefit according to the job, minimization of the total cost, and reduction of the work in process (WIP), among others.

Various techniques have been proposed in literature to solve the rescheduling problem in terms of the aforementioned performance metrics. Methods such as right-shift rescheduling (21), match-up (22), and Affected Operation Rescheduling (AOR) (23) are some of the most well-known group of heuristics and are characterized by a simple implementation process, which is however limited by the range of interruptions that they can face. Furthermore, these heuristics operate under the partial rescheduling strategy, which implies that they try to adhere to the preestablished timetable as much as possible after the interruption (24,25).

On another note, complete rescheduling techniques seek to reschedule all remaining operations after the point of interruption (26,27). Under the umbrella of this approach, diverse and sophisticated algorithms have been implemented, as is the case of genetic algorithms (4,20,53,55), which are known to improve the efficiency of timetables while ignoring stability-related metrics.

In this sense, new techniques are constantly being developed to solve combinatorial problems. JSSP is no exception, since it belongs to this class even from the rescheduling (JSRP) viewpoint, implying that timetables require more quality over time with a rational use of computational resources. Hence, the next section exposes an algorithm that has offered many advantages in other problems of the same nature.

2.3. Transgenic algorithm

In the context of evolutionary computation, defined as the study of the foundations and applications of certain heuristic techniques based on natural evolution principles (28), a variety of algorithms have been developed to face highly complex problems such as the one discussed in the present work.

Since the appearance of genetic algorithms in the article titled *Adaptation in natural and artificial systems* (29), techniques based on this metaphor have not been scarce. Some of them have inherited the basic structure of genetic algorithms to be combined with other local search techniques, paving the way for genetic/evolutionary hybrid algorithms (16,30), Lamarckian genetic algorithms (31), or general memetic algorithms (32,33).

The term *memetic algorithm* stems from the English term *meme*, coined by R. Dawkins as an analogy to the gene in the context of cultural evolution. (34) defines *memes* as the units of information coded

and transmitted by non-genetic media. These definitions are relevant for the approach described in the subsequent section, which is based on the transgenic algorithm.

• Transgenic computation

Transgenic computation (TC) is a metaphor derived from the use of memetic information (memes) and extra- and intracellular flows to plan and execute genetic manipulations in the context of evolutionary algorithms (8).

To the scope of evolutionary computation, TC brings the use of exogenous and endogenous information to infer the formation and modification processes of the individuals in a given population, to use intracellular flow as an operational mechanism in order to carry out the required manipulations amongst individuals, to explore new populational improvements using transgenic agents and competition between agents and individuals, and to guide the evolutionary process, allowing for the occurrence of evolutionary jumps (9). Further information on the basics of TC can be found in (8,10,11).

This method has been branched into two types of algorithms: the extra-intracellular transgenic algorithm (EITA) (12) and the proto-gen (ProtoG) algorithm (9). The most noticeable difference between them lies in the fact that the ProtoG algorithm does not have reproduction operators (mutation or cross), so it is not based on an extracellular approach (9).

The proposed algorithm is based on the ProtoG algorithm, whose structure and composition are detailed below.

• The ProtoG algorithm

As discussed with TC, transgenic algorithms are metaheuristics that insert information in a planned manner for improving genetic information. Their pillar lies in the intracellular paradigm, through agents that manipulate the genetic context. The information inserted by said agents is created and controlled via the epigenetic paradigm. These paradigms define the ProtoG algorithm *per se*, thus excluding the extracellular paradigm that uses sexual reproduction as the basis of information exchange between individuals (10).

• Intracellular paradigm

In this algorithm, the chromosomes are exposed to a direct attack from the agents in the intracellular flow, which must compete against each other and the defense mechanisms of chromosomes in order to consolidate the transcription of their codes (11). In the computational context, said chromosomes are part of the population C of size q , where $C = \{1, \dots, c, \dots, q\}$ is a function f called the *fitness function*. Each chromosome c is a chain of integer length h that represents a solution to the problem, such as $f : c \rightarrow \mathbb{R}^+$, $c = 1, \dots, q$, where f returns a real value.

Chromosomic alterations are only carried out by transgenic agents, which makes them essential to the evolutionary process as the only source of intensification and diversification in the search process (9).

Transgenic agents are entities used by the algorithm to insert information into the genetic context. These agents manipulate chromosomes similarly to intracellular vectors used in genetic engineering. As an analogy to the terms used by microbiologists, there are four types of transgenic agents: plasmid, virus, recombined plasmid, and transposon (11).

In the computational context, a transgenic agent λ is defined as a couple $\lambda = (I, \Phi)$, where I is a chain of information (corresponding to the memes) and Φ describes the manipulation method used by the agent. $\Phi = (p_1, \dots, p_s, \dots, p_x)$ where $p_s, s = 1, \dots, x$, are the procedures that determine the behavior of the agents. Table II depicts the procedures of the manipulation method (extracted and adapted from (11)).

In this sense, when the chain of information I of λ is a genetic code and its manipulation method uses procedures p_1, p_2 , and p_3 , λ is called a virus (11). In the case of the ProtoG algorithm, the mobile genetic particle (MGP) is a special case of virus where the virus lifetime (or blocking period) established by procedure p_3 is equal to zero, and the attack procedure p_1 only takes place when chromosome fitness is improved (9).

Table II. Procedures of the manipulation method

Procedure (p_s)	Description
Attack (p_1)	Defines a criterion that establishes whether a chromosome c is susceptible to the information of a transgenic agent λ . The function $v(c) = 'true'$ if c is vulnerable to λ , $v(c) = 'false'$ otherwise.
Transcription (p_2)	If $v(c) = 'true'$, the procedure defines the information transferred from λ to c .
Blocking/unblocking (p_3)	It establishes a time period in which the transferred information cannot be altered in c .
Identification (p_4)	It identifies the positions in c that will be used to limit the operation of λ .
Recombination (p_5)	It identifies the origin and length of two or more chains of information in λ .

- **Epigenetic paradigm**

The difficulty of considering epigenetics in the context of evolutionary computation is discussed by (34). The initial work on this matter simply linked the memes to information obtained outside the extracellular flow [10]. In memetic algorithms, according to (35) and (36), the epigenetics stage is mainly expressed through the improvement of chromosomes using local search procedures. This is where TC adopts a new approach, defining *memes* as memories with information that is stored, coded, and transmitted using non-genetic means, as stated by (33). Hence, memes can be used to adjust a chromosome or block of genes, or said memes could be subjected to competition and selection processes relevant to the cultural media (10).

Mememes are units of information that can be spread by a culture in the same way that genes are disseminated through a genetic reservoir (37). The relationship between genes and mememes is based on the fact that genes prescribe the epigenetic rules, which are regularities of sensorial perception and mental development that encourage and channel the acquisition of culture. Culture contributes to determining which prescribed genes survive and multiply from one generation to the next one. New properly sequenced genes alter the epigenetic rules of the population. The altered epigenetic rules change the direction and effectiveness of cultural acquisition channels by offering feedback to the coevolution 'gene vs. mememe' process (38).

In the computational context, these epigenetic rules are simulated by a transgenic rule-based structure. The evolution control of a population of chromosomes, transgenic agents, and the information of a memetic base is composed of three classes of rules (10,11).

Type 1 rules lead to the construction of information chain I, which is transported by the transgenic agents (11). These types of rules can have knowledge on any aspect of the problem, as well as previous knowledge stored in the memetic base (MB), which constitutes the storage bank of mememes. Mememes can be comprised of construction blocks or manipulation procedures (11). Type 2 rules define the information contained in I is transcribed into a chromosome, *i.e.*, the operator used by λ . These types of rules can evolve in terms of the resistance shown by chromosomes. Type 3 rules are present throughout the process, defining which agents are used, the number of chromosomes under attack during a given iteration, the number of agents created, and the stopping criterion, among others (11,12).

- **Pseudocode**

The ProtoG algorithm can be decomposed into two phases. The first one generates the construction blocks (mememes) and codes them using transgenic agents. In the second phase, the agents compete to transcribe their information into the chromosomes and thus improve the solutions (9).

The implementation of the ProtoG algorithm improves the fitness of the chromosome population through the manipulation carried out by the transgenic agents. However, not only chromosomes evolve; mememes also do. This process makes TC an informed and co-evolutionary search technique (9).

Transgenic algorithms, including ProtoG, have proven to be successful when compared to known techniques in the solution of high-complexity problems. Some of the problems tackled by this technique include the quadratic allocation problem (QAP) (9,11), the traveling purchaser problem (TPP) (12), the graph coloring problem (12), and sequencing in flow-shop with permutation (13), among others (39,40).

The pseudocode of the algorithm is the following (taken and adapted from (9,11)):

```
Begin  
Load a meme base with a set of solutions and rules to generate memes  
Generate and assess an initial population  
Repeat  
    Generate an agent from competition between memes  
    For each chromosome:  
        If the chromosome is sensitive to manipulation  
            Begin  
                Manipulate  
                Assess  
                If the chromosome meets the immunity criterion  
                    Then include its memes in the Memetic Base  
            End  
    Until a stop criterion is met  
End
```

2.4. Proposed algorithm

As discussed in Section 3, the proper definition of the scope of rescheduling requires an appropriate framework. The approach of this work lies in the methods used to repair a timetable that has been interrupted. Hence, it is important to initially define these interruptions, also known as *rescheduling factors* (41,42), which arise at a given time of the initial timetable known as the *interruption point*. This study contemplates all the rescheduling factors identified in the work of (43), as shown in Table III.

Given that rescheduling factors are a significantly wide group, they are classified into five classes. This classification is based on the general actions that would be needed to repair the interrupted timetable and meet the constraints imposed by the arising rescheduling factor. A description of the considered factors can be seen in (44).

2.4.1. Manufacturing environment

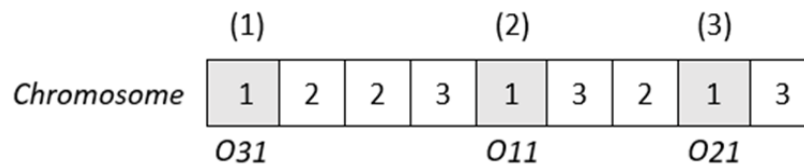
The rescheduling framework defined by (3) encompasses the elements of the proposed algorithm framework shown in Table IV.

Table III. Classification of rescheduling factors

Id.	Name	Class	Actions
1	Failure		
2	Machine maintenance		
3	Absenteeism	I	Insert inactivity time
4	Tool failure		
5	Delay in material transportation		
6	Depletion of raw materials		
7	Variation in processing time		Insert inactivity time
8	Variation in machine performance	II	+
9	Tool deterioration		Update processing times
10	Variation in preparation times		
11	Arrival of a new job		Update technological sequences
12	Reprocessing	III	+
13	Rejection		Update processing times
14	Urgent job	IV	Schedule
15	Priority shift		priority-marked operations
16	Order cancellation	V	Eliminate scheduled operations
17	Outsourcing		

2.4.2. Transgenic algorithm

As stated in the field of evolutionary computing, one of the most important factors in the success of algorithms is the representation of the problem. In this sense, (16) conducted a study of the representation forms used in the application of genetic algorithms to solve the JSSP. In this case, operation-based representation was selected, which defines n jobs and m machines to create a chain (chromosome) of $n \times m$ positions (genes), where all operations of job j are distinguished by the same symbol (number) that appears exactly m times throughout the chain. Each appearance of the symbol that represents job j corresponds to an operation in the order of the technological sequence of said job. This representation method offers the advantage that all permutations in its elements provide a feasible solution to the JSSP, thus avoiding complex repair processes, as seen in other alternatives. An example of this representation is shown, using the instance data presented in the second section:

**Figure 2.** Operation-based representation

As seen in Fig. 2, each appearance of the number 1 ($j = 1$) refers to an operation in the technological sequence. This can be replicated for the remaining jobs. The representation can be useful during the

Table IV. Defined manufacturing environment

Rescheduling environment	
Dynamic	Job shop
There is a continuous arrival of jobs to the manufacturing environment floor (set of finite jobs).	Technological sequences of jobs differ from each other (variability in the process flow).
Rescheduling strategy	
Predictive-reactive	
There are two phases: the first one generates an initial schedule timetable, while the second one is in charge of updating (repairing) the timetable.	
Rescheduling policy	
Hybrid	
Rescheduling can be carried out periodically or when a special event takes place.	
Rescheduling method	
Repair	Complete
The interrupted timetable is updated in response to the arising rescheduling factor.	All remaining operations are rescheduled after the interruption point.
Performance metrics	
Efficiency	Stability
Makespan (E): percentage-form variation of the makespan obtained for the repaired timetable compared to the initial one.	Deviation (D): average difference between the starting time of the repaired timetable operations compared to the initial one.

elaboration of the Gantt diagram. The chromosome is read from left to right, where each position (gene) delivers the information of an operation O_{kj} . The operation is inserted into the diagram by setting the starting time r_{kj} as early as possible, *i.e.*, by checking the conclusion time of the preceding operation O_{ij} and not overlapping times with a previously inserted operation. Lastly, operation O_{kj} is defined from r_{kj} to $r_{kj} + t_{kj}$. An example of the aforementioned procedure can be seen in (16).

After the representation of the solution is defined, the next task involves the design of the rescheduling method based on the ProtoG algorithm architecture for the previously defined manufacturing environment, which is divided into the following two stages:

- **Stage 1: intracellular paradigm**

The transgenic agents of the evolutionary process are defined in this stage. It is worth mentioning

that these agents have been designed in terms of the JSSP features defined in the second section. The MGP is the agent chosen to carry out the genetic modifications. The composition and general structure of the designed agents is shown below.

Let $\lambda = (I_j, \Phi)$ be a transgenic agent composed of an information chain $I_j = (g_{1j}, \dots, g_{ij}, \dots, g_{mj})$ or meme with length m , where the element g_{ij} can represent one of the following elements: a position in the processing order, a preceding job, or an adjacent job, as suggested by the evolutionary process, which is taken as a reference to schedule job j in machine i , with $i = 1, \dots, m$ and $j \in J$. Let $\Phi = (p_1, p_2, p_3)$, be the manipulation method of the agent composed of the procedures p with $s = \{1, 2, 3\}$. Table V defines each procedure.

Table V. Procedures of the manipulation method of the chosen agent

Procedure (p_s)	Definition
Attack ($p1$)	Let c be the chromosome before the modification of its structure and c' the manipulated chromosome. If $f(c') > f(c)$, then chromosome c is vulnerable, $v(c) = \text{'true'}$. Otherwise, $v(c) = \text{'false'}$, where v is the function that defines the susceptibility of the chromosome.
Transcription ($p2$)	If $v(c) = \text{'true'}$, then the operations of job j are scheduled according to the information chain I_j .
Block/unblock ($p3$)	Let y be the function that defines the number of iterations in which the information transcribed by p cannot be altered, where $v(c) = 0$ in all cases.

Three agents were designed for this algorithm. They all inherit the previously defined composition and structure, and the only difference between them is the type of information (meme) that they carry. The following section describes how the epigenetic paradigm creates, stores, and controls this information in the MB to guide the evolutionary process.

• Stage 2: epigenetic paradigm

As previously stated, there are three types of rules that represent this paradigm in the computational context. Recall that type 1 rules lead the construction of the information chain (meme) that is transported by the transgenic agent. This information is stored in the MB. To illustrate this process, Fig. 3 presents a diagram representing the flow of individuals from the population to the transformation of their information into memes. The process starts with the population of chromosomes. This population enters

a selection process, where chromosomes with the best fitness are considered to continue with the process (This procedure is controlled by a factor that will be defined later).

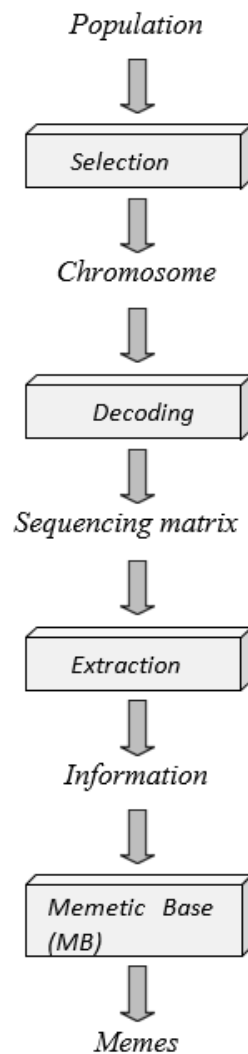


Figure 3. Meme creation process

Once the chromosome has been selected, it undergoes a new procedure called *decoding*. This refers to the conversion of a chromosome into a convenient representation form, which is used to extract the information needed by the MB to create memes. The result of this decoding stage is the sequencing matrix, defined as an array of m rows by n columns, which represents the sequence in which the jobs will be processed by each machine. An example of said procedure is depicted in Fig. 4. The sequencing matrix is derived from the examination of the Gantt diagram linked to the chromosome. In the form of a matrix, this array summarizes the information related to the order in which the jobs of each machine will be processed.

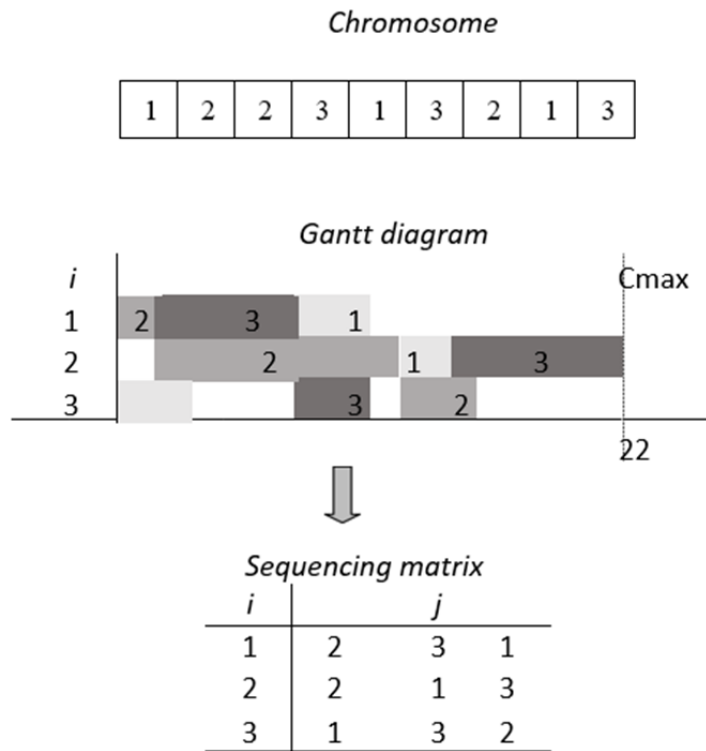


Figure 4. Decoding process of the chromosome into a sequencing matrix

Now that the decoding process has been detailed, the sequencing matrix becomes the main asset for the extraction procedure. It consists of obtaining key information from the structure of the given chromosome.

Once the information has been extracted, it is stored in the MB. The matrices that integrate said base are described below.

Let MB be a set of matrices $MB = \{Mp, Mr, Ma, Mb\}$ that store specific information from the population of chromosomes C through an evolutionary process.

Mp is defined as the *position matrix*, where the element Mp_{ijl} is the average makespan of the chromosomes that have scheduled the job j in the sequence of operations of machine i in position r , with $i = 1, \dots, m, j = 1, \dots, n, r = 1, \dots, n$.

Mr is defined as the *precedence matrix*, where element Mr_{ijl} is the average makespan of the chromosomes that have scheduled the job j in machine i before job l with $i = 1, \dots, m, j = 1, \dots, n, l = 1, \dots, n$.

Ma is defined as the adjacency matrix, where the element Ma_{ijl} is the average makespan of the chromosomes that have scheduled the job j in machine i exactly one position before the job l , with $i = 1, \dots, m, j = 1, \dots, n, l = 1, \dots, n$.

Memes are built based on the minimum values of matrices Mp , Mr , and Ma . The obtained memes are denoted as I_{pj} (meme1), I_{rj} (meme2), and I_{aj} (meme3), respectively, where $j \in J$ is a reference job chosen at random for the construction of the chain.

The last matrix that comprises the memetic base is Mb , defined as the *meme matrix*, where the previously defined memes are stored. Each meme is linked to an accumulative score S_{cw} that is updated every time that the corresponding agent uses the meme to modify the structure of a chromosome. Said score is given by the function $S_{cw}(current) = S_{cw}(previous) + [f(c') - f(c)]$, with $w = \{1, 2, 3\}$. Furthermore, memes have a counter defined by C_{ow} , which adds one unit to its previous value each time that $v(c) = 'false'$, i.e., when the chromosome is not vulnerable to the meme.

After defining the construction process of information chains I_j , type 2 rules are presented, which allow defining how the information contained in said chains is transcribed into the chromosomes. The transcription procedures of type p2 used by the designed agents are slightly different due to the type of information that they carry. The manipulation procedure consists of a positional exchange of genes within the chromosome, which are linked to the meme contained by the agent.

Lastly, type 3 rules are present throughout the evolutionary process, defining the parameters and criteria that dominate the operativity of the algorithm. Table VI summarizes the parameters and variables that complement the previously discussed terms. These are also necessary during the construction of the algorithm.

Consequently, the following criteria and rules are defined:

- The creation of the initial population of chromosomes C is performed randomly, where each chromosome represents a solution to the JSSP.
- Chromosomes are assessed based on their fitness using the function f , where $f(c) = Cmax(c)$ for $c \in C$.
- Memes are initially created with the information of the chromosomes present in the initial population. The selection procedure is controlled by the following expression: if $f(c) - min(f) \leq Qi[max(f) - min(f)]$, then the chromosome is selected to continue with the extraction procedure; otherwise, it is rejected.
- The transgenic agent that attacks the given chromosome is chosen in terms of the highest meme score regarding the Mb . In case of a tie, it is chosen at random. It is chosen in this way in the first generation since $S_{cw} = 0$ for $w = \{1, 2, 3\}$.
- Chromosomes attack each other in one generation with the selected agent.
- If chromosome c is vulnerable to the attack, the new chromosome c' takes its place in population C .

Table VI. General parameters and variables of the transgenic algorithm

Parameter/Variable	Description
Size of the population (q)	This refers to the number of chromosomes created in the initial population. This value remains constant throughout the evolutionary process.
Non-improvement counter (C_n)	This variable increases by one unit when the best value of the makespan does not change within a generation.
Non-improvement limit (C_{nmax})	This is the maximum value of generations of the variable C_n .
Immunity limit (C_{omax})	This refers to the maximum value of counter Co_w , for $w = 1, 2, 3$.
Information quality (Q_i)	This factor between 0 and 1 intervenes in the selection procedure. It refers to the information considered in the updating process of the MB.

- The score of memes is updated each time that a chromosome is manipulated.
- The matrices Mp , Mr , and Ma are updated with the information of the manipulated chromosomes. Additionally, counter Co_w , is checked for $w = \{1, 2, 3\}$. If it exceeds Co_{max} , a new meme is generated instead, and the counter and score are also reset.
- If counter $C_n = C_{nmax}/3$, the MB is completely reset by subtracting information of the current population and creating new memes from it.

The proposed algorithm has now been defined. It represents the method used to generate and update the production timetables, since it is integrated both in the predictive and reactive stages of the rescheduling process. The reader can recall that this is the chosen strategy to solve the JSRP in the presented manufacturing environment.

The corresponding integration of the algorithm with the manufacturing environment leads to the following diagram, which represents the utility and operation of the algorithm within said environment.

As seen in Fig. 5, the proposed algorithm is integrated into the manufacturing environment both in the predictive and reactive phase. An initial production timetable is obtained for the transgenic algorithm. Then, said timetable is executed, and decisor A defines whether a rescheduling factor is needed. If this is the case, then the timetable is interrupted and enters the reactive phase to be repaired by the transgenic algorithm. Otherwise, decisor B defines whether the timetable has been completely executed. The timetable is then deemed to be executed, and a new rescheduling period begins. Otherwise, the timetable continues its execution.

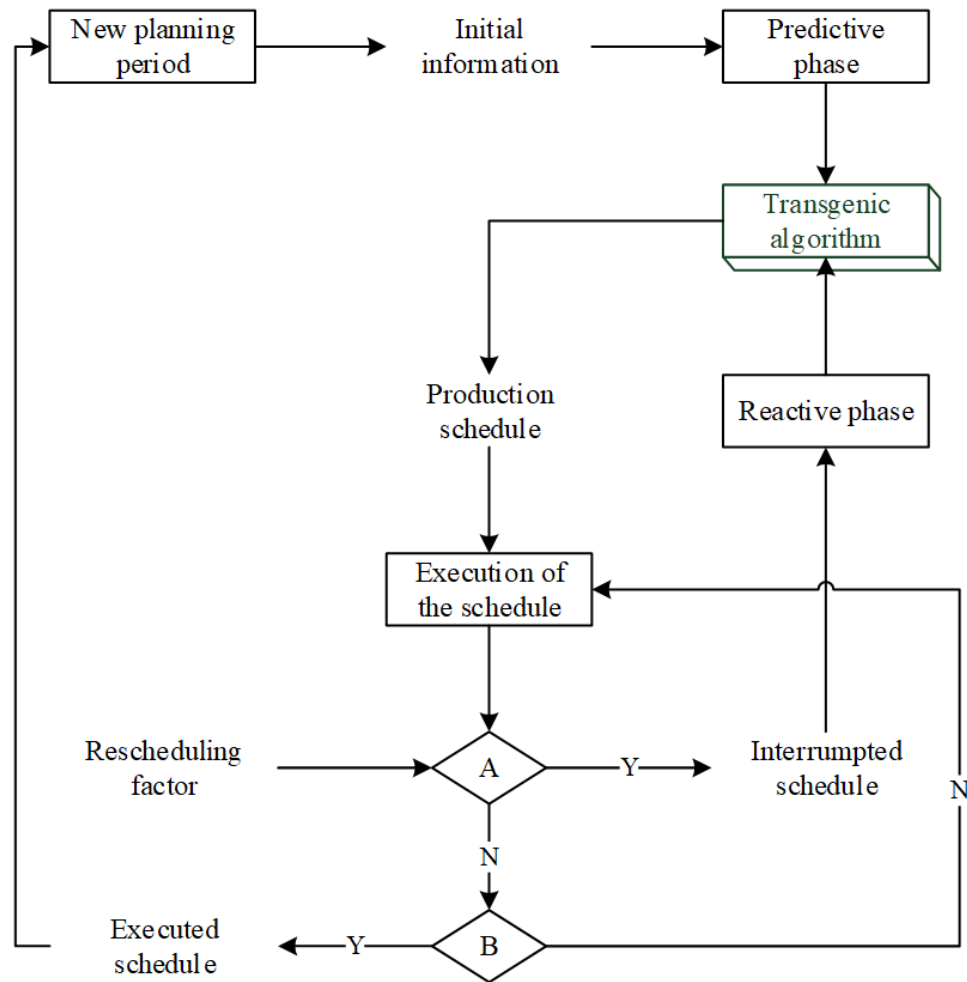


Figure 5. Integration of the transgenic algorithm in the manufacturing environment

3. Results

In order to assess the performance of the proposed algorithm, this study has been divided into two sections: the first one details the experimentation carried out with the transgenic algorithm in the predictive phase, and the second section involves testing the algorithm in the reactive phase.

3.1. Predictive phase

As described in the third section, this stage includes the generation of the initial production timetable. In order to solve the JSSP, many techniques have been developed. A study on said techniques can be found in (44). Furthermore, these techniques have been tested with comparison instances proposed by different authors. In order to validate the performance of the transgenic algorithm, we selected some alternatives, such as the ones proposed by (45–49), and (50).

The results shown below were obtained with the parameterization described in Table VII. Said parameters were set upon the basis of factorial experiments, which are not described in this article in order to avoid content saturation.

Table VII. Parameterization of the transgenic algorithm for the predictive phase

Parameter	Instance size		
	Small	Medium	Large
Population size (q)	50	300	500
Non-improvement limit (C_{nmax})	100	100	100
Immunity limit (C_{omax})	5	30	50
Information quality (Q_i)	0,1	0,1	0,1

The above-presented parameters have been defined for all three instance sizes: a small instance contains between 36 and 75 operations, a medium instance between 100 and 200, and a large instance between 225 and 400 operations.

Table VIII summarizes the results obtained for the selected instances. These instances are assessed in terms of performance compared to makespan. Hence, the BK field yields the *best value according to the literature* for each instance (some are consistent with optimal values). The BF field states the *best value found* by the proposed algorithm. The GAP field represents the relative difference of BF compared to BK in percentage form: $GAP = 100 \times (BF - BK)/BK$. The two following fields correspond to the average makespan and its standard deviation obtained for five replicas of the algorithm with the instance.

The last field corresponds to the average execution time in seconds. The BF values in bold show that the proposed algorithm has found the BK . The algorithm was implemented in MATLAB. These results were obtained using a computer with an Intel Core i5-8300H @4.0 Ghz and 8GB RAM.

Table VIII. Results obtained using the proposed algorithm for the selected instancescv

Name	n	m	BK	BF	GAP	AVG	SD	RT
Instances proposed by (46)								
Ft06	6	6	55	55	0,0	55,0	0,0	1
Ft10	10	10	930	930	0,0	941,6	10,8	7
Ft20	20	5	1.165	1.173	0,7	1.178,8	3,1	10
Instances proposed by (47)								
Abz5	10	10	1.234	1.242	0,6	1.243,7	3,1	5
Abz6	10	10	943	947	0,4	947,2	0,4	5

Abz7	20	15	656	685	4,4	692,8	4,8	52
Abz8	20	15	665	698	5,0	707,1	8,5	49
Abz9	20	15	678	697	2,8	713,4	9,4	45
Instances proposed by (48)								
Yn01	20	20	884	917	3,7	930,9	8,4	74
Yn02	20	20	904	933	3,2	942,7	8,0	84
Yn03	20	20	892	928	4,0	937,6	6,8	108
Yn04	20	20	968	1.016	5,0	1.017,8	2,5	170
Instances proposed by (49)								
Orb01	10	10	1.059	1.059	0,0	1.073,0	11,0	7
Orb02	10	10	888	894	0,7	896,6	1,0	9
Orb03	10	10	1.005	1.005	0,0	1.021,3	9,1	10
Orb04	10	10	1.005	1.011	0,6	1.019,0	7,9	8
Orb05	10	10	887	894	0,8	894,5	1,3	6
Orb06	10	10	1.010	1.010	0,0	1.026,2	6,3	8
Orb07	10	10	397	397	0,0	400,3	3,7	5
Orb08	10	10	899	912	1,4	924,8	8,1	7
Orb09	10	10	934	934	0,0	940,7	4,4	6
Orb10	10	10	944	944	0,0	955,5	8,6	9
Instances proposed by (50)								
La01	10	5	666	666	0,0	666,0	0,0	1
La02	10	5	655	655	0,0	655,0	0,0	1
La03	10	5	597	597	0,0	597,0	0,0	1
La04	10	5	590	590	0,0	590,0	0,0	1
La05	10	5	593	593	0,0	593,0	0,0	1
La06	15	5	926	926	0,0	926,0	0,0	1
La07	15	5	890	890	0,0	890,0	0,0	1
La08	15	5	863	863	0,0	863,0	0,0	1
La09	15	5	951	951	0,0	951,0	0,0	1
La10	15	5	958	958	0,0	958,0	0,0	1
La11	20	5	1.222	1.222	0,0	1.222,0	0,0	3
La12	20	5	1.039	1.039	0,0	1.039,0	0,0	3
La13	20	5	1.150	1.150	0,0	1.150,0	0,0	2
La14	20	5	1.292	1.292	0,0	1.292,0	0,0	2
La15	20	5	1.207	1.207	0,0	1.207,0	0,0	3
La16	10	10	945	945	0,0	947,6	3,6	2
La17	10	10	784	784	0,0	785,6	2,3	3
La18	10	10	848	848	0,0	850,8	5,7	4
La19	10	10	842	842	0,0	847,2	5,8	3

La20	10	10	902	907	0,6	909,2	2,0	4
La21	15	10	1.046	1.053	0,7	1.067,9	8,9	11
La22	15	10	927	935	0,9	936,0	2,1	13
La23	15	10	1.032	1.032	0,0	1.032,0	0,0	11
La24	15	10	935	943	0,9	970,0	12,9	14
La25	15	10	977	977	0,0	995,6	10,9	13
La26	20	10	1.218	1.218	0,0	1.223,8	4,8	17
La27	20	10	1.235	1.249	1,1	1.271,8	13,5	24
La28	20	10	1.216	1.227	0,9	1.241,6	10,5	26
La29	20	10	1.152	1.201	4,3	1.210,4	7,9	33
La30	20	10	1.355	1.355	0,0	1.355,0	0,0	23
La31	30	10	1.784	1.784	0,0	1.784,0	0,0	28
La32	30	10	1.850	1.850	0,0	1.850,0	0,0	33
La33	30	10	1.719	1.719	0,0	1.719,0	0,0	29
La34	30	10	1.721	1.721	0,0	1.721,0	0,0	43
La35	30	10	1.888	1.888	0,0	1.888,0	0,0	46
La36	15	15	1.268	1.297	2,3	1.301,8	7,6	53
La37	15	15	1.397	1.436	2,8	1.446,2	6,2	65
La38	15	15	1.196	1.225	2,4	1.234,8	9,2	57
La39	15	15	1.233	1.251	1,5	1.252,8	4,0	58
La40	15	15	1.222	1.243	1,7	1.252,0	8,5	59
Instances proposed by (51)								
Ta01	15	15	1.231	1.231	0,0	1.233,2	3,9	47
Ta02	15	15	1.244	1.244	0,0	1.245,4	3,1	49
Ta03	15	15	1.218	1.218	0,0	1.221,6	5,1	56
Ta04	15	15	1.175	1.200	2,1	1.209,4	6,3	93
Ta05	15	15	1.224	1.248	2,0	1.265,6	12,2	112
Ta11	20	15	1.357	1.421	4,7	1.430,6	10,8	150
Ta12	20	15	1.367	1.430	4,6	1.441,2	6,5	184
Ta13	20	15	1.342	1.391	3,7	1.426,4	24,1	157
Ta14	20	15	1.345	1.359	1,0	1.375,8	15,1	93
Ta15	20	15	1.339	1.438	7,4	1.442,0	3,5	196
Ta21	20	20	1.642	1.642	0,0	1.646,6	5,5	233
Ta22	20	20	1.600	1.645	2,8	1.656,0	7,9	265
Ta23	20	20	1.557	1.644	5,6	1.670,4	16,4	380
Ta24	20	20	1.644	1.691	2,9	1.708,4	14,8	320
Ta25	20	20	1.595	1.719	7,8	1.741,2	22,9	338

Table IX summarizes the results obtained after applying the transgenic algorithm to the comparison instances. The average values obtained for the $n \times m$ settings are shown. In general, the algorithm

performs well in the predictive phase, delivering the best possible values for 52% of the selected instances and similar values for the remaining instances. These values, on average, do not surpass 1,3% in the differences for medium instances and 4,2% for large ones. The algorithm is fairly consistent since the standard deviation is acceptable. Regarding the average execution time, the obtained values are below the minute, except for the last three settings in the set of large instances.

Table IX. Summary of the results obtained for the proposed algorithm

Small instances				
n	m	GAP _{prom.}	SD _{prom.}	RT _{prom.}
6	6	0,0	0,0	1,0
10	5	0,0	0,0	1,0
15	5	0,0	0,0	1,0
Medium instances				
20	5	0,1	0,5	3,8
10	10	0,3	5,3	6,0
15	10	0,5	7,0	12,4
20	10	1,3	7,4	24,6
Large instances				
30	10	0,0	0,0	35,8
15	15	1,5	6,6	64,9
20	15	4,2	10,3	115,8
20	20	3,9	10,4	219,1

On the other hand, it can be observed that the algorithm's performance slightly deteriorates as the complexity of the instances increases, *i.e.*, when there are more operations to process. Once the algorithm had displayed commendable performance in terms of average gap, standard deviation, and execution time for the three identified sets of instances, its performance in the reactive phase was tested.

3.2. Reactive phase

Once the initial production timetable is derived from the predictive phase, rescheduling factors will occur at different times of the execution. In this sense, a set of experiments was designed to validate the performance of the algorithm in comparison with the genetic algorithm, an essential reference in evolutionary algorithms. This technique has been used in a wide range of combinatorial problems, as mentioned in previous sections. An application of genetic algorithms for operation scheduling and rescheduling can be consulted in (19).

First, given that there are many rescheduling factors, one factor is chosen for each class. It is worth mentioning that, although only one is chosen, the entire class can be solved by the algorithm with a similar procedure. The algorithm can process any of the 17 identified factors. In general, the experiments were designed in terms of the following factors and levels:

Table X. Proposed experiment

Levels		
Factors	1	2
Instance size	Small	Large
Interruption incidence	Early	Tardive
Duration of the interruption	Short	Long

Given the previous factors and levels, a 2^k factorial design was established, with $k = 3$, corresponding to the number of factors. This setting offers a total of eight treatments, which are detailed in Table XI:

Table XI. Treatment resulting from the factorial experiment

Treatment	Size	Incidence	Duration
1	Small	Early	Short
2	Small	Early	Long
3	Small	Tardive	Short
4	Small	Tardive	Long
5	Large	Early	Short
6	Large	Early	Long
7	Large	Tardive	Short
8	Large	Tardive	Long

In general, a set of instances were chosen for each class in the predictive phase, in order to design different scenarios. Ten scenarios were built for each treatment, and five replicas were analyzed for each scenario. Regarding the specific values of the levels of each factor, instances with $n \times m$ configurations containing 100 operations were considered as small, and those with 400 operations as large. The early incidence includes a random point between 20 and 40 % of the instance makespan. The tardive instance is located between 60 and 80 % of the makespan. Lastly, a short duration corresponds to 40 % of the maximum processing time among all instance operations, and a long duration corresponds to 160 % of the same parameter.

After clarifying the structure of the experiments, the most relevant sections of the genetic algorithm design are presented, with Eq. (6) serving as a reference point to establish the comparison with the transgenic algorithm.

$$E = 1 - \left(\frac{C_{\max}^* - C_{\max}}{C_{\max}} \right) \times 100 \% \quad (6)$$

where C_{\max} corresponds to the original timetable makespan, and C_{\max}^* corresponds to the makespan of the repaired timetable. The value of E represents the efficiency level obtained for the new timetable in percentage form. A higher value of E means a higher efficiency of the initial timetable.

The *stability* of the timetable refers to the deviation of the repaired timetable when compared to the initial one (52). It can be measured by calculating the average differences between the starting times of the repaired and initial timetables. Its calculation is obtained via Eq. (7):

$$D = \frac{\sum_{j=1}^n \sum_{i=1}^m |r_{ij}^* - r_{ij}|}{\rho(R)} \quad \text{where} \quad O_{ij} \in R \quad (7)$$

where r_{ij} is the starting time of operation O_{ij} in the initial timetable, and r_{ij}^* is the starting time of the same operation in the repaired timetable. R is the set of remaining operations to be processed from the time instant at which the rescheduling factor appears. Lastly, $\rho(R)$ refers to the cardinality of set R .

On another note, the transgenic algorithm for the reactive phase encompasses what is known as the *stability factor*, which enables the planning staffer to establish a share of operations in R that need to maintain the same sequence as the initial timetable. Hence, the *nervousness* of the system can be mitigated (3). In this study, the stability factor was determined based on an additional experiment design, carried out with the same factors and levels presented in Table X.

The efficiency (E) and stability (D) results for both algorithms are presented in this section, for each class of rescheduling factor and for each treatment. They are presented in the form of charts that contain the data regarding the minimum, maximum, and average of the performance metrics obtained for the genetic algorithm (GA) and the transgenic algorithm (TA).

• **Class I: machine failure (1)**

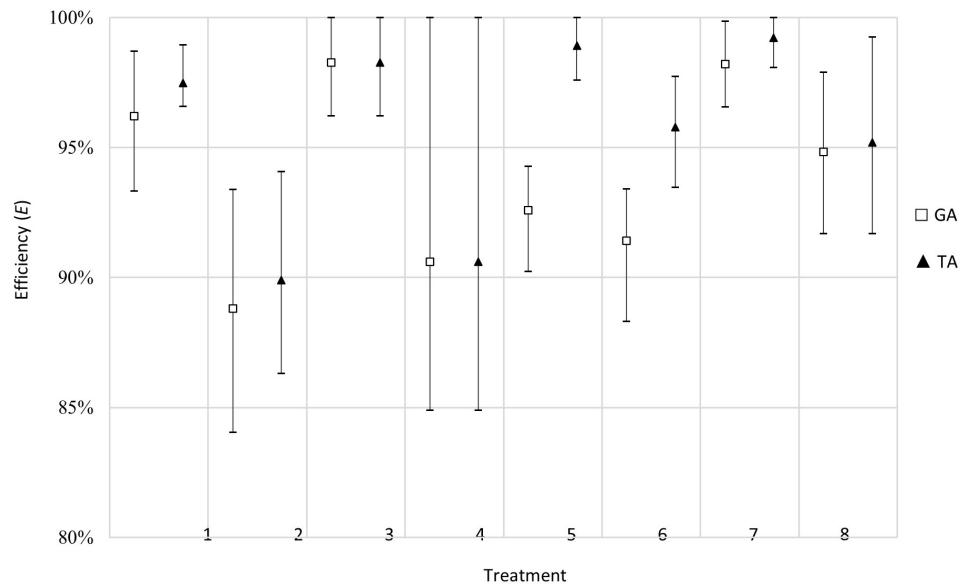


Figure 6. Efficiency results obtained for the machine breakdown rescheduling factor

In Fig. 6, the performance of the TA in terms of efficiency is equal or superior to that of the GA. Furthermore, the proposed algorithm exhibits an efficiency close to 100 % when the interruption is short.

The scenarios with the worst performance are those with small instances and long interruptions, as this could have a more harmful effect on the system floor.

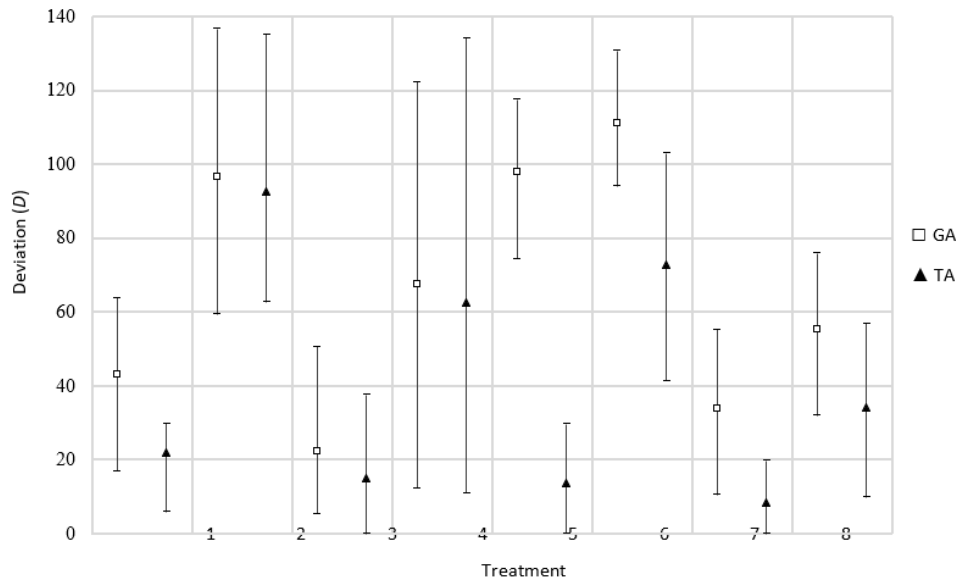


Figure 7. Deviation results obtained for the *machine breakdown* rescheduling factor

As for the deviation, a better performance is obtained, surpassing the GA in all treatments (Fig. 7). Additionally, the TA performs better in the treatments where the instance is large. One particular case regarding the performance differences between the two algorithms corresponds to treatment 5, where the GA has difficulties with delivering a less deviated schedule than the original one.

• Class II: variation in processing time (7)

In this set of treatments, a behavior similar to that of the previous rescheduling factor is observed (Fig. 8). This could indicate that these two classes have the same effects on the interrupted timetable. Another interesting fact is that treatment 4 shows a wide range of results, including the lowest performance. This could be explained by the fact that the worst scenario involves a small instance with the greatest variation in processing times for some operations at a final moment (tardive) of the timetable's execution. The combination of these factors in said levels can lead to a low action range for these algorithms, since there are not many remaining operations that can be rescheduled to compensate for these effects.

In terms of deviation, a better performance is seen once again, surpassing the GA in all treatments. Additionally, the TA shows a better performance in treatments with large instances. A particular case regarding the difference in performance between both algorithms corresponds to treatment 5 where the genetic method seems to have issues with delivering a timetable that is less deviated than the original one.

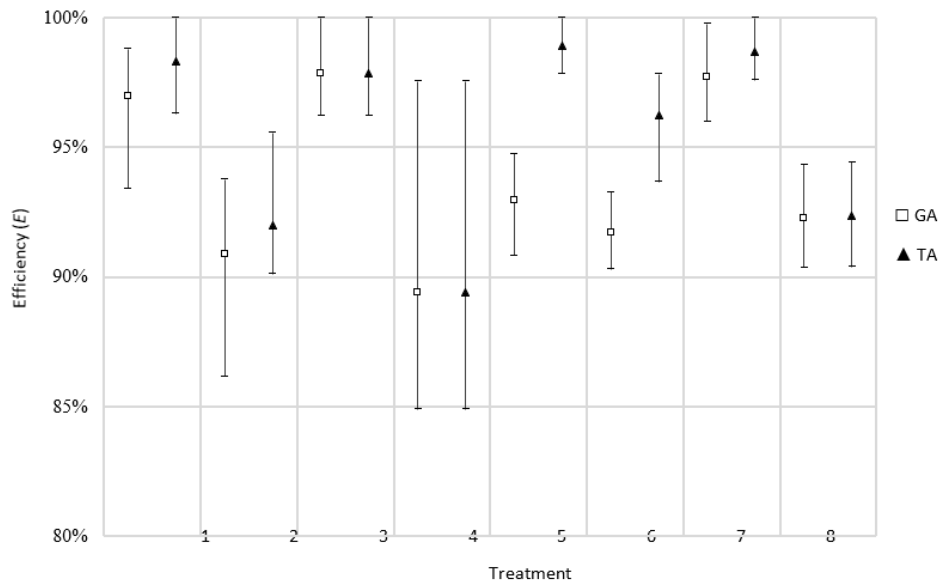


Figure 8. Efficiency results obtained for the *process time variation* rescheduling factor

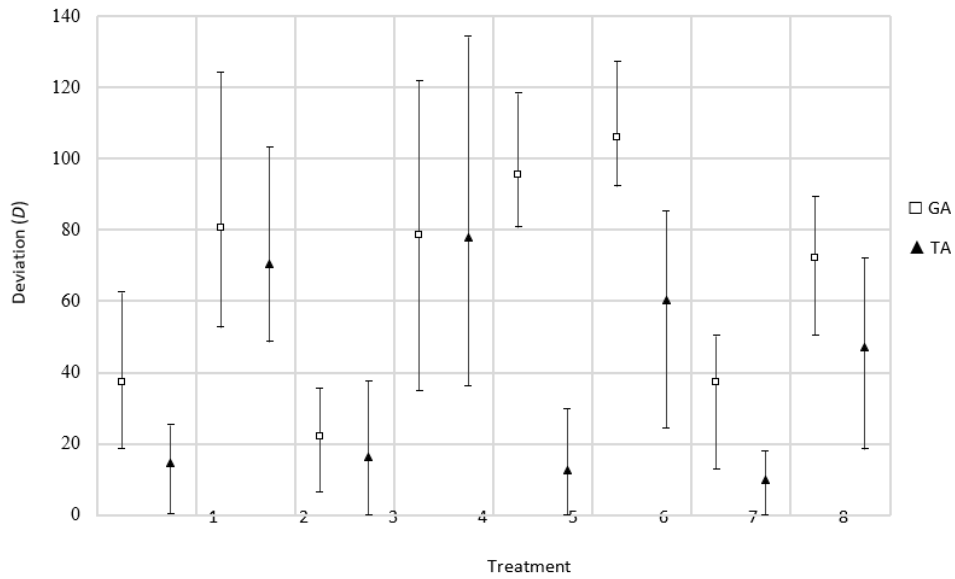


Figure 9. Deviation results obtained for the *process time variation* rescheduling factor

Regarding the deviation of the timetables, the same behavior of the previous class is evidenced (Fig. 9). Furthermore, it would seem that the interruption incidence factor had no effect in the deviation of the resulting timetables. It is key to acknowledge that, in this class, the deviations of treatments with short interruptions do not exceed 20 units of time.

• Class III: arrival of new job order (11)

In this class, it is important to highlight that the duration of the interruption is conceived analogously through the following considerations: the effect of short and long interruptions is homologated to the effect of including a new job with an average processing time between low and high operations. In this sense, to determine the processing time of the operations in the first level (low), a uniform distribution $U(20,60)$ was considered. For the second level, the distribution was $U(80,120)$. Finally, the number of operations of the incoming job was determined through a uniform distribution $U(5,10)$ for small instances and $U(10,20)$ for large instances.

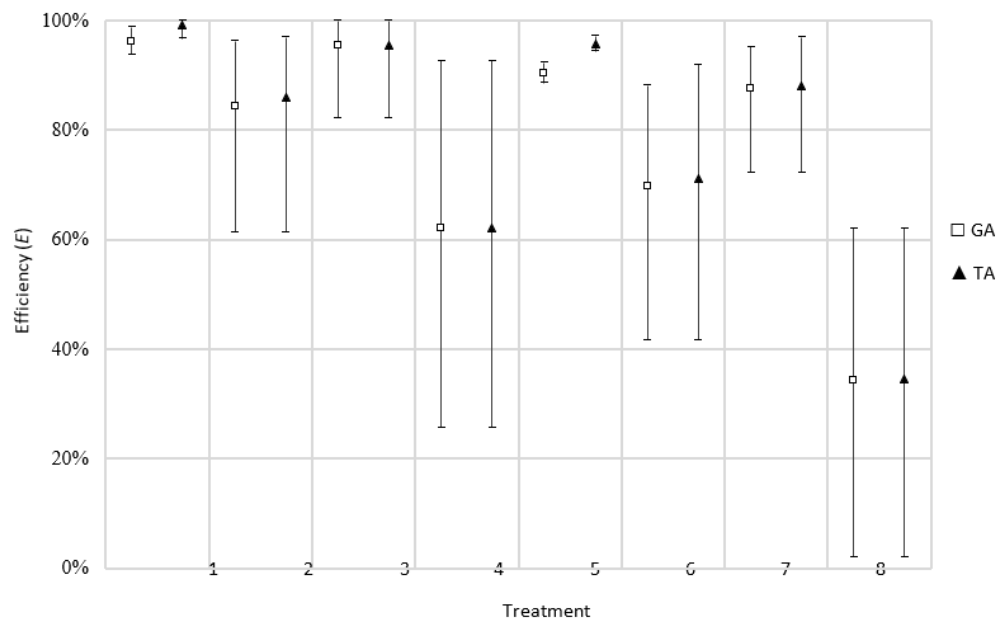


Figure 10. Efficiency results obtained for the *arrival of new job order* rescheduling factor

This leads to the results shown in Fig. 10. The performance of both algorithms is more even than in previous classes. Hence, a generalized behavior can be evidenced, indicating that long duration is the level that most affects the variability results.

In terms of the deviation of the resulting timetables, the TA shows significantly superior results (Fig. 11). These results could be revealing that the initial timetable has not been able to ‘absorb’ the new job order and has remained almost intact. Thus, the processing of the new order has been delayed for the end. This implies that the efficiency values for this class are not related to the operativity of the algorithms, but with the effect of including a new job after the timetable has begun its execution and, in the worst cases, when it is close to conclusion. Hence, this type of interruption can be handled using the periodic scheduling policy that allows putting the new job order on hold and including it in the next planning period. This ensures an efficient use of productive resources.

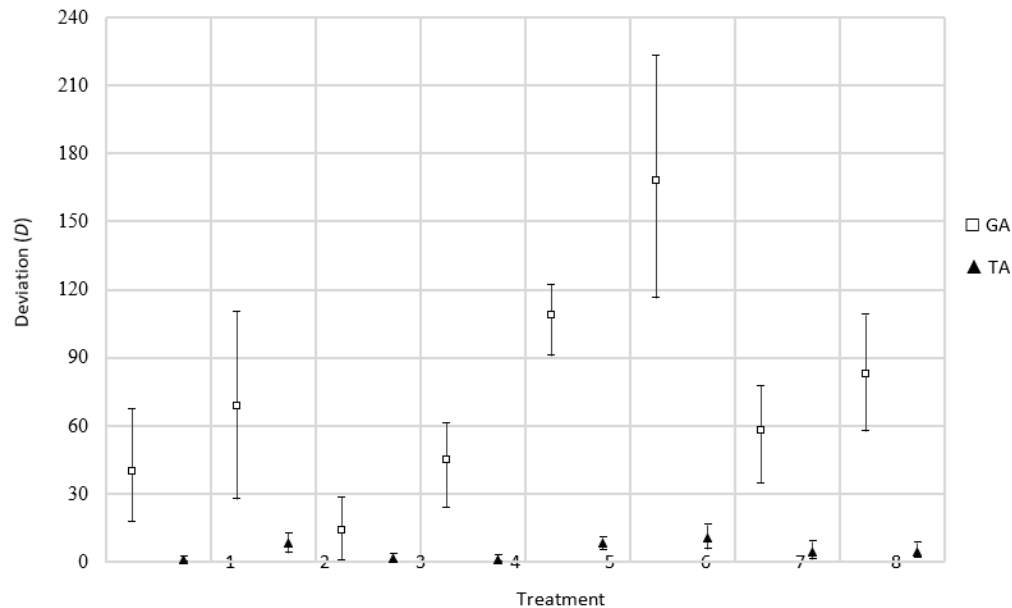


Figure 11. Deviation results obtained for the *arrival of new job order* rescheduling factor

• Class IV: urgent job (14)

In this class, given that there is a priority shift in one of the jobs, the interruption duration factor is analog to the number of remaining operations of the urgent job. This means that the duration factor is represented, in the first level, by the job with less remaining operations when the interruption point takes place. The opposite occurs in the second level.

The results obtained for the efficiency metric reveal that the TA has a superior performance (Fig. 12). The average value of this metric in all treatments surpasses 88 %. Furthermore, the most influential factor is the number of operations. When the urgent job has a higher number of remaining operations to be processed, efficiency is affected.

The algorithm once again yields superior results, exhibiting an efficiency equal or over 100 % in all treatments. The most influential factor is the number of remaining operations for the canceled job. Higher values of this parameter translate into a higher efficiency, as the capacity of resources is slightly relieved.

Regarding the deviation of the obtained timetables, this metric is sensitive to the interruption incidence factor (Fig. 13). When the interruption is early, the stability of the timetable decreases. Furthermore, this effect is amplified when the urgent job has more operations yet to be processed.

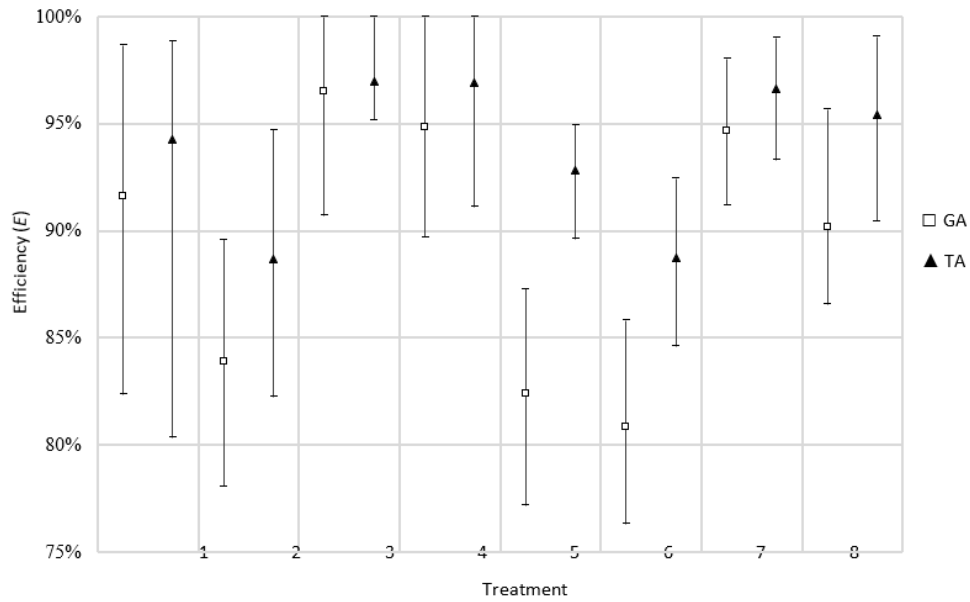


Figure 12. Efficiency results obtained for the *urgent job* rescheduling factor

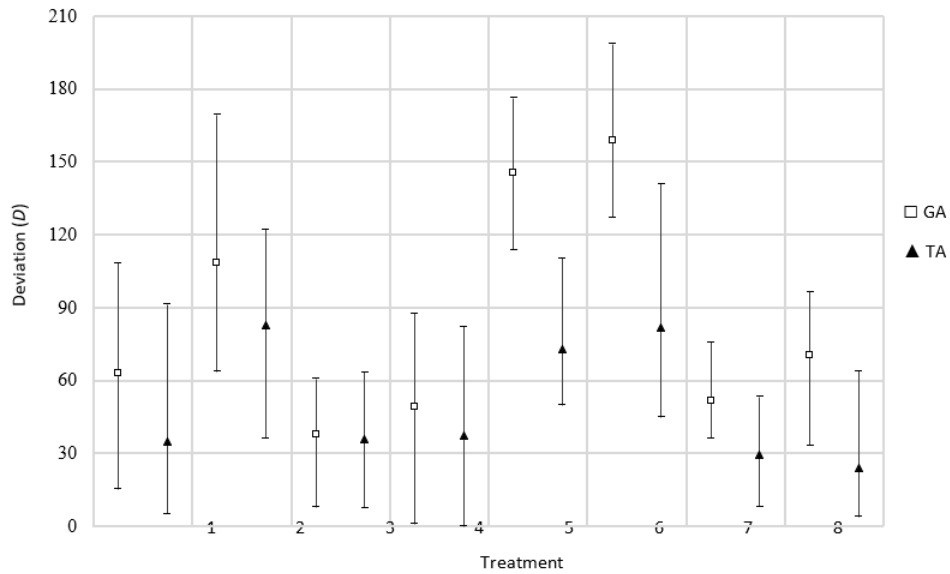


Figure 13. Deviation results obtained for the *urgent job* rescheduling factor

• **Class V: job cancellation (16)**

For this class, the interruption duration factor was approached as in the previous class. In this type of interruption, the algorithms handle the elimination of scheduled jobs in the timetable. Hence, the

makespan after the elimination of these operations can become lower than the initial one. Fig. 14 shows that the values surpass 100% while maintaining consistency in terms of efficiency.

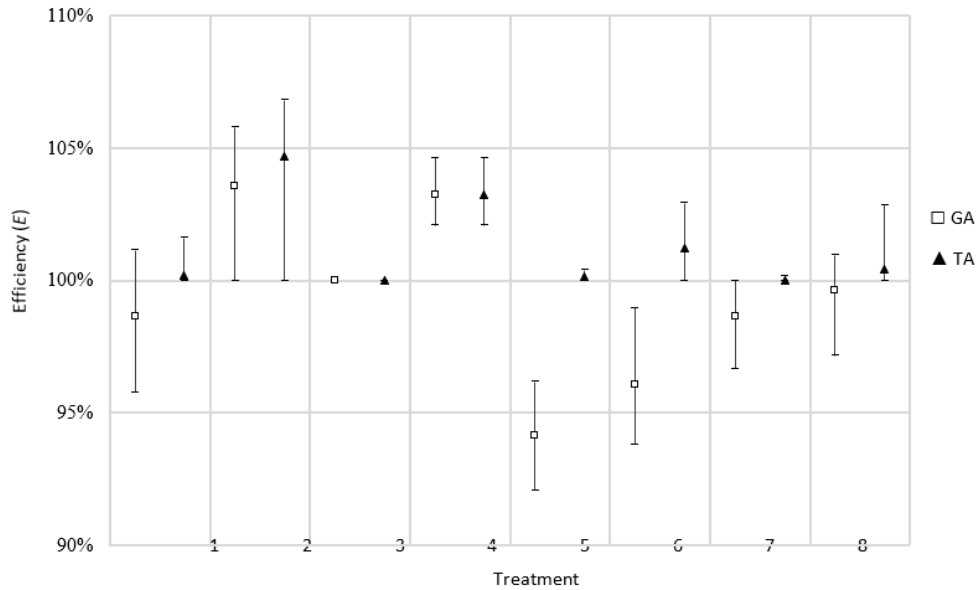


Figure 14. Efficiency results obtained for the *job cancellation* rescheduling factor

Once again, the TA demonstrates superior results, indicating an efficiency of 100% or higher in all treatments. The most influential factor is the number of remaining operations from the canceled job. A higher number of remaining operations leads to greater efficiency, as resource capacity is slightly relaxed.

The resulting deviation validates the performance of the TA, as shown in Fig. 15. There is a variability in the results, which is significantly reduced in various treatments. In general, the algorithm outperforms the GA, offering better results in 65% of the treatments in terms of efficiency and in 98% of the treatments in terms of stability. The percentage of remaining treatments for both metrics reveal similar performances for both algorithms.

The average efficiency of the TA is 2,3% higher than that of the GA. The highest difference in performance is observed in class IV, with an efficiency 4,4% higher on average when compared to the GA. In terms of the stability metric, the TA shows a standard deviation of 28 units, while the GA deviates by 67 units, thus proving that the former is a complete regeneration method that mitigates the nervousness to a greater extent than the latter.

Lastly, the efficiency and stability of a timetable can be conflictive performance metrics, so the person in charge of planning will have to make swift decisions, seeking to obtain a balanced productive system.

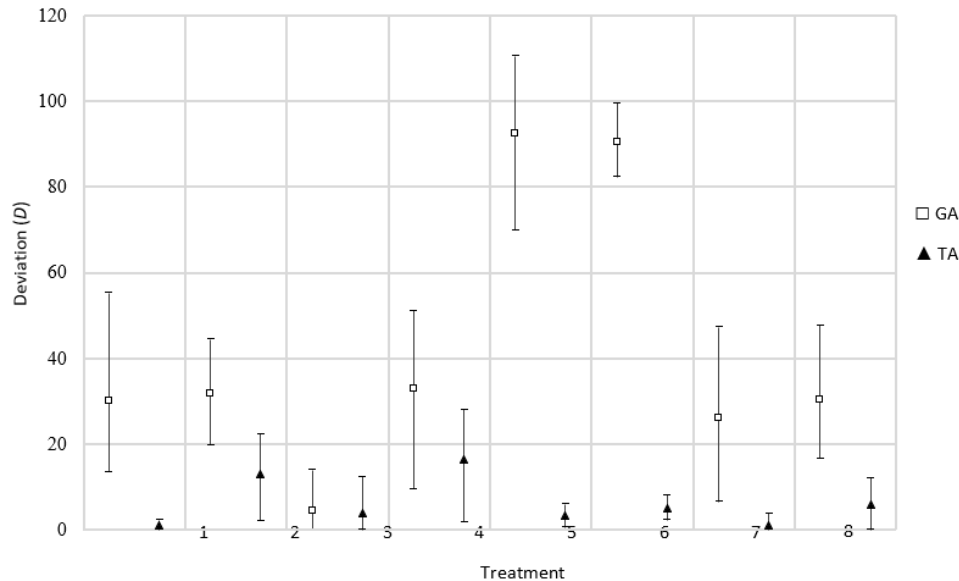


Figure 15. Deviation results obtained for the *job cancellation* rescheduling factor

4. Conclusions

This study focused on developing a computational algorithm to facilitate the job of the people in charge of scheduling production in manufacturing environments. Hence, the theoretical point of view was defined as the starting point in the definition of the Job Shop Scheduling Problem (JSSP).

Given the existing gap between theoretical models and real manufacturing environments, the appearance of unexpected events was included, as they alter the execution of timetables. This sought to provide the proposed algorithm with a more realistic scope. In this sense, a rescheduling framework was selected, which was used to define the Job Shop Rescheduling Problem (JSRP) approach.

Given the increasing complexity entailed by the addition of the aforementioned elements, an algorithm based on transgenic computing was proposed. It was developed while seeking to deliver high-quality production timetables in terms of efficiency and stability.

The performance of the algorithm was validated in both the predictive and the reactive phase. In the predictive phase, a set of well-known instances in JSSP literature were selected. The algorithm performed well, reaching the best-known value in 52% of the selected instances and similar values for the remaining ones. On average, these values do not exceed 1,3% of the difference for medium instances and 4,2% for large instances. Furthermore, as the instance size grows larger, the performance of the algorithm progressively declines. Therefore, the algorithm is not recommended for instances with more than 400 operations, *i.e.*, if similar performance levels are desired.

Regarding the reactive phase, the performance of the transgenic algorithm (TA) was compared to that of the genetic algorithm (GA). The former outperformed the latter, with better results in 65 % of treatments in terms of efficiency and 98 % of treatments in terms of stability. The percentage of remaining treatments for both metrics reveal similar performance levels for both algorithms.

5. Future work

Given the structure of TAs, there is a possibility that more complex agents can be designed, seeking to improve the performance of the algorithm in instances of higher complexity. On the other hand, the performance of the tool can be more comprehensively validated through a simulation-based study, even with the implementation in a real manufacturing environment.

Finally, given the scope of this work, which is limited to the design and validation of the TA applied to the JSRP, said algorithm could be integrated into real manufacturing environments through the design of a graphical user interface.

6. Author Contributions

All authors contributed equally to the research.

References

- [1] J. K. Lenstra and A. H. G. R. Kan, "Computational complexity of discrete optimization problems," *A. Discrete Math.*, vol. 4, 2005, pp. 121-140. [https://doi.org/10.1016/S0167-5060\(08\)70821-5](https://doi.org/10.1016/S0167-5060(08)70821-5) ↑2, 3
- [2] J. R. King, "The theory-practice gap in job-shop scheduling," *Prod. Eng.*, vol. 55, no. 3, pp. 137-143, 1976. <https://doi.org/10.1049/tpe.1976.0044> ↑3, 5
- [3] G. E. Vieira, J. W. Herrmann, and E. Lin, "Rescheduling manufacturing system: A framework of strategies, policies, and methods," *J. Sched.*, vol. 6, no. 1, pp. 39-62, 2003. <https://doi.org/10.1023/A:1022235519958> ↑3, 5, 6, 11, 25
- [4] H.-L. Fang, P. Ross, and D. Corne, "A promising genetic algorithm approach to job-shop scheduling, rescheduling, and open-shop scheduling problems," in *Fifth Int. Conf. Genet. Algorithms*, no. 623, pp. 375-382, 1993. ↑3, 5, 7
- [5] H. Li, Z. Li, L. X. Li, and B. Hu, "A production rescheduling expert simulation system," *Eur. J. Oper. Res.*, vol. 124, no. 2, pp. 283-293, 2000. [https://doi.org/10.1016/S0377-2217\(99\)00381-1](https://doi.org/10.1016/S0377-2217(99)00381-1) ↑3, 5
- [6] Y.-C. E. Li and W. H. Shaw, "Simulation modeling of a dynamic job shop rescheduling with machine availability constraints," *Comput. Ind. Eng.*, vol. 35, no. 1-2, pp. 117-120, 1998. [https://doi.org/10.1016/S0360-8352\(98\)00034-5](https://doi.org/10.1016/S0360-8352(98)00034-5) ↑3, 5

- [7] P. Moratori, S. Petrovic, and A. Vázquez, "Match-up strategies for job shop rescheduling," in *Int. Conf. Ind. Eng. Other App. Applied Intel. Sys.*, 2008, pp. 119-128. https://doi.org/10.1007/978-3-540-69052-8_13 ↑3, 5
- [8] R. E. M. Bastos, "Investigação de modelos e algoritmos para o problema do caixeiro viajante com múltiplos passageiros e lotação," doctoral thesis Universidade Federal do Rio Grande do Norte, Natal, 2023. ↑3, 8
- [9] E. Gouvêa and M. Goldbarg, "ProtoG: A computational transgenetic algorithm," in *MIC 2001-4th Metaheuristics*, 2001, pp. 625-630. ↑3, 8, 9, 10, 11
- [10] M. Goldbarg, E. Goldbarg, and P. Quadr, "Transgenética computacional: Uma aplicação ao problema quadrático de alocação," *Pesqui. Operacional*, vol. 22, pp. 359-386, 2002. <https://doi.org/10.1590/S0101-74382002000300005> ↑3, 8, 10
- [11] E. F. G. Goldbarg, M. C. Goldbarg, and L. B. Bagi, "Transgenetic algorithm: A new evolutionary perspective for heuristics design," in *Proc. GECCO 2007 Genet. Evol. Comput. Conf. Companion Mater.*, pp. 2701-2708, 2007. <https://doi.org/10.1145/1274000.1274040> ↑3, 8, 9, 10, 11
- [12] M. C. Goldbarg and E. Gouvêa, "Extra-intracellular transgenetic algorithm applied to the graph coloring problem," *Design*, pp. 321-326, 2001. ↑3, 8, 10, 11
- [13] E. F. G. Goldbarg, M. C. Goldbarg, and W. E. Costa, "A transgenetic algorithm for the permutation flow-shop sequencing problem," *WSEAS Trans. Syst.*, vol. 1, no. 3, pp. 40-45, 2004. ↑3, 11
- [14] E. L. Lawler, J. K. Lenstra, A. H. G. R. Kan, and D. B. Shmoys, "Sequencing and scheduling: Algorithms and complexity," *Handbooks Oper. Res. Manag. Sci.*, vol. 4, pp. 445-522, 1993. [https://doi.org/10.1016/S0927-0507\(05\)80189-6](https://doi.org/10.1016/S0927-0507(05)80189-6) ↑3
- [15] M. L. Pinedo, *Scheduling: Theory, algorithms, and systems*, 6th ed., New York, NY, USA: Springer, 2022. <https://doi.org/10.1007/978-3-031-05921-6> ↑3
- [16] R. Cheng, M. Gen, and Y. Tsujimura, "A tutorial survey of job-shop scheduling problems using genetic algorithms. I. Representation," *Comput. Ind. Eng.*, vol. 30, no. 4, pp. 983-997, 1996. [https://doi.org/10.1016/0360-8352\(96\)00047-2](https://doi.org/10.1016/0360-8352(96)00047-2) ↑4, 7, 12, 13
- [17] V. Suresh and D. Chaudhuri, "Dynamic scheduling: A survey of research," *Int. J. Prod. Economics*, vol. 32, no. 1, pp. 53-63, 1993. [https://doi.org/10.1016/0925-5273\(93\)90007-8](https://doi.org/10.1016/0925-5273(93)90007-8) ↑4
- [18] Y. An, X. Chen, K. Gao, L. Zhang, Y. Li, and Z. Zhao, "A hybrid multi-objective evolutionary algorithm for solving an adaptive flexible job-shop rescheduling problem with real-time order acceptance and condition-based preventive maintenance," *Expert Syst. App.*, vol. 212, art. 118711, Feb. 2023. <https://doi.org/10.1016/j.eswa.2022.118711> ↑5
- [19] C. Bierwirth and D. C. Mattfeld, "Production scheduling and rescheduling with genetic algorithms," *Evol. Comput.*, vol. 7, no. 1, pp. 1-17, 1999. <https://doi.org/10.1162/evco.1999.7.1.1> ↑5, 23
- [20] S. F. Smith, "Reactive scheduling systems," in *Intelligent scheduling systems*, New York, NY, USA: Springer, 1995, pp. 155-192. https://doi.org/10.1007/978-1-4615-2263-8_7 ↑6, 7
- [21] J. C. Bean, J. R. Birge, J. Mittenthal, and C. E. Noon, "Matchup scheduling with multiple resources, release dates and disruptions," *Oper. Res.*, vol. 39, no. 3, pp. 470-483, 1991. <https://doi.org/10.1287/opre.39.3.470> ↑7

- [22] Y. Zhang and F. Tao, *Optimization of manufacturing systems using the internet of things*, London, UK: Academic Press, 2016. ↑7
- [23] R.-K. Li, Y.-T. Shyu, and S. Adiga, "A heuristic rescheduling algorithm for computer-based production scheduling systems," *Int. J. Prod. Res.*, vol. 31, no. 8, pp. 1815-1826, 1993. <https://doi.org/10.1080/00207549308956824> ↑7
- [24] H.-H. Wu and R.-K. Li, "A new rescheduling method for computer based scheduling systems," *Int. J. Prod. Res.*, vol. 33, no. 8, pp. 2097-2110, 1995. <https://doi.org/10.1080/00207549508904804> ↑7
- [25] L. K. Church and R. Uzsoy, "Analysis of periodic and event-driven rescheduling policies in shops," *Int. J. Comput. Integr. Manuf.*, vol. 5, no. 3, pp. 153-163, 1992. <https://doi.org/10.1080/09511929208944524> ↑7
- [26] G. E. Vieira, J. W. Herrmann, and E. Lin, "Analytical models to predict the performance of a single-machine system under periodic and event-driven rescheduling strategies," *Int. J. Prod. Res.*, vol. 38, no. 8, pp. 1899-1915, 2000. <https://doi.org/10.1080/002075400188654> ↑7
- [27] M. Tomassini, "A survey of genetic algorithms," in *Annual reviews of computational physics III*, X., Ed., Singapore: World Scientific, 1995, pp. 87-118. https://doi.org/10.1142/9789812830647_0003 ↑7
- [28] J. H. Holland et al., *Adaptation in natural and artificial systems: an introductory analysis with applications to biology, control, and artificial intelligence*, Cambridge, MA, USA: MIT Press, 1992. <https://doi.org/10.7551/mitpress/1090.001.0001> ↑7
- [29] Z. H. Ahmed, "A hybrid genetic algorithm for the bottleneck traveling salesman problem," *ACM Trans. Embedded Comp. Syst.*, vol. 12, no. 1, pp. 1-10, 2013. <https://doi.org/10.1145/2406336.2406345> ↑7
- [30] G. M. Morris et al., "Automated docking using a Lamarckian genetic algorithm and an empirical binding free energy function," *J. Comput. Chem.*, vol. 19, no. 14, pp. 1639-1662, 1998. [https://doi.org/10.1002/\(SICI\)1096-987X\(19981115\)19:14<1639::AID-JCC10>3.0.CO;2-B](https://doi.org/10.1002/(SICI)1096-987X(19981115)19:14<1639::AID-JCC10>3.0.CO;2-B) ↑7
- [31] P. Moscato and C. Cotta, "A gentle introduction to memetic algorithms," in *Handbook of Metaheuristics*, Boston, MA, USA: Kluwer Academic Publishers, 2003, pp. 105-144. https://doi.org/10.1007/0-306-48056-5_5 ↑7
- [32] N. Krasnogor and J. Smith, "A tutorial for competent memetic algorithms: Model, taxonomy, and design issues," *IEEE Trans. Evol. Comput.*, vol. 9, no. 5, pp. 474-488, Oct. 2005. <https://doi.org/10.1109/TEVC.2005.850260> ↑7
- [33] H. C. Plotkin, "Non-genetic transmission of information: Candidate cognitive processes and the evolution of culture," *Behav. Processes*, vol. 35, no. 1, pp. 207-213, 1995. [https://doi.org/10.1016/0376-6357\(95\)00056-9](https://doi.org/10.1016/0376-6357(95)00056-9) ↑7, 10
- [34] E. Chattoe-Brown, "Just how (un)realistic are evolutionary algorithms as representations of social processes?" *J. Artif. Soc. Soc. Simul.*, vol. 1, no. 3, pp. 1-2, 1998. ↑7, 10
- [35] P. Merz and B. Freisleben, "A comparison of memetic algorithms, tabu search, and ant colonies for the quadratic assignment problem," in *1999 Cong. Evol. Comp.-CEC99 (Cat. No. 99TH8406)*, 1999, vol. 3, pp. 2063-2070. ↑10

- [36] N. J. Radcliffe and P. D. Surry, "Formal memetic algorithms," *Evolutionary Computing: AISB Workshop*, 1994. https://doi.org/10.1007/3-540-58483-8_1 ↑10
- [37] R. Wright, "Nonzero: The logic of human destiny," *Vintage*, vol. 46, no. 46, art. 11, 2002. ↑10
- [38] E. O. Wilson, "Consilience: The unity of knowledge," *Vintage*, vol. 31, 1999. ↑10
- [39] A. O. Barboza, "Simulação e técnicas da computação evolucionária aplicadas a problemas de programação linear inteira mista," doctoral thesis, Universidade Tecnológica Federal do Paraná, Curitiba, 2005. ↑11
- [40] Goldbarg, E. F. G., Castro, M. P., and Goldbarg M. C., "A transgenetic algorithm for the gas network pipe sizing problem," *Computational Methods*, vol. 1, pp. 893-904, 2006. ↑11
- [41] J. S. Dhingra, K. L. Musser, and G. L. Blankenehip, "Reactive operations scheduling for flexible manufacturing systems," in *24th Conf. Winter Sim.*, 1993. <https://doi.org/10.1145/167293.167745> ↑11
- [42] A. Dutta, "Reacting to scheduling exceptions in FMS environments," *IIE Trans.*, vol. 22, no. 4, pp. 300-314, 1990. <https://doi.org/10.1080/07408179008964185> ↑11
- [43] V. Subramaniam and A. S. Raheja, "mAOR: A heuristic-based reactive repair mechanism for job shop schedules," *Int. J. Adv. Manuf. Technol.*, vol. 22, no. 9-10, pp. 669-680, 2003. <https://doi.org/10.1007/s00170-003-1601-6> ↑11
- [44] A. Arisha, P. Young, and M. El Baradie, "Job shop scheduling problem: An overview," in *Int. Conf. Flex. Autom. Intell. Manuf. (FAIM 01)*, 2001, pp. 682-693. ↑11, 19
- [45] H. Fisher and G. L. Thompson, *Probabilistic learning combinations of local job-shop scheduling rules*, Englewood Cliffs, NJ, USA: Prentice Hall, 1963. ↑19
- [46] J. Adams, E. Balas, and D. Zawack, "The shifting bottleneck procedure for job shop scheduling," *Manage. Sci.*, vol. 34, no. 3, pp. 391-401, Mar. 1988. <https://doi.org/10.1287/mnsc.34.3.391> ↑19, 20
- [47] T. Yamada and R. Nakano, "A genetic algorithm applicable to large-scale job-shop problems," *Parallel Prob. Solv. Nature*, vol. 2, pp. 283-292, 1992. ↑19, 20
- [48] D. Applegate and W. J. Cook, "A computational study of the job-shop scheduling problem," *INFORMS J. Comput.*, vol. 3, pp. 149-156, 1991. <https://doi.org/10.1287/ijoc.3.2.149> ↑19, 21
- [49] S. Lawrence, "Resource constrained project scheduling: an experimental investigation of heuristic scheduling techniques," graduate thesis, Carnegie-Mellon University, 1984. ↑19, 21
- [50] E. Taillard, "Benchmarks for basic scheduling problems," *Eur. J. Oper. Res.*, vol. 64, no. 2, pp. 278-285, 1993. [https://doi.org/10.1016/0377-2217\(93\)90182-M](https://doi.org/10.1016/0377-2217(93)90182-M) ↑19, 21
- [51] M. Zweben and M. Fox, *Intelligent scheduling*, San Francisco, CA, USA: Morgan Kaufman Publishers Inc., 1994. ↑22
- [52] G. A. Deac and D. T. Lancu, "Trading strategy hyper-parameter optimization using genetic algorithm" in *24th Int. Conf. Control Syst. Comp. Sci. (CSCS)*, 2023, pp. 121-127. <https://doi.org/10.1109/CSCS59211.2023.00028> ↑25

- [53] K. Gao, F. Yang, M. Zhou, Q. Pan, and P. N. Suganthan, "Flexible job-shop rescheduling for new job insertion by using discrete Jaya algorithm," *IEEE Trans. Cybernetics*, vol. 49, no. 5, pp. 1944-1955, May 2019. <https://doi.org/10.1109/TCYB.2018.2817240> ↑3,7
- [54] L. Wang, C. Luo, and J. Cai, "A variable interval rescheduling strategy for dynamic flexible job shop scheduling problem by improved genetic algorithm," *J. Adv. Trans.*, vol. 2017, pp. 1-12, Jan. 2017. <https://doi.org/10.1155/2017/1527858> ↑6
- [55] N. Kundakci and O. Kulak, "Hybrid genetic algorithms for minimizing makespan in dynamic job shop scheduling problem," *Comp. Ind. Eng.*, vol. 96, pp. 31-51, Jun. 2016. <https://doi.org/10.1016/j.cie.2016.03.011> ↑3,5,7

Néstor Andrés Beltrán Bernal

Industrial engineer, Universidad Distrital Francisco José de Caldas, MSc in Industrial Engineering, Universidad Distrital Francisco José de Caldas. Lecturer, Industrial Engineering Program, Department of Engineering, Universidad de la Salle.

Email: nbeltran@unisalle.edu.co

José Ignacio Rodríguez Molano

Industrial engineer, Universidad Distrital Francisco José de Caldas. PhD in Informatics Engineering, Universidad de Oviedo. Full profesor, Industrial Engineering Curricular Project, Department of Engineering, Universidad Distrital Francisco José de Caldas.

Email: jirodriguez@udistrital.edu.co

Diego Ernesto Mendoza Patiño

Industrial engineer, Universidad Distrital Francisco José de Caldas. PhD in Administration, Universidad Autónoma de Querétaro, Mexico. Associate researcher, Department of Engineering, Universidad Antonio Nariño.

Email: diego.mendoza@uan.edu.co



Research

Deduction and Application of the Average Switch Model in Power Electronic Devices for Simulation Time Reduction

Deducción y aplicación de modelo promedio del interruptor en dispositivos de electrónica de potencia para reducción del tiempo de simulación

Santiago Benavides-Córdoba , Anamaría Romero-Carvajal , Nicolás Muñoz-Galeano  , Juan Bernardo Cano-Quintero , Jesús M. López-Lezama 

Universidad de Antioquia, Departamento de Ingeniería Eléctrica, Grupo de investigación GIMEL, Medellín, Colombia 

Abstract

Context: Time is a crucial issue in the simulation of power electronics (PE) devices, even more when these elements are integrated into microgrids.

Method: This paper deals with the deduction of the average switch model for PE devices with the purpose of reducing simulation times. For doing this, the average model is only applied over the power switches of PE devices, not being applied over the complete topology as traditionally done. The proposed average model switch permits eliminating the ripple of voltage and currents but keeping the transient of the signals. The average model switch is derived for Boost and Buck converter switches and then generalized to power inverter switches. The proposed approach is validated using OpenModelica software.

Results: A system featuring a battery, a DC/DC converter, and an inverter connected to the power grid was simulated. A comparison was performed between a simulation that considers the power switches and a simulation that uses the proposed average model switch, the time simulation was reduced up to 99.788%, which validates the proposed approach.

Conclusions: The proposed average switch model significantly reduces simulation times. This method offers a promising way to streamline power electronics device simulations, particularly in the context of microgrids and other applications where time efficiency is critical.

Keywords: Power electronics, Microgrids, Average model, Inverter, Converter

Article history

Received:
22th/Sep/2023

Modified:
1st/Nov/2023

Accepted:
5th/Dec/2023

Ing., vol. 29, no. 1,
2023. e21303

©The authors;
reproduction right
holder Universidad
Distrital Francisco
José de Caldas.

Open access



* **Correspondence:** nicolas.munoz@udea.edu.co

Resumen

Contexto: El tiempo es un factor crucial en la simulación de dispositivos de electrónica potencia (EP), especialmente cuando estos elementos se integran en microrredes.

Método: Este artículo deduce el modelo de interruptor promedio para dispositivos de EP con el propósito de reducir los tiempos de simulación. Para lograr esto, el modelo promedio se aplica únicamente a los interruptores de potencia de los dispositivos de EP, sin aplicarse a toda la topología como se hace tradicionalmente. El modelo promedio propuesto permite eliminar la oscilación de voltaje y corriente, pero conserva el comportamiento transitorio de las señales. El modelo promedio del interruptor se deriva para interruptores convertidores Boost y Buck y luego se generaliza a interruptores de inversores de potencia. El enfoque propuesto se valida utilizando el software OpenModelica.

Resultados: Se simuló un sistema que incluye una batería, un convertidor DC/DC y un inversor conectado a la red eléctrica. Se realizó una comparación entre una simulación que considera los interruptores de potencia y una simulación que utiliza el modelo promedio del interruptor propuesto, lo que redujo el tiempo de simulación hasta en un 99,788 %, validando así el modelo propuesto.

Conclusiones: El modelo de interruptor promedio propuesto reduce significativamente los tiempos de simulación. Este método ofrece una forma prometedora de agilizar las simulaciones de dispositivos de electrónica de potencia, especialmente en el contexto de microrredes y otras aplicaciones donde la eficiencia en el tiempo es fundamental.

Palabras clave: Electrónica de potencia, Microrredes, Modelo promedio, inversor, convertidor

Table of contents

	Page		
1. Introduction	2		
2. Deduction of average model for power electronics switches	5		
2.1. Deduction of average model for Buck converter switch	5	2.3. Deduction of average model for power inverters	10
2.2. Deduction of average model for Boost converter switch	8	2.4. Mode 1: Power inverter working as DC-AC converter	11
		2.5. Mode 2: Power inverter working as AC-DC converter	11
		3. Simulation results	12
		3.1. Subsection	16
		4. Conclusions	18
		References	20

1. Introduction

Power electronics (PE) devices are switched systems used for the exchange or conversion of energy. Their switched nature causes ripples in voltage and current signals. Such ripples are commonly reduced by using large inductors and capacitors; however, they are not completely eliminated in the final result. In view of the unavoidable presence of ripples, PE these devices are modeled using the average value of the signal (average model), ignoring the ripple (1,2). However, applying the average model not only eliminates the ripple but also the transient of voltages and currents. The transient is fundamental since

it allows to determine the extreme operating conditions of the system. Therefore, simulations must be performed to find the transient, including the dynamics of the switches and diodes which leads to a high computational burden and long simulation times.

Several applications of the average converter model are found in the specialized literature of PE converters. In (3), the modeling and control of a Floating Interleaved Boost converter (FIBC) is developed to meet the requirements of a Fuel Cell (FC) battery for vehicular applications. The average model allows reaching adequate control of the converter to improve the voltage gain and minimize the input current ripple and thus ensure the sustainability of the FC. The authors in (4) analyze the average models of nonlinear fourth-order converters operating in continuous conduction mode (CCM) to predict the frequency response. This method is based on the average model and is simpler and easier to implement than other conventional models. A detailed comparison of the CUK, D1 and D2 converters is presented in (5); using the average model, the performance of the converters is evaluated by carrying out simulations in a PV system. The authors in (6) proposed a multi-input Boost converter for renewable energy sources (RES) connected in parallel. In this case, the converter performance is maximized to maintain a constant output voltage; basically, starting from the average model, a small-signal CCM model is developed and the line-output and control-output transfer functions are derived. In (7), a PWM tapped-inductor Buck DC/DC converter is presented that aims to substantially reduce the output voltage by working with a comfortable duty cycle range and using a single-stage power converter; the average model is the basis for deriving the small-signal model to obtain the line-to-output and control-to-output transfer functions. The authors in (8) proposed a fractional order model for a Boost converter in discontinuous conduction mode (DCM), the modeling starts applying the average model of the fractional order Boost converter, and then the transfer function that relates the duty cycle with the output voltage in DCM is obtained. In (9), an equalizing converter circuit for a Half-Bridge Boost Converter operating in DCM is developed to solve the voltage unbalance that reduces the power factor. The average model is used to analyze in detail how the equalizer eliminates the voltage unbalance. The authors in (10) develop a small-signal average model of a single-stage bridgeless Boost half-bridge (AC/DC) converter with bidirectional switches using the average model. The mathematical model obtained is used to design a PI controller that proves to be stable. In (11), the transfer functions of a Buck-Boost converter are obtained using the average model of the converter. The authors in (12) present small-signal modeling for a bidirectional quasi-Z-source converter from the average model technique and provide a design guide for an AC controller for improving the stability of the converter. The authors in (13) develop modeling techniques using the average model of DC/DC converters, taking into account the non-ideal characteristics of the switching devices and improving the performance of the converters under analysis. In (14), a Luo DC-DC converter is proposed for hybrid electric vehicles. The authors perform the modeling of the converter with the state space averaging method and the average model. The authors in (15) develop a method to dynamically model the coupled-inductor Double-Boost converter. The average model of the converter is deduced to obtain the impact of the leakage inductance by using equivalent resistors.

The average model has also been widely used in PE inverters. The authors in (16) present a detailed mathematical model of a non-ideal Z-Source inverter (ZSIs) with non-minimum phase

behavior to analyze the influence of the snubber capacitance using average model approaches. In (17), a multi-harmonic modeling technique for PWM-driven DC-AC inverters not ideal for low-power applications is introduced. The average model is used to anticipate the AC signal response along with the average values of the DC signal taking into account higher-order harmonic effects.

In microgrid (MG) applications, the authors in (18) discuss the droop control strategy for a voltage source inverter (VSI) in the power exchange mode with MGs or the main grid; for this, they analyze the average model of the three-phase VSI and obtain the voltage and current transfer functions. The results show that the system maintains nominal frequency and voltage. The authors in (19) develop a fuzzy logic-cyclic reports modulation control based on the average model to improve the output power quality of the single-phase series five-cell inverter. Simulation results show that the proposed control offers high performance. The authors in (20) derive the small-signal model of a three-level neutral-point-clamped inverter connected to the grid with LCL filter. The process starts with the circuit equations and the average model; finally, a control for the grid current is designed using the average model. In (21), a time domain model called harmonic average model (HM) is presented to estimate the harmonic currents generated by the inverters, In HM the superposition principle is applied to include the dead time and switching effects provided by the average model. Also, the HM is validated in wind and a photovoltaic generation. The results indicate that HM follows the references and accurately estimates the harmonic spectra. The authors in (22) develop a circulating current model based on the average model that takes into account the effects of dead time for Parallel Two-Level Three-Phase Voltage-Source Inverters.

The specialized literature extensively uses the average model in PE devices for obtaining the small signal model, which allows obtaining the stationary state of the electrical variables. Furthermore, this permits to establish control strategies and find the nominal values of PE devices in the design stage. The stationary state permits defining set points of the variables that PE devices must follow. Although the average model has multiple applications, the simulations that must be carried out to verify the dynamic behavior must include the transient in order to verify adequate stabilization times and wave overshoots; in this case, it is not possible to use the average model as it has been conventionally used since transient information is lost.

MG simulations based on power electronics devices require the transient of the signals to be captured in order to determine how the connected devices interact. In order to obtain the transient, the differential equations or the circuit implementation of the devices must be used, which leads to high computation times. In these simulations, slow and fast dynamics are obtained. The slow dynamics correspond to the transient that is given by the resistive, inductive, and capacitive values as well as the operating point, while the fast dynamics are given by the ripple of the signals that is produced by the switches and diodes. The main contribution of this paper is the application of the average model to the system consisting of the switch and diode in order to eliminate the fast dynamics (ripple) from the simulation but keep the slow dynamics. After eliminating the fast dynamics it is possible to obtain the transient of the signals using few computational resources and achieving low simulation times.

This paper is organized as follows: Section 2 presents the deduction of the average model for the Boost and Buck converter switches along with the average model of inverter switches. Section 3 compares simulations applied on a power electronics application that includes an inverter, a converter and a battery, using the proposed approach and the conventional simulation that uses power electronics switches. Section 4 concludes and highlights the most relevant aspects of the paper.

2. Deduction of average model for power electronics switches

The objective of this section is to derive the average model for switches and diodes of power electronics based devices. The switch model will be derived for the DC/DC Buck and Boost converters; subsequently the model will be generalized for the DC/AC inverter.

2.1. Deduction of average model for Buck converter switch

Figure 1 corresponds to the Buck converter, inside the box is defined the converter switching system composed by a diode (D), and an IGBT switch (SW). The average model deduction will only be performed for the switching system, without including the passive elements (inductors or capacitors), the source, and the load. This is to eliminate the high-frequency ripple inherent to the commutation of switches and diodes but to preserve the slow dynamics inherent to the other elements of the system. In order to deduce the average model of the switching system it is necessary to define for D and SW the following: 1) the polarities of D and SW labeled as v_{SW} and v_D , respectively; 2) the current senses of D and SW , labeled as i_d and i_{SW} , respectively; 3) the input voltage (v_i) of the switching system; and 4) the output current (i_o) of the switching system. The polarities and current directions of D and SW are defined when the element is directly polarized and conducting.

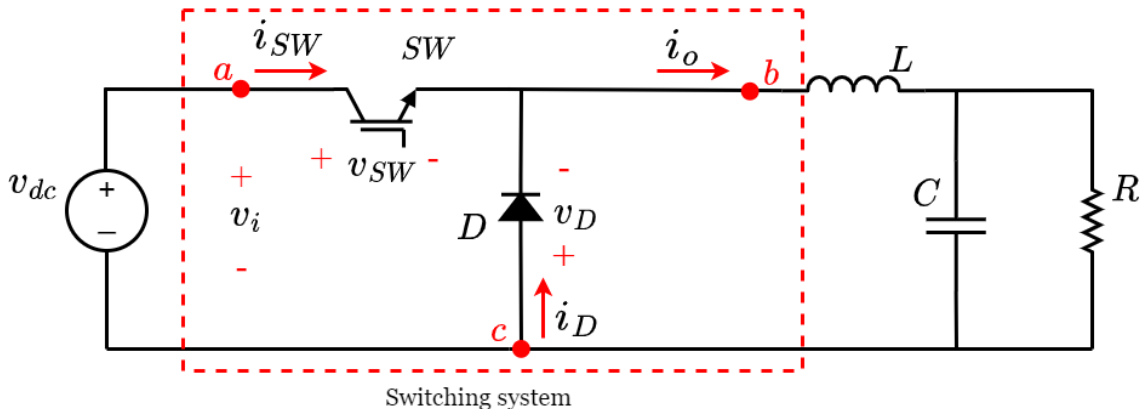


Figure 1. Buck Converter

For the modeling of the switching system it is assumed that the input voltage (v_i) and the output current (i_o) are constant for each switching cycle. The switching function u is also defined such that when $u = 1$ the IGBT closes and the diode is reverse polarized; on the other hand, when $u = 0$ the IGBT opens and the diode is directly polarized.

Figure 2a shows the switching system when $u = 1$. The diode is reverse polarized obtaining a voltage $v_D = -v_i$ and a current $i_d = 0$ while the switch being closed obtains a voltage $v_{SW} = 0$ and the current through it is $i_{SW} = i_o$. Figure 2b shows the switching system when $u = 0$. The diode when directly polarized obtains a voltage $v_D = 0$ and the current flowing through it will be $i_d = i_o$; on the other hand, the switch opens obtaining a voltage $v_{SW} = v_i$ and a current $i_{SW} = 0$.

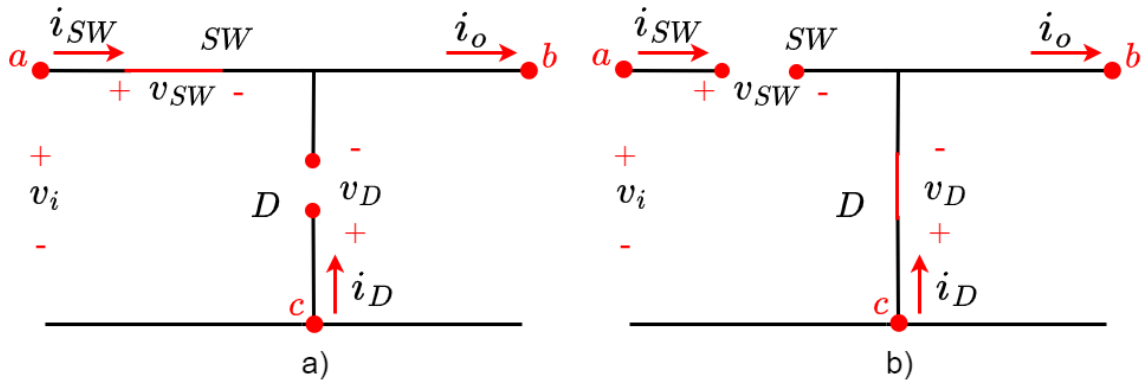


Figure 2. Buck converter switching system a) $u = 1$ y b) $u = 0$

Figure 3 illustrates the diode and switch voltage and current waveforms. Perfect alternation between their conduction states is assumed, *i.e.*, no simultaneous conduction or simultaneous non-conduction is possible. The average value (in a switching cycle) of the signals is defined as follows: the average diode voltage ($\langle V_d \rangle$), the average IGBT voltage ($\langle V_{SW} \rangle$), the average diode current ($\langle I_d \rangle$), the average switch current ($\langle I_{SW} \rangle$), and the average value of the function u ($D, 0 < D < 1$) corresponding to the duty cycle.

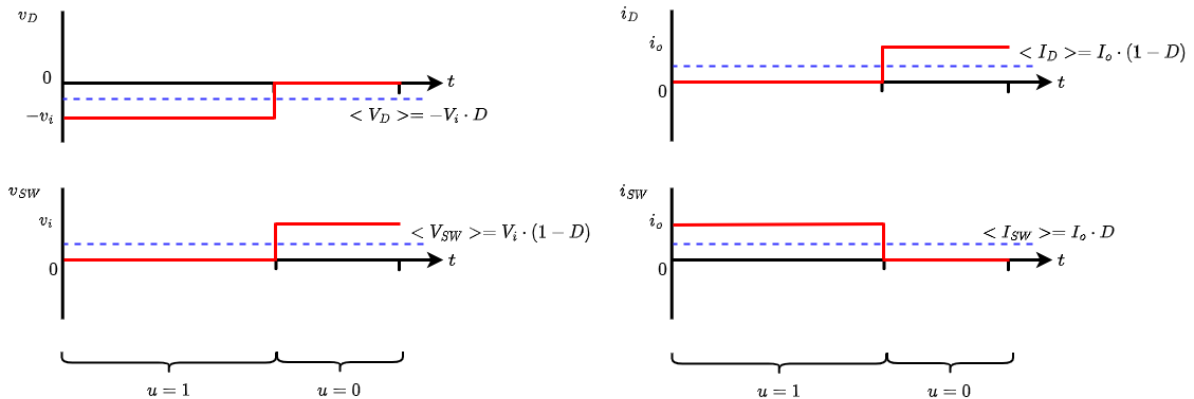


Figure 3. Buck converter waveforms

According to the above, it follows that:

$$\langle V_D \rangle = -V_i \cdot D \tag{1}$$

$$\langle V_{sw} \rangle = V_i \cdot (1 - D) \tag{2}$$

$$\langle I_d \rangle = I_o \cdot (1 - D) \tag{3}$$

$$\langle I_{sw} \rangle = I_o \cdot D \tag{4}$$

Equations (5) and (6) are obtained from the division of Equation (1) with Equation (2) and from the division of Equation (3) with Equation (4).

$$\frac{\langle V_D \rangle}{\langle V_{sw} \rangle} = \frac{-D}{(1 - D)} \tag{5}$$

$$\frac{\langle I_D \rangle}{\langle I_{sw} \rangle} = \frac{(1 - D)}{D} \tag{6}$$

According to Equations (5) and (6), the Buck converter switching system can be modeled with voltage and current dependent sources. Figure 4a shows the Buck converter switching system where the switch has been replaced by a voltage-dependent source and the diode by a current-dependent source. Figure 4b shows the Buck converter switching system where the switch has been replaced by a current-dependent source and the diode by a voltage-dependent source.

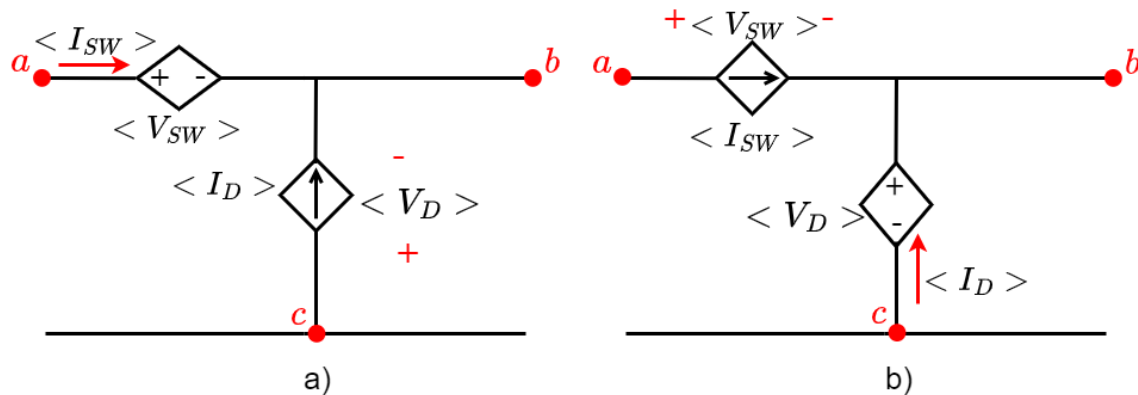


Figure 4. Buck converter with dependent current sources a) voltage and current y b) current and voltage

Note that the equivalent circuits proposed in Figure 4 allow solving the converter by means of conventional circuit analysis techniques without resorting to switching functions and neglecting the voltage and current ripple. In this way, it is possible to obtain the average transient and stationary behavior for each variable of the converter.

However, it is worth noting the assumptions that must be met for its use: a) the input voltage and output current must be constant during each switching cycle and b) there must be perfect alternation between the switch and the diode. In this case, the input voltage is related to the power supply whose value is constant (or slowly changing) in most applications. The output current is influenced by the inductor L which prevents it from changing abruptly as a result of switching. The alternating operation

of the diode and switch limits the application of this model to converters operating under the continuous conduction mode.

2.2. Deduction of average model for Boost converter switch

Figure 5 corresponds to the Boost converter. The converter switching system is depicted inside the box in dashed red, which is composed by a diode (D), and a switch (SW). The deduction of the average model will only be performed for the switching system, without including the passive elements (inductors or capacitors), the source, and the load. This is done to eliminate the high-frequency ripple inherent to the switching of these elements, and to preserve the slow dynamics inherent to the other elements of the system. In order to derive the average model of the switching system, it is necessary to define for D and SW the following: 1) the polarities of D and SW , labeled as v_D and v_{SW} , respectively; 2) the current direction of D and SW , labeled as i_D and i_{SW} , respectively; 3) the input current (i_i) of the switching system, and 4) the output voltage (v_o) of the switching system. The polarities and current directions of D and SW are defined when the element is directly polarized and conducting.

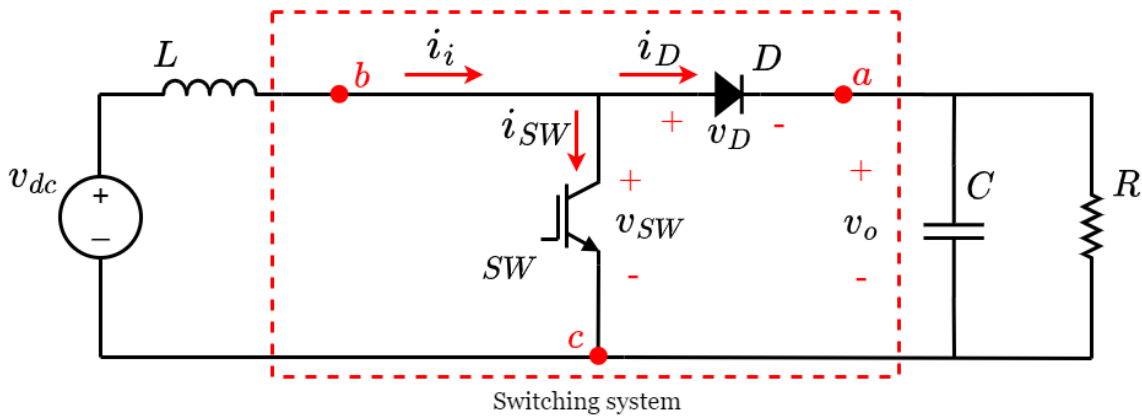


Figure 5. Boost Converter

For the modeling of the switching system it is assumed that the input current (i_i) and the output voltage (v_o) are constant for each switching cycle. The switching function u is also defined such that when $u = 1$ the IGBT closes and the diode is reversely polarized; conversely when $u = 0$ the IGBT opens and the diode is direct biased.

Figure 6a) shows the switching section when $u = 1$. The diode is reversely polarized obtaining a voltage $v_D = -v_o$ and a current $i_d = 0$ while the IGBT being closed obtains a voltage $V_{SW} = 0$ and a current $i_{SW} = i_i$. Figure 6b) depicts the switching section when $u = 0$. When the diode is directly polarized its voltage is $v_D = 0$ and the current flowing through it is $i_d = i_i$; in this case, the IGBT opens obtaining a voltage $v_{SW} = v_o$ and a current $i_{SW} = 0$.

Perfect alternation between the diode and switch conduction states is assumed, i.e., no simultaneous conduction or simultaneous non-conduction is possible. The average value (in a switching cycle) of the signals is defined as follows: the average diode voltage ($\langle V_d \rangle$), the average IGBT voltage ($\langle V_{SW} \rangle$),

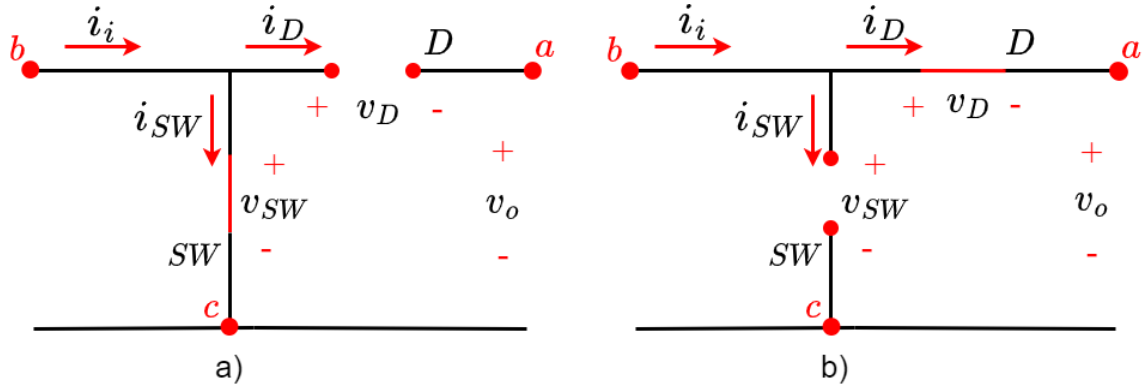


Figure 6. Switching system of the Boost converter when a) $u = 1$ and b) $u = 0$

the average diode current ($\langle I_d \rangle$), the average switch current ($\langle I_{SW} \rangle$), and the average value of the function u ($D, 0 < D < 1$) corresponding to the duty cycle. From the above, Equations (7), (8), (9), (10) are obtained.

$$\langle V_D \rangle = -V_i \cdot D \tag{7}$$

$$\langle V_{sw} \rangle = V_i \cdot (1 - D) \tag{8}$$

$$\langle I_d \rangle = I_o \cdot (1 - D) \tag{9}$$

$$\langle I_{sw} \rangle = I_o \cdot D \tag{10}$$

Equations (11) and (12) are obtained from the division of Equation (7) with Equation (8) and from the division of Equation (9) with Equation (10).

$$\frac{\langle V_D \rangle}{\langle V_{sw} \rangle} = \frac{-D}{(1 - D)} \tag{11}$$

$$\frac{\langle I_D \rangle}{\langle I_{sw} \rangle} = \frac{(1 - D)}{D} \tag{12}$$

According to Equations (11) and (12), the Boost converter switching system can be modeled with voltage and current-dependent sources. Figure 7a shows the Boost converter switching system where the switch has been replaced by a voltage-dependent source and the diode by a current-dependent source. Figure 7b shows the switching system of the Boost converter where the switch has been replaced by a current-dependent source and the diode by a voltage-dependent source.

Note the similarity to the deduction of the average model for the Buck converter. In this case, the constraints regarding abrupt changes are related to both, the input current and output voltage of the switching system. Sudden changes in the input current are limited by the inductor L and sudden changes of the output voltage are limited by the capacitor C .

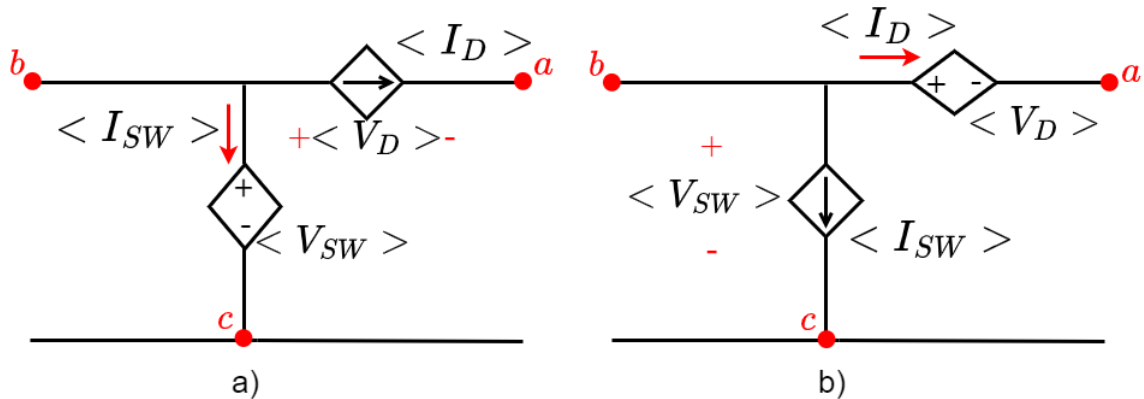


Figure 7. Boost converter with a) voltage- and current-dependent sources; and b) current- and voltage-dependent sources

2.3. Deduction of average model for power inverters

Figure 8 presents a bidirectional DC/AC inverter which is composed of a DC voltage source (v_{dc}), an AC voltage source (v_{ac}), two capacitors (C_1) and (C_2), an inductor (L), two switches (SW_1) and (SW_2) and two diodes (D_1) and (D_2).

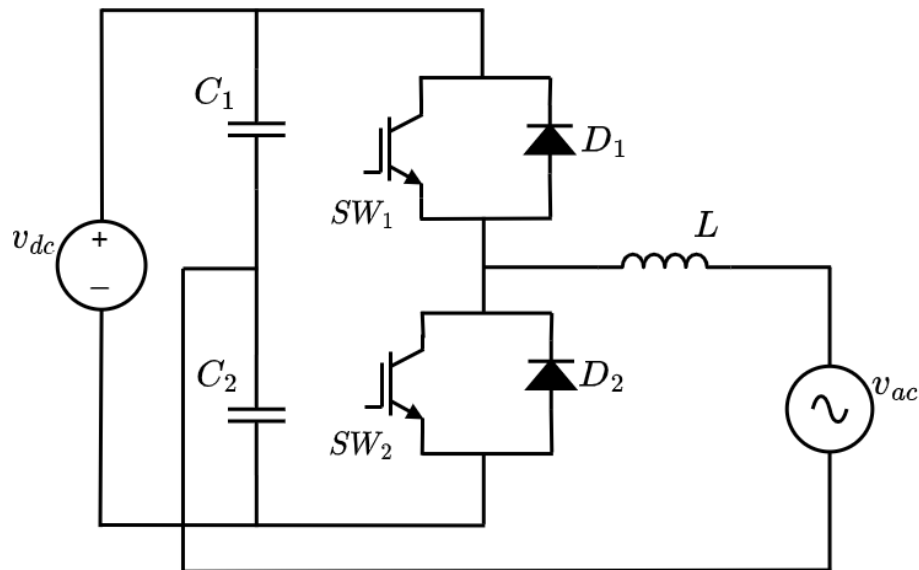


Figure 8. Inverter topology

The inverter has two operating modes: 1) In operating mode 1, the source and DC bus deliver power to the AC power system, in this operating mode the inverter delivers at the AC terminals a lower voltage with respect to the DC bus voltage. 2) In operating mode 2, the power system delivers power to the DC bus, in this operating mode the inverter increases the voltage at the DC terminals with respect to the inverter's AC voltage. The modes of operation are described below.

2.4. Mode 1: Power inverter working as DC-AC converter

In this mode of operation, the power flows from the DC bus to the power system. The inverter operates using the same semiconductors or topology of the Buck converter. The switches to be activated in this mode are SW_1 and D_2 . Note that Figure 9a, corresponds to the same topology of the Buck converter in Figure 1. Figure 9b results after replacing the controlled voltage and current sources in Figure 4a.

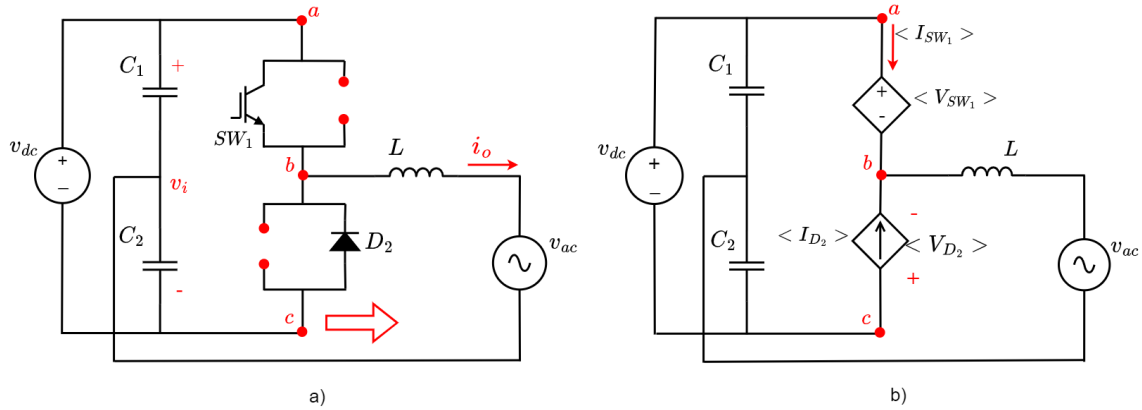


Figure 9. Inverter operation as DC-AC converter mode: a) switching state, b) model using voltage and current controlled sources

Using Equations (5) and (6) and being $n = \frac{D}{1-D}$, it follows that:

$$\langle I_{D_2} \rangle = \frac{1}{n} \cdot \langle I_{SW_1} \rangle \quad (13)$$

$$\langle V_{SW_1} \rangle = -\frac{1}{n} \cdot \langle V_{D_2} \rangle \quad (14)$$

2.5. Mode 2: Power inverter working as AC-DC converter

In this operating mode, the power flows from the power system to the DC bus. The inverter operates using the same semiconductors or topology of the Boost converter. The switches to be activated in this mode are SW_2 and D_1 . Note that Figure 10a, corresponds to the same topology of the Boost converter in Figure 5. Figure 10b results after replacing the controlled voltage and current sources in Figure 7b.

Using Equations (11) and (12) and being $n = \frac{D}{1-D}$, it follows that:

$$\langle I_{SW_2} \rangle = n \cdot \langle I_{D_1} \rangle \quad (15)$$

$$\langle V_{D_1} \rangle = -n \cdot \langle V_{SW_2} \rangle \quad (16)$$

Note that the circuit model of controlled voltage and current sources at terminals a,b, and c for operating mode 1 (Figure 9b) and operating mode 2 (Figure 10b) have the same structure. Note also that

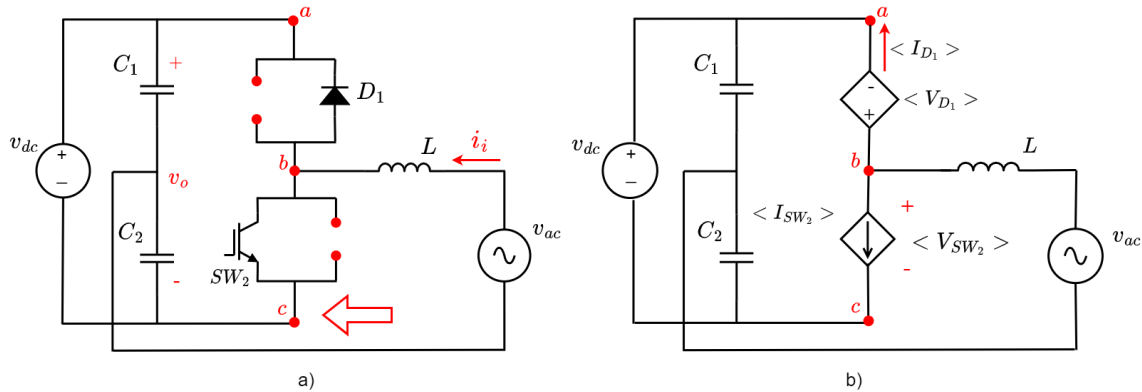


Figure 10. Inverter operation as AC-DC converter mode: a) switching state, b) model using current and voltage controlled sources

the model Equations governing the controlled sources for operating mode 1 (Equations (13) and (14)) and for operating mode 2 (Equations (15) and (16)) are the same. Observing the circuit model together with the equations model for both operating modes it can be seen that both models are equivalent; therefore, it is possible to simplify the two modes of operation into a single one and therefore model the inverter switch with a single controlled current source and a single controlled voltage source.

3. Simulation results

Figure 11 shows the system under study which is composed of a battery, a bidirectional DC/DC converter and a three-phase DC/AC bidirectional inverter connected to the power grid. The battery has a nominal voltage of 48V. Next is the DC/DC converter which is composed of an inductance $L = 30mH$ two pulse width modulated (PWM) switches and a capacitor $C = 20\mu F$. Next is the inverter which is made up of two balancing resistors $R_1 = R_2 = 1000\Omega$, two capacitors that make up a DC bus $C_1 = C_2 = 2200\mu F$, six sinusoidal PWM (SPWM) and the inductances $L_a = L_b = L_c = 30mH$ and resistors $R_a = R_b = R_c = 1\Omega$ that connect to the electrical network considered as $V_a = V_b = V_c = 120V$ AC at 50Hz.

The battery current control is carried out by the closed-loop control illustrated in Figure 12. The difference between the reference current I_{Ref} and the battery current I_{Bat} is fed to the PI_{I_L} controller which has an integral time of $T_s = 0,5s$ and a gain $K = 0,01$. In this way, the control signal D is obtained. Finally, the D signal is compared with a triangular signal using the *SwitchingPWM* block to obtain the periodic signal that is applied to the converter switches. To avoid the two converter switches to be closed at the same time, the dead time given by the PWM_{SW} block is used. The value of the reference current at $t = 0s$ is $I_{Ref} = 30A$ and at $t = 2s$ is $I_{Ref} = -50A$.

Since the three-phase DC/AC inverter has non-minimum phase, it is necessary to use a cascade controller to control the DC bus voltage made up of C_1 and C_2 . Figure 13 shows the implemented control strategy which uses the *dqz* transform to the inductor currents L_a , L_b and L_c through the SW_{con}

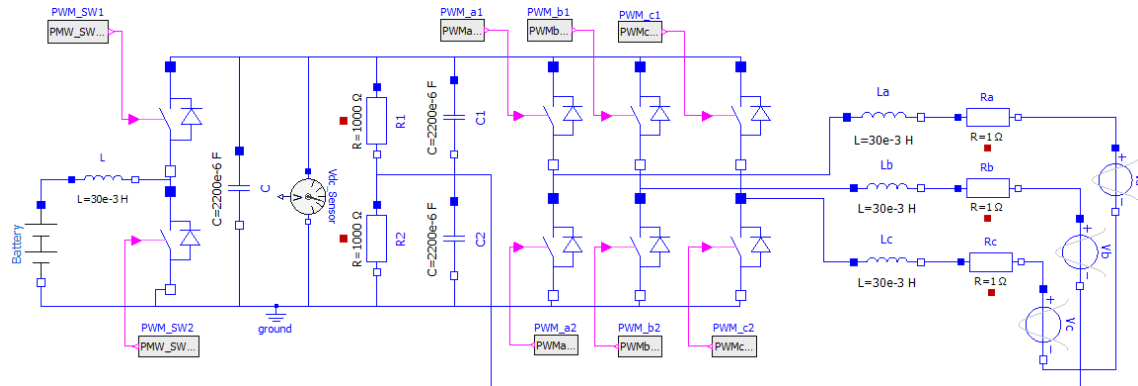


Figure 11. Simulation of inverter using conventional switches

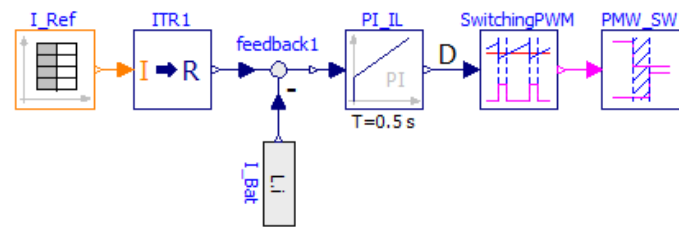


Figure 12. Current control topology, conventional switches

block. This gives the current I_d which guarantees the active power flow and I_q which guarantees the reactive power flow. Thus, current I_d is needed to control the DC voltage of capacitor C and current I_q is needed to control the reactive compensation of the system.

The DC bus voltage control consists initially in obtaining the difference between the reference voltage V_{Ref} and the DC bus voltage V_{DC} measured by the V_{dc_sensor} sensor in Figure 11. Then, this difference is taken to the $PI_{V_{dc}}$ controller which has an integral time $T_s = 0,019s$ and a gain $K = 0,335$. The resulting control signal is compared to the current I_d and the difference is taken to the PI_d controller which has a time integral $T_s = 0,00012$ and a gain $K = -1,8054$. The result is the control signal for the capacitor voltage C at dqz . The reference voltage value at $t = 0s$ is $V_{Ref} = 610V$ and at $t = 1,3s$ $V_{Ref} = 615V$.

To compensate the reactive current of the system, the difference between the reference current I_{qRef} and I_q is made. This information is given to the controller PI_q which has an integral time of $T_s = 0,00011s$ and a gain $K = -1,68069$. This provides the control with the signal for reactive current compensation at dqz .

The control signals obtained are transformed with the inverse transform of dqz and the signals A, B, C are obtained. These sinusoidal signals are normalized and an offset is added in the blocks Da, Db, Dc ; this to obtain positive signals that can be compared by the $SwitchingPWM$ blocks and subsequently introduce dead time for each pair of switches of the three branches of the inverter.

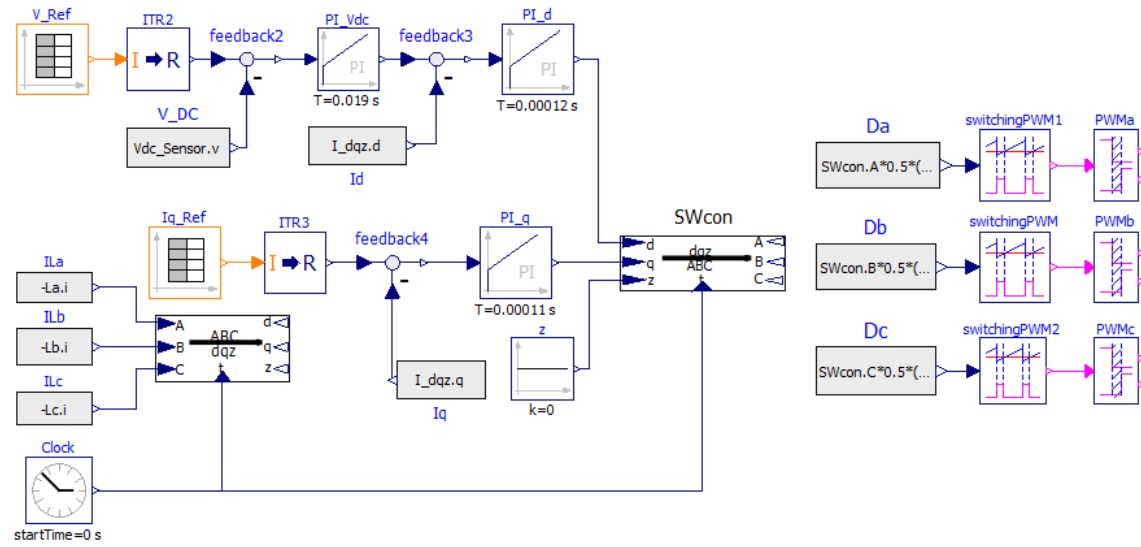


Figure 13. Voltage control topology, conventional switches

Figure 14 shows the system under study applying the proposed average switch model. Note that the switches have been replaced by voltage and current-dependent sources and the equations of these sources correspond to the equations of the average switch model.

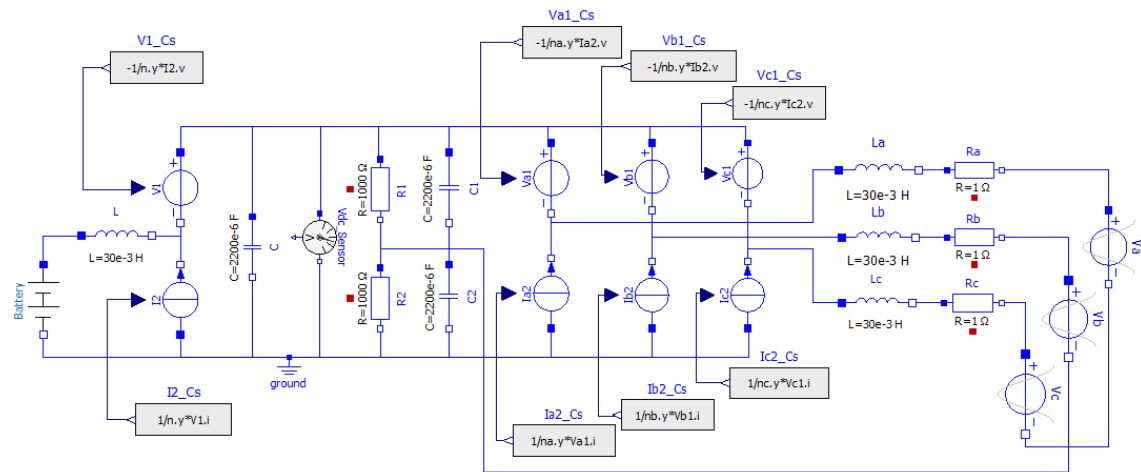


Figure 14. Simulation of inverter using the average switch model

The battery current control of the system under study using the proposed model is illustrated in Figure 15. The control is performed in the same way as developed for the system with switches but differs in that the control signal obtained from the controller PI_{I_L} is used directly in the equations of the dependent sources of the DC/DC converter as the duty.

3.1. Subsection

Table I. Caption table

Description	Switched simulation time (s)	Averaged simulation time (s)	Enhancing Percentage (%)
Simulation Time	386.284	0.816091	99.78

Figure 17 shows the time dynamics of the battery voltage. The continuous blue signal V_{Bat}^{SW} is the voltage obtained from the switched model and the dotted pink signal V_{Bat}^{AV} is the voltage obtained from the proposed average model. It is observed that initially the battery has 48V at $t = 0s$, then the battery starts to deliver power to the grid and the first transient occurs where there is a small difference between V_{Bat}^{SW} and V_{Bat}^{AV} . On the other hand, at $t = 2s$ the battery starts to absorb energy from the grid, it presents a second transient where there is no much difference between V_{Bat}^{SW} and V_{Bat}^{AV} compared to the first transient. Finally, a steady state is shown where both V_{Bat}^{SW} and V_{Bat}^{AV} converge to the same value.

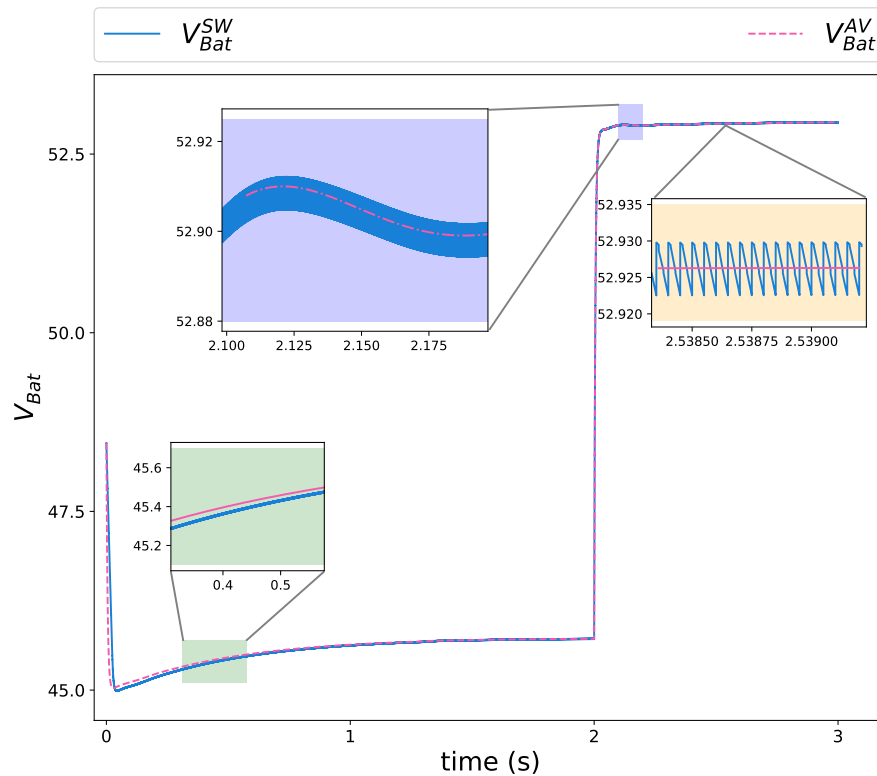


Figure 17. Voltage in the battery

Figure 18 shows the time dynamics of the current in the battery. The solid green signal I_{REF} is the reference current, the solid blue signal I_{Bat}^{SW} is the current obtained from the switched model and the

dotted pink signal I_{Bat}^{AV} is the current obtained from the proposed average model. Initially, at $t = 0s$, I_{REF} indicates a positive current of $30A$ meaning that current is flowing from the battery to the grid; then at $t = 2s$, I_{REF} changes to a negative current of $-50A$ indicating that it is flowing from the grid to the battery. In the first transient state illustrated it can be observed the difference between the I_{Bat}^{SW} and I_{Bat}^{AV} signals while in the second transient state the difference between these signals is considerably less. Both I_{Bat}^{SW} and I_{Bat}^{AV} signals converge to the reference value I_{REF} in the steady states.

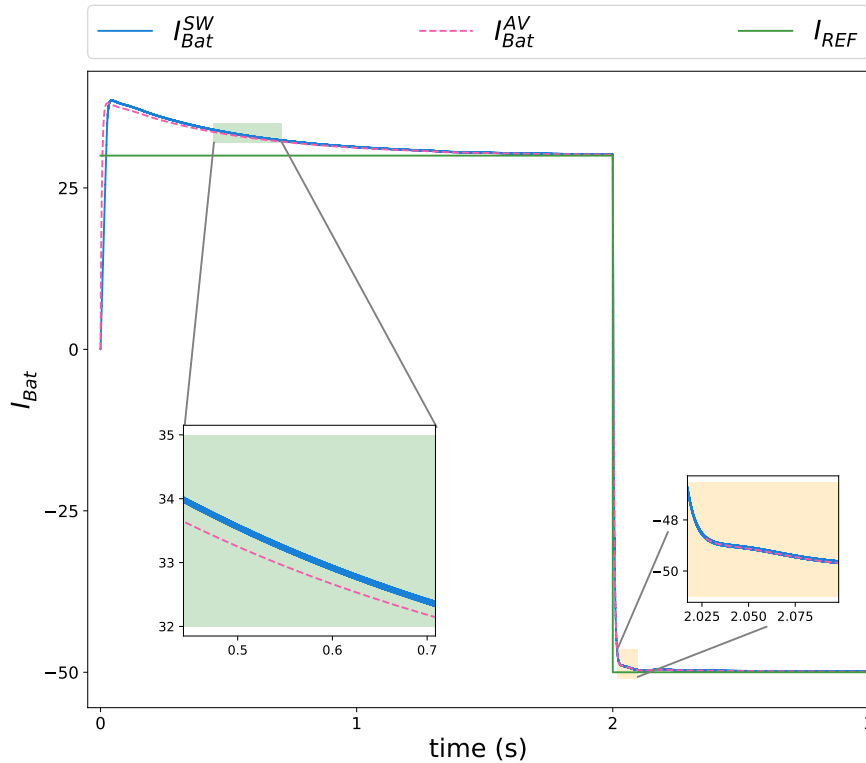


Figure 18. Current in the battery

Figure 19 shows the time response of the controlled voltage on the DC bus of the system under study. The green continuous signal V_{REF} represents the reference voltage, the blue continuous signal V_{DC}^{SW} represents the voltage obtained using the switched model and the pink dotted signal V_{DC}^{AV} represents the voltage obtained using the average model. At $t = 0s$ the V_{REF} signal indicates a DC bus voltage of $610V$, then at $t = 1,3s$ the V_{REF} signal changes to $615v$ on the DC bus. The first two transients ($t = 0s$, $t = 1,3s$) observed occur due to the change in the V_{REF} signal, while the third transient $t = 2s$ occurs due to the change in the I_{REF} signal at the battery (see Figure 18). It can be observed that in the first transient there is a difference between the V_{DC}^{SW} and V_{DC}^{AV} signals; on the other hand, in the following transients no comparable difference is seen between these signals. Before the different changes, the V_{DC}^{SW} and V_{DC}^{AV} signals reach the reference value in the steady states and present a similar settling time.

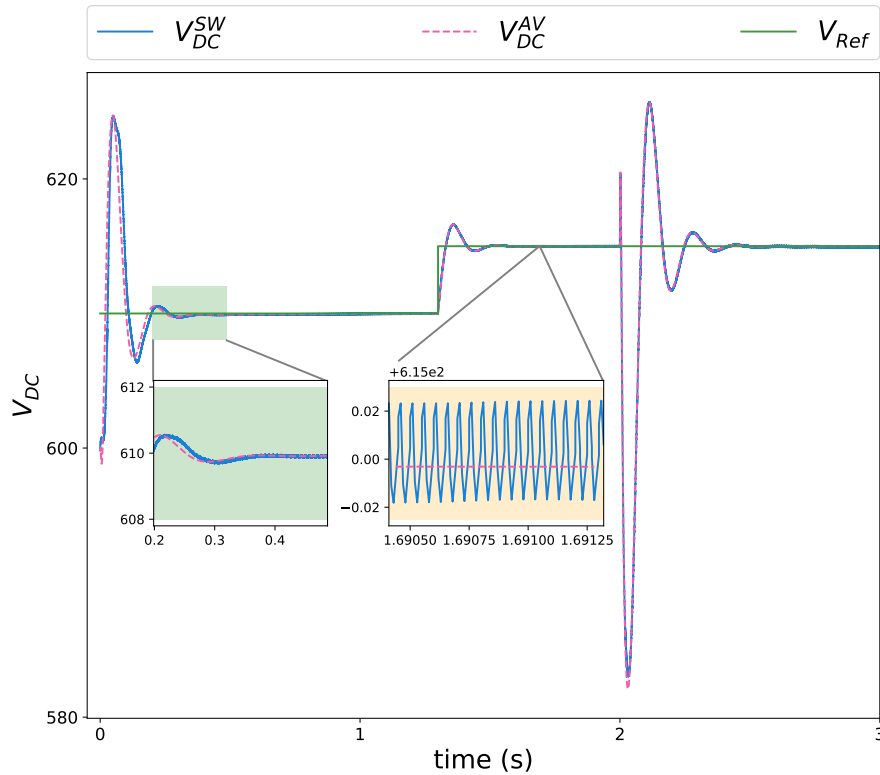


Figure 19. Inverter DC voltage

Figure 20 shows the three-phase grid currents provided by the inverter of the proposed system. Shown in blue, pink and green solid line are the I_a^{SW} , I_b^{SW} , I_c^{SW} currents obtained under the switched model and in yellow, purple and red dotted line are the I_a^{AV} , I_b^{AV} , I_c^{AV} currents obtained under the average model. Three disturbances can be observed; the first one is due to the change in voltage $V_{REF} = 610V$ of the DC bus and the change $I_{REF} = 30A$ of the battery at $t = 0s$. The second disturbance is caused by the voltage change $V_{REF} = 615V$ of the DC bus at $t = 1,3s$, the three-phase current presents a transient and stabilizes again without changing its amplitude. And finally, the third disturbance is due to the change in $I_{REF} = -50A$ at $t = 2s$, this time as the battery is absorbing energy, the amplitude of the three-phase currents increases considerably. Before the different changes, the three-phase currents obtained by the switched model and the average model reach the steady state maintaining the 120° phase difference between them.

4. Conclusions

This paper presents the deduction of the average switch model for PE devices in order to reduce simulation times. Ripple was eliminated from the simulation; nonetheless, voltage and current transients are preserved which allows determining the low behavior dynamics of PE devices. Several

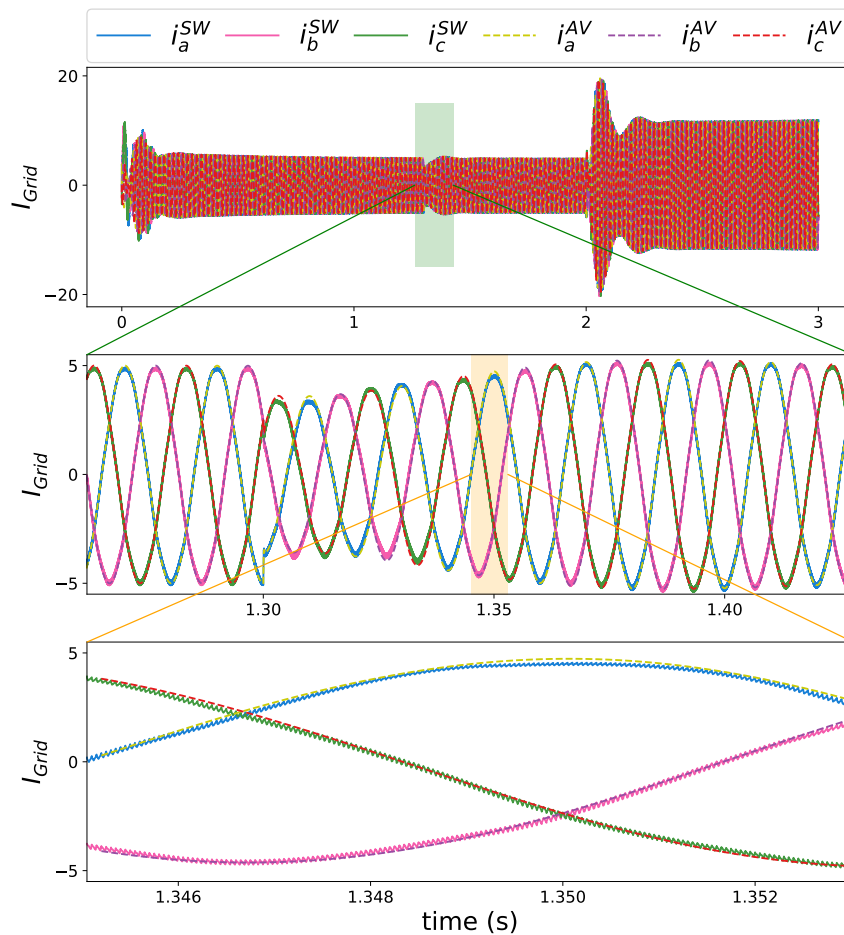


Figure 20. AC grid currents

simulations using both the conventional switch-based model and the proposed average switch model were performed using OpenModelica software. In this case, a system consisting of a battery, a DC/DC converter and a grid-connected inverter was used for validating the applicability and effectiveness of the proposed average switch model.

By comparing the switch-based model with the proposed average switch model, it is observed that voltage and current for both models match quite well, the signals of the average model correspond to the signals of switch-based model conserving the transient behavior but eliminating the ripple. It is very important to point out that the simulated system is composed of AC and DC power interfaces such as inverters and converters but also batteries that introduce other types of non-linearities in the system. In other words, a wide range of PE devices was included in the simulation.

Simulation times were substantially reduced. The simulation using the switch-based model took 386.284 seconds, while the simulation using the proposed average model took 0.816 seconds. This represents a reduction time of 99.788%. It can be concluded that applying the average model to the switch in PE devices is an alternative that allows to simulate while preserving the low dynamics of the system, with an important reduction of the simulation time, which opens the possibility to simulate more complex systems such as microgrids or other complex PE systems using home or office computers.

References

- [1] R. R. Pearson, "Photovoltaic power converter modeling in Modelica," Master's thesis, National Distance Education University, 2017. ↑ 2
- [2] R. W. Erickson and D. Maksimovic, *Fundamentals of power electronics*. Berlin, Germany: Springer Science & Business Media, 2007. ↑ 2
- [3] N. Barhoumi, H. Marzougui, F. Slah, and F. BACHA, "Modelling and control of floating interleaved boost converter for electric vehicle," in *2019 Int. Conf. Signal, Control Comm. (SCC)*, 2019, pp. 314–319. [Online]. Available: <http://doi.org/10.1109/SCC47175.2019.9116157> ↑ 3
- [4] S. Surya and S. Williamson, "Generalized circuit averaging technique for two-switch PWM DC-DC converters in CCM," *Energies*, vol. 10, p. 392, 2021. [Online]. Available: <https://doi.org/10.3390/electronics10040392> ↑ 3
- [5] N. E. Zakzouk, A. K. Khamisand, A. K. Abdelsalam, and B. W. Williams, "Continuous-input continuous-output current Buck-Boost DC/DC converters for renewable energy applications: Modelling and performance assessment," *Energies*, vol. 12, p. 2208, 2019. [Online]. Available: <https://doi.org/10.3390/en12112208> ↑ 3
- [6] R. Ali, K. Khan, M. Khalid, and A. Khan, "Multi-input boost converter for parallel connected renewable energy systems," *Renew. Energy Power Qual. J.*, vol. 18, pp. 403–408, 2020. [Online]. Available: <https://doi.org/10.24084/repqj18.361> ↑ 3
- [7] A. Chadha and M. K. Kazimierczuk, "Small-signal modeling of open-loop PWM tapped-inductor Buck DC-DC converter in CCM," *IEEE Tran. Ind. Electronics*, vol. 68, no. 7, pp. 5765–5775, 2021. [Online]. Available: <https://doi.org/10.1109/TIE.2020.2996157> ↑ 3
- [8] N. Kianpoor, M. Yousefi, N. Bayati, A. Hajizadeh, and M. Soltani, "Fractional order modelling of DC-DC Boost converters," in *2019 IEEE 28th Int. Symp. Ind. Electronics (ISIE)*, 2019, pp. 864–869. [Online]. Available: <https://doi.org/10.1109/ISIE.2019.8781387> ↑ 3
- [9] J. Bayona, N. Gelvez, and H. Espitia, "Design, analysis, and implementation of an equalizer circuit for the elimination of voltage imbalance in a half-bridge Boost converter with power factor correction," *Electronics*, vol. 9, p. 2171, 2020. [Online]. Available: <https://doi.org/10.3390/electronics9122171> ↑ 3
- [10] M. A. M. Noh, M. R. Sahid, T. K. Fei, and R. Lakshmanan, "Small-signal analysis of a single-stage bridgeless boost half-bridge AC/DC converter with bidirectional switch," *Int. J. Power Electronics and Drive Systems (IJPEDS)*, vol. 12, no. 4, pp. 2358–2371, 2021. [Online]. Available: <https://doi.org/10.11591/ijpeds.v12.i4.pp2358-2371> ↑ 3

- [11] D. K. Saini and M. K. Kazimierczuk, "Open-loop transfer functions of Buck-Boost converter by circuit-averaging technique," *IET Power Electronics*, vol. 12, no. 11, pp. 2858–2864, 2019. [Online]. Available: <https://doi.org/10.1049/iet-pel.2018.5514> ↑ 3
- [12] Z. Liang, S. Hu, H. Yang, and X. He, "Synthesis and design of the AC current controller and impedance network for the quasi-Z-source converter," *IEEE Trans. Ind. Electronics*, vol. 65, no. 10, pp. 8287–8296, 2018. [Online]. Available: <https://doi.org/10.1109/TIE.2018.2808928> ↑ 3
- [13] D. Tannir, Y. Wang, and P. Li, "Accurate modeling of nonideal low-power PWM DC-DC converters operating in CCM and DCM using enhanced circuit-averaging techniques," *ACM Trans. Design Autom. Electronic Syst.*, vol. 21, pp. 1–15, 2016. [Online]. Available: <https://doi.org/10.1145/2890500> ↑ 3
- [14] D. Jayachandran, V. Krishnaswamy, A. Lavanya, and K. Dhandapani, "Modelling and analysis of voltage mode controlled Luo converter," *American J. App. Sci.*, vol. 12, no. 10, pp. 766–774, 2015. [Online]. Available: <https://doi.org/10.3844/ajassp.2015.766.774> ↑ 3
- [15] L. Schmitz, D. C. Martins, and R. F. Coelho, "A simple, accurate small-signal model of a coupled-inductor-based DC-DC converter including the leakage inductance effect," *IEEE Trans. Circ. Syst. II: Express Briefs*, vol. 68, no. 7, pp. 2533–2537, 2021. [Online]. Available: <https://doi.org/10.1109/TCSII.2021.3061942> ↑ 3
- [16] R. Reddivari and D. Jena, "Analysis of RCD snubber based non-ideal Z-source inverter using average modelling approaches," *Int. J. Electronics*, vol. 107, no. 5, pp. 755–777, 2020. [Online]. Available: <https://doi.org/10.1080/00207217.2019.1672811> ↑ 3
- [17] F. Ghizzawi and D. Tannir, "Circuit-averaged modeling of non-ideal low-power DC-AC inverters," in *2020 IEEE Texas Power Energy Conf. (TPEC)*, 2020, pp. 1–6. [Online]. Available: <https://doi.org/10.1109/TPEC48276.2020.9042503> ↑ 4
- [18] N. Salehi, H. Martínez-García, G. Velasco-Quesada, and E. García-Vílchez, "Inverter control analysis in a microgrid community based on droop control strategy," *Renew. Energy Power Qual. J.*, vol. 19, pp. 166–170, 2021. [Online]. Available: <https://doi.org/10.24084/repqj19.247> ↑ 4
- [19] M. Hamida, A. Fekik, A. Azar, N. Kamal, A. Ardjal, and H. Denoun, "Fuzzy logic cyclic reports modulation control for a five-Cell inverter," 2022, pp. 154–159. [Online]. Available: <https://doi.org/10.1109/SMARTTECH54121.2022.00043> ↑ 4
- [20] J.-H. Cho, N.-J. Ku, R.-Y. Kim, and D.-S. Hyun, "Small-signal modeling and control of three-phase grid-connected three-level neutral-point-clamped inverter with a LCL filter," in *2013 IEEE Energy Conv. Cong. Expo.*, 2013, pp. 4076–4081. [Online]. Available: <https://doi.org/10.1109/ECCE.2013.6647242> ↑ 4
- [21] P. Moraes, A. Reis, and A. Filho, "Novel time-domain average model for harmonic current prediction in photovoltaic and wind power units," *Int. Trans. Electrical Energy Syst.*, vol. 31, 2021. [Online]. Available: <https://doi.org/10.1002/2050-7038.13253> ↑ 4
- [22] T. Itkonen, J. Luukko, A. Sankala, T. Laakkonen, and R. Pollanen, "Modeling and analysis of the dead-time effects in parallel PWM two-level three-phase voltage-source inverters," *IEEE Trans. Power Electronics*, vol. 24, no. 11, pp. 2446–2455, 2009. [Online]. Available: <https://doi.org/10.1109/TPEL.2009.2033064> ↑ 4

Santiago Benavides Córdoba

Ingeniero electricista de la Universidad de Antioquia (2016) y Magíster en Ingeniería de la misma universidad (2018). Actualmente es Candidato a Doctor en Ingeniería por parte de la Universidad de Antioquia. Sus intereses incluyen electrónica de potencia, calidad de la energía, programación de microcontroladores y aplicaciones de inteligencia artificial.

Email: santiago.benavides@udea.edu.co

Anamaría Romero Carvajal

Estudiante de Ingeniería Eléctrica de la Universidad de Anioquia, integrante del Grupo de Investigación en Manejo Eficiente de la Energía (GIMEL), sus intereses incluyen electrónica de potencia, programación y optimización aplicada.

Email: anamaria.romero@udea.edu.co

Nicolás Muñoz Galeano

Profesor Titular adscrito al Departamento de Ingeniería Eléctrica de la Universidad de Antioquia. Director del Grupo de Investigación en Manejo Eficiente de la Energía (GIMEL), sus intereses incluyen electrónica de potencia, microrredes, y optimización aplicada.

Email: nicolas.munoz@udea.edu.co

Juan Bernardo Cano Quintero

Ingeniero Electrónico de la Universidad de Antioquia (2007), Doctor en Ingeniería Electrónica de la Università di Roma Tor Vergata (2012). Actualmente es profesor del Departamento de Ingeniería Eléctrica de la Universidad de Antioquia, sus intereses incluyen electrónica de potencia, sensórica, microrredes, y aplicaciones de inteligencia artificial.

Email: bernardo.cano@udea.edu.co

Jesús María López Lezama

Ingeniero Electricista (2001) y Magister en Ingeniería Eléctrica (2006) de la Universidad Nacional de Colombia. Doctor en Ingeniería Eléctrica de la Universidad Estadual Paulista (2011). Actualmente es Profesor Titular adscrito al Departamento de Ingeniería Eléctrica de la Universidad de Antioquia, sus intereses incluyen microrredes, energías renovables y optimización aplicada.

Email: jmaria.lopez@udea.edu.co





Research

Stochastic Mixed-Integer Branch Flow Optimization for the Optimal Integration of Fixed-Step Capacitor Banks in Electrical Distribution Grids

Optimización estocástica, entera mixta y de flujo por ramas para la integración óptima de bancos de capacitores de paso fijo en redes de distribución de energía

Walter Gil-González  *, Andrés Herrera-Orozco , Alexander Molina-Cabrera 

Department of Electrical Engineering, Universidad Tecnológica de Pereira, Pereira 660003, Colombia. 

Abstract

Context: The use of capacitor banks is the most common and preferred solution for reducing power losses in electrical distribution networks, given their cost-effectiveness and low maintenance requirements. However, achieving their optimal integration in terms of location and size is a challenging problem.

Method: This paper proposes a stochastic mixed-integer convex model based on a branch flow optimization model, which incorporates three different load-generation conditions, in order to address the stochastic nature of distribution systems.

Results: The simulation results indicate that the proposed stochastic mixed-integer branch flow (SMIBF) model provides the best solution for all test feeders analyzed, reducing the objective function value by 39,81, 35,29, and 56,31 % regarding the benchmark case in the modified 33-, 69-, and 85-node test feeders, respectively.

Conclusions: An SMIBF model was developed to optimally integrate fixed-step capacitor banks into electrical distribution grids. This model considered the stochastic nature of distribution systems under multiple operating conditions and ensured that the global optimum could be found.

Keywords: stochastic mixed-integer model, branch flow optimization, fixed-step capacitor banks, electrical distribution network, global optimum

Article history

Received:
5th/Oct/2023

Modified:
12th/Nov/2023

Accepted:
28th/Dec/2023

Ing., vol. 29, no. 1,
2024. e21340

©The authors;
reproduction right
holder Universidad
Distrital Francisco
José de Caldas.

Open access



*  Correspondence: wjgil@utp.edu.co

Resumen

Contexto: El uso de bancos de capacitores es la solución más común y preferida para reducir la pérdida de energía en redes de distribución eléctrica, dados su rentabilidad y bajos requisitos de mantenimiento. Sin embargo, lograr su integración óptima en términos de ubicación y tamaño es un problema desafiante.

Métodos: Este artículo propone un modelo convexo estocástico entero-mixto basado en un modelo de optimización de flujo de ramas, el cual incorpora tres diferentes condiciones de generación-carga, para abordar la naturaleza estocástica de los sistemas de distribución.

Resultados: Los resultados de la simulación indican que el modelo SMIBF propuesto proporcionó la mejor solución para todos los sistemas de prueba analizados, reduciendo el valor de la función objetivo en un 39,81, 35,29 y 56,31 % respecto al caso de referencia para los alimentadores de prueba modificados de 33, 69 y 85 nodos respectivamente.

Conclusiones: Se desarrolló un modelo SMIBF para la integración óptima de bancos de capacitores de paso fijo en redes de distribución eléctrica. Este modelo tuvo en cuenta la naturaleza estocástica de los sistemas de distribución bajo múltiples condiciones de operación y garantizó que se pudiera encontrar el óptimo global.

Palabras clave: modelo estocástico de enteros mixtos, optimización de flujo de ramas, bancos de capacitores de paso fijo, red de distribución eléctrica, óptimo global

Table of contents

	Page		
1. Introduction	4	4.3. Test Feeder 3	13
2. Optimization model	6	4.4. Load-generation scenario	13
2.1. Optimization model objectives	6	5. Numerical results and discussions	14
2.2. Optimization model constraints	7	5.1. Results obtained for C1	14
2.3. Interpretation of the optimization model	9	5.2. Results obtained for C2	16
3. Branch flow reformulation	9	5.3. Results obtained for C3	17
3.1. Stochastic MI branch flow model	11	5.4. Discussing the influence of integrating energy storage systems and the effect of radial reconfiguration on the model	18
4. Test system under study	11	6. Conclusions and future works	18
4.1. Test Feeder 1	12	7. Acknowledgments	19
4.2. Test Feeder 2	12	8. Author contributions	19
		References	19

Nomenclature

Acronyms

AC	Alternating current.
EDN	Electrical distribution network.
GAMS	General Algebraic Modeling System.
MINLP	Mixed-integer nonlinear programming.
OF	Objective function.
PV	Photovoltaic.
SMIBF	Stochastic mixed-integer branch flow.

Parameters

ζ_s	Probability factor for scenario s .
A_k	Node-to-branch incident matrix for node k .
$C_{\text{cap}}^{\text{máx}}$	Maximum costs associated with capacitor bank installation (\$USD).
$C_{\text{loss}}^{\text{máx}}$	Maximum annual cost of energy losses (\$USD).
K_p	Cost factor of the annual energy losses (\$USD/kVA).
K_t	Cost factor of the capacitor banks (\$USD/kvar-year).
N^{cap}	Maximum number of capacitor banks.
$p^{\text{mín}}, p^{\text{máx}}$	Minimum and maximum power from renewable energy sources (W).
Q_t	Nominal power of the capacitor bank type t (kVA).
R_l	Resistive effect of the transmission line l (Ω).
$v^{\text{mín}}, v^{\text{máx}}$	Minimum and maximum voltage limits (V).
X_l	Reactance effect of the transmission line l (Ω).

Sets and Indices

\mathcal{B}	Set of network branches.
---------------	--------------------------

\mathcal{N}	Set of network nodes.
\mathcal{S}	Set of scenarios.
\mathcal{T}	Set of capacitor bank types.
k, m	Node indices ($k, m \in \mathcal{N}$).
l	Branch indices ($l \in \mathcal{B}$).
t	Capacitor bank type ($t \in \mathcal{T}$).

Variables

ω	Weighting factor.
I_l	Squared magnitude of the current at branch l (A^2).
i_l	Magnitude of the current flowing through transmission line l (A).
$p_{k,dg}$	Active power generated via renewable energy sources at node k (W).
$p_{k,d}$	Active power demanded at node k (W).
P_l	Active power flow vector of the branches (W).
p_l	Active power flow of branch l (W).
$q_{k,d}$	Reactive power demanded at node k (var).
$Q_{k,t}$	Reactive power delivered by the capacitor bank connected to node k (kvar).
Q_l	Reactive power flow vector of the branches (var).
q_l	Reactive power flow of branch l (var).
V_k	Squared magnitude of the voltage at node k (V^2).
$v_{m \text{ or } (v_k)}$	Magnitude of the voltage at node m (or k) (V).
y_{kt}	Binary variable that selects the type of capacitor t connected at node k .
z	Objective function (\$USD).
z_1	Annual costs of energy loss (\$USD).
z_2	Costs associated with capacitor bank installation (\$USD).

1. Introduction

Electrical distribution networks (EDNs) supply electricity to both rural and urban areas at medium- and low-voltage levels (1). These networks are usually designed with a radial topology, which helps reduce costs for conductors and infrastructure, and simplifies the implementation and coordination of protection schemes (2). Nevertheless, radial EDNs entail significant energy losses, as there is only one line to carry electrical energy from the generation point (substation) to each demand node. Generally, energy losses in radial EDNs are within the range of 6 to 18% of all the power delivered by the generator at the substation, whereas, in transmission systems, energy losses are approximately 2% (3).

Utility companies have various options to address the issue of power losses in EDNs. These include making changes to the network's topology and connecting shunt devices (4–6). In the case of topology changes, additional transmission lines are used, which connect to or are disconnected from the electrical system to minimize power losses for specific load conditions while maintaining their radial topologies (7). As for the incorporation of shunt systems, the following technologies have been used: distributed generator systems (*e.g.*, solar and wind energy sources) (8), distribution network flexible AC transmission system (D-FACTS) devices (*e.g.*, distribution static power compensators, or D-STATCOMs, static Var compensators, or SVCs, and fixed-step capacitor banks) (9, 10), and energy storage systems such as batteries (11). However, some of these systems are expensive when it comes to only reducing power losses, which does not allow recovering the investment made (*e.g.*, distributed generator systems and energy storage systems). As a result, it is necessary to consider other objectives to justify their installation (11). The dispatch of reactive power can reduce the power losses in EDNs. Hence, systems such as D-FACTS or fixed-step capacitor banks are ideal. Capacitor banks are cheaper compared to distribution static compensators, require minimal maintenance, have a lifespan of over 25 years (12), and are highly reliable (13). Therefore, capacitors are considered to be the most reliable and cost-effective strategy for reducing power losses (10).

Capacitor banks have long been used as a solution to reduce energy losses in EDNs (10), and determining their optimal locations and sizes is of great importance. The problem lies in their mathematical model, which is challenging to solve because it includes two sets of variables (integer and binary). This implies a model with a mixed-integer nonlinear programming (MINLP) structure (14). The variables for the location and size of the new capacitor banks are binary, while the remaining problem variables are continuous. These include voltage profiles, generated and demanded apparent power, and apparent power flows, among others.

Combinatorial methods are commonly used to find a solution for the non-convex MINLP model that determines the location and size of capacitor banks in EDNs. The most relevant methods in this regard are listed below.

The study by (10) used the flower pollination method to effectively select the sizes and positions of fixed-step capacitor banks in radial EDNs. The goal was to reduce the annual operating costs of the grid, which include energy losses and the investments made in capacitors. The flower pollination

method was evaluated in four EDNs with 33, 34, 69, and 85 nodes. The simulation results indicated that the proposed method yielded superior solutions when compared to other approaches, including analytical sensitivity methods, fuzzy logic algorithms, and classical genetic algorithms.

The work by (15) suggested using a discrete version of the vortex search approach to find and select suitable fixed-step capacitor banks for installation in EDNs. This work conducted numerical experiments on two well-known test systems consisting of 33 and 69 nodes. The findings indicated that the proposed approach was superior to the flower pollination algorithm in terms of efficiency.

The authors of (16) solved the problem regarding the optimal siting and sizing of capacitor banks in EDNs using the well-known General Algebraic Modeling System (GAMS) software. The authors improved the simulation results by incorporating the classical Chu & Beasley genetic methodology. They used two well-known test systems (33 and 69 nodes) and highlighted that the methodology could handle both EDN topologies (radial and meshed) without any modification.

Another study (17) introduced a heuristic approach for locating and sizing capacitor banks in EDNs. Its primary contribution the full incorporation of grid harmonic distortion into the heuristic optimization approach. This study utilized three IEEE test systems to demonstrate that the proposed algorithm could effectively decrease the total grid costs, surpassing the classical genetic algorithm.

The study by (18) proposed a bi-level methodology for solving the mathematical model for the optimal integration (siting and sizing) of fixed-step capacitor banks in radial EDNs. This methodology consisted of combining the generalized normal distribution algorithm with the optimal power flow method. The latter used a linearization of the power flow and iterated it consecutively to reduce the error, which is known as the *successive approximations* method. The generalized algorithm was responsible for providing the locations and sizes of the capacitor banks. Meanwhile, the optimal power flow method calculated the operating status of the system with the best configuration, minimizing the expected costs of energy losses. This methodology showed excellent results in several IEEE test feeders consisting of 33, 69, and 85 nodes.

Other algorithms employed for solving the mathematical model for the optimal integration of fixed-step capacitor banks in radial EDNs are the tabu search algorithm (19), the artificial bee colony optimizer (20), the particle swarm optimizer (21), modified genetic optimizers (22), and the cuckoo search optimizer (23), among others.

Although all of the aforementioned methods have shown excellent results, they all share the same problem: none of them ensures the best solution (global optimum) for the optimization model. This suggests that there may be better solutions. Additionally, they need to be calibrated, and, for this reason, their performance may vary among different testing systems. Furthermore, obtaining statistically reliable results requires multiple simulations. To address these issues, the study conducted by (14) proposed a conic programming model for mixed-integer (MI) optimization. This model ensures that an optimal solution to the optimization problem is obtained. However, this model was only evaluated in

test systems operating for an hour and did not consider the use of renewable energy sources, which can be impractical in today's world. Furthermore, this work neglected the stochastic aspects of renewable generators and the demand resulting from their uncertainties. Unlike the previous work, we present a stochastic MI convex model based on a branch flow optimization model. This model incorporates three different levels (*i.e.*, low, medium, and high) regarding the demand and generation by renewable energy sources, aiming to address the stochastic nature of EDNs by considering multiple operating conditions. The contributions of this study are listed below.

- i. A stochastic mixed-integer branch flow (SMIBF) model is presented for the optimal integration (siting and sizing) of fixed-step capacitor banks in EDNs. The proposed SMIBF model incorporates three operating conditions for demand and generation: low, medium, and high levels. These conditions result in a total of nine scenarios.
- ii. The proposed SMIBF model aims to minimize two objectives: the annual costs of energy losses and the costs of installing capacitor banks. These two objectives imply that the model is a multi-objective problem solved by incorporating a weighting factor.
- iii. Three simulation scenarios are suggested to showcase the stochastic model's efficiency and compare it against three solvers accessible in the GAMS software.

The structure of this paper is as follows. Section 2 formulates the non-convex MINLP model to locate and size capacitor banks in EDNs. Section 3 formulates the proposed model using the branch flow optimization model. Section 4 outlines the three test feeders implemented and the load-generation scenarios considered. The primary findings and an analysis of the developed SMIBF model are presented in Section 5. Lastly, the main conclusions and proposals for future work are provided in Section 6.

2. Optimization model

The optimal integration (*i.e.*, placement and size) of fixed-step capacitor banks in EDNs enhances their operating conditions. These conditions are the reduction of congestion in distribution lines, the reduction of power losses, and the improvement of voltage profiles. This means that it is important to carefully select nodes for locating capacitor banks, as well as the banks' appropriate size, in order to avoid any negative impact on the operation of EDNs. This implies the need for a model aimed at optimally integrating capacitor banks in EDNs. In this vein, this model incorporates both continuous and binary variables. The continuous variables denote the nodal voltages, the power flows of the transmission lines, and the power generated by conventional generation and renewable energy sources, among others. Meanwhile, the binary variables only represent the location of the capacitor banks. The MINLP model for the problem under analysis is formulated below.

2.1. Optimization model objectives

The objective function (OF) z used for the optimal integration of capacitor banks in EDNs minimizes two parameters: the annual costs of energy losses (z_1) and the costs associated with capacitor bank installation (z_2). These two objectives indicate that the proposed model is a multi-objective problem

solved by incorporating a weighting factor (ω). The use of this factor is referred to as the *weighted sum method* (24), which turns the multi-objective problem into a single-objective one by assigning weights to each objective. Furthermore, the OF is normalized to adequately balance both objectives. Thus, the proposed OF takes the following form:

$$\min z = \omega \frac{z_1}{C_{\text{loss}}^{\text{máx}}} + (1 - \omega) \frac{z_2}{C_{\text{cap}}^{\text{máx}}} \quad (1)$$

$$z_1 = K_p \sum_{l \in \mathcal{B}} R_l i_l^2, \quad (2)$$

$$z_2 = \sum_{k \in \mathcal{N}} \sum_{t \in \mathcal{T}} K_t Q_t y_{kt}, \quad (3)$$

where $\omega \in [0, 1]$ represents the weighting factor, which assigns weight to each OF based on its value; K_p is a cost factor that quantifies the power losses, yielding the annual energy losses; R_l denotes the resistive effect of the transmission line connected to branch l ; i_l is the magnitude of the current flowing through the transmission line connected to branch l ; \mathcal{B} and \mathcal{N} correspond to the sets of the branches (or lines) and nodes in the distribution network, while \mathcal{T} represents the set of capacitor bank types; K_t denotes the cost factor of the capacitor banks per kvar-year; Q_t is the nominal power of the capacitor bank type t ; y_{kt} is the binary variable associated with the type or capacity of capacitor bank t and the connected node k ; $C_{\text{loss}}^{\text{máx}}$ represents the cost of z_1 in the distribution grid without capacitor banks; and $C_{\text{cap}}^{\text{máx}}$ denotes the maximum possible costs related to the installation of these banks.

It is important to note that there are several approaches to solving multi-objective optimization problems, which can be broadly categorized into classical and evolutionary techniques, such as goal programming (25), Pareto-based methods (26), the weighted sum method (24), particle swarm optimization (27), genetic algorithms (27), differential evolution algorithms (27), the non-dominated sorting genetic algorithm II (NSGA-II) (28), the multi-objective evolutionary algorithm based on decomposition (29), and hybrid approaches. Although there are multiple methods to solve multi-objective problems, the weighted sum method was selected because it offers several advantages. These include conceptual simplicity, ease of implementation, flexibility in expressing preferences, the ability to transform the problem into a linear programming one, a unique approach, and the clear interpretation of solutions (30). However, it is also important to mention that this method has limitations and may not be suitable for all multi-objective problems, particularly those with non-convex Pareto fronts or highly non-linear problems.

2.2. Optimization model constraints

The set of model constraints for the optimal integration of fixed-step capacitor banks in EDNs is represented by the nodal power balance equations, the voltage drop in each branch, the maximum and minimum power capacity of the generators, the maximum and minimum voltage limits, and the number and size of the capacitor banks to be installed.

The nodal power balance equations are calculated so that the total power injected (or consumed) at each node is equivalent to the sum of the sending and receiving power flows through the branches

connected to it. The nodal power balance in each node can be formulated as follows:

$$A_k(P_l - R_l i_l^2) = p_{k,dg} - p_{k,d} \quad \{k \in \mathcal{N}\}, \quad (4)$$

$$A_k(Q_l - X_l i_l^2) = Q_{k,c} - q_{k,d} \quad \{k \in \mathcal{N}\}, \quad (5)$$

where A_k in the incident matrix for node k (node-to-branch); P_l and Q_l are vectors that contain the active and reactive power flows of the branches, respectively; $p_{k,dg}$ is the active power generated via renewable energy sources at node k ; $p_{k,d}$ and $q_{k,d}$ are the active and reactive power consumption at node k ; $Q_{k,c}$ is the reactive power delivered by the capacitor bank connected to node k ; and X_l is the reactance associated with branch l .

The voltage drop equation establishes a connection between the voltage and current at both ends of each branch while considering its resistance and reactance. The voltage loss in each branch can be formulated as follows:

$$v_m^2 = v_k^2 - 2(R_l p_l + X_l q_l) + (R_l^2 + X_l^2) i_l^2 \quad \{l \in \mathcal{B}\}, \quad (6)$$

where v_m (or v_k) represents the magnitude of the voltage at node m (or k), p_l denotes the active power flow of branch l , and q_l is the reactive power flow of branch l .

The squared magnitude of the apparent power flowing through the branches can be defined as

$$v_l^2 i_l^2 = p_l^2 + q_l^2 \quad \{l \in \mathcal{B}\}. \quad (7)$$

The limits regarding the maximum and minimum power from renewable energy sources and the maximum and minimum voltage bounds can be defined as follows:

$$p^{\min} \leq p_{k,dg} \leq p^{\max} \quad \{k \in \mathcal{N}\}, \quad (8)$$

$$v^{\min} \leq v_k \leq v^{\max} \quad \{k \in \mathcal{N}\}, \quad (9)$$

where p^{\min} and p^{\max} denote the renewable energy sources' minimum and maximum power; and v^{\min} and v^{\max} are the minimum and maximum voltage limits, respectively.

Box constraint (8) bounds the minimum and maximum active power available from renewable energy sources, while box constraint (9) is dictated by regulatory limits for the adequate operation of EDNs. The typical values are between $\pm 5\%$ and $\pm 10\%$ (31).

The ideal incorporation of capacitor banks in EDNs can be split into two components. The first involves determining their appropriate placement within the system, while the second determines the right size. These difficulties are addressed by implementing the following constraints:

$$Q_{k,c} = \sum_{t \in \mathcal{T}} y_{kt} Q_t^{\text{nom}} \quad \{\forall k \in \mathcal{N}\}, \quad (10)$$

$$\sum_{k \in \mathcal{N}} \sum_{t \in \mathcal{T}} y_{kt} \leq N^{\text{cap}}, \quad (11)$$

where Q_t^{nom} is the nominal power of capacitor bank type t , and N^{cap} is the maximum number of capacitor banks to be incorporated into the EDN.

2.3. Interpretation of the optimization model

The optimization model for the optimal integration (siting and sizing) of fixed-step capacitor banks in EDNs, which is described in Eqs. (1) to (11), includes continuous variables associated with the magnitudes and angles of the nodal voltages, as well as with the active power generated via renewable energy sources and the reactive power injected by the fixed-step capacitor banks. At the same time, this optimization model incorporates binary variables associated with the location of the fixed-step capacitor banks in the EDN. The objective functions (2) and (3) and the set of constraints from (4) to (11) generate a MINLP model that has the following aspects.

The objective function (1) represents the total annual operating costs of an EDN. It consists of two terms: the first one (z_1) denotes the annual costs of energy losses in the EDN, while the second one (z_2) represents the costs associated with the installation of fixed-step capacitor banks. Constraints (4) and (5) represent the nodal active and reactive power balance, respectively. The left side of these constraints represents the power flowing through the distribution lines that reach the node, taking the corresponding losses into account. The right side denotes the energy generated or demanded at the same node. Constraint (6) corresponds to the voltage drop, which is represented in terms of the magnitude of the current flowing through the distribution lines and their parameters. Constraint (7) represents the squared magnitude of the apparent power flowing through the distribution lines, while inequalities (8) and (9) define the maximum and minimum values for the active power generated by renewable energy sources and the nodal voltages, respectively. Constraint (10) denotes the reactive power injected by a fixed-step capacitor bank, while constraint (11) regulates the maximum number of capacitor banks that can be included in the EDN.

Remark. The MINLP model described from (1) to (11) contains the convex and non-convex constraints, which are represented by (4), (5), (6), and (7). This set of constraints poses significant issues in solving the MINLP model and ensuring its global optimum since, mathematically, it is not possible to demonstrate it. This means that the solution found by some methods is most likely a local optimum. Thereupon, the next section reformulates these constraints in order to transform them into a convex model and thus ensure the global optimum of the model.

3. Branch flow reformulation

Auxiliary variables are defined which will be used to transform the non-convex MINLP optimization model into a convex one. These auxiliary variables are

$$V_k = v_k^2 \quad \{k \in \mathcal{N}\}, \quad (12)$$

$$I_l = i_l^2 \quad \{l \in \mathcal{B}\}. \quad (13)$$

Now, substituting these variables into Eqs. (4), (5), (6), and (7) yields the following:

$$A_k(P_{l,t} - R_l I_l) = p_{k,dg} - p_{k,d} \quad \{k \in \mathcal{N}, \}, \quad (14)$$

$$A_k(Q_{l,t} - X_l I_l) = Q_{k,c} - q_{k,d} \quad \{k \in \mathcal{N}\}, \quad (15)$$

$$V_m = V_k - 2(R_l p_l + X_l q_l) + (R_l^2 + X_l^2) I_l \quad \{l \in \mathcal{B}\}, \quad (16)$$

$$V_l I_l = p_l^2 + q_l^2 \quad \{l \in \mathcal{B}\}. \quad (17)$$

Note that the constraints (14), (15), and (16) are linear expressions, and thus they are convex constraints. Nevertheless, the constraints in (17) continue to be a non-convex due to the product between the auxiliary variables. This product can be rewritten as follows:

$$\begin{aligned}
v_l^2 i_l^2 &= \frac{1}{4} (I_l + V_k)^2 - \frac{1}{4} (I_l - V_k)^2 = p_l^2 + q_l^2 \\
\frac{1}{4} (I_l + V_k)^2 &= p_l^2 + q_l^2 + \frac{1}{4} (I_l - V_k)^2 \\
(I_l + V_k)^2 &= 4p_l^2 + 4q_l^2 + (I_l - V_k)^2 \\
I_l + V_k &= \sqrt{4p_l^2 + 4q_l^2 + (I_l - V_k)^2}.
\end{aligned} \tag{18}$$

The constraint (18) can be expressed using norm-2, as follows:

$$I_l + V_k = \left\| \begin{array}{c} 2p_l \\ 2q_l \\ I_l - V_k \end{array} \right\|. \tag{19}$$

Note that the constraint (18) is still a non-convex expression, even though it has been transformed into a second-order conic constraint. However, it can be made convex by relaxing the equality to an inequality, as demonstrated in (32). The convex formulation of the second-order conic constraint takes the following form:

$$I_l + V_k \geq \left\| \begin{array}{c} 2p_l \\ 2q_l \\ I_l - V_k \end{array} \right\|. \tag{20}$$

The convex model for the optimal integration of fixed-step capacitor banks in EDNs is as follows:

$$\min z = \omega \frac{z_1}{C_{\text{loss}}^{\text{máx}}} + (1 - \omega) \frac{z_2}{C_{\text{cap}}^{\text{máx}}} \tag{21}$$

$$z_1 = K_p \sum_{l \in \mathcal{B}} R_l I_l, \tag{22}$$

$$z_2 = \sum_{k \in \mathcal{N}} \sum_{t \in \mathcal{T}} K_t Q_t y_{kt}, \tag{23}$$

Subject to:

$$A_k(P_{l,t} - R_l I_l) = p_{k,dg} - p_{k,d} \{k \in \mathcal{N}, \}, \tag{24}$$

$$A_k(Q_{l,t} - X_l I_l) = Q_{k,c} - q_{k,d} \{k \in \mathcal{N}\}, \tag{25}$$

$$V_m = V_k - 2(R_l p_l + X_l q_l) + (R_l^2 + X_l^2) I_l \{l \in \mathcal{B}\}, \tag{26}$$

$$I_l + V_k \geq \left\| \begin{array}{c} 2p_l \\ 2q_l \\ I_l - V_k \end{array} \right\| \{l \in \mathcal{B}, k \in \mathcal{N}\}, \tag{27}$$

$$p^{\min} \leq p_{k,dg} \leq p^{\max} \quad \{k \in \mathcal{N}\}, \quad (28)$$

$$v^{\min} \leq v_k \leq v^{\max} \quad \{k \in \mathcal{N}\}, \quad (29)$$

$$Q_{k,c} = \sum_{t \in \mathcal{T}} y_t Q_t^{\text{nom}} \quad \{\forall k \in \mathcal{N}\}, \quad (30)$$

$$\sum_{k \in \mathcal{N}} \sum_{t \in \mathcal{T}} y_{kt} \leq N^{\text{cap}}. \quad (31)$$

The main benefit of the mixed-integer branch flow model, as outlined from (21) to (31), is its ability to find the global optimum. A combination of the cutting plane algorithm and the interior point method can be used to find the solution to this optimization model. However, it is essential to note that this model does not consider the stochastic nature of demand and renewable energy sources, which will be included in the following subsection.

3.1. Stochastic MI branch flow model

An EDN experiences various operating conditions as a result of fluctuating generation from renewable energy sources and changing demand. Hence, it is crucial to establish a minimum number of potential scenarios for the problem under study. In this context, the OF value (21) can be expressed as the sum of each scenario considered, multiplied by the probability of occurrence. This approach is known as the *sample average approximation model* (33) and is defined as follows:

$$\min \Xi(z_1, z_2, \xi_s) = \sum_{s \in \mathcal{S}} \xi_s z_s, \quad (32)$$

where ξ_s is the probability factor of occurrence for scenario s , and \mathcal{S} represents the set of scenarios.

Remark. Note that the OF (32) remains linear (an affine function). As a result, it is convex, and its global optimum can be ensured. Nevertheless, it is crucial to limit the amount of scenarios in order to make the optimization model more manageable.

The proposed SMIBF model is formulated below.

$$\min \sum_{s \in \mathcal{S}} \xi_s z_s \quad (33)$$

Subject to: (21) – (31).

4. Test system under study

The proposed SMIBF model was tested through numerical experiments on three modified, well-known distribution networks, *i.e.*, the 33-, 69-, and 85-node test feeders. For the sake of simplicity, these test systems will be referred to as *Test Feeder 1*, *Test Feeder 2*, and *Test Feeder 3*, respectively. The renewable energy sources considered are photovoltaic (PV) power plants, and three of them are incorporated in each test feeder. The main features of each test feeder are outlined below.

4.1. Test Feeder 1

Test Feeder 1 is a radial EDN, with 32 transmission lines and 33 nodes. It operates at 12,66 kV at the slack node (bus 1) and has a peak apparent power demand of 3,715 kW + j 2,300 kvar. For this peak demand, the test feeder experiences apparent power losses of approximately 210,9876 kW + j 143,1283 kvar. The three PV power plants are located at buses 13, 24, and 30, and their rated powers are 801,8, 1.091,3, and 1.053,6 kW, respectively. These locations and sizes were taken from (34). Fig. 1 illustrates the topology of Test Feeder 1 with three PV power plants. This grid considers 12,66 kV and 1 MW as its voltage and power bases. The main information about this test feeder can be consulted in (35).

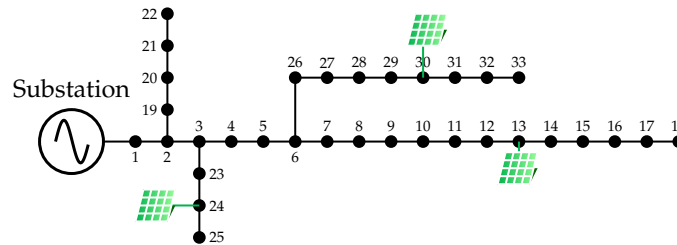


Figure 1. Topology of Test Feeder 1 with three PV power plants

4.2. Test Feeder 2

Test Feeder 2 has a radial configuration, 68 transmission lines, and 69 nodes. It operates at a voltage of 12,66 kV at the slack node (bus 1), and its peak apparent power demand is 3,890,7 kW + j 2,693,6 kvar. The apparent power losses of this peak demand are approximately 224,9520kW + j 102,3559 kvar. In this test feeder, the locations of the PV power plant are at buses 11, 18, and 61, with nominal powers of 1.631,31, 463,33, and 503,80 kW, respectively. This information has been taken from (34). Fig. 2 depicts the topology of Test Feeder 2 and the three PV power plants. The base values used for power and voltage are 1 MW and 12,66 kV. The main information about this test feeder can be consulted in (35).

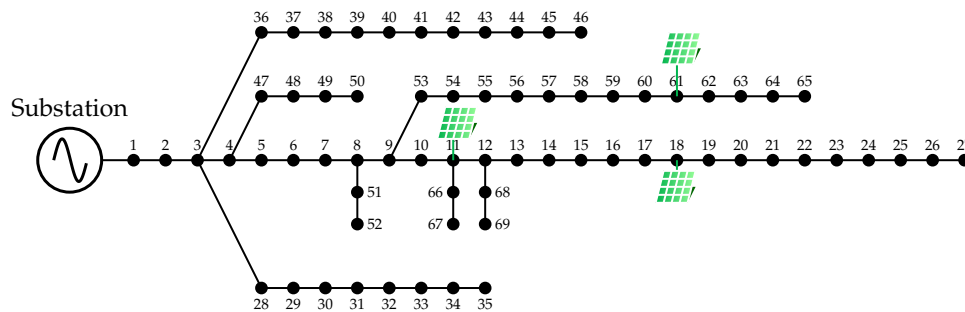


Figure 2. Topology of Test Feeder 2 with three PV power plants

4.3. Test Feeder 3

Test Feeder 3 has a radial topology, with 84 transmission lines and 85 nodes. It operates at a rated voltage of 11 kV at the slack node (bus 1) and has a peak apparent power demand of $2,570, 28 \text{ kW} + j2,622, 20 \text{ kvar}$. The nominal powers of the three PV power plants are 526,8, 380,1, and 1.719 kW, and they are located at nodes 35, 67, and 71, respectively. This information can be consulted in (36). Fig. 3 shows the topology of Test Feeder 3. This system considers 11 kV and 1 MW as its voltage and power bases.

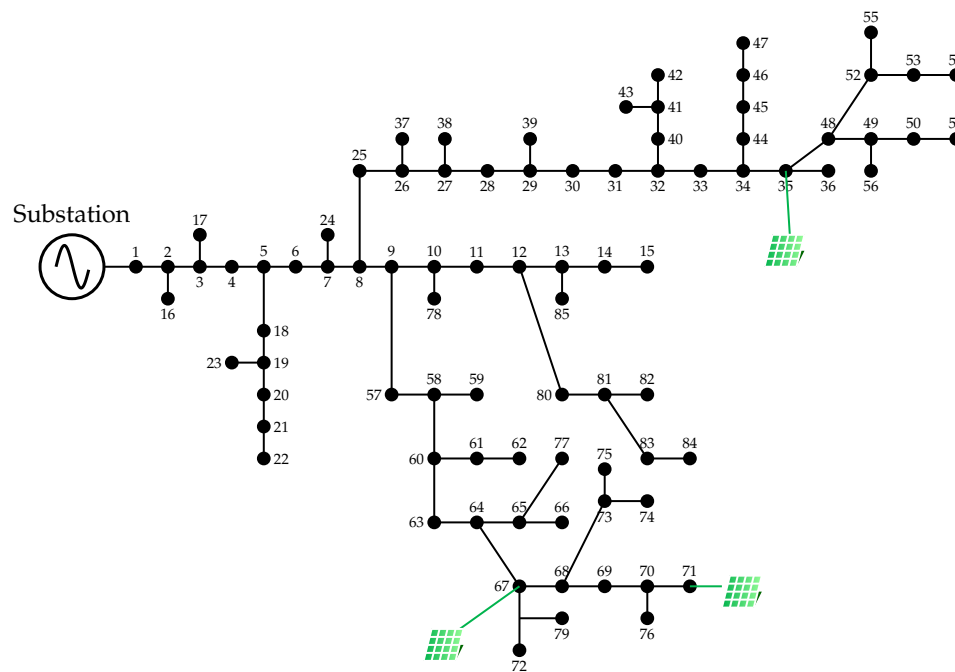


Figure 3. Topology of Test Feeder 3 with three PV power plants

4.4. Load-generation scenario

The number of scenarios plays a crucial role in analyzing uncertain situations; a reliable and manageable model must have an adequate number of scenarios. This research examines three distinct scenarios related to PV power plant generation and demand conditions. These scenarios incorporate low, medium, and high levels, resulting in nine potential combinations of renewable energy generation and load consumption, each with its own probability. The accuracy of the optimization model could be enhanced by increasing the number of scenarios. However, this would generate a large computational effort with little potential benefit. The probability factor used in this paper for each scenario can be consulted in (37).

The cost coefficient K_p used is equal to 168 US\$/kW-year, and the capacitor bank data for the optimization model are shown in Table I. This information was taken from (14).

Table I. Size and costs per capacitor bank

Type	Q_t (kvar)	Cost (USD\$/kvar-year)	Type	Q_t (kvar)	Cost (USD\$/kvar-year)
1	150	0,500	8	1.200	0,170
2	300	0,350	9	1.350	0,207
3	450	0,253	10	1.500	0,201
4	600	0,220	11	1.650	0,193
5	750	0,276	12	1.800	0,870
6	900	0,183	13	1.950	0,211
7	1.050	0,228	14	2.100	0,176

5. Numerical results and discussions

The SMIBF model was executed in the CVX interface, which allows modeling convex optimization problems in MATLAB (38). The solver used in CVX was Gurobi. Additionally, the non-convex MINLP model was implemented in GAMS and solved by employing the BONMIN, KNITRO, and DICOPT solvers. Three simulation cases were proposed to evaluate the effectiveness of the SMIBF model:

- C1 This case assumes that only three capacitor banks can be installed.
- C2 This case analyzes the effect on the OF z with varying numbers of capacitor banks on the systems. It considers a range of 0-5.
- C3 This case generates a Pareto front by varying the weighting factor between 0 and 1. This case only considers the installation of three capacitor banks.

5.1. Results obtained for C1

This case evaluates the efficiency of the SMIBF model and compares it against the non-convex model solved in GAMS using three different solvers. Table II presents the results obtained regarding the OF value in Eq. (33), its reduction compared to the benchmark case, and the reduction of power losses. The cost factors $C_{\text{loss}}^{\text{m}\acute{\text{a}}\text{x}}$ for Test Feeders 1, 2, and 3 are USD 9.010,848, USD 11.422,13, and USD 14.846,52, respectively. Moreover, $C_{\text{cap}}^{\text{m}\acute{\text{a}}\text{x}} = \text{USD}4,698$.

According to results shown in Table II, it can be stated that:

- The best solution was found by the proposed SMIBF model in the three test feeders. The OF values for these feeders are 0,6019, 0,6521, and 0,44769, which have been recalculated from the non-convex MINLP model. Regarding the benchmark cases, there were reductions of 39,81, 35,29, and 56,31 % in Test Feeders 1, 2, and 3, respectively, when compared to the best solutions. The reductions in energy losses are approximately 46,44, 40,39, and 63,77 %, respectively.
- As for Test Feeder 1, it is worth noting that the BONMIN solver achieved a solution close to that of the proposed SMIBF formulation. However, this solution is a local optimum that reduces the

Table II. Optimal integration of capacitor banks for case C1

Method	Nodes	Size (kvar)	Objective function	Reduction (%)	Reduction loss (%)
Test Feeder 1					
Benchmark case			1	–	–
BONMIN	{8,14,30}	{150,150,600}	0,6068	39,32	45,3182
KNITRO	{7,25,30}	{900,150,450}	0,6631	33,69	41,2092
DICOPT	{7,24,25}	{900,150,150}	0,7406	25,94	32,6318
SMIBF	{12,25,30}	{300,150,600}	0,6019	39,81	46,4446
Test Feeder 2					
Benchmark case			1	–	–
BONMIN	{11,61,64}	{900,900,150}	0,7884	21,16	29,7676
DICOPT	{25,50,61}	{150,150,600}	0,6619	33,81	40,4994
SMIBF	{21,61,64}	{150,600,150}	0,6471	35,29	40,3941
Test Feeder 3					
Benchmark case			1	–	–
SMIBF	{9,34,68}	{600,450,300}	0,4369	56,31	63,7771

OF and energy losses by 39,32 and 45,3182 %, respectively. On the other hand, the KNITRO and DICOPT solvers obtained the worst solutions, reducing the OF value by 33,69 and 25,94 %.

- In the case of Test Feeder 2, the KNITRO solver had convergence problems and was unable to find a feasible solution. Meanwhile, the BONMIN solver yielded the worst solution overall; it only minimally reduced the OF value by 21,16\$. On the contrary, the DICOPT solver found a solution close to that of the proposed SMIBF formulation, reducing the OF value by 33.81 %. Note that, regarding Test Feeder 3, none of the solvers could converge to any feasible solution, which is why this information is not included in Table II.
- These results demonstrate that the non-convex MINLP model for the optimal integration of fixed-step capacitor banks in EDNs is a challenging problem to solve. No solver in GAMS was able to find the best configuration. Additionally, as the test systems increase in size, the solvers encounter convergence problems. This shows that a convex formulation is better for solving this type of optimization model, even if it is relaxed.

Fig. 4 compares the average voltage profiles of the test systems, considering the presence or absence of capacitor banks. Based on this figure, it can be argued that, when capacitor banks are incorporated into the EDNs, the average voltage profiles are improved, *i.e.*, they remain closer to 1,0 pu. In Figure 4a, the worst average voltage profile, with or without capacitor banks installed, corresponds to node 18. However, it increases from 0,9804 to 0,9650 pu, *i.e.*, an improvement of approximately 1,60 %. For Test Feeder 2, the worst average voltage profiles (Fig. 4b) are 0,968 and 0,9560 pu (both at node 65) with and without capacitor banks installed. The improvement was around 1,28 %. In the case of Test Feeder 3, the improvement was around 2,91 %, going from a voltage level of 0,9464 pu (without capacitor banks) to 0,9740 pu (with capacitor banks) at node 54 (Fig. 4c). Additionally, in Figs. 4b and 4c, it can be noted that all voltages are above the minimum limit ($\geq 0,95$ pu) when the capacitor banks are installed, as opposed to not having them in the systems.

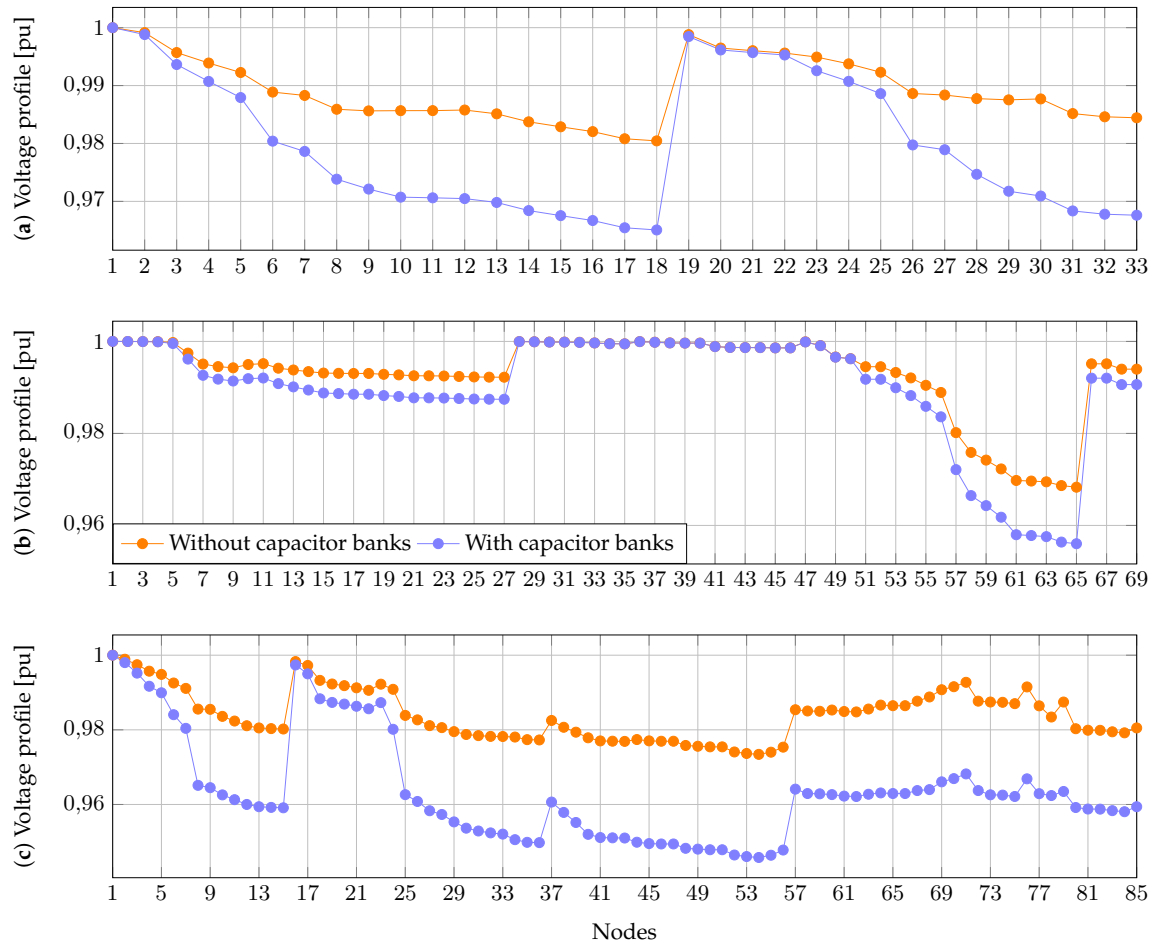


Figure 4. Comparison of average voltage profiles with and without capacitor banks installed: a) Test Feeder 1, b) Test Feeder 2, and c) Test Feeder 3

5.2. Results obtained for C2

This case analyzed how the OF is affected by changing the amount of capacitor banks installed from 0 to 5. Fig. 5 displays the value of the OF in (33) as the amount of capacitor banks increases in the three test feeders.

The results presented in Fig. 5 show that the addition of a third bank of capacitors does not lead to any improvements in the OF value; in fact, it makes it worse. This indicates that there is no significant reduction in system power losses after the third bank of capacitors – note that the installation of the capacitors increases the costs. For Test Feeder 2, the OF value is not significantly improved after installing the first capacitor bank. This improvement is reduced from having just one to three banks by only 0,35%. A similar situation occurs for Test Feeders 1 and 3: the OF is reduced by 0,30 and 1,64%, respectively, when going from two to three banks.

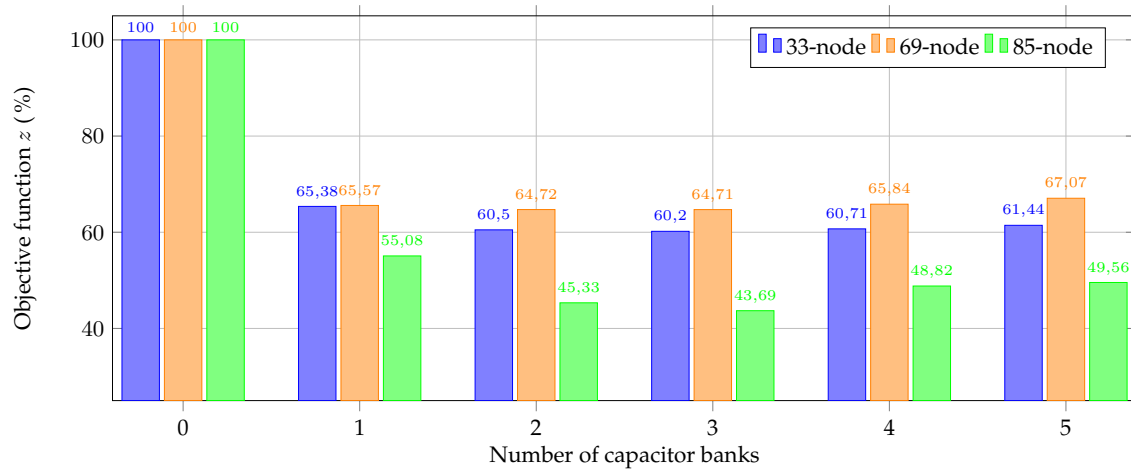


Figure 5. Variations in the objective function value with respect to the number of capacitor banks

5.3. Results obtained for C3

This case analyzes the Pareto set by increasing the ω factor by 0,1 from 0 to 1 in the OF z described in (21). Table III presents the OF values for all test feeders, which have been calculated via the SMIBF model.

Table III. Pareto data regarding the objective functions for the proposed SMIBF model

Factor (ω)	Test Feeder 1			69-node test feeder			Test Feeder 3		
	z	z_1	z_2	z	z_1	z_2	z	z_1	z_2
0,0	1	1	0	1	1	0	1	1	0
0,1	0,6601	0,6320	0,0280	0,6761	0,6480	0,0280	0,6078	0,5797	0,0280
0,2	0,6601	0,6320	0,0280	0,6761	0,6480	0,0280	0,4573	0,3971	0,0561
0,3	0,6050	0,5545	0,0504	0,6761	0,6480	0,0280	0,4573	0,3971	0,0561
0,4	0,6050	0,5545	0,0504	0,6471	0,5961	0,0510	0,4387	0,3660	0,0727
0,5	0,6019	0,5355	0,0664	0,6471	0,5961	0,0510	0,4369	0,3622	0,0746
0,6	0,6031	0,5303	0,0727	0,6471	0,5961	0,0510	0,4369	0,3622	0,0746
0,7	0,6031	0,5303	0,0727	0,6601	0,5841	0,0759	0,4369	0,3622	0,0746
0,8	0,6031	0,5303	0,0727	0,6601	0,5841	0,0759	0,4552	0,3664	0,0887
0,9	0,6031	0,5303	0,0727	0,6654	0,5830	0,0823	0,4552	0,3664	0,0887
1,0	0,6031	0,5303	0,0727	0,6654	0,5830	0,0823	0,4552	0,3664	0,0887

From the Pareto set results in Table III, it is possible to conclude that:

- Both objective functions, z_1 and z_2 , are in conflict because, as the value of the first one decreases (improves), that of the second one increases (deteriorates). The extreme solutions occur at the minimum and maximum values of the weighting factor, *i.e.*, when $\omega = 0$ and $\omega = 1$. The maximum weighting factor solution reveals that the annual energy losses costs for Test Feeders 1, 2, and 3 are

USD 9.010,848, 11.422,13, and USD 14.846,52, respectively. An analysis of the minimum weighting factor reveals that the investment costs for installing capacitor banks are highest at USD 341,5446, 386,6454, and 416,7126 per year for the modified Test Feeders 1, 2, and 3, respectively. However, in this solution, the annual energy losses costs are the lowest for the three test systems.

- The optimal solution of the OF z (*i.e.*, the multi-objective scenario) was found for $\omega = 0,5$ in each test feeder. This shows that the weighting factor for the single-objective scenario does not substantially impact the final result of the proposed SMIBF model. Nevertheless, the benefit of the Pareto set lies in having a spectrum of solutions that energy companies can use to make better decisions for their electrical systems.

5.4. Discussing the influence of integrating energy storage systems and the effect of radial reconfiguration on the model

In modern distribution systems, the integration of energy storage systems (ESS) introduces a dynamic element that could influence the optimal location and sizing of capacitors. The presence of ESS alters the overall energy flow patterns and affects the voltage profile across the grid. When incorporating fixed-step capacitor banks, co-optimization with storage systems becomes crucial. Storage systems can help alleviate the intermittency of renewable energy sources, which affects the requirements for reactive power compensation. The optimal placement of capacitors is intricately linked to the temporal and spatial dynamics of energy storage, as the latter influence load profiles and voltage stability. This dynamic interaction adds a layer of complexity to the model by introducing non-linearities caused by the time-dependent nature of storage systems (39). Consequently, the stochastic mixed-integer branch flow optimization model needs to evolve to capture these complex relationships, considering the dynamic nature of energy flow and voltage support in the presence of storage technologies.

On the other hand, the reconfiguration of electric distribution networks, particularly the transition to new radial configurations, could significantly influence the integration of fixed-step capacitors. Radial reconfiguration aims to enhance system reliability and minimize power losses by modifying the network's topology. In this context, the integration of fixed-step capacitors is a strategic endeavor. The new radial configurations may result in changes in load distribution and voltage profiles. To optimize the integration of capacitors, their location and size must be recalibrated to align with the new network conditions. Capacitors play a crucial role in compensating for reactive power demand and minimizing losses. Therefore, the strategic deployment of these devices is essential for achieving the objectives of the reconfigured network, such as minimizing losses and enhancing overall reliability. This is particularly important when considering altered power flow paths. Control strategies for capacitor banks may also need to be adapted in order to effectively address the dynamic changes introduced by radial reconfiguration (40).

6. Conclusions and future works

This paper proposes an SMIBF model to optimally integrate fixed-step capacitor banks into EDNs. The aim is to reduce the annual costs of energy losses and those of installing this technology. Our

proposal is based on a branch flow optimization model that incorporates two sets of auxiliary variables in order to generate a convex model and thus the global optimum. Furthermore, the model incorporates the sample average approximation model to address the stochastic nature of EDNs under multiple operating conditions. This allows for the inclusion of three different conditions into the developed model with regard to demand and renewable generation, namely low, medium, and high levels. The performance of the proposed model was evaluated on three test feeders and compared to the solutions provided by the BONMIN, KNITRO, and DICOPT solvers available in the GAMS software. The simulation results indicate that the developed SMIBF model provides the best solution for all three systems, reducing the OF value by 39,81, 35,29, and 56,31 % in Test Feeders 1, 2, and 3 when compared to the benchmark case. At the same time, the annual energy losses were reduced by 46,44, 40,39, and 63,77 %, respectively. No GAMS solver was able to achieve the global optimum of the optimization model. Additionally, the solver exhibited convergence problems as the size of the test feeders increased. This demonstrates that our proposal is a better option for optimally integrating fixed-step capacitor banks, even though it corresponds to a relaxed model.

The impact of increasing the amount of capacitor banks on the OF value was analyzed, finding that, after adding three capacitor banks, the OF value becomes worse. This implies that the energy losses were not significantly reduced after three capacitor banks. On the other hand, the use of the weighting factor allowed implementing a multi-objective approach. When $\omega = 0,50$, this approach yields the best solution (minimum). This finding confirms that the developed SMIBF model successfully identifies the global optimum in every evaluation.

The following future works could be conducted: (i) considering fixed-step switched capacitor banks in the proposed model, (ii) simultaneously integrating fixed-step capacitor banks and D-FACTS devices, and (iii) extending the developed SMIBF model to large-scale transmission systems with new objective functions.

7. Acknowledgments

This study received funding from Universidad Tecnológica de Pereira's project no. 6-23-7, titled *Desarrollo de una metodología para la compensación óptima de potencia reactiva en sistemas eléctricos de distribución* [Developing a methodology for optimal reactive power compensation in electrical distribution systems].

8. Author contributions

All authors contributed equally to the research.

References

- [1] M. I. M. Ridzuan, N. F. M. Fauzi, N. N. R. Roslan, and N. M. Saad, "Urban and rural medium voltage networks reliability assessment," *SN Appl. Sci.*, vol. 2, no. 2, jan 2020. [Online]. Available:

- <https://doi.org/10.1007/s42452-019-1612-z> ↑ 4
- [2] L. C. Kien, T. T. Nguyen, T. D. Pham, and T. T. Nguyen, "Cost reduction for energy loss and capacitor investment in radial distribution networks applying novel algorithms," *Neural Comput. Appl.*, vol. 33, no. 22, pp. 15 495–15 522, jun 2021. [Online]. Available: [SpringerScienceandBusinessMedia\(LLC\)](https://doi.org/10.1007/s42452-019-1612-z) ↑ 4
- [3] A. Paz-Rodríguez, J. F. Castro-Ordoñez, O. D. Montoya, and D. A. Giral-Ramírez, "Optimal Integration of Photovoltaic Sources in Distribution Networks for Daily Energy Losses Minimization Using the Vortex Search Algorithm," *Appl. Sci.*, vol. 11, no. 10, p. 4418, may 2021. [Online]. Available: <https://doi.org/10.3390/app11104418> ↑ 4
- [4] A. Águila, L. Ortiz, R. Orizondo, and G. López, "Optimal location and dimensioning of capacitors in microgrids using a multicriteria decision algorithm," *Heliyon*, vol. 7, no. 9, p. e08061, sep 2021. [Online]. Available: <https://doi.org/10.1016/j.heliyon.2021.e08061> ↑ 4
- [5] E. P. Madruga and L. N. Canha, "Allocation and integrated configuration of capacitor banks and voltage regulators considering multi-objective variables in smart grid distribution system," in *2010 9th IEEE/IAS International Conference on Industry Applications - INDUSCON 2010*, 2010, pp. 1–6. [Online]. Available: <https://doi.org/10.1109/INDUSCON.2010.5740055> ↑ 4
- [6] L. A. G. Pareja, J. M. L. Lezama, and O. G. Carmona, "Optimal placement of capacitors, voltage regulators, and distributed generators in electric power distribution systems," *Ingeniería*, vol. 25, no. 3, pp. 334–354, oct 2020. [Online]. Available: <https://doi.org/10.14483/23448393.16925> ↑ 4
- [7] S. Mishra, D. Das, and S. Paul, "A comprehensive review on power distribution network reconfiguration," *Energy Syst.*, vol. 8, no. 2, pp. 227–284, mar 2016. [Online]. Available: <https://doi.org/10.1007/s12667-016-0195-7> ↑ 4
- [8] S. Dhivya and R. Arul, "Demand side management studies on distributed energy resources: A survey," *TESEA Trans.*, vol. 2, no. 1, pp. 17–31, jul 2021. [Online]. Available: <https://doi.org/10.32397/tesea.vol2.n1.2> ↑ 4
- [9] R. Sirjani and A. R. Jordehi, "Optimal placement and sizing of distribution static compensator (D-STATCOM) in electric distribution networks: A review," *Renew. Sust. Energ. Rev.*, vol. 77, pp. 688–694, sep 2017. [Online]. Available: <https://doi.org/10.1016/j.rser.2017.04.035> ↑ 4
- [10] V. Tamilselvan, T. Jayabarathi, T. Raghunathan, and X.-S. Yang, "Optimal capacitor placement in radial distribution systems using flower pollination algorithm," *Alex. Eng. J.*, vol. 57, no. 4, pp. 2775–2786, dec 2018. [Online]. Available: <https://doi.org/10.1016/j.aej.2018.01.004> ↑ 4
- [11] A. Valencia, R. A. Hincapie, and R. A. Gallego, "Optimal location, selection, and operation of battery energy storage systems and renewable distributed generation in medium-low voltage distribution networks," *J. Energy Storage*, vol. 34, p. 102158, feb 2021. [Online]. Available: <https://doi.org/10.1016/j.est.2020.102158> ↑ 4
- [12] S. Griot and A. Moreau, "Vacuum circuit breaker's electrical life for shunt capacitor switching," in *24th ISDEIV 2010*, 2010, pp. 194–197. [Online]. Available: <https://doi.org/10.1109/DEIV.2010.5625750> ↑ 4

- [13] R. M. A. Velásquez and J. V. M. Lara, "Reliability, availability and maintainability study for failure analysis in series capacitor bank," *Eng. Fail. Anal.*, vol. 86, pp. 158–167, apr 2018. [Online]. Available: <https://doi.org/10.1016/j.engfailanal.2018.01.008> ↑ 4
- [14] O. D. Montoya, W. Gil-González, and A. Garcés, "On the conic convex approximation to locate and size fixed-step capacitor banks in distribution networks," *Computation*, vol. 10, no. 2, p. 32, 2022. [Online]. Available: <https://doi.org/10.3390/computation10020032>
- [15] W. Gil-González, O. D. Montoya, A. Rajagopalan, L. F. Grisales-Noreña, and J. C. Hernández, "Optimal selection and location of fixed-step capacitor banks in distribution networks using a discrete version of the vortex search algorithm," *Energies*, vol. 13, no. 18, p. 4914, sep 2020. [Online]. Available: <https://doi.org/10.3390/en13184914> ↑ 5
- [16] F. E. Riaño, J. F. Cruz, O. D. Montoya, H. R. Chamorro, and L. Alvarado-Barrios, "Reduction of losses and operating costs in distribution networks using a genetic algorithm and mathematical optimization," *Electronics*, vol. 10, no. 4, p. 419, feb 2021. [Online]. Available: <https://doi.org/10.3390/electronics10040419> ↑ 5
- [17] I. P. Abril, "Capacitors placement in distribution systems with nonlinear load by using the variables' inclusion and interchange algorithm," *DYNA*, vol. 88, no. 217, pp. 13–22, may 2021. [Online]. Available: <https://doi.org/10.15446/dyna.v88n217.91145> ↑ 5
- [18] O. D. Montoya, W. Gil-González, and J. C. Hernández, "Efficient integration of fixed-step capacitor banks and D-STATCOMs in radial and meshed distribution networks considering daily operation curves," *Energies*, vol. 16, no. 8, p. 3532, 2023. [Online]. Available: <https://doi.org/10.3390/en16083532> ↑ 5
- [19] Y. Ogita and H. Mori, "Parallel dual tabu search for capacitor placement in smart grids," *Procedia Comput. Sci.*, vol. 12, pp. 307–313, 2012. [Online]. Available: <https://doi.org/10.1016/j.procs.2012.09.076> ↑ 5
- [20] A. A. El-Fergany and A. Y. Abdelaziz, "Capacitor placement for net saving maximization and system stability enhancement in distribution networks using artificial bee colony-based approach," *Int. J. Electr. Power Energy Syst.*, vol. 54, pp. 235–243, 2014. [Online]. Available: <https://doi.org/10.1016/j.ijepes.2013.07.015> ↑ 5
- [21] K. Prakash and M. Sydulu, "Particle swarm optimization based capacitor placement on radial distribution systems," in *2007 IEEE Power Engineering Society General Meeting*, 2007, pp. 1–5. [Online]. Available: <https://doi.org/10.1109/PES.2007.386149> ↑ 5
- [22] A. Augugliaro, L. Dusonchet, S. Favuzza, M. G. Ippolito, S. Mangione, and E. R. Sanseverino, "A modified genetic algorithm for optimal allocation of capacitor banks in MV distribution networks," *Intell. Ind. Syst.*, vol. 1, no. 3, pp. 201–212, sep 2015. [Online]. Available: <https://doi.org/10.1007/s40903-015-0019-4> ↑ 5
- [23] K. Devabalaji, T. Yuvaraj, and K. Ravi, "An efficient method for solving the optimal sitting and sizing problem of capacitor banks based on cuckoo search algorithm," *Ain Shams Eng. J.*, vol. 9, no. 4, pp. 589–597, dec 2018. [Online]. Available: <https://doi.org/10.1016/j.asej.2016.04.005> ↑ 5
- [24] R. T. Marler and J. S. Arora, "The weighted sum method for multi-objective optimization: new insights," *Struct. Multidiscipl. Optim.*, vol. 41, pp. 853–862, 2010. [Online]. Available: <https://doi.org/10.1007/s00158-009-0460-7> ↑ 7

- [25] D. Jones, M. Tamiz et al., *Practical goal programming*. Springer, 2010, vol. 141. [Online]. Available: <https://doi.org/10.1007/978-1-4419-5771-9> ↑ 7
- [26] S. Dutta and K. N. Das, “A survey on pareto-based eas to solve multi-objective optimization problems,” in *Soft Computing for Problem Solving*. Springer Singapore, 2019, pp. 807–820. [Online]. Available: https://doi.org/10.1007/978-981-13-1595-4_64 ↑ 7
- [27] M. T. Emmerich and A. H. Deutz, “A tutorial on multiobjective optimization: fundamentals and evolutionary methods,” *Nat. Comput.*, vol. 17, pp. 585–609, 2018. [Online]. Available: <https://doi.org/10.1007/s11047-018-9685-y> ↑ 7
- [28] L. Zhihuan, L. Yinhong, and D. Xianzhong, “Non-dominated sorting genetic algorithm-ii for robust multi-objective optimal reactive power dispatch,” *IET Gener. Transm. Distrib.*, vol. 4, no. 9, pp. 1000–1008, 2010. [Online]. Available: <https://doi.org/10.1049/iet-gtd.2010.0105> ↑ 7
- [29] S. Özdemir, B. A. Attea, and Ö. A. Khalil, “Multi-objective evolutionary algorithm based on decomposition for energy efficient coverage in wireless sensor networks,” *Wirel. Pers. Commun.*, vol. 71, pp. 195–215, 2013. [Online]. Available: <https://doi.org/10.1007/s11277-012-0811-3> ↑ 7
- [30] J. B. Chagas and M. Wagner, “A weighted-sum method for solving the bi-objective traveling thief problem,” *Comput Oper Res*, vol. 138, p. 105560, 2022. [Online]. Available: <https://doi.org/10.1016/j.cor.2021.105560> ↑ 7
- [31] P. Yu, C. Wan, M. Sun, Y. Zhou, and Y. Song, “Distributed voltage control of active distribution networks with global sensitivity,” *IEEE Trans. Power Syst.*, vol. 37, no. 6, pp. 4214–4228, 2022. [Online]. Available: <https://doi.org/10.1109/TPWRS.2022.3153954> ↑ 8
- [32] M. Farivar and S. H. Low, “Branch flow model: relaxations and convexification—part i,” *IEEE Trans. Power Syst.*, vol. 28, no. 3, pp. 2554–2564, aug 2013. [Online]. Available: <https://doi.org/10.1109/tpwrs.2013.2255317> ↑ 10
- [33] B. Verweij, S. Ahmed, A. J. Kleywegt, G. Nemhauser, and A. Shapiro, “The sample average approximation method applied to stochastic routing problems: a computational study,” *Comput Optim Appl*, vol. 24, pp. 289–333, 2003. [Online]. Available: <https://doi.org/10.1023/A:1021814225969> ↑ 11
- [34] W. Gil-González, A. Garces, O. D. Montoya, and J. C. Hernández, “A mixed-integer convex model for the optimal placement and sizing of distributed generators in power distribution networks,” *Appl. Sci.*, vol. 11, no. 2, p. 627, 2021. [Online]. Available: <https://doi.org/10.3390/app11020627> ↑ 12
- [35] O. D. Montoya, W. Gil-González, and L. Grisales-Noreña, “An exact MINLP model for optimal location and sizing of DGs in distribution networks: A general algebraic modeling system approach,” *Ain Shams Eng. J.*, vol. 11, no. 2, pp. 409–418, 2020. [Online]. Available: <https://doi.org/10.1016/j.asej.2019.08.011> ↑ 12
- [36] O. D. Montoya, L. F. Grisales-Noreña, L. Alvarado-Barrios, A. Arias-Londoño, and C. Álvarez-Arroyo, “Efficient reduction in the annual investment costs in AC distribution networks via optimal integration of solar PV sources using the newton metaheuristic algorithm,” *Appl. Sci.*, vol. 11, no. 23, p. 11525, 2021. [Online]. Available: <https://doi.org/10.3390/app112311525> ↑ 13

- [37] W. Gil-González, "Optimal placement and sizing of d-statcoms in electrical distribution networks using a stochastic mixed-integer convex model," *Electronics*, vol. 12, no. 7, p. 1565, 2023. [Online]. Available: <https://doi.org/10.3390/electronics12071565> ↑ 13
- [38] M. Grant and S. Boyd, "CVX: Matlab software for disciplined convex programming, version 2.1," mar 2014. [Online]. Available: <http://cvxr.com/> ↑ 14
- [39] H. A. Taha, M. H. Alham, and H. K. M. Youssef, "Multi-objective optimization for optimal allocation and coordination of wind and solar dgs, besss and capacitors in presence of demand response," *IEEE Access*, vol. 10, pp. 16 225–16 241, 2022. [Online]. Available: <https://doi.org/10.1109/ACCESS.2022.3149135> ↑ 18
- [40] L. H. Macedo, G. Muñoz-Delgado, J. Contreras, and R. Romero, "Optimal service restoration in active distribution networks considering microgrid formation and voltage control devices," *IEEE Trans. Ind. Appl.*, vol. 57, no. 6, pp. 5758–5771, 2021. [Online]. Available: <https://doi.org/10.1109/TIA.2021.3116559> ↑ 18

Walter Gil-González

He received his BSc, MSc, and PhD degrees in Electrical Engineering from Universidad Tecnológica de Pereira (Colombia) in 2011, 2013, and 2019, respectively. He worked as an adjunct professor at Institución Universitaria Pascual Bravo. He is currently working as a professor in the Department of Electric Power Engineering, Universidad Tecnológica de Pereira. His research interests include power system control, stability, optimization, and operation.

Email: wjgil@utp.edu.co

Andrés Herrera-Orozco

He received BSc and MSc degrees in Electrical Engineering from Universidad Tecnológica de Pereira (Colombia) in 2010 and 2013, respectively, as well as a PhD from Universidade Federal do Rio Grande do Sul (Brazil) in 2017. He is currently a Professor at Department of Electrical Engineering School of Universidad Tecnológica de Pereira. He is a member of ICE3-UTP and CAFE-UTP research groups. His research interests include electrical smart grids, microgrid protection, power quality, fault analysis, and power systems analysis.

Email: arherrera@utp.edu.co

Alexander Molina-Cabrera

He received his BSc and MSc degrees in Electrical Engineering from Universidad Tecnológica de Pereira (Colombia) in 2004 and 2005. In 2018, he received a PhD from Universidad de los Andes (Colombia). He is currently the dean of the Engineering Faculty at Universidad Tecnológica de Pereira, where he also serves as an associate professor in the Department of Electric Power Engineering. His research focuses on nonlinear systems and power systems control and stability. Other areas of interest include artificial intelligence and electrical machines.

Email: almo@utp.edu.co



Research

Energy Management Systems for Microgrids: Evolution and Challenges within the Framework of the Energy Transition

Sistemas de gestión de energía para microrredes: evolución y desafíos en el marco de la transición energética

Carlos Santiago Vidal-Martínez¹, Maximiliano Bueno-López²  *, Juan Fernando Flórez-Marulanda² , Álvaro René Restrepo²

¹Department of Engineering of Corporación Universitaria Autónoma del Cauca, Popayán
Colombia 

²Universidad del Cauca, Popayán Colombia 

Abstract

Context: Microgrids have been gaining space and credibility in terms of research and real applications. Technological maturity and new regulations have allowed these types of systems to position themselves as a real alternative to increase the coverage of the energy service and improve its quality. One of the biggest challenges of microgrids is the management of resources and their synchronization with conventional grids. In order to overcome the inconvenience of synchronizing and managing the components of a microgrid, research on management systems has been conducted, which usually consist of a set of modules and control strategies that manage the available resources. However, these studies have not reached unanimity on the best method to perform these tasks, which is why it is necessary to perform a systematic collection of information and clearly define the state of research in energy systems management for this type of network.

Method: Based on the above, a systematic mapping was carried out in this article, wherein a significant number of papers that have contributed to this area were compiled. Taxonomies were generated based on the nature of the variables collected. These variables correspond to the data or information that enters and/or leaves the microgrid management system, such as meteorological variables, power, priority loads, intelligent loads, economic, operating states, and binary outputs.

Conclusions: It was observed that, despite the advances in studying different techniques and strategies microgrid control and management, other factors that may affect performance have not been covered in a relevant way, such as the nature of variables and microgrid topology, among others.

Keywords: microgrid, management system, input and output variables

Article history

Received:
8th / Aug / 2022

Modified:
9th / Apr / 2023

Accepted:
10th / May / 2023

Ing., vol. 29, no. 1,
2024. e19777

©The authors;
reproduction right
holder Universidad
Distrital Francisco
José de Caldas.

Open access



*  **Correspondence:** mbuenol@unicauca.edu.co

Resumen

Contexto: Las microrredes eléctricas han venido ganando espacio y credibilidad a nivel de investigación y aplicaciones reales. La madurez tecnológica y las nuevas regulaciones han permitido que este tipo de sistemas se posicionen como una alternativa real para aumentar la cobertura del servicio de energía y mejorar su calidad. Uno de los mayores retos de las microrredes es la gestión de los recursos y su sincronización con la red convencional. Con el fin de superar el inconveniente de sincronizar y gestionar los componentes de la microrred, se ha investigado sobre sistemas de gestión, los cuales normalmente consisten en un conjunto de módulos y estrategias de control que administran los recursos disponibles. Sin embargo, estas investigaciones no han llegado a una unanimidad sobre el mejor método para realizar estas tareas, por lo cual se hace necesario realizar una recopilación sistemática de información y definir claramente el estado de la investigación en gestión de sistemas de energía para este tipo de redes.

Método: Con base en lo anterior, en este artículo se realizó un mapeo sistemático, donde se recopiló un importante número de artículos que han aportado a este campo. Se generaron taxonomías basadas en la naturaleza de las variables que se recopilaron. Dichas variables corresponden a los datos o información que entran y/o salen del sistema de gestión de la microrred, tales como variables meteorológicas, potencia, cargas prioritarias, cargas inteligentes, económicas, estados de operación y salidas binarias.

Conclusiones: Se observa que, a pesar de los avances en el estudio de las diferentes técnicas y estrategias de control y gestión de microrredes, no se han cubierto de forma relevante otros factores que pueden afectar al rendimiento, como la naturaleza de las variables y la topología de la microrred, entre otros.

Palabras clave: microrred, sistema de gestión, variables de entrada y salida

Table of contents

		3.1. Management system inputs	5
		3.2. Management system outputs . . .	14
		4. Analysis	19
		5. Conclusions	20
		6. Author contributions	21
		References	21
1. Introduction	2		
2. Microgrid management systems	4		
3. Variables involved in a microgrid management system	5		

1. Introduction

Since the emergence of microgrids, the incidence of renewable energies in the energy landscape has increased (1). A microgrid consists of the interconnection of loads of different nature, communication systems, metering, control, and distributed energy sources. This system can operate in standalone mode and connect with other microgrids or the main power grid (1,2). A microgrid has the following sections: a physical plant where the distributed energy components are located (generation and storage

elements, load groups, flexible loads, smart loads, and protection and connection elements); a control section, which governs the components of the physical plant and may be centralized (the management system controls the microgrid as a single entity) or decentralized (the control of each component is independent); and a management section, where the flow of energy depends on data from inside and outside the microgrid, according to specific objectives (3) (Fig. 1). Microgrids have become more relevant due to changes in regulatory aspects (4) and the cost reduction of different components (5). These characteristics have also led to increased research aimed at solving various problems associated with these systems (6), particularly focusing on the development of a good energy management system (EMS) (7).

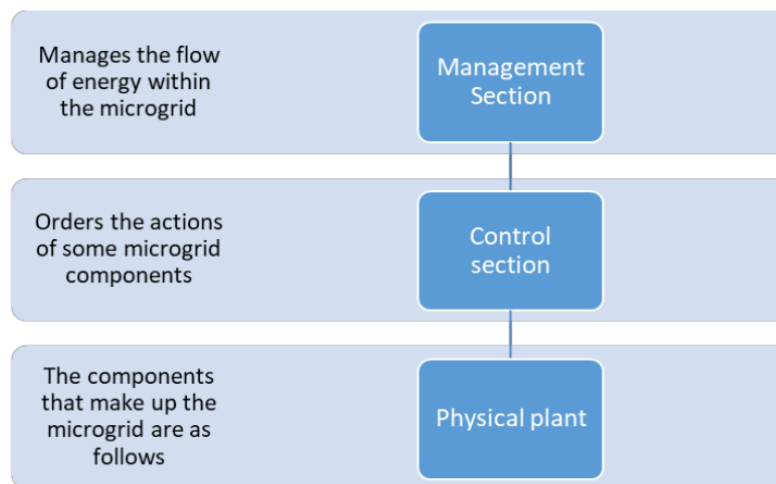


Figure 1. Microgrid sections

The first publications on microgrids date back to the early 2000s (8), which could be counted by the dozen. Nowadays, publications amount to approximately 1.500 articles per year (9). A wide variety of factors affect microgrids, such as generation, energy demand, storage status, and the cost of energy, without omitting any regulations that apply. These factors must be synchronized and managed in order to ensure the most efficient operation (10, 11). To this effect, a microgrid must have a suitable local generation system that allows it to operate in any scenario (desired and undesired) (12).

Different approaches have studied the problems associated with energy resource management (13), (14). A variety of research works focus on microgrid control methods and configurations (15), management system functionalities (16), architectures and the components to be controlled (17), and input and output variables. Different objectives and factors influence microgrid energy flow (18). However, these works have not reached unanimity on these aspects. Therefore, a systematic compilation of these works is necessary, in addition to a clear definition of the state of research on EMS for this type of grid.

This paper presents a descriptive review of the factors involved in the management system of a microgrid, such as input and output variables, topology configurations, and the control method and

strategy. This review seeks to be a reference tool that will be available for all those interested in working on microgrid energy management to find a compendium of the main components in this type of system.

The structure of this paper is as follows: Section 2 presents the concept of a microgrid management system; Section 3 explains the variables involved in a microgrid management system; Section 4 presents them; and Section 5 provides some conclusions based on the collected information.

2. Microgrid management systems

In IEC 61970, the International Electrotechnical Commission defines a management system in electrical environments as "a computer program comprising a software platform that provides basic support services and a set of applications providing the functionality necessary for the efficient operation of electrical generation and transmission facilities to ensure adequate security of power supply at minimum cost" (19). A microgrid management system generally consists of modules such as energy resource distribution and load forecasting systems, human-machine interfaces, and supervisory control and data acquisition (SCADA) systems, which ensure the efficient implementation of decision-making strategies by sending orders to generation, storage, and load unit components (20). The management system performs various functions, such as monitoring, analyzing, and forecasting power generation from distributed energy resources, load consumption, energy market prices, auxiliary markets, and meteorological factors. These functions help the management system improve the microgrid's performance while compensating for its limitations (21).

Management systems implement one of two control strategies: centralized and decentralized. In the centralized one, a central controller accumulates information from the energy resources distribution and load forecasting modules, such as meteorological and energy data and user consumption patterns, among others. These data enter the SCADA module, which determines the energy programming of the microgrid and sends orders to the local controller, which is in charge of executing them in the different components of the microgrid (15). In contrast, in the decentralized control strategy, the central microgrid controller sends and receives all information from the local controllers of the microgrid components in real time. Each local controller proposes a current and future order to the central controller of the microgrid, and the central controller determines the most beneficial scheduling and delivers it to the local controllers. The latter may disagree with the current operation and may continue negotiating until global and local objectives are achieved (22).

With the integration of renewable energy resources, storage systems, electric vehicles, and demand response, the objectives of microgrid management systems have diversified, *e.g.*, scheduling distributed energy resources and loads, minimizing system losses and outages, controlling the intermittency and volatility of renewable energy resources, and achieving economical, sustainable, and reliable operation for the microgrid (16).

3. Variables involved in a microgrid management system

Unlike traditional power systems, in a microgrid, it is possible to evaluate multiple variables thanks to the installation of smart meters and a better knowledge of the system's operation. These variables can be inputs or outputs of the management system.

3.1. Management system inputs

Different works focused on implementing EMS (23–26) show the diverse use of input variables and different alternatives in decision-making.

The input variables can be divided into three categories:

- External variables
- Internal variables
- Economic variables

External variables

The external inputs of the microgrid are related to the factors that influence energy generation and are usually of a meteorological nature. They change with respect to the type of renewable energy used.

For photovoltaic energy, the relevant variables are

- Solar irradiance
- Environment temperature
- Effective hours of sunlight

For wind energy, there is

- Wind speed
- Air density
- Rotor area or surface area in contact with the air

The external variables can be subdivided into two new categories:

- Meteorological
- Generation system power

Meteorological

In (28–32), the authors use solar irradiance, temperature, and wind speed as external variables of a meteorological nature. Uncertainty prediction methods establish the variable values to obtain an approximation of the microgrid's energy and ability to supply the demand of its loads. Although these

references share these common aspects, they implement different architectures, generation systems, strategies, and control methods (16). Although there is a difference in generation sources, the treatment of information and the obtention methods are similar. A general review of this subject is presented in Table I.

Table I. External meteorological variables

Ref.	Year	Management techniques	External variables	Microgrid architecture	Control strategy	Microgrid generation
(27)	2016	Integer and mixed linear programming	Wind speed, solar irradiance, temperature	Grid-connected mode	Centralized	Photovoltaic, wind power, diesel generators, grid connection
(28)	2016	Mixed linear programming	Solar irradiance, hydrogen flux, temperature	Grid-connected mode	Centralized	Fuel cells, photovoltaics, grid connection
(29)	2016	Mixed linear programming	Solar irradiation, water flow, temperature	Grid-connected mode	Centralized	Photovoltaics, geothermal, thermal energy storage, grid connection
(30)	2014	Mixed linear programming	Solar irradiance, wind speed	Islanded mode	Centralized	Photovoltaic, wind power
(31)	2013	Dynamic programming	Wind speed, temperature	Grid-connected mode	Centralized	Wind power, grid connection
(32)	2016	Genetic algorithm	Solar irradiance, wind speed, photovoltaic and wind power forecasting	Grid-connected mode	Centralized	Photovoltaic, wind power, diesel generator, grid connection
(33)	2015	Swarm optimization	Solar irradiance, wind speed, photovoltaic and wind energy prediction	Grid-connected mode	Centralized	Photovoltaic, wind power, grid connection
(34)	2016	Ant colony optimization	Solar irradiation, wind speed, photovoltaic and wind power forecasting	Grid-connected mode	Centralized	Photovoltaic, wind power, micro gas turbine, grid connection
(35)	2014	Gravitational search algorithm	Solar irradiation, wind speed	Islanded mode	Centralized	Photovoltaic, wind power, micro gas turbine
(36)	2017	Fuzzy logic	Wind speed, solar irradiation, temperature, photovoltaic and wind energy forecasting	Grid-connected mode	Centralized	Photovoltaic, wind power, grid connection
(37)	2011	Fuzzy logic	Temperature, solar irradiation, wind speed, photovoltaic, wind energy output power	Grid-connected mode	Centralized	Photovoltaic, wind power, fuel cells, grid connection
(38)	2016	Multi-agent system	Wind speed, solar irradiance, temperature, etc.	Islanded mode	Decentralized	Photovoltaic, wind power
(39)	2017	Multi-agent system	Solar irradiance, temperature	Grid-connected mode	Decentralized	Fuel cells, photovoltaic, wind power, grid connection

The most relevant meteorological variables are solar irradiance, temperature, and wind speed. Fig. 2 shows the use percentage of these variables. Irradiance is the most frequently mentioned due to the technological advances for measuring it and the availability of official information in some countries. Methods based on artificial intelligence have led the field by predicting behavior and due to their ability

to use large volumes of data to estimate the generation potential.

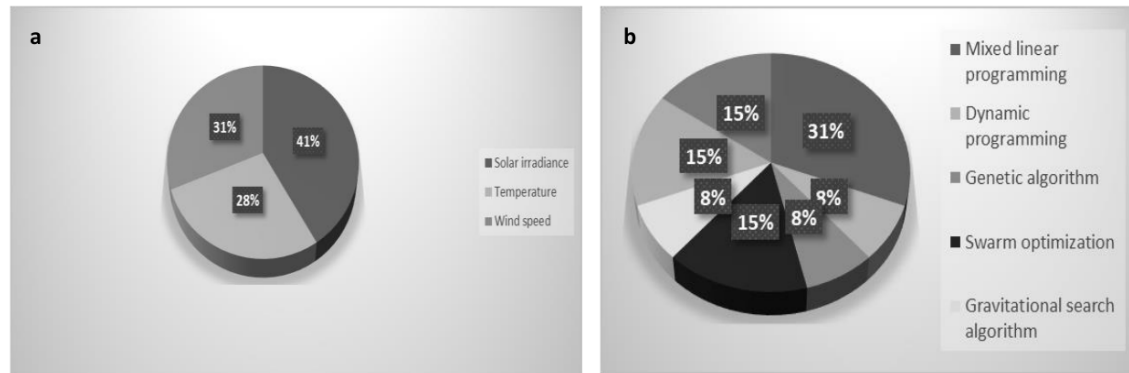


Figure 2. a) Relevant meteorological variables, b) management techniques relevant to meteorological variables

Generation system power

In several works (18,40–46), the variables used by the management system involve the output power of the generation systems in order to determine the maximum power that can be supplied via historic data or by directly measuring the output power. Hence, they only consider the result of the microgrid's energy generation (Table II).

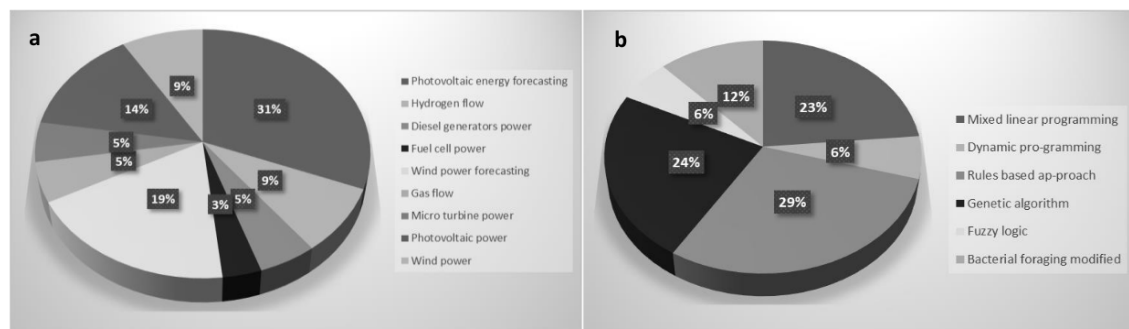


Figure 3. a) Relevant power generation system variables, b) relevant management techniques regarding the power variables of generation systems

Internal variables

The information handled by the internal variables is electrical. Within this category the following groups can be mentioned:

- The state of charge and capacity of the storage system
- The state of charge of an electric vehicle

Table II. External variables associated with generation system power

Ref.	Year	Management techniques	External variables	Microgrid architecture	Control strategy	Microgrid generation
(40)	2014	Mixed linear programming	Maximum solar power available, maximum wind power available	Grid-connected mode	Centralized	Photovoltaic, wind power, grid connection
(42)	2017	Mixed linear programming	Photovoltaic power, diesel generator power	Islanded mode	Centralized	Photovoltaic, diesel generators
(47)	2017	Mixed linear programming	Photovoltaic power, photovoltaic energy generation	Grid-connected mode	Centralized	Photovoltaic, grid-connected
(41)	2011	Mixed non-linear programming	Photovoltaic and wind power	Grid-connected mode	Centralized	Micro gas turbines, fuel cells, wind power, photovoltaics, grid connections
(43)	2017	Dynamic programming	Photovoltaic power, diesel generators power	Islanded mode	Centralized	Diesel generators, photovoltaic
(44)	2016	Rule-based approach	Prediction of photovoltaic power, fuel cell power, hydrogen flow	Grid-connected mode	Centralized	Photovoltaic, fuel cell, grid connection
(48)	2011	Rule-based approach	Prediction of photovoltaic power, micro turbine power, gas flow	Grid-connected mode	Centralized	Photovoltaic, micro gas turbine, grid connection
(46)	2015	Rule-based approach in a load-bearing state	Prediction of photovoltaic and wind power, micro turbine power, gas flow	Grid-connected mode	Centralized	Photovoltaic, wind power, micro turbine gas, grid connection
(18)	2015	Rule-based approach in a load-bearing state	Photovoltaic and wind power forecasting	Grid-connected mode	Centralized	Photovoltaic, wind power, grid connection
(49)	2013	Rule-based approach	Photovoltaic power	Grid-connected mode	Centralized	Photovoltaic, grid connection
(23)	2016	Genetic algorithm	Prediction of photovoltaic and wind power generation	Grid-connected mode	Centralized	Photovoltaic, wind power, fuel cells, micro gas turbine, grid connection
(26)	2016	Genetic algorithm	Load demand forecasting, photovoltaic generation forecasting	Islanded mode	Centralized	Photovoltaic, diesel generators
(50)	2017	Genetic algorithms	Photovoltaic and wind power	Grid-connected mode	Centralized	Photovoltaic, wind power, grid connection
(20)	2011	Coded genetic array algorithm	Photovoltaic energy prediction	Grid-connected mode	Centralized	Photovoltaic, grid connection
(51)	2016	Differential evolution	Photovoltaic and wind power forecasting	Grid-connected mode	Centralized	Photovoltaic, wind power, micro gas turbine, grid connection
(52)	2012	A self-adaptive gravitational search algorithm	Photovoltaic and wind power	Grid-connected mode	Centralized	Photovoltaic, wind power, grid connection
(53)	2013	Bacterial foraging modified	Photovoltaic and wind power forecasting, fuel cost, hydrogen flow	Grid-connected mode	Centralized	Photovoltaic, wind, fuel cells, grid connection
(54)	2014	Bacterial foraging modified	Wind power forecasting, gas flow, installed power of gas microturbines	Grid-connected mode	Centralized	Wind, gas microturbines, grid connection
(55)	2012	Fuzzy logic	Prediction of photovoltaic and wind power generation, hydrogen flow	Grid-connected mode	Centralized	Photovoltaic, wind, fuel cells, grid connection

- The power output of the generation or prediction
- The frequency of the generated power
- Load demand, smart loads, and flexible loads

There are two subcategories:

- Priority loads
- Controllable loads

Priority loads

Within this category, (27,28,42,43,48), and (56) control variables that are inherent to the microgrid. There are loads with a degree of priority, as the network is operated via a management system with a hierarchy of consumption. This system prioritizes the supply of loads with a higher value regarding decision-making (Table III).

The most relevant variables used in this category are shown in Fig. 4.

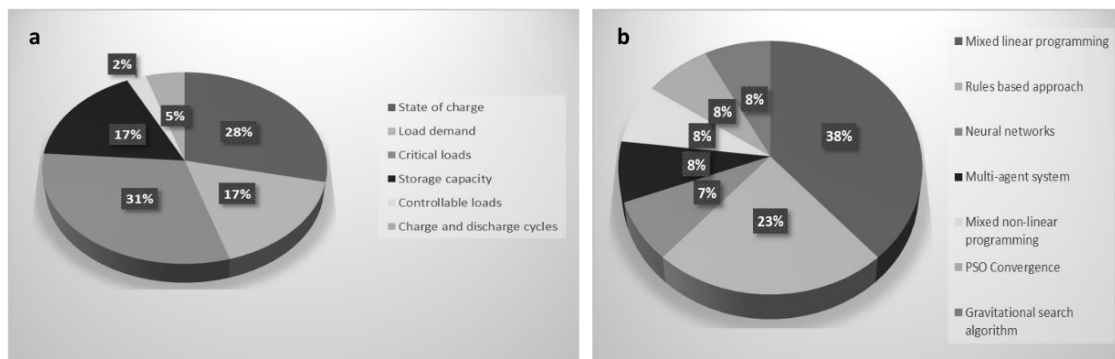


Figure 4. a) Relevant variables of priority loads, b) relevant management techniques for priority load variables

Controllable loads

In (10, 48, 50–52), the implementation of controllable or intelligent loads that help to prevent the network from overloading or destabilizing also facilitates communication with the management system. This configuration allows the EMS to adjust the power supplied or the actions to be taken from a predetermined range of parameters. Thus, the loads can operate partially, preserving their primary functions (Table IV).

Economic variables

The economic variables of the microgrid are mainly related to its operation and maintenance costs, *e.g.*,

- The cost of operation (maintenance and start-up)
- Energy purchase price
- Energy sale price

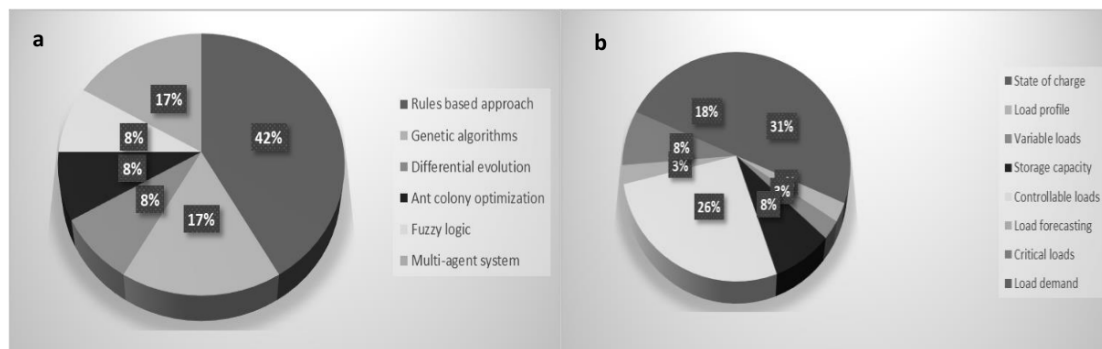
This financial information is usually obtained through energy sales exchanges (61) and has two sub-

Table III. Internal variables for priority loads

Ref.	Year	Management techniques	Internal variables	Microgrid architecture	Control strategy	Microgrid generation
(27)	2016	Integer and mixed linear programming	Battery status, charging capacity, priority, interruptible or switchable loads	Grid-connected mode	Centralized	Photovoltaic, wind, diesel generators, grid connection
(56)	2015	Mixed linear programming	Priority and non-priority loads, battery status, charging capacity	Grid-connected mode	Centralized	Micro gas turbines, fuel cells, grid connection
(28)	2016	Mixed linear programming	Battery status, storage capacity, priority, and non-priority loads	Grid-connected mode	Centralized	Fuel cells, photovoltaic, grid connection
(40)	2014	Mixed linear programming	Several charging points, EV charging capacity, EV charging status, charging and discharging efficiency, critical loads, adjustable loads, and network capacity	Grid-connected mode	Centralized	Photovoltaic, wind, grid connection
(42)	2017	Mixed linear programming	Battery charge factor, nominal discharge time, storage capacity, critical and non-critical loads, charge and discharge cycles	Islanded mode	Centralized	Photovoltaic, diesel generators
(41)	2011	Mixed non-linear programming	Load status of the core system, critical and non-critical loads, and set points for active and reactive power	Grid-connected mode	Centralized	Micro gas turbines, fuel cells, wind, photovoltaic, grid connection
(48)	2011	Ruler-based approach	Load forecasting, critical loads, controllable loads, battery state of charge, ultracapacitor state of charge	Grid-connected mode	Centralized	Photovoltaic, micro gas turbine, grid connection
(46)	2015	Rule-based approach in the load state	Load forecasting, critical loads, controllable loads, battery state of charge, and ultracapacitor state of charge	Grid-connected mode	Centralized	Photovoltaic, wind power, micro gas turbine, grid connection
(18)	2015	Rule-based approach in the load state	Critical loads, controllable loads, state of charge batteries.	Grid-connected mode	Centralized	Photovoltaic, wind power, grid connection.
(57)	2016	PSO Convergence	Battery state of charge, load demand, critical loads	Islanded mode	Centralized	Photovoltaic, wind power, diesel generator
(35)	2014	Gravitational search algorithm	Battery state of charge, load demand, critical loads	Islanded mode	Centralized	Photovoltaic, wind power, micro gas turbine
(58)	2016	Neural networks	Load status, storage capacity, load demand, load shedding, critical loads	Grid-connected mode	Centralized	Photovoltaic, wind power, fuel cells, diesel generators, grid connection
(38)	2016	Multi-agent system	Load demand, critical loads, state of charge, storage capacity	Islanded mode	Decentralized	Photovoltaic, wind power

Table IV. Internal variables for controllable loads

Ref.	Year	Management techniques	Internal variables	Microgrid architecture	Control strategy	Microgrid generation
(44)	2016	Rule-based approach	Battery state of charge, load profile, variable loads, reference system	Grid-connected mode	Centralized	Photovoltaic, fuel cell, grid connection
(48)	2011	Rule-based approach	Load forecasting, critical loads, controllable loads, battery state of charge, ultracapacitor state of charge, energy price	Grid-connected mode	Centralized	Photovoltaic, micro gas turbine, grid connection
(49)	2013	Rule-based approach	Load demand, controllable loads, battery state of charge	Grid-connected mode	Centralized	Photovoltaic, grid connection
(50)	2017	Genetic algorithms	Battery state of charge, load demand, controllable loads	Grid-connected mode	Centralized	Photovoltaic, wind power, co-connection to the grid
(20)	2011	Genetic algorithms	Load demand, controllable loads, battery state of charge	Grid-connected mode	Centralized	Photovoltaic, grid connection
(51)	2016	Differential evolution	Load demand, controllable loads, battery state of charge	Grid-connected mode	Centralized	Photovoltaic, wind power, micro gas turbine, grid connection
(34)	2016	Ant colony optimization	Load demand, battery charging status, controllable loads	Grid-connected mode	Centralized	Photovoltaic, wind power, micro gas turbine, grid connection
(59)	2017	Fuzzy logic	Load demand, controllable loads, storage capacity, battery state of charge	Connected to the grid and other microgrids	Centralized	Photovoltaic, wind power, grid-connected, other microgrids
(39)	2017	Multi-agent system	Load demand, controllable loads, battery state of charge, storage capacity	Grid-connected mode	Decentralized	Fuel cells, photovoltaic, wind power, grid connection
(60)	2015	Multi-agent system	Load demand, controllable loads, battery state of charge, storage capacity	Grid-connected mode	Decentralized	Photovoltaic, wind power, fuel cells, grid connection

**Figure 5.** a) Relevant variables of controllable loads, b) relevant management techniques for controllable load variables

categories:

1. Energy value
2. Cost of generation

Table V. Internal variables for controllable loads

Ref.	Year	Management techniques	Economic variables	Microgrid architecture	Control strategy	Microgrid generation
(27)	2016	Integer and mixed linear programming	Fuel cost, generator maintenance cost, power cost, energy price	Grid-connected mode	Centralized	Photovoltaic, wind power, diesel generators, grid connection
(56)	2015	Mixed linear programming	Fuel cost, generator maintenance cost, power cost, energy price	Grid-connected mode	Centralized	Micro gas turbines, fuel cells, grid connection
(32)	2016	Genetic algorithm	Energy price, fuel cost	Grid-connected mode	Centralized	Photovoltaic, wind power, diesel generator, grid connection
(29)	2015	Mixed linear programming	Energy price	Grid-connected mode	Centralized	Photovoltaic, geothermal, thermal energy storage, grid connection
(40)	2014	Mixed linear programming	Battery wear cost, energy price	Grid-connected mode	Centralized	Photovoltaic, wind power, grid connection
(31)	2013	Dynamic programming	Energy price	Grid-connected mode	Centralized	Wind power, grid connection
(48)	2011	Rule-based approach	Energy price	Grid-connected mode	Centralized	Photovoltaic, micro gas turbine, grid connection
(46)	2015	Rule-based approach in the load state	Energy price	Grid-connected mode	Centralized	Photovoltaic, wind, micro gas turbine, grid connection
(23)	2016	Genetic algorithms	Energy sales and purchase price, operating costs	Grid-connected mode	Centralized	Photovoltaic, wind, fuel cells, micro gas turbine, grid connection
(50)	2017	Memory-based genetic algorithms	Energy prices, operating costs	Grid-connected mode	Centralized	Photovoltaic, wind power, grid connection
(34)	2016	Ant colony optimization	Energy prices, operating costs	Grid-connected mode	Centralized	Photovoltaic, wind power, micro gas turbine, grid connection
(53)	2013	Modified bacterial foraging	Energy price, fuel cost	Grid-connected mode	Centralized	Photovoltaic, wind power, fuel cells, grid connection
(36)	2017	Fuzzy logic	Energy price	Grid-connected mode	Centralized	Photovoltaic, wind power, grid connection
(55)	2012	Fuzzy logic	Operating and maintenance costs, energy prices	Grid-connected mode	Centralized	Photovoltaic, wind power, fuel cells, grid connection

(58)	2016	Neural networks	Fuel price, energy price	Grid-connected mode	Centralized	Photovoltaic, wind power, fuel cells, diesel generators, grid connection
(39)	2017	Multi-agent system	Energy sales and purchase price, maintenance, operating costs	Grid-connected mode	Decentralized	Fuel cells, photovoltaic, wind power, grid connection
(60)	2015	Multi-agent system	Energy price, maintenance, operating costs	Grid-connected mode	Decentralized	Photovoltaic, wind power, fuel cells, grid connection
(62)	2016	Game theory	Energy sales and purchase price, operating cost	Grid-connected mode	Decentralized	Photovoltaic, fuel cells, grid connection
(63)	2013	Game theory	Operating costs, energy prices	Grid-connected mode	Decentralized	Photovoltaic, wind power, micro gas turbine, grid connection
(39)	2017	Multi-agent system	Energy sales and purchase price, maintenance, operating costs	Grid-connected mode	Decentralized	Fuel cells, photovoltaic, wind power, grid connection
(60)	2015	Multi-agent system	Energy price, maintenance, operating costs	Grid-connected mode	Decentralized	Photovoltaic, wind power, fuel cells, grid connection
(62)	2016	Game theory	Energy sales and purchase price, operating costs	Grid-connected mode	Decentralized	Photovoltaic, fuel cells, grid connection

Energy value

As per (29,30,33,46), and (?), this category has associated operating costs and values, with particular emphasis on the energy price. The energy value generated can be similar to the energy price for the time during which the microgrid operates autonomously. This results in a saving that justifies the resources spent, contributing to the viability of the microgrid's implementation (Table V).

The most relevant variables used in this category are shown in Fig. 6.

Cost of generation

In (26, 30, 42), and (43), factors such as the fuel or generation cost, the operating costs, and the maintenance costs of the microgrid take on greater relevance. The price of energy supplied by the conventional power grid is not considered by these authors, as the microgrid operates in islanded mode (Table VI).

The most relevant variables used in this category are shown in Fig. 7.

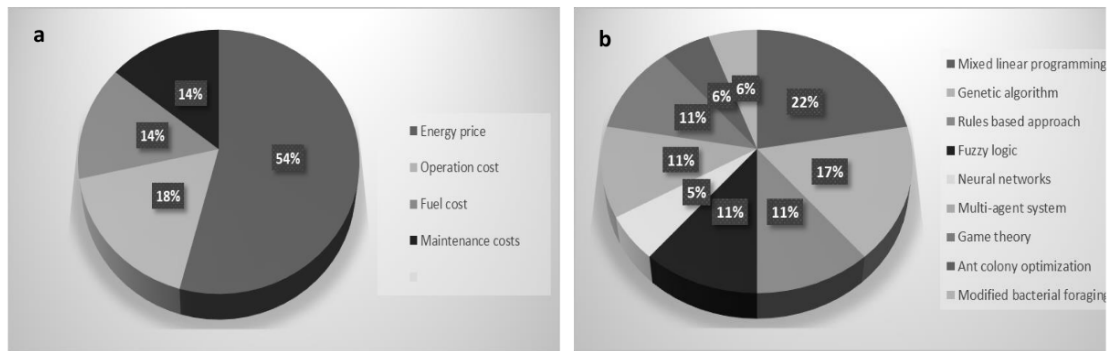


Figure 6. a) Economic variables regarding energy value, b) relevant management techniques regarding energy value

Table VI. Economic variables regarding the cost of generation

Ref.	Year	Management techniques	Economic variables	Microgrid architecture	Control strategy	Microgrid generation
(42)	2017	Mixed linear programming	Fuel price	Islanded mode	Centralized	Photovoltaic, diesel generators
(30)	2017	Mixed linear programming	Cost of components, operating costs	Islanded mode	Centralized	Photovoltaic, wind power
(43)	2017	Dynamic programming	Fuel price	Islanded mode	Centralized	Diesel generators, photovoltaic
(26)	2016	Genetic algorithms	Fuel price	Islanded mode	Centralized	Photovoltaic, diesel generators
(57)	2016	PSO Convergence	Fuel price	Islanded mode	Centralized	Photovoltaic, wind power, diesel generator
(35)	2014	Gravitational search algorithm	Fuel price	Islanded mode	Centralized	Photovoltaic, wind power, micro gas turbine
(38)	2016	Multi-agent system	Maintenance cost, generation cost	Islanded mode	Decentralized	Photovoltaic, wind power
(64)	2013	Multi-agent system	Maintenance cost, generation cost	Connected to other microgrids	Decentralized	Photovoltaic, connection to other microgrids

3.2. Management system outputs

A management system's output is the instruction or orders that the system executes to fulfill an objective. These instructions influence the routing of the energy flow and the operation or shutdown of components.

The outputs of the management system can be divided into two categories:

A. Preset operating status

B. Binary decisions

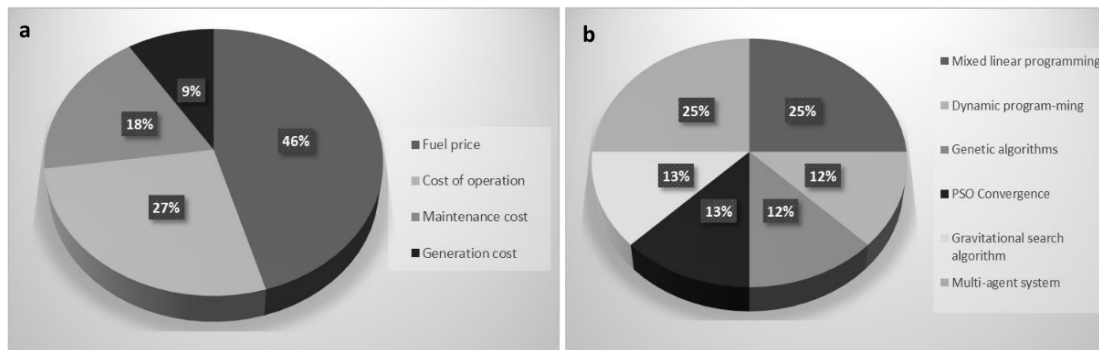


Figure 7. a) Economic variables regarding the cost of generation, b) relevant management techniques for economic variables regarding the cost of generation

A. Preset operating status

(28, 41–43), and (48) propose, as outputs of their management systems, pre-defined scenarios that are activated when the microgrid parameters reach previously defined values. These scenarios focus on directing the energy flow to meet a specific objective, maintaining the microgrid in islanded mode, feeding the storage components, or reducing the demand of the loads, among others (Table VII)

Table VII. Preset operating status

Ref.	Year	Management techniques	Preset operating status	Microgrid architecture	Control strategy	Microgrid generation
(28)	2017	Mixed linear programming	Continuous operation mode, power-sharing mode	Grid-connected mode	Centralized	Fuel cells, photovoltaic, grid connection
(40)	2014	Mixed linear programming	Power-sharing mode, connection status at the EV charging point	Grid-connected mode	Centralized	Photovoltaic, wind power, grid connection
(42)	2017	Mixed linear programming	Scenarios: charging and consumption of diesel generators, charging and consumption of solar panels, energy from batteries	Islanded mode	Centralized	Photovoltaic, diesel generators

(41)	2011	Mixed non-linear programming	Load switching, load shedding scenario, grid connection scenario, grid disconnection scenario	Grid-connected mode	Centralized	Micro gas turbines, fuel cells, wind power, photovoltaic, grid connection
(65)	2016	Non-linear programming	Cell charging scenario, EV charging, grid connection scenario, grid disconnection scenario	Grid-connected mode	Centralized	Fuel cell, photovoltaic, grid connection
(48)	2011	Rule-based approach	Load switching, load mode, mains connection -disconnection	Grid-connected mode	Centralized	Photovoltaic, micro gas turbine, connection to the main grid
(46)	2015	Rule-based approach in the load state	Load switching, load mode, mains connection-disconnection	Grid-connected mode	Centralized	Photovoltaic, wind power, micro gas turbine, grid connection
(18)	2015	Rule-based approach in the load state	Load switching, load mode, mains connection-disconnection	Grid-connected mode	Centralized	Photovoltaic, wind power, grid connection
(49)	2013	Rule-based approach	Charging mode, grid connection-disconnection, load disconnection, load connection scenario, panel consumption	Grid-connected mode	Centralized	Photovoltaic, connection to the grid
(23)	2016	Genetic algorithms	Grid connection-disconnection, control of generation sources	Grid-connected mode	Centralized	Photovoltaic, wind power, fuel cells, micro gas turbine, grid connection
(50)	2017	Memory-based genetic algorithms	Grid connection-disconnection, generation source control, load mode	Grid-connected mode	Centralized	Photovoltaic, wind, grid connection
(20)	2011	Genetic algorithm	Demand control response, battery charge-discharge, import-export to the grid, control of generation sources	Grid-connected mode	Centralized	Photovoltaic, grid connection
(32)	2016	Genetic algorithm	Demand control response, battery charge-discharge, EV charging, import-export to the grid, generation source control.	Grid-connected mode	Centralized	Photovoltaic, wind power, diesel generator, grid connection.
(33)	2015	Swarm optimization	Renewable energy generation scenario, grid connection scenario, supply, load scenario	Grid-connected mode	Centralized	Photovoltaic, wind power, grid connection

(51)	2016	Differential evolution	Demand control response, battery charge-discharge, import-export to the grid, control of generation sources	Grid-connected mode	Centralized	Photovoltaic, wind power, micro gas turbine, grid connection
(52)	2012	A self-adaptive gravitational search algorithm	Import-export to the grid, demand control response, battery charge-discharge	Grid-connected mode	Centralized	Photovoltaic, wind power, grid connection
(53)	2012	Modified bacterial foraging	State of charge, load switching, generation source control, import-export to the grid	Grid-connected mode	Centralized	Photovoltaic, wind power, fuel cells, grid connection
(54)	2014	Modified bacterial foraging	Load status, load switching, import-export to the grid	Grid-connected mode	Centralized	Wind power, micro gas turbine, grid connection
(36)	2017	Fuzzy logic	Demand control response, state of charge, import-export to the grid	Grid-connected mode	Centralized	Photovoltaic, wind power, grid connection
(38)	2016	Multi-agent system	Consumption hierarchy, demand control response, state of charge	Islanded mode	Decentralized	Photovoltaic, wind power
(63)	2013	Game theory	Control response, demand response, import-export to the grid, state of charge	Grid-connected mode	Decentralized	Photovoltaic, wind power, micro gas turbine, grid connection

The most relevant variables used in this category are shown in Fig. 8.

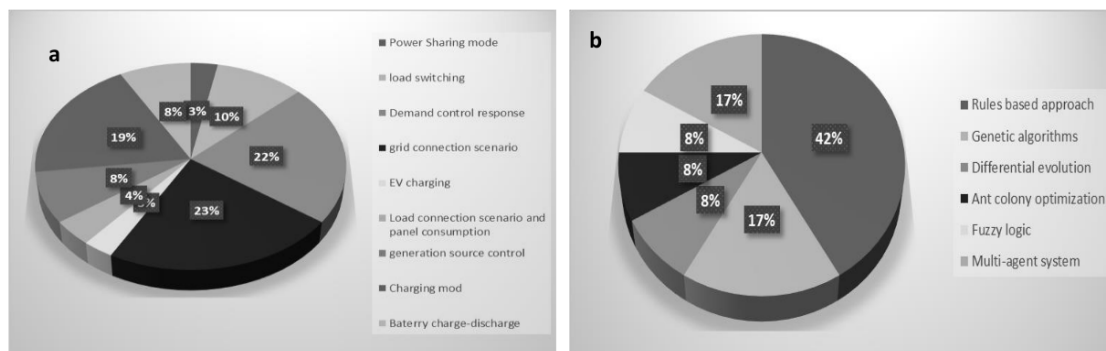


Figure 8. a) Output variables for the preset operating status, b) relevant management techniques regarding the output variables for the preset operating status

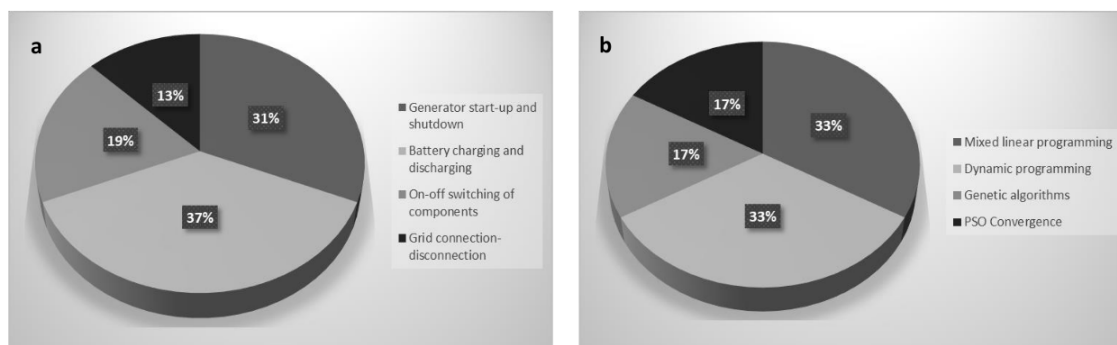
B. Binary decisions

In (26, 27, 30), and (43), the management systems' outputs correspond to the connection or disconnection of microgrid elements, as well as to the flow of energy (Table VIII).

Table VIII. Binary decisions

Ref.	Year	Management techniques	Binary decisions	Microgrid architecture	Control strategy	Microgrid generation
(27)	2016	Integer and mixed linear programming	Load disconnection, partial load supply, generator start-up, grid connection-disconnection, battery discharge-charge	Grid-connected mode	Centralized	Photovoltaic, wind power, diesel generators, grid connection
(30)	2017	Mixed linear programming	Charging-discharging of batteries, photovoltaic energy consumption and load, wind energy consumption and load	Islanded mode	Centralized	Photovoltaic, wind power
(31)	2013	Dynamic programming	On-off switching of components, heat flow, grid connection-disconnection, storage system charging-discharging	Grid-connected mode	Centralized	Wind power, grid connection
(26)	2016	Genetic algorithms	Generator start-up and shutdown, battery charging and discharging	Islanded mode	Centralized	Photovoltaic, diesel generators
(43)	2017	Dynamic programming	Charging-discharging of batteries, connection-disconnection of diesel generators	Islanded mode	Centralized	Diesel generators, photovoltaic
(57)	2016	PSO convergence	Charging-discharging of batteries, connection-disconnection of diesel generators	Islanded mode	Centralized	Photovoltaic, wind power, diesel generator

The most relevant variables used in this category are shown in Fig. 9.



4. Analysis

This systematic review shows the importance of microgrid components and their influence on the data to be considered by the management system. The importance is primarily evident in the type of generation of the microgrid, where solar irradiance is the most relevant input of the external category. The meteorological subsection, which pertains to more than 40 % of the papers studied, shows a more effective implementation in microgrids that have photovoltaic generation sources. The same trend is visible in the category of external variables related to generation power, where photovoltaic power prediction is the most recurrent, with 31 % of the papers studied. This also applies to the category of external variables, with wind speed being the second most relevant meteorological variable (31 %). Similarly, for generation power, wind energy prediction variable is present in 19 % of the papers studied, which contrasts with the implementation of microgrids that use fossil fuels as generation sources, (5 %). This can be better seen in Fig. 10a. These results show a clear trend regarding the implementation of renewable energies in microgrids.

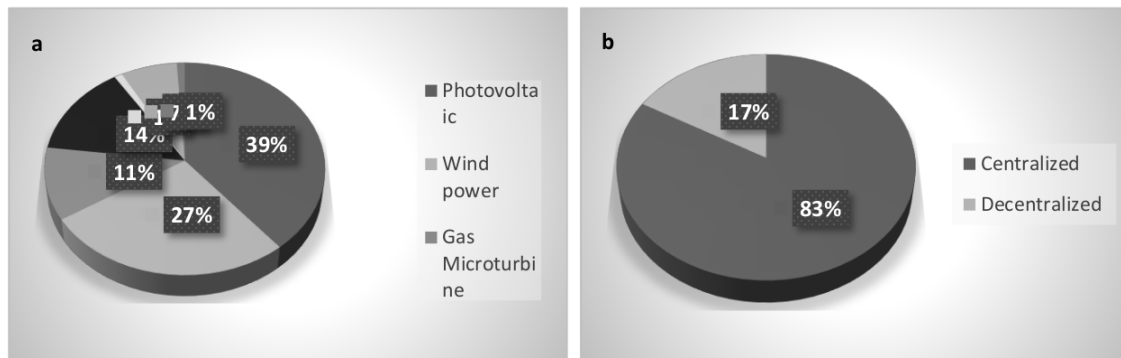


Figure 10. a) Microgrid generation in the reviewed papers, b) microgrid control strategies in the reviewed papers

Although some microgrid components influence the data used by the EMS, there is no significant impact. The methods for collecting and processing data are so varied that they do not reflect a significant statistical difference in the inputs and outputs of the management system. On the other hand, a more effective implementation of centralized control strategies is noticeable, which is present in 83 % of the papers studied (Fig. 10b). A meticulous analysis of the papers' year of publication shows a trend towards decentralized control strategies. This may be due to the fact that these strategies are more flexible and ensure a better fulfillment of the objectives, although the computational effort and resources required are more significant (16). The control techniques implemented by the management systems of the studied papers are so varied that they do not represent a significant statistical difference, as seen in Fig. 11a.

The inputs follow the needs of the management system modules and the specific components of the microgrid. This need is evident since more than 90 % of the papers studied implement some type of storage system, mainly batteries, whose state of charge and storage capacity are used for monitoring. The other variables in this category depend more on the type of loads that the microgrid must supply. The economic variables depend primarily on the microgrid architecture, as they are directly related to

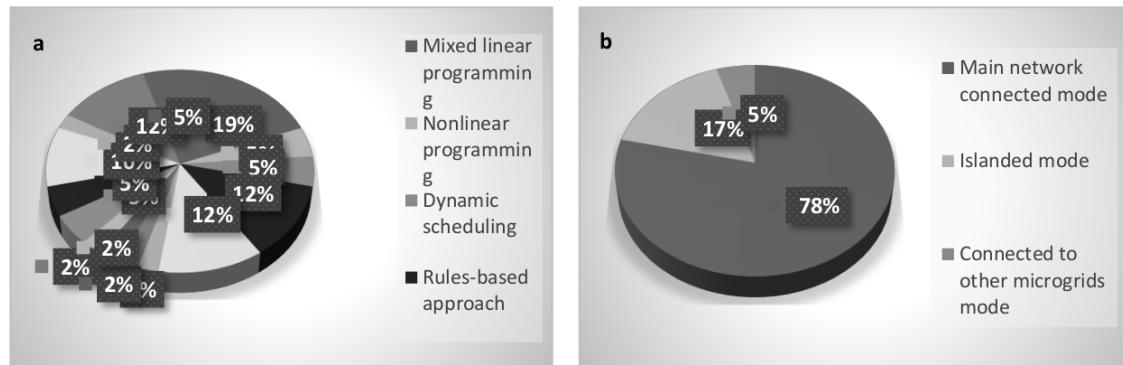


Figure 11. a) Microgrid control strategies in the reviewed papers, b) microgrid architecture in the reviewed papers

the connection to the main grid or other microgrids. If the microgrid is islanded, the economic variables focus on the costs of operation and the fuel prices, given that diesel generators or similar resources are used to guarantee a constant flow of energy. The connection with the primary grid entails a focus on the energy sales price and the operating costs. This type of architecture is the most used in the analyzed papers (78%) (Fig. 11b).

The output variables do not show any direct relationship with the EMS modules studied when compared to the input variables. The outputs depend more on how the author wants decision-making to take place, *e.g.*, by having binary decisions involving the connection or disconnection of microgrid components. Decisions on the generation and autonomy of the microgrid are the most implemented when compared to those aimed at managing the demand.

5. Conclusions

This review article started with a brief description of the management systems applied to microgrids, in order to determine the functions they should perform. With these definitions, the data to be collected and its associated variables were determined, which would be the input for a correct EMS performance. With these variables as a basis, an analysis of their properties was conducted. The variables that shared properties were grouped into categories while considering the functions for which they provide information. In light of the above, this article proposes a taxonomy for the input and output variables of a microgrid management system.

Progress has been made in microgrid management using different control and management techniques and strategies, evaluating their pros and cons. However, it is relevant to consider other factors that may affect performance, such as the nature of the variables and the topology of the microgrid, among others.

It is important to know the variables that serve as the inputs and outputs of management systems in order to ensure a good microgrid performance. In this vein, this paper helps those interested in delving into the implementation of these systems. The proposed taxonomy could serve as a guide to perform the conceptual and basic engineering of projects in this sector.

Given that most of the papers studied used simulation environments, it is also necessary to test management systems in real-world scenarios to evaluate their effects and performance.

6. Author contributions

These are contributions of each author according to the CRediT taxonomy:

- **Carlos Santiago Vidal Martínez:** Writing – original draft
- **Maximiliano López Bueno:** Writing – review and editing
- **Juan Fernando Flórez Marulanda:** Writing – review and editing
- **Álvaro René Restrepo Garcés:** Writing – review and editing

References

- [1] Z. Shuai *et al.*, “Microgrid stability: Classification and a review,” *Renew. Sustain. Energy Rev.*, vol. 58, pp. 167-179, 2016. <https://doi.org/10.1016/j.rser.2015.12.201> ↑2
- [2] O. O. Approach, K. Rahbar, S. Member, J. Xu, and R. Zhang, “Real-time energy storage management for renewable integration in microgrid: An off-line optimization approach,” *IEEE Trans. Smart Grid*, vol. 6, no. 1, pp. 124-134, 2015. <https://doi.org/10.1109/TSG.2014.2359004> ↑2
- [3] C. L. Nge, I. U. Ranaweera, O. M. Midtgård, and L. Norum, “A real-time energy management system for smart grid integrated photovoltaic generation with battery storage,” *Renew. Energy*, vol. 130, pp. 774-785, 2019. <https://doi.org/10.1016/j.renene.2018.06.073> ↑3
- [4] W. El-Baz, P. Tzscheutschler, and U. Wagner, “Integration of energy markets in microgrids: A doublesided auction with device-oriented bidding strategies,” *Appl. Energy*, vol. 241, pp. 625-639, 2019. <https://doi.org/10.1016/j.apenergy.2019.02.049> ↑3
- [5] K. Markov and N. Rajaković, “Multi-energy microgrids with ecotourism purposes: The impact of the power market and the connection line,” *Energy Convers. Manag.*, vol. 196, pp. 1105-1112, 2019. <https://doi.org/10.1016/j.enconman.2019.05.048> ↑3
- [6] T. Ahmad and D. Zhang, “A critical review of comparative global historical energy consumption and future demand: The story told so far,” *Energy Reports*, vol. 6, pp. 1973-1991, 2020. <https://doi.org/10.1016/j.egyrs.2020.07.020> ↑3
- [7] L. Miller and R. Carriveau, “Energy demand curve variables – An overview of individual and systemic effects,” *Sustain. Energy Technol. Assessments*, vol. 35, pp. 172-179, 2019. <https://doi.org/10.1016/j.seta.2019.07.006> ↑3

- [8] R. S. Jayashree and P. J. A. Kenis, "Micro fuel cells for portable applications," *AICHE Annu. Meet. Conf. Proc.*, no. 42, art. 3390, 2005. ↑3
- [9] E. Bullich-massagué, F. Díaz-gonzález, M. Aragués-peñalba, F. Girbau-llistiuella, P. Olivella-rosell, and A. Sumper, "Microgrid clustering architectures," *Appl. Energy*, vol. 212, pp. 340-361, 2018. <https://doi.org/10.1016/j.apenergy.2017.12.048> ↑3
- [10] J. Shen, C. Jiang, Y. Liu, and X. Wang, "A microgrid energy management system and risk management under an electricity market environment," *IEEE Access*, vol. 4, pp. 2349-2356, 2016. <https://doi.org/10.1109/ACCESS.2016.2555926> ↑3,9
- [11] D. Giaouris et al., "A systems approach for management of microgrids considering multiple energy carriers, stochastic loads, forecasting and demand side response," *Appl. Energy*, vol. 226, pp. 546-559, 2018. <https://doi.org/10.1016/j.apenergy.2018.05.113> ↑3
- [12] D. Petreus, R. Etz, T. Patarau, and M. Cirstea, "An islanded microgrid energy management controller validated by using hardware-in-the-loop emulators," *Int. J. Electr. Power Energy Syst.*, vol. 106, pp. 346-357, 2019. <https://doi.org/10.1016/j.ijepes.2018.10.020> ↑3
- [13] W. Su and J. Wang, "Energy management systems in microgrid operations," *Electr. J.*, vol. 25, no. 8, pp. 45-60, 2012. <https://doi.org/10.1016/j.tej.2012.09.010> ↑3
- [14] L. A. Dao, A. Dehghani-Pilehvarani, A. Markou, and L. Ferrarini, "A hierarchical distributed predictive control approach for microgrids energy management," *Sustain. Cities Soc.*, vol. 48, art. 101536, 2019. <https://doi.org/10.1016/j.scs.2019.101536> ↑3
- [15] T. Morstyn, B. Hredzak, and V. G. Agelidis, "Control strategies for microgrids with distributed energy storage systems: An overview," *IEEE Trans. Smart Grid*, vol. 9, no. 4, pp. 3652-3666, 2018. <https://doi.org/10.1109/TSG.2016.2637958> ↑3,4
- [16] M. F. Zia, E. Elbouchikhi, and M. Benbouzid, "Microgrids energy management systems: A critical review on methods, solutions, and prospects," *Appl. Energy*, vol. 222, pp. 1033-1055, 2018. <https://doi.org/10.1016/j.apenergy.2018.04.103> ↑3,4,6,19
- [17] T. Dragicevic, X. Lu, J. C. Vasquez, and J. M. Guerrero, "DC microgrids - Part I: A review of control strategies and stabilization techniques," *IEEE Trans. Power Electron.*, vol. 31, no. 7, pp. 4876-4891, 2016. <https://doi.org/10.1109/TPEL.2015.2478859> ↑3
- [18] J. Pascual, J. Barricarte, P. Sanchis, and L. Marroyo, "Energy management strategy for a renewable-based residential microgrid with generation and demand forecasting," *Appl. Energy*, vol. 158, pp. 12-25, 2015. <https://doi.org/10.1016/j.apenergy.2015.08.040> ↑3,7,8,10,16
- [19] International Electrotechnical Commission, "IEC 61970-1:2005 | IEC Webstore | automation, cyber security, smart city, smart energy, smart grid," pp 5-7 2005. <https://webstore.iec.ch/publication/6208> (accessed Oct. 16, 2020). ↑4
- [20] C. C. S. Duan and T. C. B. Liu, "Smart energy management system for optimal microgrid economic operation," *IET Rene. Power Gen.*, vol. 5, no. 3, pp. 258-267, 2011. <https://doi.org/10.1049/iet-rpg.2010.0052> ↑4,8,11,16
- [21] A. Ahmad Khan, M. Naeem, M. Iqbal, S. Qaisar, and A. Anpalagan, "A compendium of optimization objectives, constraints, tools and algorithms for energy management in microgrids,"

- Renew. Sustain. Energy Rev.*, vol. 58, pp. 1664-1683, 2016. <https://doi.org/10.1016/j.rser.2015.12.259> ↑4
- [22] M. Hu, J. W. Xiao, S. C. Cui, and Y. W. Wang, "Distributed real-time demand response for energy management scheduling in smart grid," *Int. J. Electr. Power Energy Syst.*, vol. 99, pp. 233-245, 2018. <https://doi.org/10.1016/j.ijepes.2018.01.016> ↑4
- [23] M. Elsied, A. Oukaour, T. Youssef, H. Gualous, and O. Mohammed, "An advanced real time energy management system for microgrids," *Energy*, vol. 114, pp. 742-752, 2016. <https://doi.org/10.1016/j.energy.2016.08.048> ↑5, 8, 12, 16
- [24] K. Say, M. John, and R. Dargaville, "Power to the people : Evolutionary market pressures from residential PV battery investments in Australia," *Energy Policy*, vol. 134, art. 110977, 2019. <https://doi.org/10.1016/j.enpol.2019.110977> ↑5
- [25] T. R. Nudell, M. Brignone, M. Robba, A. Bonfiglio, F. Delfino, and A. Annaswamy, "A dynamic market mechanism for combined heat and power microgrid energy management," *IFAC-PapersOnLine*, vol. 50, no. 1, pp. 10033-10039, 2017. <https://doi.org/10.1016/j.ifacol.2017.08.2040> ↑5
- [26] S. Chalise, J. Sternhagen, T. M. Hansen, and R. Tonkoski, "Energy management of remote microgrids considering battery lifetime," *Electr. J.*, vol. 29, no. 6, pp. 1-10, 2016. <https://doi.org/10.1016/j.tej.2016.07.003> ↑5, 8, 13, 14, 17, 18
- [27] J. Shen, C. Jiang, Y. Liu, and J. Qian, "Electric power components and systems a microgrid energy management system with demand response for providing grid peak shaving a microgrid energy management system with demand response for providing grid peak shaving," *Elec. Power Comp. Syst.*, vol. 44, no. 8, 2016. <https://doi.org/10.1080/15325008.2016.1138344> ↑6, 9, 10, 12, 17, 18
- [28] S. Sukumar, H. Mokhlis, S. Mekhilef, and K. Naidu, "Mix-mode energy management strategy and battery sizing for economic operation of grid-tied microgrid," *Energy*, vol. 118, pp. 1322-1333, 2017. <https://doi.org/10.1016/j.energy.2016.11.018> ↑5, 6, 9, 10, 15
- [29] G. Comodi et al., "Multi-apartment residential microgrid with electrical and thermal storage devices: Experimental analysis and simulation of energy management strategies," *Appl. Energy*, vol. 137, pp. 854-866, 2015. <https://doi.org/10.1016/j.apenergy.2014.07.068> ↑5, 6, 12, 13
- [30] M. H. Amrollahi, S. Mohammad, and T. Bathaee, "Techno-economic optimization of hybrid photovoltaic / wind generation together with energy storage system in a stand-alone micro-grid subjected to demand response," *Appl. Energy*, vol. 202, pp. 66-77, 2017. <https://doi.org/10.1016/j.apenergy.2017.05.116> ↑5, 6, 13, 14, 17, 18
- [31] M. Štřelec and J. Berka, "Microgrid energy management based on approximate dynamic programming," in *IEEE PES ISGT Europe 2013*, Lyngby, Denmark, 2013, pp. 1-5. <https://doi.org/10.1109/ISGTEurope.2013.6695439> ↑5, 6, 12, 18
- [32] S. Golshannavaz, S. Afsharnia, and P. Siano, "A comprehensive stochastic energy management system in reconfigurable microgrids," *Int. J. Energy, Res.*, vol. 40, no. 11, pp. 1518-1531, 2016. <https://doi.org/10.1002/er.3536> ↑5, 6, 12, 16

- [33] J. Radosavljevi, M. Jevti, and D. Klimenta, "Engineering optimization energy and operation management of a microgrid using particle swarm optimization," *Energy Opt.*, vol. 48, no. 5, pp. 811-813, 2015. <https://doi.org/10.1080/0305215X.2015.1057135> ↑6, 13, 16
- [34] M. Marzband, E. Yousefnejad, A. Sumper, and J. L. Domínguez-García, "Real time experimental implementation of optimum energy management system in stand-alone Microgrid by using multi-layer ant colony optimization," *Int. J. Electr. Power Energy Syst.*, vol. 75, pp. 265-274, 2016. <https://doi.org/10.1016/j.ijepes.2015.09.010> ↑6, 11, 12
- [35] M. Marzband, M. Ghadimi, A. Sumper, and J. L. Domínguez-garcía, "Experimental validation of a real-time energy management system using multi-period gravitational search algorithm for microgrids in islanded mode," *Appl. Energy*, vol. 128, pp. 164-174, 2014. <https://doi.org/10.1016/j.apenergy.2014.04.056> ↑6, 10, 14
- [36] D. Arcos-Aviles, J. Pascual, F. Guinjoan, L. Marroyo, P. Sanchis, and M. P. Marietta, "Low complexity energy management strategy for grid profile smoothing of a residential grid-connected microgrid using generation and demand forecasting," *Appl. Energy*, vol. 205, pp. 69-84, 2017. <https://doi.org/10.1016/j.apenergy.2017.07.123> ↑6, 12, 17
- [37] Y.-K. Chen, Y.-C. Wu, C.-C. Song, and Y.-S. Chen, "Design and implementation of energy management system with fuzzy control for DC microgrid systems," *IEEE Trans. Power Elect.*, vol. 28, no. 4, pp. 1563-1570, April 2013. <https://doi.org/10.1109/TPEL.2012.2210446> ↑6
- [38] T. Bogaraj and J. Kanakaraj, "Intelligent energy management control for independent microgrid," *Sadhana - Acad. Proc. Eng. Sci.*, vol. 41, no. 7, pp. 755-769, 2016. <https://doi.org/10.1007/s12046-016-0515-6> ↑6, 10, 14, 17
- [39] A. Anvari-moghaddam, A. Rahimi-kian, M. S. Mirian, and J. M. Guerrero, "A multi-agent based energy management solution for integrated buildings and microgrid system," *Appl. Energy*, vol. 203, pp. 41-56, 2017. <https://doi.org/10.1016/j.apenergy.2017.06.007> ↑6, 11, 13
- [40] C. Corchero and M. Cruz-zambrano, "Optimal energy management for a residential microgrid including a vehicle-to-grid system," *IEEE Trans. Smart Grid*, vol. 5, no. 4, pp. 2163-2172, 2014. <https://doi.org/10.1109/TSG.2014.2318836> ↑7, 8, 10, 12, 15
- [41] A. G. Tsikalakis and N. D. Hatziargyriou, "Centralized control for optimizing microgrids operation," *IEEE Trans. Energy Conv.*, vol. 23, no. 1, pp. 241-248, March 2008. <https://doi.org/10.1109/TEC.2007.914686> ↑7, 8, 10, 15, 16
- [42] N. Anglani, G. Oriti, and M. Colombini, "Optimized energy management system to reduce fuel consumption in remote military microgrids," *IEEE Trans. Ind. App.*, vol. 53, no. 6, pp. 5777-5785, 2017. <https://doi.org/10.1109/TIA.2017.2734045> ↑7, 8, 9, 10, 13, 14, 15
- [43] B. Heymann, J. F. Bonnans, P. Martinon, F. J. Silva, and F. L. G. Jiménez-estévez, "Continuous optimal control approaches to microgrid energy management," *Energy Syst.*, vol. 9, pp. 59-77, 2017. <https://doi.org/10.1007/s12667-016-0228-2> ↑7, 8, 9, 13, 14, 15, 17, 18
- [44] J. B. Almada, R. P. S. Leão, R. F. Sampaio, and G. C. Barroso, "A centralized and heuristic approach for energy management of an AC microgrid," *Renew. Sustain. Energy Rev.*, vol. 60, pp. 1396-1404, 2016. <https://doi.org/10.1016/j.rser.2016.03.002> ↑7, 8, 11

- [45] K. Hassan Youssef, "Optimal management of unbalanced smart microgrids for scheduled and unscheduled multiple transitions between grid-connected and islanded modes," *Electr. Power Syst. Res.*, vol. 141, pp. 104-113, 2016. <https://doi.org/10.1016/j.epsr.2016.07.015> ↑7
- [46] A. Choudar, D. Boukhetala, S. Barkat, and J. Brucker, "A local energy management of a hybrid PV - storage based distributed generation for microgrids," *Energy Convers. Manag.*, vol. 90, pp. 21-33, 2015. <https://doi.org/10.1016/j.enconman.2014.10.067> ↑7, 8, 10, 12, 13, 16
- [47] P. P. Vergara, J. C. López, L. C. P. Silva, and M. J. Rider, "Security-constrained optimal energy management system for three-phase residential microgrids," *Electr. Power Syst. Res.*, vol. 146, pp. 371-382, 2017. <https://doi.org/10.1016/j.epsr.2017.02.012> ↑8
- [48] H. Kanchev, D. Lu, F. Colas, V. Lazarov, B. Francois, and S. Member, "Energy management and operational planning of a microgrid with a PV-based active generator for smart grid applications," *IEEE Trans. Ind. Electronics*, vol. 58, no. 10, pp. 4583-4592, 2011. ↑8, 9, 10, 11, 12, 15, 16
- [49] M. Sechilariu, B. Wang, and F. Locment, "Building-integrated microgrid: Advanced local energy management for forthcoming smart power grid communication," *Energy Build.*, vol. 59, pp. 236-243, 2013. <https://doi.org/10.1016/j.enbuild.2012.12.039> ↑8, 11, 16
- [50] A. Askarzadeh, "A memory-based genetic algorithm for optimization of power generation in a microgrid," *IEEE Trans. Sust. Energy*, vol. 9, no. 3, pp. 1081-1089, 2017. <https://doi.org/10.1109/TSTE.2017.2765483> ↑8, 9, 11, 12, 16
- [51] N. Tiwari and L. Srivastava, "Generation scheduling and micro-grid energy management using differential evolution algorithm," *2016 Int. Conf. Circuit, Power Comp. Tech. (ICCPCT)*, Nagercoil, India, 2016, pp. 1-7. <https://doi.org/10.1109/ICCPCT.2016.7530218> ↑8, 9, 11, 17
- [52] T. Niknam, F. Golestaneh, and A. Malekpour, "Probabilistic energy and operation management of a microgrid containing wind / photovoltaic / fuel cell generation and energy storage devices based on point estimate method and self-adaptive gravitational search algorithm," *Energy*, vol. 43, no. 1, pp. 427-437, 2012. <https://doi.org/10.1016/j.energy.2012.03.064> ↑8, 9, 17
- [53] M. Motevasel and T. Niknam, "Multi-objective energy management of CHP (combined heat and power)-based micro-grid," *Energy*, vol. 51, pp. 123-136, 2013. <https://doi.org/10.1016/j.energy.2012.11.035> ↑8, 12, 17
- [54] M. Motevasel and A. R. Seifi, "Expert energy management of a micro-grid considering wind energy uncertainty," *Energy Convers. Manag.*, vol. 83, pp. 58-72, 2014. <https://doi.org/10.1016/j.enconman.2014.03.022> ↑8, 17
- [55] G. Kyriakarakos, A. I. Dounis, K. G. Arvanitis, and G. Papadakis, "A fuzzy logic energy management system for polygeneration microgrids," *Renew. Energy*, vol. 41, pp. 315-327, 2012. <https://doi.org/10.1016/j.renene.2011.11.019> ↑8, 12
- [56] D. Tenfen and E. C. Finardi, "A mixed integer linear programming model for the energy management problem of microgrids," *Electr. Power Syst. Res.*, vol. 122, pp. 19-28, 2015. <https://doi.org/10.1016/j.epsr.2014.12.019> ↑9, 10, 12
- [57] M. Abedini, M. H. Moradi, and S. M. Hosseinian, "Optimal management of microgrids including renewable energy sources using GPSO-GM algorithm," *Renew. Energy*, vol. 90, pp. 430-439, 2016. <https://doi.org/10.1016/j.renene.2016.01.014> ↑10, 14, 18

- [58] G. K. Venayagamoorthy and R. Sharma, "Dynamic energy management system for a smart microgrid," *IEEE Trans. Neural Networks Learning Syst.*, vol. 27, no. 8, pp. 1-14, 2016. <http://dx.doi.org/10.1109/TNNLS.2016.2514358> ↑10, 13
- [59] E. De Santis, A. Rizzi, and A. Sadeghian, "Hierarchical genetic optimization of a fuzzy logic system for energy flows management in microgrids," *Appl. Soft Comput. J.*, vol. 60, pp. 135-149, 2017. <https://doi.org/10.1016/j.asoc.2017.05.059> ↑11
- [60] C. S. Karavas, G. Kyriakarakos, K. G. Arvanitis, and G. Papadakis, "A multi-agent decentralized energy management system based on distributed intelligence for the design and control of autonomous polygeneration microgrids," *Energy Convers. Manag.*, vol. 103, pp. 166-179, 2015. <https://doi.org/10.1016/j.enconman.2015.06.021> ↑11, 13
- [61] H. S. V. S. K. Nunna, A. M. Saklani, A. Sesetti, S. Battula, S. Doolla, and D. Srinivasan, "Multi-agent based demand response management system for combined operation of smart microgrids," *Sustain. Energy, Grids Networks*, vol. 6, pp. 25-34, 2016. <https://doi.org/10.1016/j.segan.2016.01.002> ↑10
- [62] L. Ma, N. Liu, J. Zhang, and W. Tushar, "Energy management for joint operation of CHP and PV prosumers inside a grid-connected microgrid: A game theoretic approach," *IEEE Tran. Ind. Informatics*, vol. 12, no. 5, 2016. <https://doi.org/10.1109/TII.2016.2578184> ↑13
- [63] G. E. Asimakopoulou, A. L. Dimeas, and N. D. Hatziargyriou, "Leader-follower strategies for energy management of multi-microgrids," *IEEE Trans. Smart Grid*, vol. 4, no. 4, pp. 1909-1916, Dec. 2013. <https://doi.org/10.1109/TSG.2013.2256941> ↑13, 17
- [64] H. S. V. S. Kumar Nunna and S. Doolla, "Energy management in microgrids using demand response and distributed storage – A multiagent approach," *IEEE Trans. Power Delivery*, vol. 28, no. 2, pp. 939-947, April 2013. <https://doi.org/10.1109/TPWRD.2013.2239665> ↑14
- [65] L. Kumar, S. R. K. A. Verma, B. K. Panigrahi, and R. Kumar, "An operation window constrained strategic energy management (OWCSEM) of micro grid with electric vehicle and distributed resources," *IET Gen. Trans. Dist.*, vol. 11, no. 3, 615-626. <https://doi.org/10.1049/iet-gtd.2016.0654> ↑16

Carlos Santiago Vidal Martínez

Born in Popayán, Colombia. He obtained an engineering degree in Industrial Automation from Universidad del Cauca. Since 2023, he has been employed as a full professor at the Department of Engineering of Corporación Universitaria Autónoma del Cauca. His areas of interest include renewable sources, energy transition, energy management, and energy generation and distribution.

Email: carlosvidal@unicauca.edu.co

Maximiliano Bueno López

Born in Pereira, Colombia. He obtained an Electronics Engineering degree and a Master's degree in Electrical Engineering from Universidad Tecnológica de Pereira, as well as a PhD in Engineering from Universidad Nacional Autónoma de México. He is an associate professor of the Electronics,

Instrumentation, and Control Department of Universidad del Cauca. His areas of interest include rural energy, signal analysis, and control theory.

Email: mbuenol@unicauca.edu.co

Juan Fernando Flórez Marulanda

Born in Cali, Colombia. He obtained an engineering degree in Electronics and Telecommunications from Universidad del Cauca. Since 2003, he has been employed as a full professor by the Department of Electronics and Telecommunications Engineering of Universidad del Cauca. His areas of interest include industrial instrumentation, process control, energy efficiency, and AMR/AMI systems.

Email: jflores@unicauca.edu.co

Álvaro R. Restrepo Garcés

In 1997, he graduated as an Industrial Engineer from Universidad Nacional de Colombia. Since April 2001, he works as a professor of the Electronics, Instrumentation, and Control Department of Universidad del Cauca, Popayán, Colombia. In 2001, he specialized in University Teaching, and he obtained a specialist degree in Project Management from Universidad del Cauca in 2002. In 2006, he graduated from the Master's program in Engineering of Universidad del Valle, Colombia. In 2016, he obtained a Doctoral degree in Engineering from Universidad del Valle, Colombia. He currently works as the Director of the Regionalization Center of Universidad del Cauca. His main areas of interest are project planning in the industrial sector, energy portfolio optimization and modeling, energy markets, and renewable energy sources.

Email: arestrepo@uniucauca.edu.co

